Numerical modelling of the microphysical foundation of astrophysical particle acceleration

C Schreiner
25738356

Thesis submitted for the degree *Philosophiae Doctor* in Space Physics at the Potchefstroom Campus of the North-West University

Promoter: Prof F Spanier

November 2016

Abstract

The acceleration and transport of solar energetic particles have been intensively studied ever since the discovery of relativistic particles originating from the Sun. Both processes are tightly connected to the dynamics of the solar wind and the turbulent interactions of plasma waves. While advances in both theoretical modeling and observations have been made over the years, there are still many details which are not understood yet. Solar wind turbulence on its own is a complicated matter, and especially the regime of kinetic turbulence poses many open questions.

Kinetic turbulence involves plasma waves at high frequencies and small wave lengths, where their interactions with the charged particles in the plasma become important. Compared to the well-understood energy spectrum in the inertial range, a steepening of the spectral slope is expected in the kinetic regime, which is generally attributed to the effects of dispersion and energy dissipation by resonant interactions with the particles. However, no complete model for the composition and behavior of the turbulent waves in this so-called dissipation range is available, yet. Observations suggest that kinetic Alfvén waves are responsible for turbulence in the dissipation range. However, whistler waves, which are also detected in various regions of the solar wind, may also contribute. This latter case is especially interesting, because whistler waves allow for the transport of energy to frequencies above the proton cyclotron frequency and may, therefore, interact with both thermal and high energy electrons in the solar wind plasma.

A particle-in-cell code is employed to simulate dispersive waves and their interaction with charged particles in the plasma. As a preliminary study and a first step towards simulations of dissipation range turbulence, the cyclotron resonance of thermal protons and dispersive Alfvén waves and their strongly damped analog at higher frequencies, the proton cyclotron waves, is modeled. To quantitatively analyze the dissipation of these waves, a method is developed which allows to extract the waves' damping rates from simulation data. Extensive tests show that cyclotron damping is recovered correctly in the simulation, which is a crucial prerequisite for a correct model of dissipation range turbulence.

Similar to the case of turbulence, sophisticated models for the transport of solar energetic particles in an environment that is dominated by non-dispersive waves are available. However, the effect of dispersive waves on particle transport is less well-understood, which is partly due to the more difficult treatment of dispersive waves in theoretical models. The theoretical approach to describe particle transport is usually based on the quasi-linear approximation, which assumes that resonant scattering processes can be described by diffusion in phase space.

Using particle-in-cell simulations again, the resonant interaction of energetic electrons and dispersive waves is studied. The particles are scattered off of the waves' electromagnetic fields, creating a specific resonance pattern in phase space. The simulation data is compared to analytical predictions, which can be obtained from a model originally based on magnetostatic quasi-linear theory and which has recently been enhanced in order to allow for the description of dispersive waves. While the model predictions and the simulation results generally agree, it can be seen that the resonant interaction of energetic particles and a single wave does not lead to diffusion, but rather to trapping of the particles in the electromagnetic fields of the wave. Diffusion can only occur when several waves with different frequencies, wave lengths, or directions of propagation are present. Even though these simulations do not model particle transport in turbulence, they contribute to a better understanding of the micro-physical properties of the scattering processes which are responsible for the transport and acceleration of solar energetic particles.

Finally, kinetic turbulence is directly studied in simulations. A set of initially excited whistler waves is used as a seed population for the development of a turbulent cascade. Whistler waves are chosen because they allow for a continuation of the spectrum above the proton cyclotron frequency into a regime where the interaction of the waves with electrons becomes dominant. The simulations are analyzed especially with regard to the shape of the energy spectrum, since very little is known about the typical spectral index. However, no consistent picture of the dependence of the spectral shape on the physical parameters is obtained, yet. Extended parameter studies, which might yield more conclusive results, are hindered by the limited amount of computational resources available for this work. They remain as an eligible task for future projects.

Despite the absence of a detailed picture of kinetic turbulence, the simulations support the idea that the magnetic energy spectrum in the kinetic regime is steeper than in Alfvénic turbulence. It can also be assumed that a spectral break is produced at the transition into the dissipation range. The spectrum forms an even steeper power law after the break.

Choosing two similar setups for simulations of whistler turbulence as a basis, the transport of energetic electrons in kinetic turbulence is investigated. The analysis shows that the steep energy spectra in the kinetic regime lead to a particular dominance of waves at low wave numbers. These waves carry most of the energy and, thus, are most important for the interactions with the energetic particles. Although particles may resonate with waves at higher wave numbers (in the dispersive or dissipative regime), these interactions do not seem to contribute significantly to the transport mechanism.

Comparison with a theoretical model suggests that the turbulent spectrum can be approximated by the relatively flat regime at low wave numbers, before the spectral break is encountered. Although the model predictions are not very accurate, the basic features of the pitch angle diffusion coefficient derived from the particle data can be recovered. This is especially interesting, since the model is derived for Alfvénic turbulence.

Keywords

solar wind, heliosphere, turbulence, kinetic plasma, plasma waves, wave damping, particle transport, scattering, particle-in-cell, numerical simulation

Contents

Preface

The Sun has been studied by humans for thousands of years. However, details have become known only since the introduction of the first telescopes in the early seventeenth century, and a more complete understanding of the physical processes has been obtained only during the past century. Since the middle of the twentieth century, it has become obvious that the Sun is not located in perfect vacuum, but is the source of a permanent stream of charged particles, which has been named the *solar wind*. The complex dynamics of the solar wind plasma has soon become the focus of a new area in physical science.

The solar wind constitutes the connection between the energetic processes at the surface of the Sun and the physics of the planetary atmospheres or ionospheres. The direct observation of the solar wind has become possible by means of satellite measurements, both close to the Earth and farther away, at various distances from the Sun. This has lead to the establishment of a new discipline of space weather research and forecasts, the latter becoming more and more important to predict the impact of energetic events originating near the Sun on the complex electronic devices on and near Earth and to protect satellites and other equipment from the hazardous effects of highly energetic charged particles.

Over the past decades, the measurements of the solar wind plasma have become more and more detailed and comprehensive, and the theoretical models describing the physical processes responsible for the observed data have become more sophisticated. Additionally to the two classical pillars of physics, observation and (analytical) theory, the field of *numerical experiments* has developed. Especially in astrophysics or space physics, where no laboratory experiments under externally defined conditions are possible, computer simulations are a valuable tool to test theories and reproduce observations. Furthermore, a consistent numerical model can even be applied to physical regimes which are not accessible to observation and inadequately described by theory, thus opening new windows for the exploration of space.

The work at hand is concerned with one of the latter cases, namely the micro-physics of space plasma turbulence and the transport of energetic particles. Turbulence in itself is a complicated phenomenon. Solar wind turbulence in particular can only be observed from a few points in space (i.e. the positions of satellites), producing mainly time series of the electromagnetic fluctuations in the plasma. Thus, the observational data cannot give a complete picture of the turbulence and yields only reduced spectra. Nonetheless, advances in the research of turbulence in a magnetized plasma together with observations have lead to a rather complete and consistent model of the solar wind turbulence in the long wavelength, low frequency regime of the so-called *inertial range*. As the turbulent cascade progresses to smaller and smaller spatial scales and higher frequencies, the physical processes involved in the production of the turbulent cascade change and a different model has to be found. However, no complete theory for this *kinetic* or *dissipation range turbulence* is available so far, and current satellites are not capable of providing sufficiently detailed data to narrow down the range of possible models. At this point, self-consistent computer simulations can help out and allow to shed some light on the complex processes leading to kinetic turbulence. This especially requires a microscopic approach in order to model the necessary interactions of electromagnetic fields and the charged particles in the plasma.

Apart from studying plasma turbulence, which is a phenomenon mainly involving the thermal particles in the plasma, it is also interesting to analyze its effect on the transport of *solar energetic particles*. As the name suggests, these are highly energetic particles which are produced in the vicinity of the Sun (e.g. in solar flares) or accelerated at large scale shock fronts (e.g. shocks driven by coronal mass ejections). These particles can reach relativistic speeds and their transport is dominated by the interaction with magnetic field fluctuations. Since individual particles cannot be marked and tracked on their journey through the solar wind, our knowledge about these particles comes from the statistical analysis of large numbers of particle detections. Again, theory and observation have lead to a consistent picture of particle acceleration and transport in a limited physical regime. Especially the transport of protons, which mostly interact with the magnetic fields of plasma waves in the inertial range of solar wind turbulence, is well-understood. However, little is known about the effect of kinetic turbulence on the transport of particles. Energetic electrons are, in particular, assumed to interact with plasma waves in the dissipation range of the turbulent spectrum. In contrast to reality, numerical simulations allow to track individual particles and to analyze their trajectories in detail. Thus the characteristics of the interaction processes can be investigated on a micro-physical level. From the behavior of single particles it is then possible to derive statistical properties of the whole particle population.

The two problems described above, i.e. the composition and behavior of kinetic turbulence and the transport characteristics of energetic particles on kinetic scales, are addressed in the work at hand, using a self-consistent numerical approach to model the micro-physics of wave-particle interactions in simulations. The thesis is organized in five chapters, beginning with a brief introduction to the macroscopic phenomena observed at the Sun and in the solar wind in Chapter 1. However, since the work is focused on the micro-physical properties of the solar wind plasma, detailed explanations are omitted. Chapter 2 presents an overview of kinetic plasma theory and provides information on the physics of wave modes, plasma turbulence, and particle transport. Besides well-established theoretical models it also includes a newly derived approach to describe the interaction of energetic particles and kinetic plasma waves in Sect. 2.6.2. The numerical approach used for the simulations is summarized in Chapter 3. The description is focused on the particle-in-cell code ACRONYM, including a general overview of its features and a more detailed presentation of recent extensions to the code in Sect. 3.3. Chapter 3 also explains the tools developed to analyze the simulation data with respect to the topics of this thesis, including a new method to measure dissipation processes such as wave damping (Sect. 3.4.2). The simulations and results are presented in Chapter 4, which is divided into three major sections. Section 4.1 discusses simulations of cyclotron damped waves. This study analyzes damping processes in kinetic simulations, since an accurate model of dissipation processes is crucial for simulations of dissipation range turbulence. Particle transport is examined in Sect. 4.2, which focuses on the resonant interaction of energetic electrons and dispersive waves. In a simplified setup the simulation results are compared to theoretical predictions to establish a detailed understanding of the microscopic processes involved in the scattering of particles and waves. The simulations can also be seen as a validation of the numerical method and a test of the theoretical basis, both of which are important steps towards a more complete picture of particle transport in kinetic turbulence. Turbulence simulations are discussed in Sect. 4.3, especially focusing on the spectral shape of the turbulent energy cascade and particle transport in whistler turbulence. Finally, Chapter 5 presents a short summary and conclusions.

1 Introduction

1.1 Different Kinds of Plasma

Although most of the matter in the universe is in the plasma state, the concept of plasma is often perceived as unfamiliar and exotic. Plasmas are seldom encountered in daily experience, maybe with a few exceptions, such as flames or discharge tubes. This chapter therefore aims at pointing to a few “different kinds” of plasmas, i.e. plasmas in different physical regimes, to describe their behavior, and to address some of the phenomena one might come across.

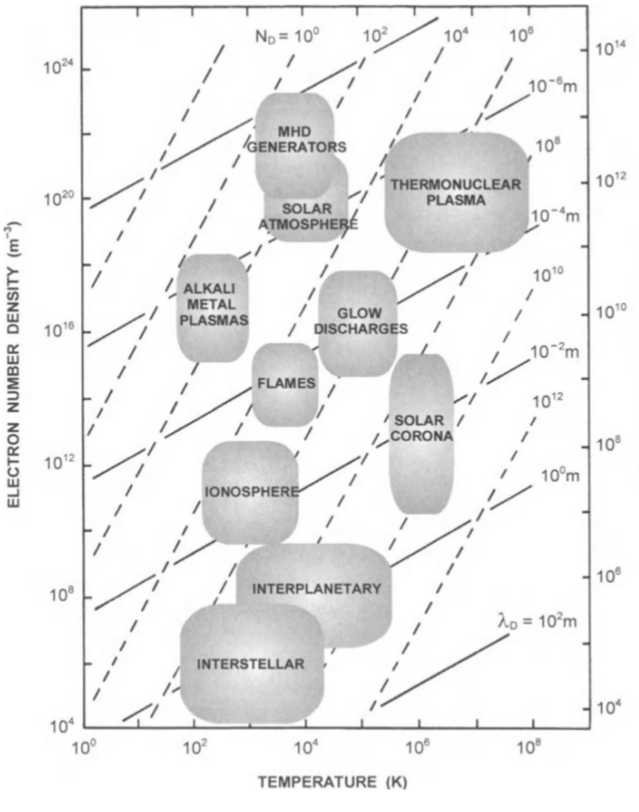

Fig. 1.1: Characterization of different plasmas by their typical electron densities n_e (or respective electron plasma frequencies $\omega_{\mathrm{p,e}}$) and temperatures. Solid and dashed lines mark constant Debye lengths λ_D and numbers of electrons N_D per Debye sphere, respectively. It can be seen that astrophysical plasmas occur in a variety of densities and temperatures. Figure taken from Bittencourt (2004, Chapter 1, Fig. 2).

In simple terms, a plasma is an ionized gas. The grade of ionization defines the degree of plasma-like behavior and is itself determined by the density and temperature of the gas or plasma. Figure 1.1 presents an overview of different plasmas in their typical density and temperature regimes. It can be seen that the parameter range expands over several orders of magnitude from the very high densities and temperatures required for thermonuclear reactions in fusion reactors or stars, down to the dilute and relatively cold plasmas in interstellar space.

In the work at hand the *solar wind plasma* is considered. The solar wind is a stream of charged particles, consisting mostly of electrons and protons, which is produced at the surface of the Sun and which travels outwards through the Sun's atmosphere and corona into interplanetary space. As can be seen in Fig. 1.1, these three regimes already span a wide range of physical parameters.

On its way through interplanetary space the solar wind encounters the different planets and other bodies of the solar system, interacting with the planets' magnetospheres – as far as these exist – and thereby forming bow shocks. Farther away from the Sun the solar wind finally reaches the interstellar medium and forms a termination shock as the solar wind speed drops below the Alfvén speed. This defines the boundary of the *heliosphere*.

The following sections will give a brief overview of the heliosphere, starting with the production of the solar wind at the Sun. The journey of the solar wind from the surface of the Sun into interplanetary space is then considered. Planetary bow shocks and the outer heliosphere will be omitted. The phenomenology of large scale structures, such as *coronal mass ejections* and interplanetary shocks, which are assumed to be responsible for the acceleration of charged particles in the solar wind, will be described.

However, since the key topics of this work are the micro-physical effects in the solar wind plasma, the macroscopic phenomena are explained in less detail. Therefore, this chapter does not raise the claim to name and discuss all of the processes in the heliosphere. For a more complete picture the interested reader is referred to the textbooks of Schwenn and Marsch (1990), Lang (2009)[1], or Koskinen (2011), or to some of the excellent review articles on different subjects, such as e.g. Reames (1999) for particle acceleration in the heliosphere or Bruno and Carbone (2013) for turbulence in the solar wind.

1.2 The Heliosphere

The heliosphere comprises the entire solar system and is governed by the energy and particle output of the Sun. The stream of charged particles originating from the Sun constitutes the solar wind, which also carries the Sun's magnetic field into interplanetary space. In the following section, a few of the processes and phenomena found inside and around the Sun are introduced.

1.2.1 The Sun

The Sun can be seen as the center of the solar system and also as the central engine which drives most of the processes in the heliosphere. It is therefore worthwhile to take a look at the Sun itself and to briefly consider its inner structure, its surface, and the regions just above the solar surface.

---

[1] This book also includes a chapter describing a variety of satellite missions, as well as time lines of important discoveries in a specific subject area at the end of each chapter. It also features a truly impressive list of additional links and literature (more than 100 pages) for further reading.

Inner Structure

In the hot, dense core of the Sun vast amounts of energy are released by the fusion of protons into deuterium and helium. These nuclear fusion processes are known as the *proton-proton chains* and were found by Bethe and Critchfield (1938). They produce 98.8% of the Sun's energy output (Stix, 2002, Chapter 2.3.6). The energy is released in the form of both neutrinos and photons. Whereas the neutrinos can escape easily, the photons undergo a slow diffusion process on their way out of the Sun. This so-called *radiative diffusion* transports most of the energy from the core through the *radiative zone*, i.e. the layer above the solar core (see Fig. 1.2). The matter in the radiative zone is still dense enough that the photons are permanently absorbed and re-emitted, traveling only a marginal distance in between. It is assumed that the diffusion of photons through the radiative zone takes about $1.7 \cdot 10^5$ years (Koskinen, 2011, Chapter 1.1).

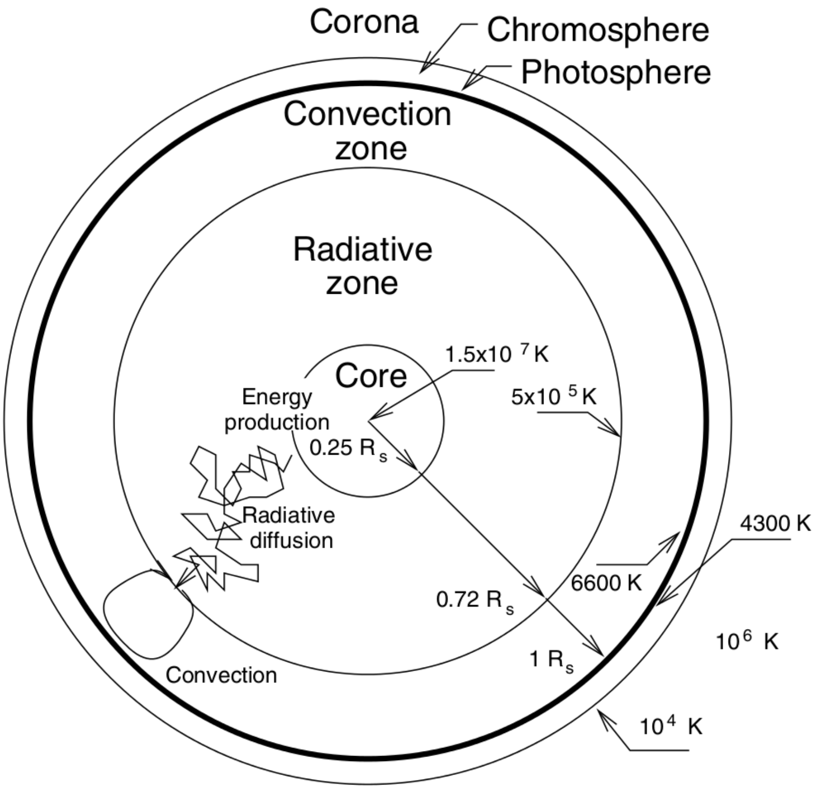

Fig. 1.2: Schematic picture of the inner structure of the Sun. Energy is produced by nuclear fusion in the core and transported outwards by radiation and convection processes. Note that the chromosphere and the solar corona are hotter than the Sun's surface, indicated by the photosphere. Figure taken from Koskinen (2011, Chapter 1.1, Fig. 1.1).

Radiative energy transport ceases as the solar matter becomes opaque. A *convection zone* is established (see Fig. 1.2), where energy is transferred outward by turbulent convection, i.e. by moving volumes of plasma. Matter is heated at the bottom of the convection zone, expands and reduces its density, and thus rises towards the surface, while colder, denser matter sinks back deeper into the Sun. At the top of the convection zone a granular structure is formed, which is also visible at the surface of the Sun. The convection zone also plays an important role for the Sun's magnetic field, which is assumed to be produced by the motion of the plasma at the bottom of this zone (Koskinen, 2011, Chapter 1.1).

The surface of the Sun is defined by the *photosphere*, which is a thin layer located above the convection zone. The photosphere absorbs the energy transported upwards in the convection zone and emits it as radiation, i.e. photons. The energy distribution of the emitted photons can be described by a black body spectrum with a temperature of 5778 K (Stix, 2002, Chapter 1.5). However, the temperature in the photosphere is not uniform, but changes with the distance to the core of the Sun.

The Sun is not a rigid body, but consists of gas and plasma. The rotation of the Sun, therefore, does not proceed with a constant angular velocity, but differs according to the distance to the core and the latitude. This phenomenon is named *differential rotation*.

On the surface of the Sun the angular velocity or rotation period can be determined from the observation of distinct features, such as sunspots, or from the Doppler shift of the emitted radiation. It is found that the rotation is fastest at the equator and becomes slower towards the poles. The rotation period is of the order of 25 days at the equator (Koskinen, 2011), but smaller changes in the rotation rate are also observed (e.g. Pulkkinen and Tuominen, 1998). So-called *helioseismology* allows to measure the rotation of the matter inside the Sun as well. Observations with the SOHO satellite revealed that the rotation period becomes more uniform inside the Sun, especially in the radiative zone (Kosovichev et al., 1997).

Surface and Atmosphere

The temperature decreases from the core of the Sun outwards to the surface. At the top of the photosphere the temperature is of the order of 4300 K (Koskinen, 2011, Chapter 1.1). However, farther above the surface of the Sun the plasma temperature rises again.

In the simple picture drawn in Fig. 1.2 the hotter region above the photosphere is a relatively thin layer which is called *chromosphere*. The temperature rises inside the chromosphere and reaches a few ten thousand Kelvin. Its outer edge is defined at a temperature of 25000 K (Koskinen, 2011, Chapter 1.1). The plasma then transitions into the *solar corona*, which expands even further out from the Sun and has a typical temperature of 10^6 K. However, Schrijver (2001) discusses that this simplified model of photosphere, chromosphere and corona does not live up to reality. Instead of distinct layers there is a complex interplay of the different regimes, and especially the chromosphere and the corona are often spatially inhomogeneous and mixed.

The heating processes which lead to the high temperatures in the chromosphere and to the even higher temperatures in the corona are not fully understood, yet. Ideas trying to explain the steep increase in temperature involve shock fronts emerging from the photosphere, electromagnetic plasma and acoustic waves, current sheets, and magnetic reconnection. Generally it is believed that energy is extracted from the magnetic field of the Sun and converted into heat in the corona. Due to the dilute state of the coronal plasma it can be assumed that the corona is not in thermodynamic equilibrium. This at least explains why the corona does not heat the lower layers of the chromosphere and photosphere.

Magnetic Field

The observation of *sunspots*, which exhibit Zeeman splitting of spectral lines, lead to the discovery of the Sun's magnetic field (Hale, 1908). Today it is known that these sunspots are regions where magnetic flux tubes penetrate the surface of the Sun and extend into the surrounding plasma. However, sunspots have been observed for centuries, long before they have been associated with a magnetic field structure.

An eleven-year cycle, called *Schwabe cycle* (Schwabe, 1844), has been found in the appearance of sunspots: At the beginning of each cycle sunspots are formed at high latitudes (around 30°–40°), whereas later on more sunspots can be found closer to the equator. With measurements of the magnetic field and its polarity, it can be seen that sunspots always appear in pairs. Both spots of a pair are located on the same hemisphere, but at different latitudes and longitudes. The polarity of the so-called *preceding spot* is the same as the predominant polarity of the corresponding hemisphere, whereas the *following spot*, located farther to the west, has the opposite polarity (e.g. Stix, 2002, Chapter 8.3). This is consistent with the idea of flux tubes, which connect the two corresponding sunspots. The distribution of sunspots on both hemispheres is roughly symmetric, as can be seen in Fig. 1.3.

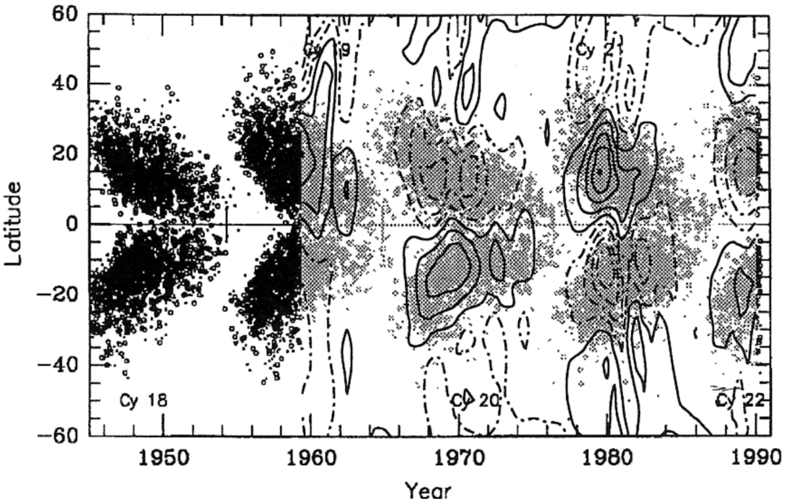

Fig. 1.3: So-called *butterfly diagram* showing the appearance of sunspots at different latitudes over the years. The eleven-year cycle, in which sunspots first appear at high latitudes and then move towards the equator, can be clearly seen. Contour lines on the right side of the plot indicate magnetic field strengths and polarities. Note the alternating polarity (solid and dashed lines) in two consecutive cycles. Figure taken from Schlichenmaier and Stix (1995).

Observations of the magnetic field also show that the polarity is reversed between two consecutive Schwabe cycles, leading to the 22-year *Hale cycle* (Hale et al., 1919), during which the Sun's magnetic field reverses its polarity (see Fig. 1.3).

During the eleven-year Schwabe cycle the number of sunspots changes, first rising to a maximum which is reached after a few years, and then decaying again. Between two cycles there are hardly any sunspots. Apart from the variations of the sunspot number per eleven-year cycle, there are also long-term fluctuations, which can be described by additional cycles with durations of a few ten to a few hundred years (Koskinen, 2011, Chapter 1.1).

The question of how the magnetic field of the Sun is initially produced is still not entirely answered. It is assumed that a *dynamo process* in the convection zone is responsible for the generation of the field, as mentioned earlier. Details on this theory can be found in Stix (2002, Chapter 8) and will not be discussed here. However, one interesting property of the Sun's magnetic field is its global structure. Assume that a dipole field is established by the dynamo processes in the convection zone. This dipole field is then distorted by the differential rotation of the Sun, because the field lines are frozen into the plasma, i.e. coupled to the motion of the solar matter. This creates additional *toroidal* components of the magnetic field, i.e. field lines which are coiled around the rotation axis of the Sun (Koskinen, 2011, Chapter 1.1). The toroidal fields are built up during times of increasing solar activity (increasing number of sunspots), and decay later on by magnetic reconnection. This cycle, corresponding to the eleven-year sunspot cycle, can be described by a so-called $\alpha\,\omega$*-dynamo* (see Stix, 2002; Koskinen, 2011, Chapters 8.4 and 8.3, respectively).

1.2.2 The Solar Wind

General Picture

The idea of an ionized gas escaping the Sun and traveling through interplanetary space was first established by Biermann (1951, 1957). Parker (1958) then found that this constant stream of particles is a result of the solar corona not being in a static equilibrium. Therefore, he predicted an expansion of the corona by means of a supersonic flow of particles away from the Sun. This flow became known as the *solar wind*. While many details have been added to this simple model since the 1950s, the general picture has maintained its validity.

The magnetic field of the Sun also expands into the solar wind. Due to the almost perfect conductivity of the solar wind plasma, the magnetic field lines are bound to the motion of the plasma. This so-called *frozen-in flux* (see e.g. Koskinen, 2011, Chapter 6 for details) leads to a magnetic field structure that can be described by an Archimedean spiral. This structure was already found by Parker (1958) and is therefore known as the *Parker spiral*.

Koskinen (2011, Chapter 1.2) derives the behavior of the magnetic field and its transition from a radial field at the surface of the Sun to a spiral farther out in the solar wind. To do so, the magnetic field can be separated into a radial and an azimuthal component, i.e. components perpendicular and parallel to the solar surface. It can be found that the radial component decreases faster with increasing distance from the surface than the azimuthal component, which explains the Parker spiral.

The solar wind accelerates on its way outward (e.g. Koskinen, 2011, Chapter 1.2). The *Alfvén speed*, a characteristic velocity in magnetized plasmas, is of particular importance here: Close to the Sun the solar wind flows at sub-Alfvénic speed, whereas it becomes super-Alfvénic at greater distances. At sub-Alfvénic speed the solar wind plasma is dragged along with the motion of the matter on the surface of the Sun. This is a result of the frozen-in magnetic flux. Only after the solar wind speed has become super-Alfvénic, its motion can decouple from the motion of the Sun itself.

Because of the rotation of the Sun and the spiral structure of the magnetic field lines, the total magnetic field strength develops differently at different polar angles. In the equatorial plane the field strength is proportional to the inverse of the distance to the Sun, whereas at the poles a proportionality to the inverse of the distance squared is found. At arbitrary polar angles the orientation and strength of the magnetic field are more complicated. Generally, a helical structure is found between the polar direction and the plane of the equator (Koskinen, 2011).

Generation and Perturbation of the Solar Wind

The exact mechanisms which lead to the emission of the solar wind from the solar surface are still subject of current research. However, a classification of the solar wind into two types with different characteristics and origins is well established. Typical speeds and densities for the two types called *fast* and *slow solar wind* are depicted in Fig.1.4. The emission processes are briefly described in the following.

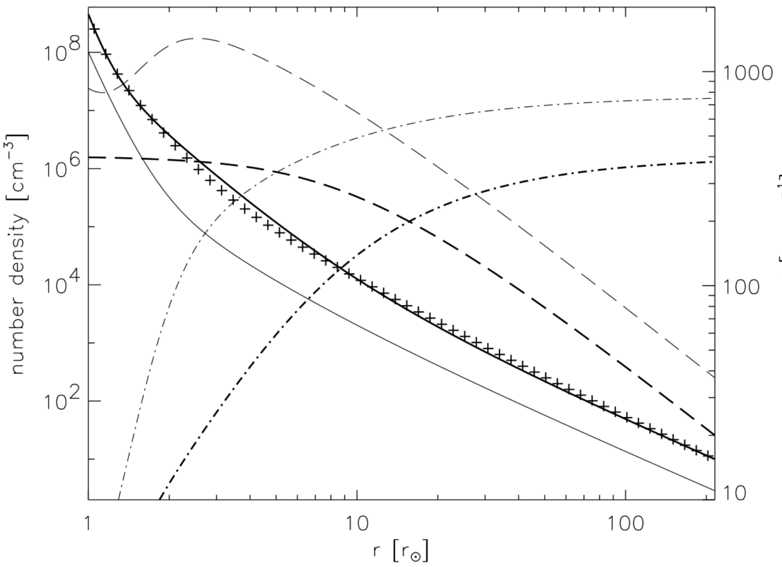

Fig. 1.4: Characteristic speeds and densities of the fast (thin lines) and slow solar wind (thick lines) as functions of the distance to the Sun in units of solar radii $r_\odot$. The bulk velocities of the solar wind plasma are given by the dash-dotted lines, the Alfvén speed is indicated by the dashed lines. Solid lines represent the number densities. Crosses are a fit to observational data of the electron density in the equatorial plane. All lines result from an analytical model by Vainio et al. (2003), where the figure is also taken from.

The *fast solar wind* is emitted from so-called *coronal holes*, where the plasma density is low and the magnetic field configuration allows the plasma to escape. Such a field configuration can be found between neighboring regions on the solar surface which have the same polarity, i.e. magnetic field lines which either point up- or downwards on both sides of the coronal hole. This leads to “open” field lines inside the hole, which expand far into space without connecting back to the Sun. Thus, particles traveling along these field lines can escape the atmosphere of the Sun and form the fast solar wind, which has a typical speed of 700 km/s (Koskinen, 2011, Chapter 1.2).

Coronal holes seem to form preferentially at high latitudes. Around the solar minimum, i.e. when almost no sunspots are present, most of the fast solar wind is emitted from only two large coronal holes at the poles of the Sun (Koskinen, 2011, Chapter 1.2). When the Sun is more active the emission patterns become more complicated, as coronal holes are created at several spots across the solar surface.

The *slow solar wind* emerges from the equatorial regions of the Sun. Its origin is assumed to be associated with so-called *streamers*, which are formed above active regions on the solar surface. The magnetic field structure of a streamer connects regions of opposite polarity and can expand far above the solar surface. At the tip of a streamer the outgoing and incoming magnetic field lines lie almost parallel, allowing for reconnection and the separation of the tip itself from the bottom of the streamer. The emission of plasma by this process is assumed to feed the slow solar wind, which travels with about 400 km/s away from the Sun.

So far, the description of the solar wind might have made the impression that the plasma flows outward in an orderly manner. However, this is not the case, since the fast flow rate itself gives rise to turbulence, and the interaction of fast and slow solar wind or the influence of *coronal mass ejections* (CMEs) can create shock fronts which perturb the plasma flow.

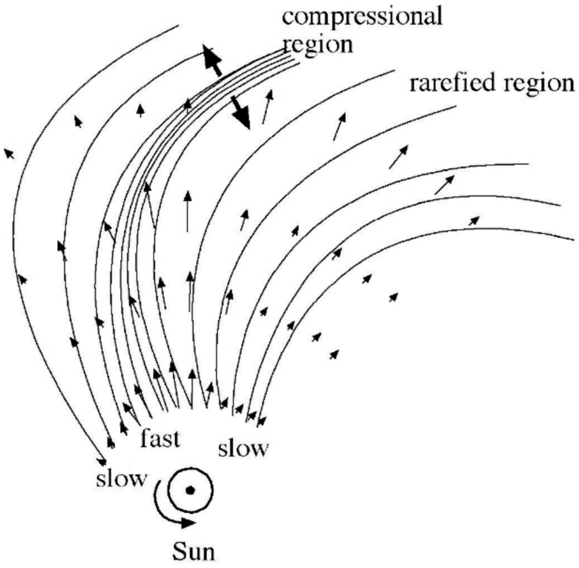

Fig. 1.5: Due to the frozen-in magnetic fields faster regions cannot overtake or mix with slower regions of the solar wind. Instead, a compressed boundary or co-rotating interaction region is formed, from which shock fronts may emerge (thick arrows). The thin arrows indicate the flow rate of the plasma, lines represent magnetic field lines. Figure taken from Koskinen (2011, Chapter 1.2, Fig. 1.12).

In a region where slow solar wind is followed by fast solar wind, a so-called *co-rotating interaction region* (CIR) can be generated (see Fig. 1.5). Due to the frozen-in magnetic field the plasma cannot mix and is therefore compressed in the region where fast and slow solar wind meet. On both sides of the compressed plasma shock fronts can be driven into the surrounding plasma, which then cause particle acceleration and the creation of turbulent waves. Note that these shocks are typically not formed near the Sun, but develop and propagate in interplanetary space at distances larger than 2 AU (Koskinen, 2011, Chapter 1.2).

Coronal mass ejections (CMEs) on the other hand are produced closer to the Sun. However, contrary to what the name suggests, most of the matter in a CME comes from the lower layers of the solar atmosphere. One possible model (e.g. Shibata et al., 1995; Shiota et al., 2005) for the generation of CMEs can be described as follows: The matter first rises from the surface of the Sun in a *prominence* (sometimes associated with a *solar flare*), i.e. an eruption

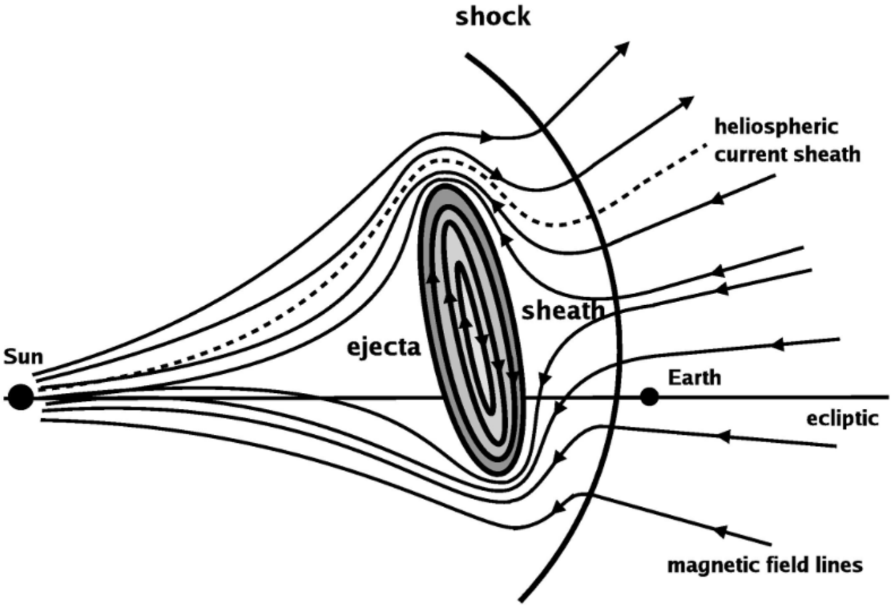

Fig. 1.6: Schematic picture of an interplanetary coronal mass ejection (ICME) driving a shock front. The ejecta are confined by closed magnetic field lines and disturb the surrounding magnetic field in the unperturbed solar wind. This leads to a compression of both the magnetic field lines and the plasma and may produce a shock in front of the ICME. Figure taken from Koskinen (2011, Chapter 1.2, Fig. 1.11).

which expands into the corona, but is still bound to the surface via magnetic field lines (see Koskinen, 2011, Chapter 12.3). By reconnection of magnetic field lines a volume of plasma can be separated from the flare, which then forms a plasmoid and propagates away from the Sun. While this explanation seems convincing, it is not entirely supported by observations, since only about 40% of the observed CMEs can be associated with a flare. Nonetheless, it is generally assumed that the CME plasma is cut free from the Sun by a process of magnetic reconnection and that the resulting plasmoid is then confined by closed magnetic field lines in its interior. However, observations also show that not all CMEs become fully detached from the magnetic field of the Sun. Large interplanetary CMEs (ICMEs), which form *flux ropes* that are connected to the Sun on one or both ends, are also commonly found (Koskinen, 2011, Chapter 12.4).

CMEs are a common phenomenon, with four to six events per day during times of high solar activity (Koskinen, 2011, Chapter 12.4). Most CMEs are launched close to the solar equator and propagate away from the Sun with speeds between 200 km/s and 2000 km/s. On their way through the solar wind the slower CMEs are accelerated, whereas the faster ones are decelerated, so that their speed adapts to the flow rate of the surrounding medium. Similar to the interaction region between fast and slow regions in the solar wind, a fast CME can compress the magnetic field and the plasma in front of it. If the CME travels at super-Alfvénic speed it also generates a shock front (see Fig. 1.6).

1.2.3 Turbulence

Besides the massive disruptions of the solar wind by CMEs and shocks, the plasma flow is also perturbed in itself due to turbulence. The high velocities of the dilute plasma lead to high *magnetic Reynolds numbers*. The magnetic Reynolds number in a magnetized plasma describes the relative influence of the induction of magnetic fields by the motion of the plasma compared to the diffusion of the magnetic field. Similar to the Reynolds number in hydrodynamics, the magnetic Reynolds number can be seen as a measure for turbulence. Borovsky and Funsten (2003) give a magnetic Reynolds number of 10^{14} for the solar wind, which indicates that the plasma is strongly turbulent.

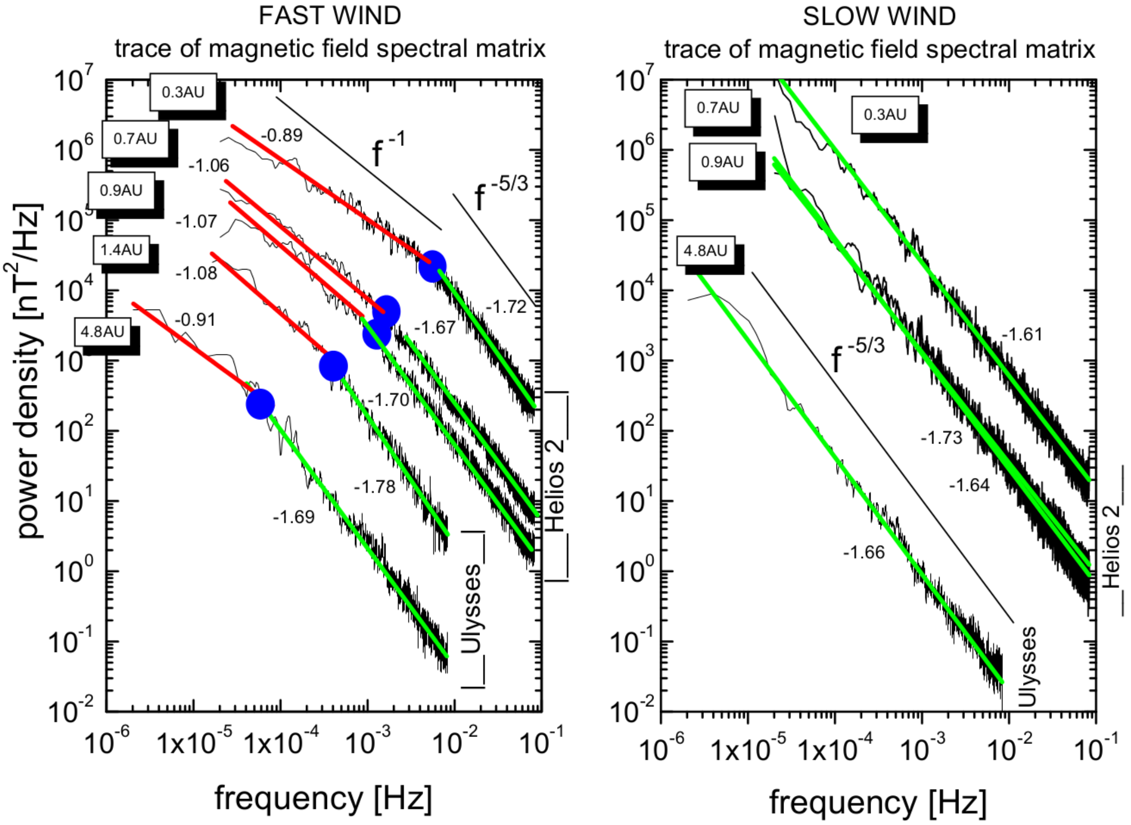

Fig. 1.7: Helios 2 and Ulysses measurements of the power density of the magnetic field fluctuations as functions of the frequency at various distances from the Sun. In the fast solar wind (left panel) the injection range can be clearly distinguished from the inertial range: The spectrum is flatter in the injection range (red lines) and reaches a spectral break (blue circles) at a specific frequency. In the inertial range the spectrum is steeper (green lines) and roughly follows the predicted slope with a spectral index of $-5/3$. Note that the spectral break shifts to smaller frequencies with increasing distance from the Sun. The measurements in the slow solar wind (right panel) do not show a spectral break or any dependence on the distance from the Sun. Figure taken from Bruno and Carbone (2013).

Turbulence manifests itself in a spectrum of plasma waves at various length scales and frequencies. The energy distribution as a function of the frequency[2] follows a characteristic

---

[2] The power law spectrum can be found both in frequency and wave number, which is attributed to the fact

power law, as can be seen in Fig. 1.7. The current understanding of the turbulent processes is such that energy is injected at large scales (i.e. small wave numbers and frequencies) and then cascades to smaller spatial scales.

The energy spectrum can be divided into several regimes, which each may span several orders of magnitude in wave number or frequency. At largest scales the *injection range* is found, which then transitions into the *inertial range*. The inertial range can be described by magnetohydrodynamic (MHD) theory and turbulence is dominated by the interaction of Alfvén waves. At smaller scales kinetic effects of the particles come into play. This regime is referred to as *kinetic*, *dispersive*, or *dissipation range*, since the waves become dispersive and dissipation starts to set in. While the spectrum extends to even smaller scales, damping eventually becomes dominant and leads to an exponential cutoff of the energy spectrum.

Power law distributions of the energy are expected in the injection, inertial, and dissipation range of the spectrum. However, the spectral indices may differ among the individual regimes. Unfortunately, detailed models allowing for a deeper understanding of the physical processes leading to a turbulent energy cascade are only available for the inertial range. Here, especially the work of Sridhar and Goldreich (1994) and Goldreich and Sridhar (1995) can be named. Their model predicts a spectral index of $-5/3$, which actually seems to be realized in the solar wind.

Kinetic turbulence in the dissipation range is an active field of research (see e.g. Howes, 2015b, for a review). Especially the composition of the wave spectrum is subject to discussion, because a transition from non-dispersive Alfvén waves to dispersive wave modes is expected. Possible candidates for the waves in the dissipation range are so-called *kinetic Alfvén* and *whistler waves* (Gary and Smith, 2009).

1.3 Particle Acceleration

The solar wind and the phenomena therein, which have been introduced in the previous sections, form the background for the acceleration and transport of energetic particles in the heliosphere. Although they represent only a small fraction of the particle spectrum in the solar wind, it is worthwhile to take a closer look at the high energy particles. Therefore, a brief overview of the different classes of energetic particle events and the corresponding acceleration sites is presented in the following.

1.3.1 Solar Energetic Particles

The existence of radiation (also in the form of ionized particles) from outside the Earth's atmosphere has been known since the famous balloon experiments of Hess (1912). Part of this radiation has its origin far outside of the solar system or even our galaxy (e.g. Compton, 1935) and has therefore been named *cosmic rays*. However, Forbush (1946) found that there are also energetic particles, which originate from the Sun. This dilute population of particles is often referred to as *solar energetic particles* (SEPs). Solar energetic particles comprise electrons of energies up to 100 MeV (e.g. Datlowe, 1971) and protons and heavier ions with energies up to 10 GeV (e.g. Reames, 2004).

---

that the turbulent spectrum consists mainly of Alfvén waves. For Alfvén waves the frequency is directly proportional to the wave number.

Observations suggest that there are two classes of solar energetic particle events, i.e. processes which generate SEPs, which are called *impulsive* and *gradual events*. The discrimination between these two types of events is based on the composition of the resulting particle population and the assumed acceleration mechanism. Lang (2009, Chapter 7.3.4) lists the properties of the measured particles of both SEP event types in detail. In short, impulsive events mainly produce highly energetic electrons and fewer protons and ions. However, the relative abundances of heavier ions are larger than in the solar wind plasma. Impulsive events are associated with solar flares, which are brief but rather violent and frequent events. The acceleration sites are therefore assumed to be close to the Sun. This is supported by the observations of particles originating from a small angular range, suggesting that they follow magnetic field lines that connect to a confined region on the surface of the Sun.

Gradual SEP events accompany CMEs and can last for several days. Energetic particles are found to be widespread in terms of solar longitudes, which hints at an extended production site. CME-driven shocks close to the Sun or in interplanetary space are assumed to accelerate the particles in a gradual SEP event. Farther out in the heliosphere, CIR shocks or the bow shocks of planets can also play a role in the generation of energetic particles. Unlike the case of impulsive events, the acceleration mechanism does not favor heavy ions, resulting in the low ion abundances typical for the solar wind and a large number of protons in a gradual event.

After this brief characterization of solar energetic particles, the acceleration mechanisms will be discussed in a bit more detail.

1.3.2 Acceleration at Shock Fronts

Shocks in a magnetized plasma can be created if the relative difference of the flow rates of two volumes of plasma exceeds the Alfvén speed. The Alfvén speed in the solar wind is of the order of a few ten kilometers per second, whereas the plasma streams with a few hundred kilometers per second (e.g. Koskinen, 2011, Chapter 1-2). Thus, if a stream of plasma encounters an obstacle, such as the magnetosphere of a planetary body, or simply a slower region of the solar wind, a shock front is created. The former case would be a planetary bow shock, the latter case would result in a CIR shock or a CME shock. In the following the case of a CME-driven shock is explained in more detail.

Reames et al. (1997) state that CMEs always develop a shock if their propagation is faster than the fast solar wind, i.e. their speed is higher than 750 km/s. The propagation of the CME leads to a deformation and compression of the magnetic field, as seen in Fig. 1.8 and the shock front expands over a wide range of solar longitudes. The acceleration of particles at collisionless shock fronts in magnetized plasmas is described by so-called *Fermi acceleration*[3]. This process is based on the interaction of a particle with magnetic fields, which leads to a change in the particle's energy when it scatters back and forth across the shock.

Based on an idea originally proposed by Fermi (1949), a particle entering a region with stronger magnetic field can be reflected and return to a region with weak magnetic field. In a rest frame in which the magnetic field is static, this process corresponds to elastic

---

[3] Fermi acceleration not only works on shock fronts, but on any form of moving magnetic irregularities (e.g. plasma waves). However, the exact acceleration mechanisms differ and are commonly referred to as Fermi-I and Fermi-II acceleration. The former describes the acceleration at a shock front, the latter the statistical gain of energy by the repeated scattering off of magnetic irregularities moving in random directions.

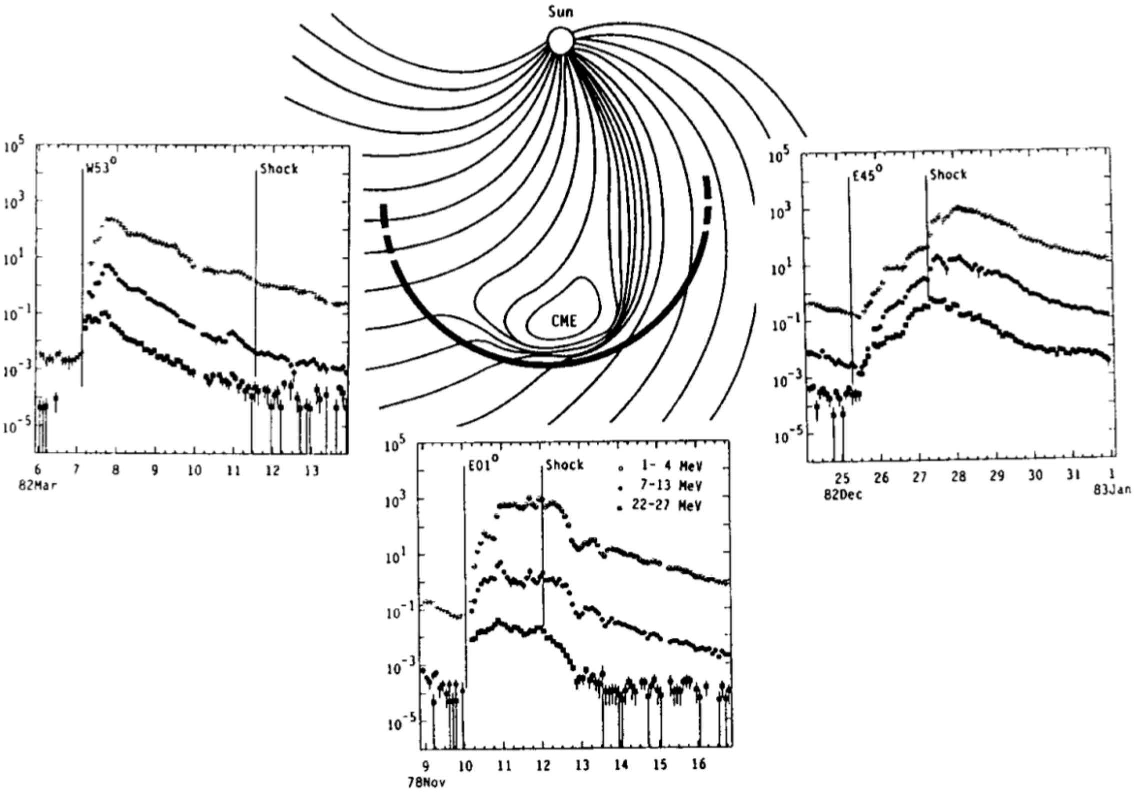

Fig. 1.8: The center image depicts the magnetic field structure (thin lines) of a CME-driven shock (thick line). The three insets show intensity-time profiles measured at the western flank (left panel), the center or "nose" (center panel), and the eastern flank of the CME shock (right panel). Figure taken from Reames (1999).

scattering and the particle does not gain or lose energy. However, in the case of a moving magnetic field the particle will experience a net change of energy. Depending on the relative direction of propagation of the particle and the magnetic field structure the particle either gains ("head-on collision") or loses energy ("overtaking collision").

Applied to the situation at a collisionless shock front (see Fig. 1.8 for the magnetic field structure) this means that a particle which crosses the shock from the upstream into the downstream region can be reflected back into the upstream while gaining energy. If this is repeated, because the shock outruns the particle or the particle is scattered back towards the shock, an efficient acceleration process can set in. At a sufficiently high energy, the particle can finally escape the shock region and the acceleration stops.

Although this mechanism is believed to be responsible for the acceleration of particles (especially protons) at interplanetary shocks (Krymskii, 1977), it has the problem that it only works on supra-thermal particles. This so-called *injection problem* implies that a pre-accelerated particle population must be present, which can then gain more energy from shock acceleration, or that the particles in the high energy tail of the thermal distribution are primarily accelerated (Gosling et al., 1981).

Shock acceleration can be subdivided into two categories, depending on the relative directions of the magnetic field and the shock normal (see e.g. Jones and Ellison, 1991; Reames, 1999, for details). If the magnetic field is parallel to the shock normal, one speaks of *diffusive shock acceleration* (DSA), which works as described above. As can be seen in Fig. 1.8, this field configuration is usually found at the flanks of the shock front, where the Parker spiral is barely disturbed.

Close to the CME the Parker spiral is deformed and the field lines are perpendicular to the shock normal. In this case the acceleration process is a little different and also more efficient. Particles gyrating about the magnetic field lines close to the shock inevitably cross the shock from the upstream into the downstream and back again during each gyration. This traps the particles in the shock region and allows them to gain energy by an additional drift acceleration: The motion of the shock front (with speed $\boldsymbol{v}_\mathrm{S}$), which is perpendicular to the direction of the magnetic field $\boldsymbol{B}$, creates an electric field $-\boldsymbol{E} \propto \boldsymbol{v}_\mathrm{S} \times \boldsymbol{B}$. This field then accelerates the particles perpendicular to the magnetic field, making *shock drift acceleration* (SDA) much more efficient than DSA (e.g. Jokipii, 1987).

The acceleration efficiency can be further improved if sufficiently large numbers of particles are accelerated by the shock. The energetic particles may then excite plasma waves, which trap the particles and help to further accelerate them (Lee, 1983; Zank et al., 2000; Vainio and Laitinen, 2007; Ng and Reames, 2008).

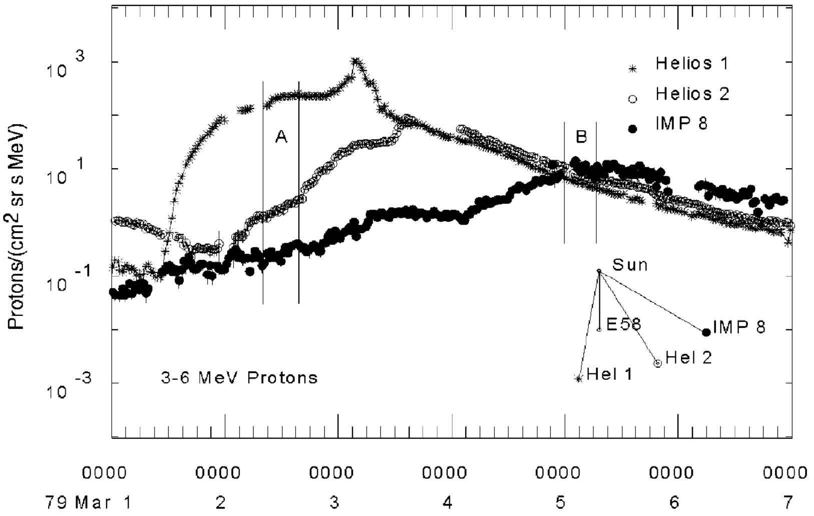

Fig. 1.9: Measurements of the intensity-time profile of energetic protons from three spacecraft at different positions relative to the shock. Figure taken from Reames (1999).

From an observational point of view, the measured intensity-time profiles of the energetic particles differ depending on the position of the observer (i.e. the satellite) relative to the CME and its shock (see e.g. Reames, 1999, Sect. 3.2). This can be seen both in Figs. 1.8 and 1.9. To understand the different intensity-time profiles, it is important to remember that the CME follows the rotation of the Sun and thus travels east on its way outwards.

An observer to the west of the CME (left panel in Fig. 1.8) sees a steep increase in the particle count long before it is passed by the shock. The reason for this is that the observer was connected to the shock via a magnetic field line when the CME was still close to the Sun. The accelerated particles escape the shock and follow their field line, eventually reaching the observer. Over time the CME moves west and the observer becomes connected to field lines on the flank of the shock, where acceleration is less efficient. The particle count slowly decreases.

An observer close to the center of the CME may see a gradual increase of the particle count early on, as it is connected to field lines to the east of the CME, where acceleration is inefficient. However, as the observer becomes connected to the field lines directly in front of the CME, the particle count rises steeply and then remains at a relatively constant level (see center image in Fig. 1.8 and Helios 1 in Fig. 1.9). Depending on the size of the CME (especially its longitude extent is important) this plateau can last for several days. Shortly after the shock front has passed the particle count drops, as the observer enters the CME, whose field lines may still be connected to the Sun. After this initial drop a gradual decrease of the particle count is seen.

Finally, an observer to the east of the CME detects a slow increase of the intensity before the shock arrives and a gradual decrease afterwards (right panel in Fig. 1.8 and Helios 2 and IMP 8 in Fig. 1.9). Note that this observer is never connected to field lines in front of the CME. Instead, it is passed by the eastern flank of the shock (with an increase of the particle count as the shock approaches) and then connects to field lines behind the CME, i.e. between the CME and the Sun. This is where the highest intensity is measured, before the particle count decreases again as the CME moves further east.

Figure 1.9 shows that the measured intensity-time profiles from the three spacecraft at different positions align at late times, when the shock has passed all three observers. This is known as *(spatial) invariance* of the spectra. The effect is attributed to the energetic particles being trapped by the magnetic field structure behind the CME shock (Reames et al., 1996). Over time, the trapped particles expand the volume in which they are confined and thereby lose energy, which explains the gradual decrease of the intensity.

1.3.3 Acceleration in Flares

While the shock acceleration leading to gradual SEP events is rather well-understood, the acceleration processes in solar flares are significantly less clear. From the observations it is obvious that the acceleration region is relatively small. It is also known that specific particle species are predominantly affected by the acceleration mechanism. Here, especially the high ratio of the abundances of ^{3}He and ^{4}He has to be explained.

Fisk (1978) suggested the acceleration of ^{3}He by electrostatic ion cyclotron waves. These waves would have to be generated at frequencies above the cyclotron frequency of ^{4}He in order not to be damped by the heavier and more common isotope. If this was the case ^{3}He could resonate with the waves and be accelerated. It is also theorized whether heavier ions, such as certain isotopes of iron, could resonate with the same waves through higher harmonics of their cyclotron frequencies. These processes would primarily lead to heating of the ion species. However, this would allow the ions in the high energy tail of the thermal distribution to be affected by stochastic acceleration (Möbius et al., 1982).

The downside of this theory is that a high ratio of the abundances of ^{4}He and ^{1}H (i.e. protons) is required for the generation of the electrostatic ion cyclotron waves. This is, however, not supported by measured data (Reames, 1999, Sect. 4.4 and references therein). Therefore, it has been suggested that electron beams may excite *electromagnetic ion cyclotron waves*, which then interact with ^{3}He and heavier ions (Temerin and Roth, 1992; Roth and Temerin, 1997). A similar process can be observed in the Earth's ionosphere and it is plausible that an equivalent mechanism exists in the solar atmosphere.

Miller et al. (1997) give an overview of different theories for the acceleration of particles in solar flares. While they state that the high ^{3}He abundances cannot be explained so far, they favor a model where Alfvén waves are initially excited at low frequencies and then produce waves at higher and higher frequencies via a turbulent cascade. With increasing frequency the cyclotron resonances of the heavier ions are gradually encountered, which nicely explains the acceleration of these ions. However, there is no mechanism that preferentially accelerates specific ions or isotopes.

Today the processes leading to the specific signature of the impulsive SEP events are still not fully understood. This might be partly due to the fact that there is also no generalized model for solar flares. Koskinen (2011, Chapter 12.3) presents a brief overview of different ideas. Besides the understanding that magnetic reconnection is involved in the massive outburst of energy during a solar flare, many details are still unclear.

1.4 Open Questions

The explanations in the previous sections have barely scratched the surface of the variety of different interesting topics and there are a lot more details which could have been added. However, there are also topics which are still poorly understood and where the details are yet to be found. Sometimes the problems are so complicated that it is even hard to find the right questions in order to advance with new studies.

A few of the many open questions will be stated in this section and (hopefully) addressed in the following chapters. While the previous sections have mainly described the large scale picture, this work is primarily concerned with the *micro-physics*. Observations are limited to processes and regions that can be "seen" or measured. These are typically large spatial structures or ensembles of large numbers of particles. By means of computer simulations, however, it is possible to take a closer look at the microscopic processes in a plasma. For example, numerical simulations allow to study the behavior of individual particles in a predefined physical setup.

Instruments on satellites, which measure the power spectrum of magnetic field fluctuations, for example, are bound to a specific frequency regime. This is typically not the case in simulations, where the time and length scales which are resolved can be adapted to the typical scales of the problem. More importantly, simulations provide the opportunity to analyze electromagnetic field data in a spatially resolved volume, whereas individual satellites only measure time variations at a single point. These advantages of numerical simulations will be used to address some of the questions which cannot be answered by analyzing measured data.

The key problem which has been chosen for the subject of this work is the process of particle acceleration and transport in turbulence. As was mentioned in the previous sections, particle acceleration near shock fronts and Alfvénic turbulence in the inertial range are well-understood. However, turbulence on kinetic scales still poses problems for both observations and modeling.

From the observations it is not entirely clear which types of plasma waves constitute the spectrum of turbulent waves in the dispersive and dissipative regime. *Kinetic Alfvén* and *whistler waves* are both possible candidates (e.g. Gary and Smith, 2009). While kinetic Alfvén waves (KAWs) simply represent the continuation of the Alfvén mode in the dispersive regime, whistler waves are part of a different wave mode with different polarization. It is perfectly reasonable to assume that non-dispersive Alfvén waves simply transition to KAWs.

However, observations reveal that whistler waves are also present in various regions of the heliosphere, such as in the interplanetary medium (Dröge, 2000), close to interplanetary shocks (Coroniti et al., 1982; Aguilar-Rodriguez et al., 2011) or planetary bow shocks (Fairfield, 1974), and also in the Earth's ionosphere and foreshock region (Kennel and Petschek, 1966; Palmroth et al., 2015).

Whereas Alfvén waves are damped by protons and cannot cascade to frequencies above the proton cyclotron frequency, a spectrum of whistler waves may extend to way higher frequencies. Whistler waves primarily interact with electrons and are also damped by electrons at higher frequencies (close to the electron cyclotron frequency). This is an interesting aspect of kinetic turbulence, since a population of whistler waves can heat the electrons in the solar wind or even accelerate particles in the high energy tail of the thermal spectrum.

However, besides the question whether whistler waves actually contribute to turbulence in the dissipation range in a noticeable way, there is also very little knowledge about the properties of their turbulence spectrum. For the inertial range the spectral index is known and the processes leading to the energy cascade to higher frequencies and wave numbers is well-understood. For kinetic turbulence this is not the case. Although advances are made – especially by means of numerical simulations, such as Gary (2015, and references therein) – there are still questions which are not finally answered (see also Howes, 2015a):

- What does the turbulence spectrum in the dissipation range look like?
- Is there a straight spectral slope, or does the energy spectrum have a break?
- Is the energy cascade anisotropic in space?
- Which processes ultimately lead to the dissipation of the electromagnetic field energy?

Another question that comes to mind is how kinetic turbulence affects the transport of energetic particles. Here, especially the electrons are of interest. The transport of energetic protons is well-described by models of Alfvénic turbulence, since the protons mainly interact with these waves at low frequencies. The theoretical framework of quasi-linear theory (QLT) can be used to describe particle transport by a series of resonant interactions with the magnetic fields of Alfvén waves, which leads to scattering of the particles (e.g. Jokipii, 1966; Lee and Lerche, 1974; Schlickeiser, 1989). This theory describes changes of the particles' pitch angles (i.e. the angle of the velocity vector relative to a background magnetic field), momenta, or positions as diffusion processes and allows to predict diffusion coefficients and other quantities, such as the mean free path, which can be compared to observations.

Dispersive waves are more difficult to handle in (analytical) theory. Nonetheless, QLT can also yield predictions for particle transport in a medium containing dispersive waves, as Steinacker and Miller (1992) or Vainio (2000) show. The introduction of dispersive waves can even solve some of the problems which are encountered if a purely Alfvénic spectrum of waves is assumed (Achatz et al., 1993). Still, the model remains an approximation and computer simulations are used to clarify some of the details which are not included in the analytical theory. Different kinds of simulations are used to study different physical regimes and processes, from the acceleration of particles (e.g. Ng and Reames, 1994; Vainio and Kocharov, 2001) to the transport of energetic particles, considering both non-dispersive (e.g. Lange et al., 2013) and dispersive waves (e.g. Gary and Saito, 2003; Camporeale, 2015).

Especially considering the effect of dissipation range turbulence on the transport of energetic particles the following questions may still be addressed:

- How does particle transport in kinetic turbulence differ from the transport in the inertial range?
- Is the transport of energetic electrons qualitatively different from proton transport?
- Do the micro-physical processes leading to particle diffusion in phase space change in the dispersive or dissipative regime?

The questions raised in this section are, of course, not entirely answered in the work at hand[4]. However, at least a small contribution is made to a better understanding of basic micro-physical processes in the solar wind.

---

[4] This would spoil all the fun for future generations of scientists, wouldn't it?

2 Theory

2.1 Units and Notation

In the thesis at hand the Gaussian-cgs unit system is used. Although some would favor the proper use of the SI system, cgs units are still common in the astro- and space plasma physics community[5] and thus are used for consistency with the literature. However, conversion factors for different units, constants and physical quantities may be found e.g. in Huba et al. (2007) or elsewhere[6].

For the designation of variables and physical quantities this work orients itself on standard literature. Denotations of most quantities are identical to those in Stix (1992) and Schlickeiser (2003).

Scalar quantities are written in italics (e.g. x), vectors and tensors are denoted in bold italics ($\boldsymbol{x}$). Regular multiplication is typically not marked with a mathematical sign, scalar or vector products, however, are denoted by "$\cdot$" and "$\times$", respectively. Indices denoting a component of a vector or a tensor are in italics (x_i), descriptive subscripts are upright (x_i).

2.2 Basic Plasma Characteristics

2.2.1 Definition

> "What is Plasma?"

This is not only the title of chapter 2.1 in the book *Physics of Space Storms* by Hannu Koskinen (2011), but it is also an excellent question, because our experiences in daily life do not give us an intuitive definition of the plasma state. We know very well what "gas", "fluid" or "solid" means, but what else can there be? Plasma is often called "the fourth state of matter", but how does it behave? In his book Koskinen (2011) presents the following answer to his initial question:

> "Plasma is *quasi-neutral* gas with so many *free charges* that *collective electromagnetic phenomena* are important to its physical behavior."

This definition contains the most important properties of a plasma: it contains charged particles which can move freely and whose electromagnetic interactions dominate the behavior of the entire medium. In the case of space plasma, such as the solar wind plasma, the particle density is so low, that there are basically only electromagnetic interactions and direct collisions of individual particles can often be neglected. Although assuming that the solar wind plasma in general is collisionless might not be a good idea (if it were, there would be no thermalization for example), this assumption holds very well for the time and length scales

---

[5] With some exceptions, such as the textbooks by Bittencourt (2004) or Koskinen (2011).

[6] It seems that there are even entire articles about transformations between different systems of units, such as Weibel (1968).

of interest for the work presented in this thesis. In the following description of a plasma direct particle-particle collisions will therefore be neglected.

However, many early works which are now seen as fundamentally important for plasma theory dealt with electromagnetic effects in fluids or dense gases. Debye and Hückel (1923), for example, developed a theory for liquid electrolytes and found a fundamental length scale, the so-called Debye length λ_D which is an intrinsic length scale of plasmas as well. Magneto-hydrodynamic waves, later called Alfvén waves, have first been described in a liquid (Alfvén, 1942a,b). Later, Åström (1950a,b) found equivalent waves in ionized gas and derived their behavior from the electromagnetic properties of plasmas.

Another important equation used in plasma physics was derived to describe the ionization of atoms in the chromosphere of stars (Saha, 1920, 1921). Under the assumption of charge neutrality in the plasma the so-called Saha equation can be used to derive the fraction of ionized atoms in a gas. In the notation of Lang (1980, Eq. 3-127) the Saha equation (or Saha Boltzmann ionization equation) reads

$$\frac{n_{r+1}}{n_r} n_\mathrm{e} = \frac{u_{r+1}}{u_r} \frac{2(2\,\pi\, m_\mathrm{e}\, k_\mathrm{B}\, T)^{3/2}}{h^3} \exp\left(\frac{-\chi_r}{k_\mathrm{B}\, T}\right) \tag{2.1}$$

and describes the ratio of the number densities n_r and n_{r+1} of atoms with a degree of ionization r or $r+1$, respectively. The other quantities in Eq. (2.1) are the number density n_e of free electrons, the partition functions u_r and u_{r+1} of the ions of stages r and $r+1$, the electron mass m_e, the Boltzmann constant k_B, the temperature T, the Planck constant h and the ionization potential χ_r of an ion of stage r.

Unfortunately, being able to calculate the ionization of a gas with a given temperature T does not make it easier to define the plasma state. There is no definite degree of ionization which turns a gas into a plasma. As a rule of thumb, if at least one percent of the atoms in a gas are ionized, the gas is already almost perfectly conductive (Koskinen, 2011, Chapter 2.1). This is also the reason why there are no large scale electric fields in space plasmas: If there was an electric field it would immediately create an electric current (and a stream of particles) which would neutralize any space charges and restore the plasma to a state with no electric field.

After this attempt to define the plasma state and declare a few characteristics of a plasma, it is still difficult to imagine how a plasma behaves. To bring a little more clarity into this matter, the next few sections will describe some basic properties and mechanisms which are typical and necessary for a plasma.

2.2.2 Time and Length Scales

As mentioned earlier, Debye and Hückel (1923) derived a theory for electrolytic solutions to explain changes in osmotic pressure, vapor pressure, and freezing and boiling point temperatures in such liquids. They found a characteristic length scale which they describe as the radius of a virtual “atmosphere” of charged particles around a given ion. This length scale is now known as the Debye length and can be written as (see e.g. Huba et al., 2007):

$$\lambda_\mathrm{D} = \left(\frac{k_\mathrm{B}\, T}{4\,\pi \sum\limits_\alpha n_\alpha q_\alpha^2}\right)^{1/2} , \tag{2.2}$$

if the electrons and protons have the same temperature. The Debye length depends on the plasma temperature T and the number densities n_α and electric charges q_α of the particles of species α. Although derived for electrolytic solutions, the Debye length is also valid in plasmas and can be used to deduce criteria for the definition of a plasma.

The importance of the Debye length comes from the effect of so-called Debye shielding. While a single charged particle in a vacuum has a Coulomb potential which stretches out to infinity, the electrostatic potential of a charged particle in a plasma has an exponential cutoff. This new potential is sometimes called a “shielded potential” (e.g. Koskinen, 2011, Chapter 2.1) and the length scale at which shielding occurs is the Debye length. Debye shielding basically means that a charged particle can only directly interact with other charged particles within its Debye sphere, i.e. a sphere with radius λ_D. Other particles outside this sphere do not “feel” its potential and thus cannot be affected by the particle.

A more intuitive understanding of the Debye sphere might be obtained by considering the following ideas: Debye and Hückel (1923) propose to look at a particle with charge q. Due to its potential this particle will attract mainly other charged particles with electric charges of different sign. Thus the particle aggregates an atmosphere of charged particles, which will effectively neutralize the original charge q as seen from outside the atmosphere. Koskinen (2011) suggests a different picture. Assuming a particle with charge q again, the Debye length describes the distance from this particle at which other charged particles can escape its Coulomb potential due to their thermal speed.

Based on the Debye length and the shielding effect, criteria can be derived to define a plasma (e.g. Bittencourt, 2004, Chapter 1, Sect. 2.2): First, the collective electromagnetic interaction of charged particles, which leads to Debye shielding, can only occur on length scales larger than the Debye length λ_D. To exhibit plasma behavior an ionized gas must therefore have a characteristic length scale $L \gg \lambda_\mathrm{D}$. Secondly, Debye shielding can only be effective if there are enough charged particles inside a Debye sphere. With n being the number density of charged particles in the plasma, the condition $n\,\lambda_\mathrm{D}^3 \gg 1$ must be satisfied[7]. This condition also implies that the kinetic energy of the particles is much higher than their potential energy, thus preventing the recombination of electrons and ions (Schlickeiser, 2003, Chapter 8.1). Thirdly, charge neutrality on macroscopic scales can be seen as both a requirement for and a consequence of plasma behavior. Due to Debye shielding, space charges can only occur at scales smaller than a Debye sphere (unless they are caused by external factors, which is usually not the case for space plasmas). At scales larger than λ_D a plasma is always quasi-neutral.

Similar to the Debye length, which forms a characteristic length scale for the plasma, a characteristic time scale or frequency can also be found. An oscillation of electrons in gas discharge tubes was found by Langmuir (1928), who also noticed that these oscillations exhibit a specific frequency which depends on the plasma parameters. This so-called *plasma oscillation* was later theoretically derived by Tonks and Langmuir (1929) and its characteristic frequency is given by

$$\omega_{\mathrm{p},\alpha} = \left(\frac{4\,\pi\,n_\alpha\,q_\alpha^2}{m_\alpha}\right)^{1/2} \tag{2.3}$$

---

[7] The dimensionless quantity $n\,\lambda_\mathrm{D}^3$ (e.g. Koskinen, 2011) or its inverse (e.g. Schlickeiser, 2003; Bittencourt, 2004) is sometimes called the *plasma parameter*. However, due to its inconsistent application in the literature this term will not be used in this work. In this work “plasma parameter(s)” can mean any physical quantity that is used to characterize the plasma (e.g. density, temperature, etc.), but it will never refer to $n\,\lambda_\mathrm{D}^3$.

and describes the *plasma frequency* of particles of species α, i.e. particles with number density n_α, charge q_α and mass m_α. The plasma frequency is the natural frequency with which the particles in a plasma react to perturbations of charge neutrality.

In a plasma with several components, i.e. different particle species which make up the plasma, a combined plasma frequency for the whole plasma can be defined:

$$\omega_\mathrm{p} = \left(\sum_\alpha \omega_{\mathrm{p},\alpha}^2 \right)^{1/2} . \tag{2.4}$$

This combined plasma frequency is the relevant frequency for plasma behavior and an important quantity for the derivation and characterization of various plasma waves.

Bittencourt (2004) uses the plasma frequency to define another criterion for plasma behavior. He argues that particles must be able to oscillate more or less undisturbed, i.e. without colliding into other particles. If the interaction of charged particles was dominated by collisions, they would behave more like a neutral gas than like a plasma. Therefore, in a plasma the condition $\omega_\mathrm{p}\,\tau > 1$ has to be satisfied, where τ is the average time between particle collisions. Note that this condition is of no practical importance for the work at hand, since only collisionless plasmas ($\tau \to \infty$) are studied.

According to Schlickeiser (2003, Chapter 8.1) the condition $\omega_\mathrm{p}\,\tau > 1$ is necessarily satisfied, if $n\,\lambda_\mathrm{D}^3 \gg 1$ is assumed. This can be found from a derivation of τ via the consideration of cross-sections of particle-particle collisions, which yields

$$\tau \propto \frac{n\,\lambda_\mathrm{D}^3}{\omega_\mathrm{p}}. \tag{2.5}$$

With $n\,\lambda_\mathrm{D}^3 \gg 1$ the above approximation results in $\tau \gg 1/\omega_\mathrm{p}$, which is the condition which was motivated in the previous paragraph.

The plasma frequencies of the individual particle species can further be employed to define additional length scales. The quotient of the speed of light c and the plasma frequency yields the so-called *inertial length* of particles of species α:

$$\lambda_\alpha = \frac{c}{\omega_{\mathrm{p},\alpha}}. \tag{2.6}$$

2.2.3 Magnetization

In the previous section it was explained that no large scale electric fields can persist in a plasma. Magnetic fields, however, can very well exist on a global scale, penetrating the whole plasma and influencing the motion of the particles.

To describe the magnetization of the plasma, i.e. the importance of a global magnetic field for the behavior of the plasma, the pressure in the plasma can be considered. Additionally to the thermal or kinetic pressure of the particles, a component describing the magnetic pressure contributes to the total pressure in a plasma. The ratio of the kinetic pressure p and the magnetic pressure is denoted as *plasma beta* or simply β and yields a measure for the magnetization. The plasma beta can be written as (e.g. Huba et al., 2007)

$$\beta = \frac{8\,\pi\,n\,k_\mathrm{B}\,T}{B_0^2}, \tag{2.7}$$

where B_0 is the background magnetic field strength and the kinetic pressure is expressed as a function of temperature $p = n\,k_\mathrm{B}\,T$ with the total number density $n = \sum\limits_\alpha n_\alpha$ of particles in the plasma.

The evolution of the magnetic field is determined by the plasma in the case of $\beta > 1$, where the plasma is only weakly magnetized. For $\beta \ll 1$, however, the magnetic field dominates the plasma behavior. A brief overview of plasma betas in different parts of the heliosphere can be found in Koskinen (2011, Chapter 2.3.3). According to Koskinen (2011) a value of around one is a good estimate for a solar wind plasma.

It is interesting to note that plasmas with $\beta < 1$ can actually be confined by external magnetic fields, which is especially important for laboratory plasmas or fusion devices (Bittencourt, 2004, Chapter 12, Sect. 7). In such a confined plasma the total pressure inside the plasma is equal to the magnetic pressure at the boundary, where the kinetic pressure vanishes. This implies that the kinetic pressure cannot exceed the magnetic pressure at the boundary and that the magnetic field inside the plasma is always weaker than the external field.

Another effect in a magnetized plasma is the loss of isotropy. With the introduction of a global magnetic field a preferred direction is established – namely the direction along the magnetic field. The behavior of the plasma, of plasma waves and of the particles themselves often differs along the directions parallel and perpendicular to the magnetic field. Magnetized plasmas also host a variety of additional wave phenomena, as will be shown in Sect. 2.3.

Together with the magnetic field B_0, the *cyclotron frequencies* of the different particle species can be introduced as further characteristic frequencies. The cyclotron frequency of a particle of species α is given by

$$\Omega_\alpha = \frac{B_0\,q_\alpha}{m_\alpha\,c} \tag{2.8}$$

and has a sign according to the sign of the electric charge q_α.

2.2.4 Characteristic Velocities

Similar to the previously found characteristic time and length scales, there are also some characteristic velocities which are of importance for certain plasma phenomena. First of all, there is, of course, the speed of light c, which is the speed at which electromagnetic waves propagate in vacuum. In a plasma, electromagnetic waves cannot propagate with the speed of light, but their phase speed approaches c asymptotically for high frequencies and large wave numbers, as will be shown in Sect. 2.3.

Regarding the particles, two velocities are often encountered: the speed of sound v_s and the thermal velocity v_th. The speed of sound is given by (e.g. Koskinen, 2011, Chapter 6.6)

$$v_{\mathrm{s},\alpha} = \left(\frac{\gamma_\alpha\,k_\mathrm{B}\,T_\alpha}{m_\alpha}\right)^{1/2}, \tag{2.9}$$

where γ_α denotes the adiabatic index. Similarly, the thermal velocity can be defined as (e.g. Huba et al., 2007)

$$v_{\mathrm{th},\alpha} = \left(\frac{k_\mathrm{B}\,T_\alpha}{m_\alpha}\right)^{1/2}. \tag{2.10}$$

Note that thermal velocities are defined per particle species, since mass and temperature may vary among species.

In a magnetized plasma an additional characteristic velocity is found. While studying a conductive fluid in a magnetic field, Alfvén (1942a,b) found a phenomenon which he called "electromagnetic-hydrodynamic waves". These waves, now called *Alfvén waves*, exhibit a specific group velocity which depends on the magnetic field strength. Alfvén (1942b) realized this behavior and suggested that the characteristic speed, now called *Alfvén speed*, may also play an important role in solar physics and the motion of sun spots.

The Alfvén speed can be written as

$$v_{\mathrm{A}} = \frac{B_0}{\sqrt{4\,\pi \sum\limits_{\alpha} n_\alpha\, m_\alpha}} = \frac{B_0}{\sqrt{\sum\limits_{\alpha} \omega_{\mathrm{p},\alpha}^2\, m_\alpha^2 / q_\alpha^2}} \tag{2.11}$$

in the most general case. For an electron-proton plasma the above equation reduces to

$$v_{\mathrm{A}} = \frac{B_0\, e}{\sqrt{\omega_{\mathrm{p,e}}^2\, m_{\mathrm{e}}^2 + \omega_{\mathrm{p,p}}^2\, m_{\mathrm{p}}^2}}, \tag{2.12}$$

where e denotes the elementary charge and the indices e and p stand for electrons and protons. However, the effect of electrons is often neglected and the usual notation of the Alfvén speed is as follows (e.g. Huba et al., 2007):

$$v_{\mathrm{A}} = \frac{B_0}{\sqrt{4\,\pi\, n_{\mathrm{p}}\, m_{\mathrm{p}}}} = \frac{B_0\, e}{\omega_{\mathrm{p,p}}\, m_{\mathrm{p}}} = \frac{\Omega_{\mathrm{p}}}{\omega_{\mathrm{p,p}}}\, c. \tag{2.13}$$

2.3 Plasma Oscillations and Waves in Cold Plasma

Thinking of plasma one might imagine matter in a very hot state. However, many astrophysical and space plasmas can be assumed to be "cold". When speaking of cold plasmas this is meant in the sense that electromagnetic interactions of the particles dominate thermal effects. This is typically the case when the thermal velocities of the particles are non- or only weakly relativistic, which is the case in the solar wind. For example, to be able to neglect relativistic effects when deriving dispersion relations, Bergman and Eliasson (2001) state that the electron temperature should be below $k_{\mathrm{B}}\, T_{\mathrm{e}} = 5\,\mathrm{keV}$, which corresponds to a thermal velocity $v_{\mathrm{th,e}} = 0.14\, c$. Additional constraints are that the plasma is (almost) completely ionized and that thermal velocities are small compared to typical phase speeds of collective plasma phenomena, such as waves (Canuto et al., 1978).

With the simple approximation of a cold ($T = 0$) and collisionless plasma, which is governed only by electromagnetic interactions, many plasma phenomena can already be derived. Especially plasma oscillations and waves can be easily derived in the framework of cold plasma theory. Results from cold plasma theory already yield many insights into the dynamics of a plasma, although corrections for thermal effects might be needed to describe certain effects.

The following sections present a brief overview of the course of actions required to derive the dispersion relations, i.e. the relation of wave number and corresponding frequency, of various wave modes in a cold plasma. The properties of plasma waves are discussed with a focus on those wave modes which are essential to the numerical studies described later on.

2.3.1 Derivation of the Maxwell Tensor

Under the assumption of a collisionless cold plasma only the electromagnetic interaction is relevant. In this simple approximation only a small set of equations is needed as a starting point, namely the equation of motion for charged particles of species α in electromagnetic fields $\boldsymbol{E}$ and $\boldsymbol{B}$ (e.g. Stix, 1992, Chapter 1-2)

$$m_\alpha \frac{d\boldsymbol{v}_\alpha}{dt} = q_\alpha \left(\boldsymbol{E} + \frac{\boldsymbol{v}_\alpha}{c} \times \boldsymbol{B}\right) \tag{2.14}$$

and Maxwell's equations (Maxwell, 1865, modern notation e.g. Huba et al. (2007))

$$\nabla \cdot \boldsymbol{E} = 4\pi\rho, \tag{2.15}$$

$$\nabla \cdot \boldsymbol{B} = 0, \tag{2.16}$$

$$\nabla \times \boldsymbol{E} = -\frac{1}{c}\frac{\partial \boldsymbol{B}}{\partial t}, \tag{2.17}$$

$$\nabla \times \boldsymbol{B} = \frac{1}{c}\frac{\partial \boldsymbol{E}}{\partial t} + \frac{4\pi}{c}\boldsymbol{j}, \tag{2.18}$$

where ρ is the net charge density, $\boldsymbol{j}$ is the current density, and a permittivity $\epsilon = 1$ and a permeability $\mu = 1$ have been assumed (which is a reasonable approximation in plasmas according to Huba et al., 2007). In the following the trail of thought is described which will culminate in the so-called Maxwell tensor, which is the basis for the derivation of the various wave modes which may be present in a cold plasma. For the sake of brevity a detailed execution of each and every step will be omitted. The interested reader may find such a step-by-step guideline in textbooks, such as Canuto et al. (1978) or Stix (1962, 1992).

The following explanations are based on Stix (1992, Chapters 1-2 and 1-3), where a uniform plasma is assumed. The electric and magnetic fields are assumed to be static (i.e. vanishing electric field, and constant magnetic field $\boldsymbol{B}_0$) with first-order perturbations $\boldsymbol{\delta E}$ and $\boldsymbol{\delta B}$ in the form of plane waves, i.e. $\exp(\imath(\boldsymbol{k}\cdot\boldsymbol{r} - \omega t))$, where $\boldsymbol{k}$ and $\boldsymbol{r}$ are wave vector and position, and ω and t are frequency and time. Note that both $\boldsymbol{k}$ and ω are real quantities.

The basic idea is to solve Maxwell's equations for plane waves. These solutions lead to the dispersion relations of plasma waves. Since the perturbations $\boldsymbol{\delta E}$ and $\boldsymbol{\delta B}$ are assumed to be harmonic oscillations, all further calculations can be performed in Fourier space, i.e. treating the electric $\boldsymbol{E}(\boldsymbol{k},\omega) = \boldsymbol{\delta E}(\boldsymbol{k},\omega)$ and magnetic field $\boldsymbol{B}(\boldsymbol{k},\omega) = \boldsymbol{B}_0 + \boldsymbol{\delta B}(\boldsymbol{k},\omega)$ as functions of wave number and frequency. Thus, the wave equation (in a homogeneous plasma) can be written as

$$\boldsymbol{k} \times (\boldsymbol{k} \times \boldsymbol{E}) + \frac{\omega^2}{c^2}\boldsymbol{\epsilon}\cdot\boldsymbol{E} = 0, \tag{2.19}$$

which can be obtained from combining Eqs. (2.17) and (2.18), where the right-hand side of Eq. (2.18) is reformulated using the dielectric tensor $\boldsymbol{\epsilon}$:

$$\frac{1}{c}\frac{\partial \boldsymbol{E}}{\partial t} + \frac{4\pi}{c}\boldsymbol{j} = \frac{1}{c}\frac{\partial \boldsymbol{D}}{\partial t}, \tag{2.20}$$

$$\boldsymbol{D} = \boldsymbol{\epsilon}\cdot\boldsymbol{E}, \tag{2.21}$$

where $\boldsymbol{D}$ denotes the electric displacement.

The next step is to derive the dielectric tensor $\boldsymbol{\epsilon}$, which is also done in Fourier space. Solving Eq. (2.20) yields

$$\boldsymbol{\epsilon} \cdot \boldsymbol{E} = \boldsymbol{E} + \frac{4\,\pi\,\imath}{\omega}\,\boldsymbol{j}. \tag{2.22}$$

The current density $\boldsymbol{j}$ can be expressed either via the motion of the charged particles directly, or via the definition of the susceptibility $\boldsymbol{\chi} = \sum_\alpha \boldsymbol{\chi}_\alpha$:

$$\boldsymbol{j} = \sum_\alpha n_\alpha\, q_\alpha\, \boldsymbol{v}_\alpha, \tag{2.23}$$

$$\boldsymbol{j} = \frac{\omega}{4\,\pi\,\imath} \sum_\alpha \boldsymbol{\chi}_\alpha \cdot \boldsymbol{E}. \tag{2.24}$$

Equation (2.24) can be inserted into Eq. (2.22) to yield the expression

$$\boldsymbol{\epsilon} = \mathbf{1} + \sum_\alpha \boldsymbol{\chi}_\alpha \tag{2.25}$$

for the dielectric tensor, where $\mathbf{1}$ is the unit dyadic. The susceptibility tensor on the other hand can be found by inserting new expressions for $\boldsymbol{v}_\alpha$ into Eq. (2.23) and comparing the result to Eq. (2.24).

To this end the equation of motion (2.14) can be rewritten with the Fourier transformed quantities:

$$-\,\imath\,\omega\, m_\alpha\, \boldsymbol{v}_\alpha = q_\alpha \left(\boldsymbol{E} + \frac{\boldsymbol{v}_\alpha}{c} \times \boldsymbol{B}_0 \right). \tag{2.26}$$

Note that only harmonic oscillations in $\boldsymbol{v}$ are assumed and that the first-order perturbations of the magnetic field do not contribute to the equation of motion in this case. Defining the zeroth order static magnetic field as $\boldsymbol{B}_0 \parallel \hat{\boldsymbol{z}}$, with $\hat{\boldsymbol{z}}$ being the unit vector in z-direction, the individual components of $\boldsymbol{v}_\alpha$ can be written as follows:

$$v_\alpha^\pm \;=\; \frac{\imath\, q_\alpha}{m_\alpha}\,\frac{E^\pm}{\omega \mp \Omega_\alpha}, \tag{2.27}$$

$$v_{\alpha,z} \;=\; \frac{\imath\, q_\alpha}{m_\alpha}\,\frac{E_z}{\omega}. \tag{2.28}$$

Here, Ω_α is the cyclotron frequency as defined in Eq. (2.8) and the x and y components of the velocity and electric field vectors have been combined to $v_\alpha^\pm = (v_{\alpha,x} \pm \imath\, v_{\alpha,y})/2$ and $E^\pm = (E_x \pm \imath\, E_y)/2$.

Setting Eq. (2.23) equal to Eq. (2.24) allows to find the individual components of the susceptibility $\boldsymbol{\chi}$ and thus to obtain a representation of the dielectric tensor via Eq. (2.25):

$$\boldsymbol{\epsilon} = \begin{pmatrix} S & -\imath\, D & 0 \\ \imath\, D & S & 0 \\ 0 & 0 & P \end{pmatrix}. \tag{2.29}$$

The quantities S (*sum*), D (*difference*) and P (*plasma*), together with additional expressions

R (*right*) and L (*left*), are the so-called *Stix parameters*:

$$\begin{aligned} S &= \frac{1}{2}\,(R+L), && (2.30)\\ D &= \frac{1}{2}\,(R-L), && (2.31)\\ P &= 1-\sum_\alpha \frac{\omega_{\mathrm{p},\alpha}^2}{\omega^2}, && (2.32)\\ R &= 1-\sum_\alpha \frac{\omega_{\mathrm{p},\alpha}^2}{\omega\,(\omega+\Omega_\alpha)}, && (2.33)\\ L &= 1-\sum_\alpha \frac{\omega_{\mathrm{p},\alpha}^2}{\omega\,(\omega-\Omega_\alpha)}. && (2.34) \end{aligned}$$

Having obtained an expression for the dielectric tensor $\boldsymbol{\epsilon}$ finally allows to return to the wave equation (2.19). The wave equation is often rewritten with the index of refraction

$$\boldsymbol{n} = \frac{\boldsymbol{k}\,c}{\omega} \tag{2.35}$$

or the *Maxwell tensor* $\boldsymbol{\Lambda}$:

$$\boldsymbol{n} \times (\boldsymbol{n} \times \boldsymbol{E}) + \boldsymbol{\epsilon} \cdot \boldsymbol{E} = \boldsymbol{\Lambda} \cdot \boldsymbol{E} = 0. \tag{2.36}$$

The components of the Maxwell tensor can be explicitly derived from the above equation. Assuming that the Maxwell tensor is explicitly known, its determinant can be calculated and set equal to zero. This yields the dispersion relations of several wave modes, as will be shown in the next section.

2.3.2 Dispersion Relations in a Cold Plasma

In order to write down the Maxwell tensor explicitly the wave vector $\boldsymbol{k}$ needs to be defined. With the static magnetic field $\boldsymbol{B}_0 = B_0\,\hat{\boldsymbol{z}}$ it is convenient to define the wave vector as

$$\boldsymbol{k} = k \begin{pmatrix} \sin(\theta)\,\cos(\phi) \\ \sin(\theta)\,\sin(\phi) \\ \cos(\theta) \end{pmatrix}. \tag{2.37}$$

Note that this general form is not required and that it is sufficient to reduce $\boldsymbol{k}$ to two dimensions to derive the wave modes in a cold plasma. Stix (1992) chooses $\phi = 0$ and thus defines the wave vector to lie in the x-z-plane, which leads to considerable simplifications in the following equations. The characteristics of the wave modes do not change with a different choice of ϕ which legitimates the two-dimensional approach to the problem. However, for the practical use in a simulation code, for example, the general representation of the wave vector turns out to be advantageous. Therefore, the general form including an arbitrary azimuthal angle ϕ will be kept in this section.

Deriving the Maxwell tensor from Eq. (2.36) is a straight forward, but cumbersome task and finally yields:

$$\mathbf{\Lambda}=\begin{pmatrix} S-n^2(\cos^2\theta+\sin^2\theta\,\sin^2\phi) & -\imath\,D+n^2\sin^2\theta\,\cos\phi\,\sin\phi & n^2\cos\theta\,\sin\theta\,\cos\phi \\ \imath\,D+n^2\sin^2\theta\,\cos\phi\sin\phi & S-n^2(\cos^2\theta+\sin^2\theta\,\cos^2\phi) & n^2\cos\theta\,\sin\theta\,\sin\phi \\ n^2\cos\theta\,\sin\theta\,\cos\phi & n^2\cos\theta\,\sin\theta\,\sin\phi & P-n^2\sin^2\theta \end{pmatrix}. \tag{2.38}$$

The dispersion relations of the plasma modes can be found by setting the determinant of this tensor equal to zero (e.g. Stix, 1992, Chapter 1-4):

$$|\mathbf{\Lambda}| = A\,n^4 - B\,n^2 + C = 0, \tag{2.39}$$

where the newly introduced quantities are

$$\begin{aligned} A &= S\,\sin^2\theta + P\,\cos^2\theta, && (2.40)\\ B &= R\,L\,\sin^2\theta + P\,S\,(1+\cos^2\theta), && (2.41)\\ C &= P\,R\,L. && (2.42) \end{aligned}$$

Note that the determinant is independent of the azimuthal angle ϕ, as mentioned earlier. The solution to Eq. (2.39) can be written as (e.g. Stix, 1992, Chapter 1-4)

$$n^2 = \frac{B \pm F}{2\,A}, \tag{2.43}$$

with

$$F^2 = (R\,L - P\,S)^2\,\sin^4\theta + 4\,P^2\,D^2\,\cos^2\theta, \tag{2.44}$$

where the identity $R\,L = S^2 - D^2$ has been used. The dispersion relations of the different wave modes can then be obtained from Eq. (2.43).

Relatively simple dispersion relations can be quickly obtained for propagation parallel ($\theta = 0$) or perpendicular ($\theta = \pi/2$) to the background magnetic field:

$$\begin{aligned} \text{parallel}: &\quad P = 0,\ n^2 = R,\ n^2 = L, && (2.45)\\ \text{perpendicular}: &\quad n^2 = P,\ n^2 = R\,L/S. && (2.46) \end{aligned}$$

Equation (2.45) describes the dispersion relations of the longitudinal *plasma oscillations*, the transverse right-handed circularly polarized *R-mode* (including *whistler* and *electron cyclotron waves*), and the transverse left-handed circularly polarized *L-mode* (including *Alfvén* and *ion cyclotron waves*). For perpendicular propagation Eq. (2.46) contains the dispersion relation for the *ordinary* or *O-mode* and a more complex expression which yields the dispersion relations of the *extraordinary* or *X-mode*, the *slow X-* or *upper hybrid mode*, and the *lower hybrid waves.* All of these wave modes will be discussed in more detail in Sect. 2.3.4.

2.3.3 Field Properties and Particle Oscillations

Before the properties of the individual wave modes will be discussed, a few more general expressions can be derived for later use. One interesting feature of a wave is its polarization, i.e. orientation of its electric or magnetic field relative to the wave vector (see note on polarization below). It is convenient to look at the electric field first. The physical electric field $\boldsymbol{E}(\boldsymbol{r},t)$ in real space may be defined with the help of the complex electric field $\boldsymbol{E}(\boldsymbol{k},\omega)$

in Fourier space:

$$\boldsymbol{E}(\boldsymbol{r},t) = \Re\,\boldsymbol{E}(\boldsymbol{k},\omega)\,\exp(\imath\,\boldsymbol{k}\cdot\boldsymbol{r} - \imath\,\omega\,t), \tag{2.47}$$

where $\Re$ denotes the real part of the expression on the right-hand side. Inserting the explicit notation of the Maxwell tensor, Eq. (2.38), into the wave equation (2.36) yields the following properties of the (complex) components of the electric field $\boldsymbol{E}(\boldsymbol{k},\omega)$:

$$\frac{\imath\,E_x(\boldsymbol{k},\omega)}{E_y(\boldsymbol{k},\omega)} = \frac{D\left(2\,P - n^2(1-\cos 2\theta)\right) + \imath n^2(P-n^2)\,\sin^2\theta\,\sin 2\phi}{2\Big(n^2\big(P\,\cos^2\theta + \sin^2\theta\,(S + (P-n^2)\sin^2\phi)\big) - P\,S\Big)}, \tag{2.48}$$

$$E_z(\boldsymbol{k},\omega) = \frac{n^2\cos\theta\,\sin\theta\,(E_x\cos\phi + E_y\,\sin\phi)}{n^2\,\sin^2\theta - P}. \tag{2.49}$$

Note that these relations might yield undefined results (e.g. division by zero) in some cases, so care has to be taken while evaluating the above equations for each individual wave mode and for different polar and azimuthal angles θ and ϕ.

By use of Eq. (2.17) the complex magnetic field $\boldsymbol{B}(\boldsymbol{k},\omega)$ can be defined as

$$\boldsymbol{B}(\boldsymbol{k},\omega) = \frac{c}{\omega}\,\boldsymbol{k}\times\boldsymbol{E}(\boldsymbol{k},\omega). \tag{2.50}$$

The real part of the magnetic field can be obtained similar to Eq. (2.47):

$$\boldsymbol{B}(\boldsymbol{r},t) = \boldsymbol{B}_0 + \Re\,\boldsymbol{B}(\boldsymbol{k},\omega)\,\exp(\imath\,\boldsymbol{k}\cdot\boldsymbol{r} - \imath\,\omega\,t). \tag{2.51}$$

Having obtained the expressions for the electromagnetic fields, the particle velocities can be written explicitly as well. The complex components of the particle velocity $\boldsymbol{v}_\alpha(\boldsymbol{k},\omega)$ can be defined with the help of Eqs. (2.27) and (2.28) and the definitions of $v^\pm$ and $E^\pm$ (see Sect. 2.3.1):

$$v_{\alpha,x}(\boldsymbol{k},\omega) = \frac{\imath\,q_\alpha\,(\omega\,E_x(\boldsymbol{k},\omega) + \imath\,\Omega_\alpha\,E_y(\boldsymbol{k},\omega))}{m_\alpha\,(\omega^2 - \Omega_\alpha^2)}, \tag{2.52}$$

$$v_{\alpha,y}(\boldsymbol{k},\omega) = \frac{q_\alpha\,(\Omega_\alpha\,E_x(\boldsymbol{k},\omega) + \imath\,\omega\,E_y(\boldsymbol{k},\omega))}{m_\alpha\,(\omega^2 - \Omega_\alpha^2)}, \tag{2.53}$$

$$v_{\alpha,z}(\boldsymbol{k},\omega) = \frac{\imath\,q_\alpha\,E_z(\boldsymbol{k},\omega)}{m_\alpha\,\omega}. \tag{2.54}$$

The particle velocity $\boldsymbol{v}(\boldsymbol{r},t)$ in real space can then be obtained in the same way as the electromagnetic fields. This can help to model the particle oscillations caused by the electromagnetic fields of a plasma wave.

Note on the Definition of Polarization

The polarization of a wave is usually derived from the orientation of the electric or magnetic field vector of the wave relative to a fixed direction. However, different definitions exist, depending on the choice of the reference direction. Schlickeiser (2003, Chapter 9.2.3.1) names two definitions: the *astronomical* definition, which relates the orientation of the electric field to the direction of the wave vector, and the *plasma physics* definition, which uses the direction of the static background magnetic field as a reference. Although the plasma physics definition is widely used (e.g. Stix, 1992; Schlickeiser, 2003) it is not entirely intuitive, since the polarization state of a wave may change depending on its direction of propagation. For example, a whistler wave would be right-handed circularly polarized when propagating parallel to $\boldsymbol{B}_0$, but left-handed when propagating anti-parallel to $\boldsymbol{B}_0$.

In this work the polarization is defined as suggested by Bittencourt (2004, Chapter 4) or Koskinen (2011, Chapter 4.1.2): Define a coordinate system where the wave vector $\boldsymbol{k}$ points in z'-direction and the transverse electric field lies in the x'-y'-plane. The polarization state P may then be given by an expression similar to Eq. (2.48):

$$P = \frac{\imath \, E_{x'}}{E_{y'}}. \tag{2.55}$$

The wave is *linearly polarized* if $E_{x'}$ and $E_{y'}$ are in phase, i.e. if P is a purely imaginary number (or zero). If P is a complex number then the wave is *elliptically polarized.* This is the most general case. For the special case of $P = \pm 1$ the wave is *circularly polarized.* In this case the wave is said to be *right-handed* (“+” sign) or *left-handed* (“−” sign), according to the definition (Koskinen, 2011, Chapter 4.1.2):

> “The wave vector of a right-handed polarized wave, propagating along the magnetic field, rotates in the same sense as an electron.”

This definition is in agreement with the plasma physics definition of the handedness of parallel propagating waves.

Note that the terms *longitudinal* and *transverse* are used to describe a wave’s polarization, i.e. the orientation of a field vector relative to the wave vector. This is not to be confused with the terms *parallel* and *perpendicular*, which describe the orientation of the wave vector relative to the background magnetic field. For example, a perpendicular (propagating) wave can still be longitudinal, since the two terms describe different properties of the wave.

2.3.4 Characterization of Wave Modes

With the expressions derived in Sects. 2.3.2 and 2.3.3 the individual wave modes in a cold plasma can be distinguished and characterized. Each wave mode has a unique dispersion relation, i.e. relation of wave number k and frequency ω, and polarization state. Additionally, the particle response to the electromagnetic fields of a wave may differ among wave modes.

Note that some authors like to introduce a signed frequency, where the sign may change according to the polarization state of a wave. This convention will not be used here and the frequency will be defined as $\omega \geq 0$ throughout this work.

In the following, a description of several wave modes will be presented. First, the different wave modes will be briefly introduced and ordered according to their respective frequency regimes. The wave modes will be subdivided into two categories: Wave modes with typical frequencies around or above the plasma frequency will be identified as “high frequency waves”, whereas wave modes below the cyclotron frequency of electrons will be called “low frequency waves”. Since “high” and “low frequency” are only relative terms, many different conventions are in use[8]. Thus, it is important to keep the above definition in mind to avoid confusion.

---

[8] For example, other authors may refer to non-dispersive Alfvén waves as “low frequency”, whereas ion cyclotron waves are already dubbed “high frequency waves”.

Frequency Ordering and General Remarks

Before the plasma modes can be ordered according to their typical frequency regimes it is necessary to define the order of cyclotron and plasma frequencies. Koskinen (2011, Chapter 4.3) defines "high plasma density" as $\omega_{\mathrm{p,e}} \gg |\Omega_{\mathrm{e}}|$ and "low plasma density" as $\omega_{\mathrm{p,e}} \ll |\Omega_{\mathrm{e}}|$. Adopting this definition, only high density plasmas will be discussed in the following. It is consistent to study only high density plasmas, because the previous definition of high and low frequency waves would lead to confusion otherwise: In a low density plasma certain wave modes would contain frequency regimes above and below the plasma frequency.

The different plasma modes will be introduced by means of their dispersion relations or their so-called *dispersion surfaces*, i.e. frequency $\omega(\boldsymbol{k})$ as a function of the wave vector. In principle, such a representation of the frequency can be found from Eq. (2.43). Writing down Eq. (2.43) explicitly, i.e. as an expression containing k, ω, $\omega_{\mathrm{p},\alpha}$ and Ω_α, readily yields an expression for the wave number $k(\theta, \phi, \omega)$, which is a polynomial of ω of tenth degree. It is possible to solve the polynomial numerically for ω, which then yields the desired dispersion surfaces.

A different but also common way of representing the various wave modes in frequency space and characterizing their physical properties is the *CMA diagram* (named after Clemmow and Mullaly (1955) and Allis (1955)). This type of diagram will not be discussed here, but it is readily available in the literature (e.g. Bellan (2008, Chapter 6.2.7), Koskinen (2011, Chapter 4.3.4), Stix (1992, Chapter 2-2)).

Following the article of André (1985), the dispersion surfaces in a magnetized plasma are depicted in Fig. 2.1[9]. Starting from the top (i.e. high frequencies) and continuing to the bottom the following wave modes can be identified (and named according to André, 1985):

1. The R-X-surface includes the *R-* and the *(fast) X-mode* for parallel and perpendicular propagation. At sufficiently high frequencies the group velocity of these modes approaches the speed of light from below, whereas the phase speed approaches c from above. The cutoff frequency of the R-X-surface lies above the plasma frequency ω_{p}.

2. The L-O-surface is named after the parallel propagating *L-mode* and the perpendicular propagating *O-mode*. The group velocity of these modes also approaches the speed of light at high frequencies. The plasma frequency ω_{p} serves as a lower cutoff. Note that there is a sharp kink in the dispersion surface at $k_\perp = 0$. For small $k_\parallel$ and $k_\perp = 0$ the dispersion surface is completely flat and runs exactly along the plasma frequency.

3. The next dispersion surface is the upper hybrid surface which includes waves of different names in different regimes. For small k the frequency lies below ω_{p}. This regime is often called the *Z-mode*. Setting $k_\perp = 0$ and increasing $k_\parallel$ again leads to a kink in the dispersion surface, at the same position as for the L-O-surface. At higher $k_\parallel$ the dispersion surface is flat and contains plasma oscillations or *Langmuir waves*. For $k_\parallel = 0$ and large $k_\perp$ the frequency rises above ω_{p} and approaches the *upper hybrid frequency* ω_{uh}. Waves in this regime are therefore attributed to the *upper hybrid mode.*

---

[9] To cover all relevant physical regimes and to be able to show the different dispersion surfaces in the same plot André (1985) uses logarithmic scales for wave numbers and frequencies. This is not done here, however, since the numerical simulations discussed later work on linear scales. It is therefore important to choose physical parameters which allow to reproduce all relevant physical processes within only a few orders of magnitude in both time and space (or frequency and wave number). The following figures have been prepared with respect to these limitations.

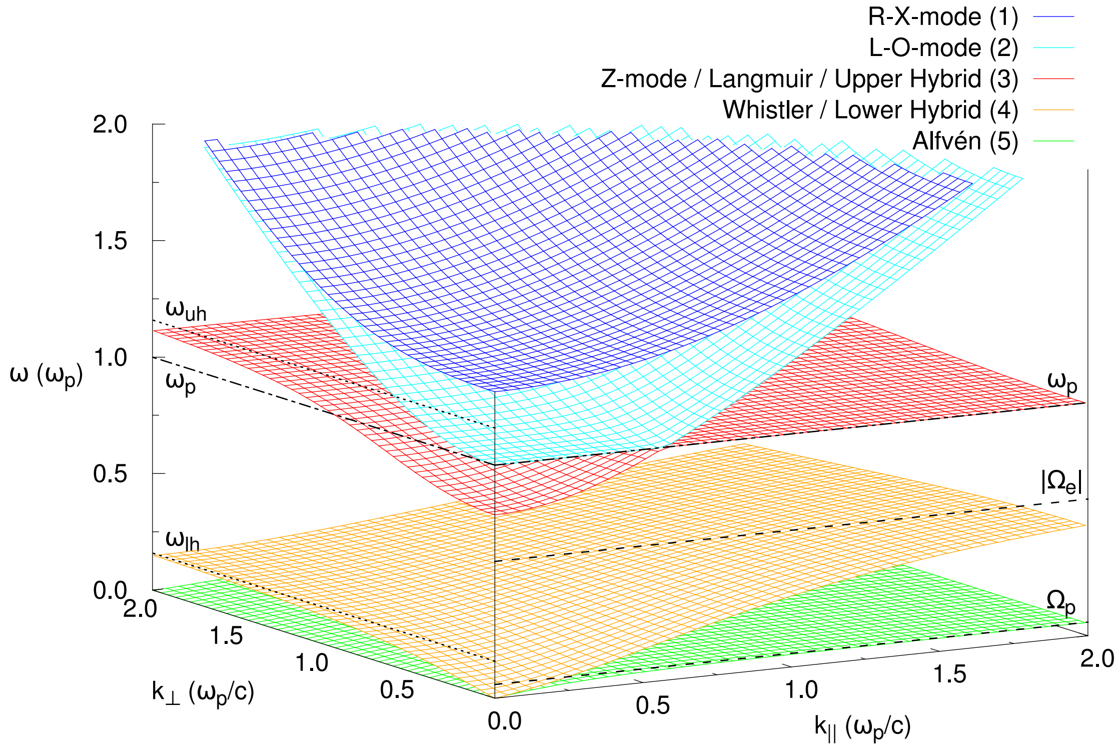

Fig. 2.1: Dispersion surfaces, i.e. frequency as a function of the wave vector, in a cold, magnetized plasma. The different dispersion surfaces which can be obtained from Eq. (2.43) are shown in different colors and labeled and numbered according to their description in the text. Some selected frequencies are marked in the plot: the plasma frequency ω_p (dash-dotted line), the upper and lower hybrid frequencies ω_uh and ω_lh (dotted lines), and the electron and proton cyclotron frequencies Ω_e and Ω_p (dashed lines). Note that the plot has been prepared assuming a mass ratio of $m_\mathrm{p}/m_\mathrm{e} = 10$, i.e. with a drastically lowered proton mass, to make all features of the different dispersion surfaces visible.

4. According to the defined frequency ordering the electron cyclotron frequency lies below the plasma frequency and serves as the asymptotic upper limit of the lower hybrid surface. Note that this limit is only approached by parallel propagating waves, the so-called *electron cyclotron waves*. At smaller $k_\|$ and small $k_\perp$ the electron cyclotron waves turn into the *whistler branch*. At large $k_\perp$ the frequency of perpendicular propagating waves approaches the *lower hybrid frequency* ω_lh, which lies below the electron cyclotron frequency. Waves of the lower hybrid surface are sometimes also referred to as *fast magnetosonic waves* at small k.

5. Finally, at lowest frequencies the Alfvén branch can be found. The frequency of this dispersion surface drops to zero for perpendicular propagation, i.e. no perpendicular propagating waves can exist here. For parallel propagation two regimes exist: At small $k_\|$ the non-dispersive *Alfvén waves* are found. These turn into *ion cyclotron waves* at higher frequencies. The frequency range is limited by the ion cyclotron frequency.

Starting from this short characterization of the different dispersion surfaces a few additional comments can be made.

The dispersion surfaces plotted in Fig. 2.1 have been obtained from the general dispersion relation, Eq. (2.43). However, it is often sufficient to concentrate on purely parallel or perpendicular propagating waves and their respective dispersion relations, Eqs. (2.45) and (2.46). If one does so, a slightly different picture than the one presented in Fig. 2.1 is found. In the case of parallel propagating waves Eq. (2.45) yields a solutions for plasma oscillations ($P = 0$), for the L-mode ($n^2 = L$), and for the R-mode ($n^2 = R$). While the R-mode is equivalent to the dispersion surface along $k_\perp = 0$ in Fig. 2.1, the L-mode and the plasma oscillations are not. The solution $n^2 = L$ produces a high frequency wave mode with a lower cutoff below the plasma frequency which then smoothly crosses ω_p (i.e. no kink) and whose phase speed approaches the speed of light for high frequencies. Relating these findings to the nomenclature of André (1985) a mixture of the Z-mode and the L-mode is produced. However, when looking only at parallel propagating waves the whole solution $n^2 = L$ is often referred to as L-mode, both above and below ω_p. Similarly, the solution $P = 0$ is called “plasma oscillation”, since it enforces that the frequency of these waves is always equal to ω_p.

Without an ordered background magnetic field ($B_0 = 0$) the predominant direction in the plasma is lost. Therefore, the dispersion surfaces become centrally symmetric across $k = 0$. This can also be seen by looking at the behavior of the different frequencies discussed above if B_0 is reduced to zero. Of course, the cyclotron frequencies become zero, in accordance with Eq. (2.8). The upper and lower hybrid frequencies

$$\begin{aligned}
\omega_\mathrm{uh} &= \sqrt{\frac{1}{2}\left(\Omega_\mathrm{e}^2+\Omega_\mathrm{p}^2+\omega_\mathrm{p}^2+\sqrt{\left(\Omega_\mathrm{e}^2-\Omega_\mathrm{p}^2+\omega_\mathrm{p,e}^2\right)^2+2\left(\Omega_\mathrm{p}^2-\Omega_\mathrm{e}^2+\omega_\mathrm{p,e}^2\right)\omega_\mathrm{p,p}^2+\omega_\mathrm{p,p}^4}\right)} \\
&\approx \sqrt{\omega_\mathrm{p}^2+\Omega_\mathrm{e}^2}, \qquad (2.56) \\
\omega_\mathrm{lh} &= \sqrt{\frac{1}{2}\left(\Omega_\mathrm{e}^2+\Omega_\mathrm{p}^2+\omega_\mathrm{p}^2-\sqrt{\left(\Omega_\mathrm{e}^2-\Omega_\mathrm{p}^2+\omega_\mathrm{p,e}^2\right)^2+2\left(\Omega_\mathrm{p}^2-\Omega_\mathrm{e}^2+\omega_\mathrm{p,e}^2\right)\omega_\mathrm{p,p}^2+\omega_\mathrm{p,p}^4}\right)} \\
&\approx \sqrt{\frac{\left(\omega_\mathrm{p,p}^2+\Omega_\mathrm{p}^2\right)\left|\Omega_\mathrm{e}\right|\Omega_\mathrm{p}}{\omega_\mathrm{p,p}^2+\Omega_\mathrm{p}^2+\left|\Omega_\mathrm{e}\right|\Omega_\mathrm{p}}} \qquad (2.57)
\end{aligned}$$

become $\omega_\mathrm{uh} = \omega_\mathrm{p}$ and $\omega_\mathrm{lh} = 0$. Finally, the cutoff frequencies

$$\begin{aligned}
\omega_\mathrm{R-X} &= \frac{1}{2}\left(\sqrt{\left(\Omega_\mathrm{p}-\Omega_\mathrm{e}\right)^2+4\,\omega_\mathrm{p}}-\left(\Omega_\mathrm{p}+\Omega_\mathrm{e}\right)\right), \qquad (2.58) \\
\omega_\mathrm{Z} &= \frac{1}{2}\left(\sqrt{\left(\Omega_\mathrm{p}-\Omega_\mathrm{e}\right)^2+4\,\omega_\mathrm{p}}+\left(\Omega_\mathrm{p}+\Omega_\mathrm{e}\right)\right) \qquad (2.59)
\end{aligned}$$

of the R-X-surface and Z-mode both become equal to the plasma frequency. Thus, the Alfvén and lower hybrid surfaces vanish (all frequencies drop to zero) and the upper hybrid surface forms a plane with $\omega = \omega_\mathrm{p}$. The R-X-surface and the L-O-surface join together, as both have the same cutoff and the same slope, and form the *electromagnetic mode* with the simple dispersion relation $n^2 = P$, which is the same as for the perpendicular propagating O-mode.

High Frequency Waves

In the following only purely parallel or purely perpendicular propagating waves are considered. The dispersion relations can be obtained from Eqs. (2.45) and (2.46), respectively. In Fig. 2.2 the different wave modes are shown in a limited wave number and frequency regime. The color scheme is mainly the same as in Fig. 2.1, with the exception of the L-mode and the plasma oscillations: The plasma oscillations refer to the equation $P = 0$, whereas the L-mode results from $n^2 = L$. As mentioned above, the kinks in the L-O- and upper hybrid dispersion surfaces (see Fig. 2.1) are not recovered in the dispersion relations for parallel propagating waves, Eq. (2.45).

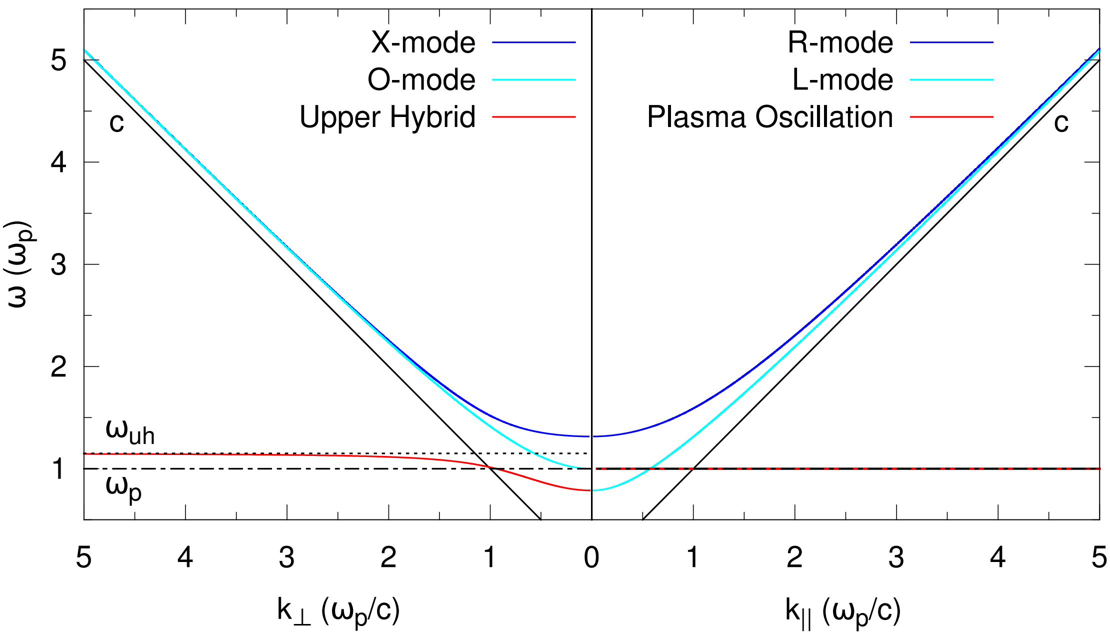

Fig. 2.2: Dispersion relations of perpendicular (left) and parallel (right) propagating high frequency waves. The perpendicular wave modes result from the dispersion relations in Eq. (2.46), the parallel modes from Eq. (2.45). The solid black lines mark the speed of light c, which is the asymptotic phase speed of the X-, O-, R- and L-mode for large wave numbers and high frequencies. Note that the proton mass has been reduced to $m_\mathrm{p} = 10\, m_\mathrm{e}$ (in consistency with Figs. 2.1 and 2.4).

Plasma oscillations, as the name suggests, are longitudinal oscillations of particles at the plasma frequency. The wave mode is electrostatic (i.e. the group speed v_g is zero) and develops an electric field only, since no longitudinal fluctuations in the magnetic field are possible. Electrostatic plasma oscillations only occur parallel to $\boldsymbol{B}_0$ in a magnetized plasma, but can propagate in all directions isotropically in an unmagnetized plasma. They are the only wave mode with purely longitudinal polarization.

The upper hybrid mode also becomes electrostatic at high $k_\perp$, when the frequency approaches the upper hybrid frequency ω_uh, but is electromagnetic at small $k_\perp$ (Z-mode, see description of Fig. 2.1). The electric field vector of waves on the upper hybrid branch lies in the plane perpendicular to $\boldsymbol{B}_0$ and therefore has a longitudinal and a transverse component. According to Eq. (2.48) the ratio of longitudinal to transverse electric field component is given by

$$\frac{\delta E_{\text{long}}}{\delta E_{\text{trans}}} = \left|\frac{D}{S}\right| \tag{2.60}$$

and therefore depends on the frequency of the wave. In Fig. 2.3 it can be seen that the transverse and longitudinal components have equal magnitudes at the cutoff frequency ω_Z, but that the longitudinal component dominates for higher wave numbers and frequencies. At the upper hybrid frequency the electric field becomes purely longitudinal. The magnetic field vector is perpendicular to the wave vector and to the electric field vector and thus parallel to $\boldsymbol{B}_0$.

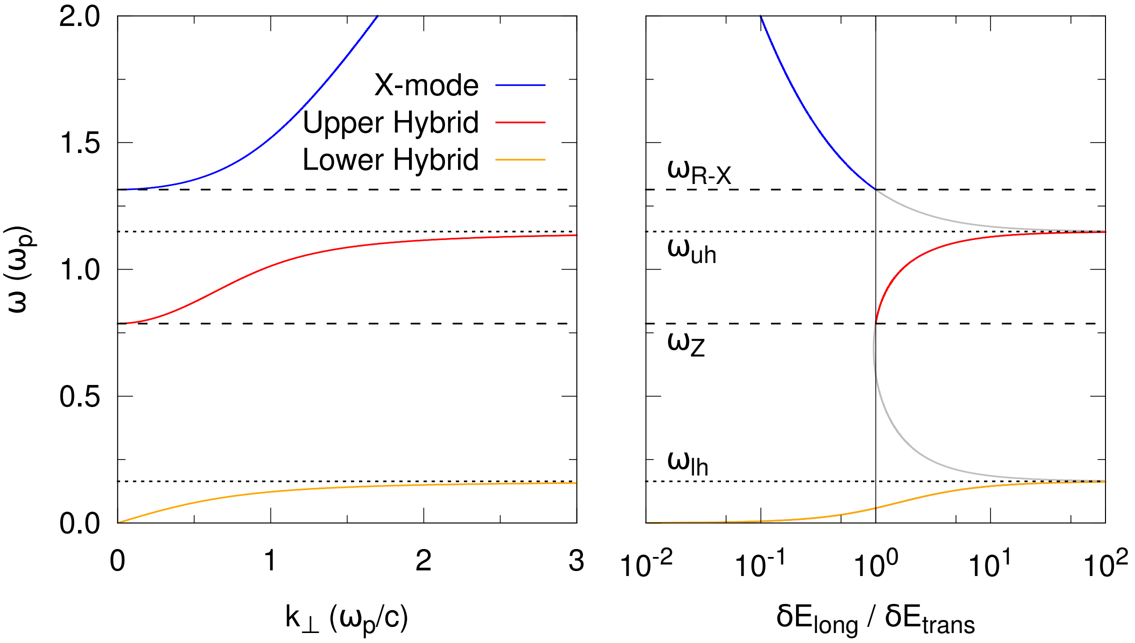

Fig. 2.3: Left panel: Plots of the dispersion relation $n^2 = RL/S$ of perpendicular propagating waves according to Eq. (2.46). Right panel: Ratio of the longitudinal (δE_{long}) and transverse components (δE_{trans}) of the electric field according to Eq. (2.60). A ratio $\delta E_{\text{long}}/\delta E_{\text{trans}} > 1$ (< 1) means that the electric field has a predominantly longitudinal (transverse) polarization.

All other four high frequency modes are electromagnetic and have similar dispersion characteristics, but different polarizations. As already mentioned above, the phase and group velocities of the X-, O-, R- and L-mode approach the speed of light c for high frequencies. Since the phase speed $v_{\text{ph}} = \omega/k$ is always greater than c waves of these modes are sometimes referred to as *superluminal*.

For the parallel propagating waves of the R- and L-mode one finds purely transverse, circular polarization. As indicated by the Stix parameters R and L, Eqs. (2.33) and (2.34), which also describe the dispersion relations of these waves, the R-mode is right-handed, whereas the L-mode is left-handed. The circular polarization of the transverse electric fields can be found by evaluating Eq. (2.48) with $\theta = \phi = 0$ and yields:

$$\frac{\imath E_x}{E_y} = \frac{D}{n^2 - S} = \begin{cases} 1 \text{ for } n^2 = R, \\ -1 \text{ for } n^2 = L. \end{cases} \tag{2.61}$$

This relation shows the circular polarization, where the absolutes of E_x and E_y are equal, independent of the wave number or frequency[10]. The polarization of the magnetic field follows that of the electric field, but the magnetic field vector is always perpendicular to the electric field vector. This can be interpreted as a phase shift of $\pi/2$ between the electric and the magnetic field.

The polarization of the X-mode is given by Eq. (2.60), which also defines the polarization of the upper hybrid mode. Again, the electric field vector lies in the plane perpendicular to $\boldsymbol{B}_0$ and the longitudinal and transverse components have equal magnitudes at the cutoff $\omega_{\mathrm{R-X}}$. However, other than for the upper hybrid mode the transverse component dominates at higher wave numbers and frequencies, as the longitudinal field component vanishes for $\omega \to \infty$ (see Fig. 2.3). The magnetic field vector is purely transverse and parallel to $\boldsymbol{B}_0$.

Finally, the O-mode has a purely transverse, linear polarization, with the electric field vector parallel to $\boldsymbol{B}_0$ and the magnetic field vector perpendicular to both $\boldsymbol{B}_0$ and $\boldsymbol{k}$. Since the dispersion relation of the O-mode is the same as for the electromagnetic mode in an unmagnetized plasma, the electromagnetic mode is also linearly polarized. Without the background magnetic field the directions of the electric and magnetic field vectors of an electromagnetic wave are not fixed. However, the transverse polarization remains and the electric and magnetic field vectors are perpendicular to each other.

Equation (2.50) can be used to relate the amplitude of the fluctuating magnetic field, δB, to the amplitude of the electric field, δE:

$$\frac{\delta B}{\delta E} = \frac{c}{v_{\mathrm{ph}}} \sin \xi, \tag{2.62}$$

where ξ is the angle between the wave vector $\boldsymbol{k}$ and the wave's electric field vector $\boldsymbol{\delta E}$[11]. From Eq. (2.62) it can be seen that $\delta B \approx \delta E$ for transverse electromagnetic waves ($\xi = \pi/2$) at high frequencies, since $v_{\mathrm{ph}} \approx c$ for $\omega \gg \omega_{\mathrm{p}}$.

Low Frequency Waves

In the low frequency regime only two dispersion surfaces exist (see Fig. 2.1). At lowest frequencies the Alfvén surface can be found, which vanishes for purely perpendicular propagation. Therefore, for perpendicular propagation, only the lower hybrid mode exists (left side of Fig. 2.4). For parallel propagation two dispersion branches can be found (right side of Fig. 2.4). All three wave modes propagate with Alfvén speed (see Eq. (2.13)) at low frequencies, as indicated by the black lines in Fig. 2.4.

For perpendicular propagation an electromagnetic wave mode exists, which then transits into an electrostatic regime at large wave numbers $k_\perp$. This electrostatic plateau is sometimes called the *lower hybrid plateau*, whereas the region near $k_\perp = 0$ may be referred to as *fast*

---

[10] Stix (1992) finds $\imath E_x/E_y = (n^2 - S)/D$, i.e. the inverse of the expression on the right-hand side of Eq. (2.61). This, however, yields the same polarization states for the R- and L-mode, of course.

[11] Note that $\boldsymbol{\delta E} = \boldsymbol{E}$, since it was assumed that there is no ordered electric field $\boldsymbol{E}_0$, whereas $\boldsymbol{\delta B} = \boldsymbol{B} - \boldsymbol{B}_0$ (see Sect. 2.3.1).

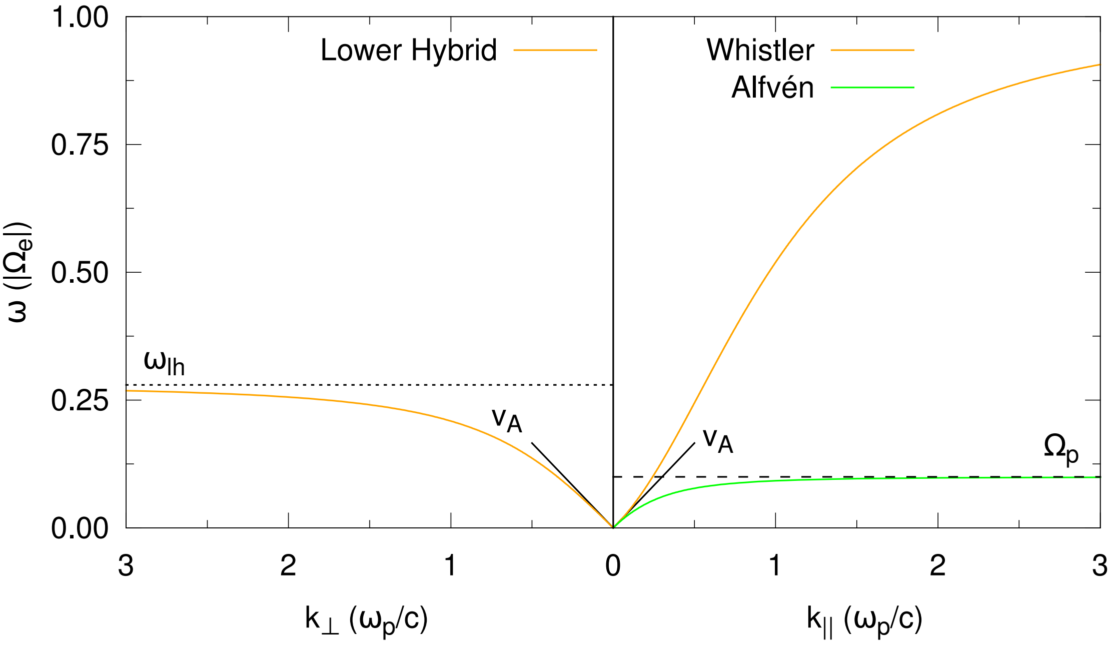

Fig. 2.4: Dispersion relations of perpendicular (left) and parallel (right) propagating low frequency waves. The perpendicular wave mode results from the second dispersion relation in Eq. (2.46), the parallel modes result from Eq. (2.45). The black lines mark the Alfvén speed v_A, which is the phase speed of the low frequency waves at small wave numbers and very low frequencies $\omega \ll \Omega_p$. The proton to electron mass ratio has been set to $m_\mathrm{p}/m_\mathrm{e} = 10$ to make the different wave modes visible in the same plot.

magnetosonic mode (André, 1985). The perpendicular propagating mode can be found by evaluating the dispersion relation $n^2 = RL/S$, Eq. (2.46), and has similar polarization characteristics as the high frequency branches which can be derived from this dispersion relation. The electric field lies in the plane perpendicular to $\boldsymbol{B}_0$ with a strong longitudinal (transverse) component near the lower hybrid frequency ($\omega = 0$), as seen in Fig. 2.3. The magnetic field is oriented parallel to the background field $\boldsymbol{B}_0$ and purely transverse. As the phase speed is much smaller than c, the amplitude of the electric field is much smaller than the amplitude of the magnetic field (see Eq. (2.62)). This is typical for all low frequency wave modes.

The two wave modes with parallel propagation are included in the dispersion relations $n^2 = R$ and $n^2 = L$, Eq. (2.45), and possess the same polarization states as the R- and the L-mode, i.e. transverse, right- or left-handed circular polarization. The right-handed mode propagates with Alfvén speed at very small wave numbers, but its phase and group speeds increase with increasing $k_\parallel$. Waves in this regime are called *whistler waves* and an approximate dispersion relation might be given by (e.g. Steinacker and Miller, 1992):

$$\omega = \frac{k_\parallel^2 \, c^2 \, |\Omega_\mathrm{e}|}{\omega_\mathrm{p}^2}. \tag{2.63}$$

Note that this dispersion relation is derived with the assumption of $m_\mathrm{p} \gg m_\mathrm{e}$ and is therefore not applicable in cases where the proton mass is artificially reduced (e.g. Fig. 2.4). For the natural mass ratio $m_\mathrm{p}/m_\mathrm{e} = 1836$ Eq. (2.63) holds up to $\omega/|\Omega_\mathrm{e}| \approx 0.1$. Whistler waves also exist at oblique propagation angles, where their polarization state changes with the propagation angle. The magnetic field remains circularly polarized, but the electric field becomes elliptical (Verkhoglyadova et al., 2010; Bellan, 2013).

At higher frequencies the group speed of the right-handed parallel wave mode decreases and finally becomes zero as the frequency approaches the electron cyclotron frequency. Waves in this regime are called *electron cyclotron waves.*

The left-handed parallel propagating wave mode contains the *proton cyclotron waves* at high frequencies near the proton cyclotron frequency[12]. Similar to the electron cyclotron waves these waves become electrostatic, as the group speed is reduced to zero. At low frequencies and small $k_\|$ the wave mode is electrodynamic and has a group speed which is always smaller than the Alfvén speed. Left-handed waves at smallest frequencies are called *Alfvén waves*, since they are equivalent to the hydrodynamic waves in electrolytic fluids found by Alfvén (1942a,b). Alfvén waves are assumed to be non-dispersive, since the dispersion relation is linear at small frequencies and the phase and group speed is equal to the Alfvén speed. Note that this is also true for right-handed waves at smallest frequencies and some authors therefore introduce the term *right-handed Alfvén waves.* A simplified dispersion relation for Alfvén waves may be given by:

$$\omega = v_\mathrm{A}\, k_\| . \tag{2.64}$$

This relation is applicable for $\omega \ll \Omega_\mathrm{p}$ independent of the mass ratio $m_\mathrm{p}/m_\mathrm{e}$.

For oblique propagation a good approximation of the dispersion relation of the Alfvén mode can be obtained by introducing an additional cosine term:

$$n^2 \cos^2\theta = L, \tag{2.65}$$

where the index of refraction is $n = |\boldsymbol{k}|\, c/\omega$ and the parallel component of the wave vector is $k_\| = |\boldsymbol{k}| \cos\theta$. The dispersion relation Eq. (2.65) is a modified version of the dispersion relation of the parallel propagating L-mode in the frequency regime $\omega < \Omega_\mathrm{p}$. It reproduces the behavior of the Alfvén dispersion surface (see Fig. 2.1) for polar angles $\theta > 0$ reasonably well and models the vanishing of this wave mode at perpendicular propagation. In the low frequency regime, $\omega \ll \Omega_\mathrm{p}$, the phase and group speed of obliquely propagating Alfvén waves can be approximated by $v_\mathrm{g} = v_\mathrm{ph} = v_\mathrm{A} \cos\theta$.

2.4 Waves in Warm Plasma

After the derivation of wave modes in a cold plasma in the previous section the effects of finite plasma temperature will be discussed. However, this discussion will not be initiated by a rigorous presentation of the theoretical basis, as for the cold plasma case. Instead the focus lies on the description of the consequences of finite temperature, such as wave damping, additional wave modes, or alterations of the dispersion relations of the cold plasma modes.

---

[12] The more general terms *ion cyclotron waves* and *ion cyclotron frequency* are often used in the literature. However, to stress that only electron-proton plasmas are considered here, the term “ion” is replaced by “proton”.

The interested reader is referred to the textbook by Gary (1993), which provides a detailed derivation and discussion of "space plasma microinstabilities" (or, in other words, wave modes). Similar, although less elaborate, essays can be found in Bellan (2008, Chapter 8), Piel (2010, Chapter 9), Schlickeiser (2003, Chapters 8 and 10), and Stix (1992, various chapters).

The basic difference between the description of cold and warm plasmas is the distribution function $f_\alpha(\boldsymbol{r}, \boldsymbol{v}, t)$ of particles of species α. In the cold plasma approach the particles are assumed to be stationary (with small harmonic perturbations), which makes for a rather simple distribution function. In a warm plasma the particles have non-vanishing velocities and different kinds of velocity distributions may arise (such as a Maxwellian distribution in a thermal plasma). The distribution function can evolve over time and energy may be transferred from the particles to electromagnetic fields or vice versa. This leads to the growth and damping of plasma instabilities and wave modes, which cannot be treated in the cold plasma approximation.

To obtain a basis for the description of warm plasmas Maxwell's equations have to be coupled with a *kinetic equation*, which characterizes the time evolution of the distribution function $f_\alpha(\boldsymbol{r}, \boldsymbol{v}, t)$. The important part of the kinetic equation is that the particles' velocities are considered, which allows to recover the physics of wave-particle interactions (Gary, 1993, Chapter 1). The interaction of waves and particles leads to plasma heating, particle acceleration, or the damping and growth of wave modes, and generally shifts energy between particles and electromagnetic fields. A general representation of the kinetic equation used to model the evolution of $f_\alpha(\boldsymbol{r}, \boldsymbol{v}, t) := f_\alpha$ in non-relativistic plasmas can be given by the *Boltzmann equation* (Gary, 1993, Chapter 1):

$$\frac{\partial f_\alpha}{\partial t} + \boldsymbol{v} \cdot \frac{\partial f_\alpha}{\partial \boldsymbol{r}} + \frac{q_\alpha}{m_\alpha} \left(\boldsymbol{E} + \frac{1}{c} \boldsymbol{v} \times \boldsymbol{B} \right) \cdot \frac{\partial f_\alpha}{\partial \boldsymbol{v}} = \left(\frac{\partial f_\alpha}{\partial t} \right)_{\text{collision}} . \tag{2.66}$$

In the case of a collisionless plasma the collision term on the right-hand side of the above equation vanishes. This is generally the case if the plasma is tenuous or hot enough – a condition which can be described by $n \, \lambda_\mathrm{D} \gg 1$, where n is the number density of charged particles in the plasma (see Sect. 2.2.2). The resulting form of the kinetic equation is known as the *Vlasov equation* (Vlasov, 1938):

$$\frac{\partial f_\alpha}{\partial t} + \boldsymbol{v} \cdot \frac{\partial f_\alpha}{\partial \boldsymbol{r}} + \frac{q_\alpha}{m_\alpha} \left(\boldsymbol{E} + \frac{1}{c} \boldsymbol{v} \times \boldsymbol{B} \right) \cdot \frac{\partial f_\alpha}{\partial \boldsymbol{v}} = 0. \tag{2.67}$$

The kinetic or Vlasov equation describes the micro-physical properties of the plasma. However, macroscopic quantities can be obtained by computing the so-called *velocity moment integrals* (following Gary, 1993, Chapter 1):

The particle density results from the zeroth moment and can be expressed as

$$n_\alpha = \int d^3v \, f_\alpha. \tag{2.68}$$

The first moment yields the *particle flux density*

$$\boldsymbol{\Gamma}_\alpha = \int d^3v \, \boldsymbol{v} \, f_\alpha, \tag{2.69}$$

which defines the *momentum density* $\boldsymbol{P}_\alpha = m_\alpha \boldsymbol{\Gamma}_\alpha$ and the *drift velocity* $\boldsymbol{V}_{\mathrm{d},\alpha} = \boldsymbol{\Gamma}_\alpha / n_\alpha$. The kinetic energy density and the plasma temperature can be derived from the second moments. The kinetic energy density can be represented by a tensor[13] or a scalar,

$$\boldsymbol{W}_{\mathrm{kin},\alpha} = \frac{m_\alpha}{2} \int d^3v\, \boldsymbol{v} \otimes \boldsymbol{v}\, f_\alpha, \tag{2.70}$$

$$W_{\mathrm{kin},\alpha} = \frac{m_\alpha}{2} \int d^3v\, v^2\, f_\alpha, \tag{2.71}$$

whereas the temperature is always a scalar. It is expressed by central moments and may be defined either globally (T_α) or with different values parallel or perpendicular ($T_{\|\alpha}$, $T_{\perp\alpha}$) to the ordered background magnetic field $\boldsymbol{B}_0$:

$$T_\alpha = \frac{m_\alpha}{3\, n_\alpha} \int d^3v\, (\boldsymbol{v} - \boldsymbol{V}_{\mathrm{d},\alpha})^2\, f_\alpha, \tag{2.72}$$

$$T_{\|\alpha} = \frac{m_\alpha}{3\, n_\alpha} \int d^3v\, (v_\| - V_{\|\mathrm{d},\alpha})^2\, f_\alpha, \tag{2.73}$$

$$T_{\perp\alpha} = \frac{m_\alpha}{3\, n_\alpha} \int d^3v\, (\boldsymbol{v}_\perp - \boldsymbol{V}_{\perp\mathrm{d},\alpha})^2\, f_\alpha. \tag{2.74}$$

Finally, the third moment describes the *kinetic energy flux density* or *heat flux density*:

$$\boldsymbol{q}_\alpha = \frac{m_\alpha}{2\, n_\alpha} \int d^3v\, \boldsymbol{v}\, v^2\, f_\alpha. \tag{2.75}$$

The definition of the macro-physical quantities by means of the moments of the distribution function f_α, Eqs. (2.68) through (2.75), together with the Vlasov equation (2.67) and Maxwell's equations (2.15) through (2.18) builds the basis for the description of a warm, kinetic plasma, i.e. a description which allows wave-particle interactions to be considered. To derive plasma instabilities and wave modes in a linearized theory a similar approach as described for cold plasmas can be chosen: The Vlasov-Maxwell system of equations is considered in Fourier space and small fluctuations in particle (flux) density are assumed. By inserting these fluctuations into Maxwell's equations a dispersion relation can be obtained. However, the wave vector and the frequency can now be complex quantities. A common convention is to assume the wave vector $\boldsymbol{k}$ to be real and to define a complex frequency $\omega_c = \omega + \imath\,\Gamma$, where ω is the real frequency (same as in the cold plasma case) and Γ is the growth or damping rate (e.g. Stix, 1992; Gary, 1993; Schlickeiser, 2003).

Often one finds a discrimination of plasma phenomena according to the ratio Γ/ω: For $\Gamma/\omega > 0$ (i.e. $\Gamma > 0$) a growing fluctuation arises, which might be called *instability.* Negative ratios refer to damped fluctuations, which may be subdivided into *weakly damped waves* with $0 > \Gamma/\omega > -1$ and *strongly damped waves* with $\Gamma/\omega < -1$. The latter are also referred to as *quasi-periodic oscillations*, since they do not propagate like regular waves due to the strong damping.

As stated at the beginning of this section a thorough derivation of wave modes and instabilities in warm plasmas will be omitted here. Generally speaking, it can be said that

---

[13] However, the tensor notation used by Gary (1993) is less common. More often the Cartesian product $\boldsymbol{v} \otimes \boldsymbol{v}$ in Eq. (2.70) is replaced by $(\boldsymbol{v} - \boldsymbol{V}_{\mathrm{d},\alpha}) \otimes (\boldsymbol{v} - \boldsymbol{V}_{\mathrm{d},\alpha})$ and the resulting quantity is referred to as the *stress tensor.*

the procedure of obtaining and solving dispersion relations in a warm plasma is much more complicated than in the cold plasma approximation. Analytical solutions often cannot be found at all and it is either necessary to simplify the equations by appropriate assumptions or to solve them numerically. However, a small number of wave modes will be named and briefly described in Sect. 2.4.1, since finite temperature effects change the behavior of certain modes or produce entirely new ones which are not present in the cold plasma description. A short discussion of wave damping follows in Sect. 2.4.2, but growing plasma instabilities are not considered[14].

2.4.1 Dispersion Relations in Warm Plasma

Hydromagnetic Waves

Finite temperature effects and the interaction of waves and particles lead to a change in the cold plasma dispersion relations and eventually also to entirely new wave modes. At lowest frequencies ($\omega \ll \Omega_{\mathrm{p}}$) a set of *hydromagnetic* or *magnetohydrodynamic (MHD) modes* can be found. Note that, as the name suggests, these wave modes can be derived in the MHD approximation and a kinetic description is not needed (see e.g. Koskinen, 2011, Chapter 6.6).

In a warm plasma three distinct MHD modes can be found and named according to their phase speed characteristics: *fast magnetosonic waves*, *(shear) Alfvén waves*, and *slow magnetosonic waves*. The Alfvén mode (or shear Alfvén mode for oblique propagation) could already be found in a cold plasma and its dispersion relation is given by Eq. (2.65). In a warm, magnetized plasma the interplay of density fluctuations (sound waves) and magnetic field fluctuations (Alfvén waves) leads to two additional wave modes which can be described by the dispersion relation (Koskinen, 2011, Chapter 6.6):

$$\frac{\omega^2}{k^2} = \frac{1}{2}\left(v_{\mathrm{s}}^2 + v_{\mathrm{A}}^2\right) \pm \frac{1}{2}\sqrt{\left(v_{\mathrm{s}}^2 + v_{\mathrm{A}}^2\right)^2 - 4\,v_{\mathrm{s}}^2\,v_{\mathrm{A}}^2\,\cos^2\theta}. \tag{2.76}$$

The "+" and "−" signs refer to the fast and slow magnetosonic mode, respectively. In the case of a magnetized electron-proton plasma the sound speed is given by (Balogh and Treumann, 2013, Chapter 3.5.1)

$$v_{\mathrm{s}}^2 = \frac{4\,k_{\mathrm{B}}\,T_{\mathrm{p}}}{m_{\mathrm{p}}}, \tag{2.77}$$

which is obtained from the limit $k_\parallel \to 0$ of the dispersion relation of the parallel propagating *ion acoustic wave*:

$$\frac{\omega^2}{k_\parallel^2} \approx \frac{\gamma_{\mathrm{p}}\,k_{\mathrm{B}}\,T}{m_{\mathrm{p}}} + \frac{\gamma_{\mathrm{e}}\,k_{\mathrm{B}}\,T}{m_{\mathrm{p}}}\,\frac{1}{1 + k_\parallel^2\,\lambda_{\mathrm{D}}^2}. \tag{2.78}$$

Here, equal electron and proton temperatures $T_{\mathrm{e}} = T_{\mathrm{p}} = T$ and adiabatic indices $\gamma_{\mathrm{e}} = 1$ and $\gamma_{\mathrm{p}} = 3$ have been assumed.

As all MHD waves are non-dispersive it is common to characterize them by their respective phase speed $v_{\mathrm{ph}} = \omega/k$. In Fig. 2.5 the phase speeds of the shear Alfvén mode and the fast and slow magnetosonic mode are shown as functions of the propagation angle θ towards the background magnetic field $\boldsymbol{B}_0$. The phase speed of the shear Alfvén mode is independent of the sound speed (or the plasma temperature) and decreases with increasing θ until it becomes

---

[14] The interested reader is referred to (Boyd and Sanderson, 2003, Chapter 6), Gary (1993, Chapters 3, 4, 7), Schlickeiser (2003, Chapter 11), or Schlickeiser (2010).

zero at perpendicular propagation. As the phase speeds of the fast and slow magnetosonic modes depend on the sound speed, different v_s have been chosen to illustrate the effect of a rising plasma temperature. Figure 2.5 therefore shows ten curves for the phase speeds of the fast and the slow mode at ten temperature settings, resulting in sound speeds in the range $0 < v_\mathrm{s}/v_\mathrm{A} < 0.65$.

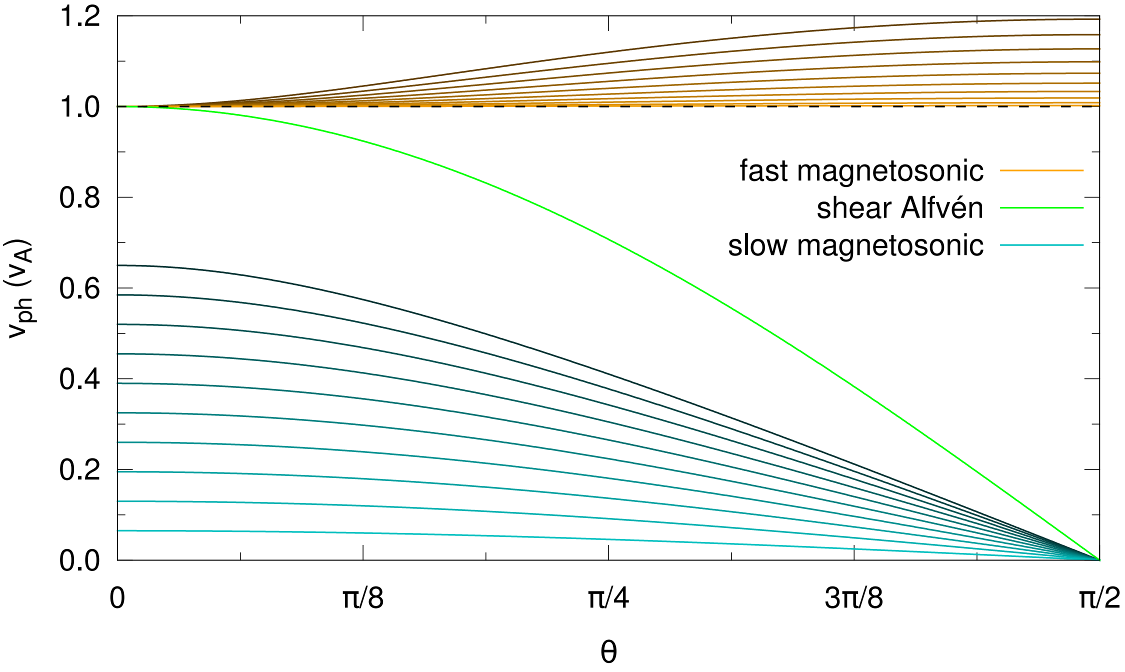

Fig. 2.5: Phase speeds of MHD waves as a function of the propagation angle θ with respect to the background magnetic field $\boldsymbol{B}_0$. For finite temperatures the phase speeds of the fast and slow magnetosonic mode change, as indicated by the curves of different color. Darker colors refer to higher temperatures. Ten different plasma temperatures ($v_\mathrm{th,e}/c \in \{0.01, 0.02, \ldots, 0.10\}$) and a mass ratio of $m_\mathrm{p}/m_\mathrm{e} = 10$ were assumed.

For $v_\mathrm{s} < v_\mathrm{A}$ ($v_\mathrm{s} > v_\mathrm{A}$) the fast mode has a phase speed $v_\mathrm{ph} = v_\mathrm{A}$ ($v_\mathrm{ph} = v_\mathrm{s}$) and the slow mode has a phase speed $v_\mathrm{ph} = v_\mathrm{s}$ ($v_\mathrm{ph} = v_\mathrm{A}$) at $\theta = 0$. The phase speeds at $\theta = \pi/2$ are independent of the ratio $v_\mathrm{s}/v_\mathrm{A}$: For the slow mode the phase speed is zero, whereas the fast mode has a phase speed

$$v_\mathrm{ms} = \sqrt{v_\mathrm{s}^2 + v_\mathrm{A}^2}, \tag{2.79}$$

which is sometimes called *magnetosonic speed* (Koskinen, 2011, Chapter 6.6). For all other propagation angles the phase speed of the fast magnetosonic mode is always larger and that of the slow magnetosonic mode is always smaller than v_A.

Note that the fast magnetosonic mode transits into the lower hybrid dispersion surface at higher frequencies (see Figs. 2.1 and 2.4). The slow magnetosonic mode has no equivalent in cold plasma dispersion theory.

Modified Dispersion Relations of Parallel Propagating Waves

After the brief introduction of the MHD waves, the effect of finite temperature on dispersive waves will be discussed. Most high frequency waves will be excluded. Since the R-X- and L-O-waves have frequencies above the plasma frequency, particles hardly interact with the fast fluctuations of the electromagnetic fields caused by these waves. It can also be shown that these waves do not undergo any damping due to their superluminal phase speed (Schlickeiser, 1995; Schlickeiser et al., 1997). However, waves at lower frequencies are affected by temperature effects. In the following parallel propagating waves will be considered.

The simplest example are the longitudinal plasma oscillations discovered by Langmuir (1928). From the cold plasma dispersion relation $P = 0$, Eq. (2.45), one expects oscillations at the plasma frequency only. However, observations and the theoretical work by Tonks and Langmuir (1929) show that this is not the case. Instead, a wave mode with the dispersion relation (e.g. Gary, 1993, Chapter 2.2.1)

$$\omega^2 = \omega_\mathrm{p}^2 + 3k_\|^2\, v_\mathrm{th,e}^2 \tag{2.80}$$

is found, which describes the relation of the real part of the frequency (ω) and the parallel wave number ($k_\|$). This wave mode is called *Langmuir mode*. The non-vanishing imaginary part of the complex frequency of the Langmuir mode leads to damping at large $k_\|$ (see Eq. (2.91) in Sect. 2.4.2), whereas the wave may propagate at small wave numbers. In Fig. 2.6 the dispersion relation of the Langmuir mode is illustrated for different plasma temperatures.

Moving to lower frequencies the right-handed whistler and the left-handed Alfvén branch can be found. These wave modes reside below the electron or proton cyclotron frequency, respectively, and therefore may interact with particles of the respective species. On the one hand, this leads to cyclotron damping, which will be discussed in Sect. 2.4.2. On the other hand, the real part of the frequency also changes compared to the cold plasma dispersion relation and both wave modes are shifted to lower frequencies.

The full dispersion relation of left- and right-handed parallel propagating low frequency waves in a warm plasma is given by (Kennel and Petschek, 1966):

$$0 = D(\omega_c, k_\|) = \omega_c^2 - k_\|^2\, c^2 + \sum_\alpha \omega_{\mathrm{p},\alpha}^2\, Y_\alpha, \tag{2.81}$$

where $\omega_c = \omega + \imath\,\Gamma$ is the complex frequency. Considering a bi-Maxwellian velocity distribution (allowing for different temperatures $T_\|$ and $T_\perp$ parallel and perpendicular to $\boldsymbol{B}_0$) the function Y_α becomes (Chen et al., 2013):

$$Y_\alpha = \frac{v_{\perp\,\alpha}^2}{v_{\|\,\alpha}^2} - 1 + \left(\frac{v_{\perp\,\alpha}^2}{v_{\|\,\alpha}^2}\, \frac{\omega_c \mp \Omega_\alpha}{\pm\Omega_\alpha} + 1 \right) \frac{\pm\Omega_\alpha}{\sqrt{2}\, k_\|\, v_{\|\,\alpha}}\, Z(\zeta_\alpha), \tag{2.82}$$

with the *plasma dispersion function* $Z(\zeta_\alpha)$ (Fried and Conte, 1961) and its argument

$$\zeta_\alpha = (\omega_c \mp \Omega_\alpha)/(\sqrt{2}\, k_\|\, v_{\|\,\alpha}). \tag{2.83}$$

The temperature is expressed by the thermal speeds $v_{\|\,\alpha}$ and $v_{\perp\,\alpha}$ parallel and perpendicular to $\boldsymbol{B}_0$ (according to definition Eq. (2.10), but with $T_\|$ or $T_\perp$ instead of T). Note that

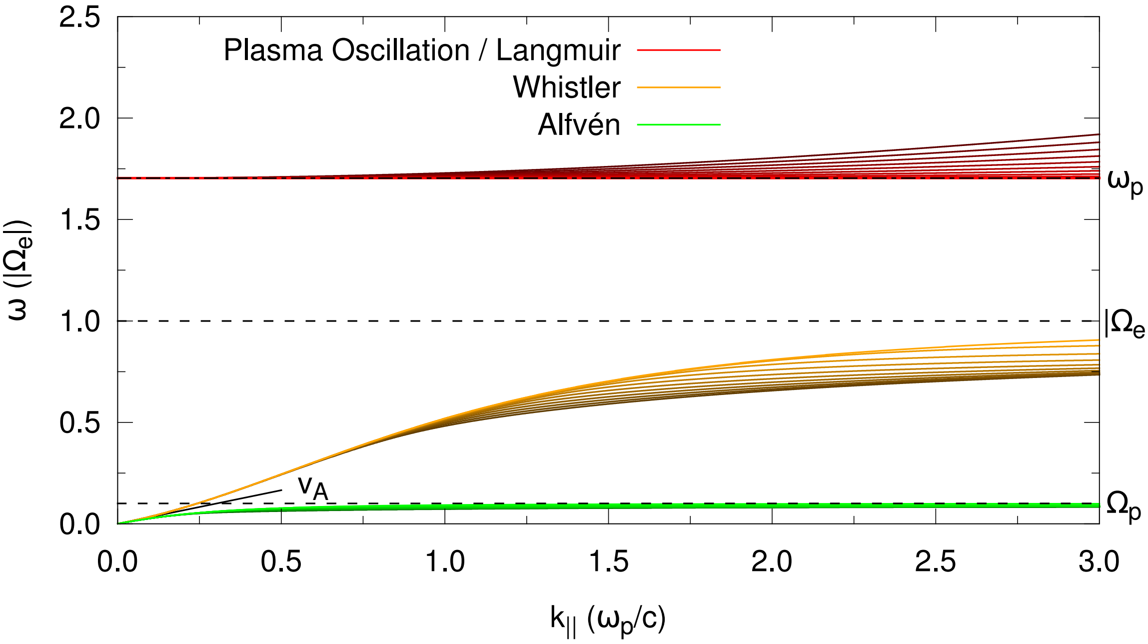

Fig. 2.6: Dispersion relations of parallel propagating waves in a warm plasma. Shown are the cold plasma dispersion relations together with the warm plasma dispersion relations for ten plasma temperatures ($v_{\mathrm{th,e}}/c = \{0.01, 0.02, \ldots, 0.10\}$). Lines in darker colors refer to higher temperatures. A mass ratio of $m_\mathrm{p}/m_\mathrm{e} = 10$ was used.

Eq. (2.82) yields the left-handed or right-handed wave mode, depending on whether the upper or lower signs are chosen in Eqs. (2.82) and (2.83).

The final dispersion relation, a combination of Eqs. (2.81) and (2.82), cannot be solved analytically[15]. However, solutions can be obtained numerically and are shown in Fig. 2.6 for different plasma temperatures (with the assumption of a Maxwellian plasma with $T_\| = T_\perp = T$). Compared to the cold plasma dispersion relation it can be seen that the frequency decreases at large $k_\|$ with increasing temperature. This is especially noticeable for the whistler branch and less obvious for the Alfvén branch.

Perpendicular Propagating Wave Modes

A set of peculiarly interesting wave modes are the perpendicular propagating *Bernstein modes*. These wave modes have first been found by Bernstein (1958), who solved the Vlasov-Maxwell system of equations for a magnetized plasma and considered ion effects. The so-called *ion Bernstein modes* are electrostatic waves with perpendicular propagation which occur at harmonics of the ion cyclotron frequency. The perhaps most interesting aspect of these waves is that they are neither growing nor damped.

Similar waves, the *electron Bernstein modes*, exist at harmonics of the electron cyclotron

---

[15] It is, however, possible to derive analytic continuations of the exact dispersion functions, which can then be discussed in certain limits (e.g. Lazar and Schlickeiser, 2006; Seough and Yoon, 2009), or to derive entirely analytic dispersion relations under special conditions (e.g. Sonnerup and Su, 1966).

frequency. Their dispersion relations can be expressed by (Boyd and Sanderson, 2003)

$$1 - \frac{2\,\Omega_{\mathrm{e}}^2 \exp(-\lambda)}{k_\perp^2\,\lambda_{\mathrm{D}}^2} \sum_{n=0}^{\infty} \frac{n^2\,I_n(\lambda)}{\omega^2 - n^2\,\Omega_{\mathrm{e}}^2} = 0, \tag{2.84}$$

with the modified Bessel functions of the first kind $I_n(\lambda)$ (see e.g. Abramowitz and Stegun, 1983, Chapter 9) and the parameter $\lambda = (k_\perp^2\,k_{\mathrm{B}}\,T)/(m_{\mathrm{e}}\,\Omega_{\mathrm{e}}^2)$. The dispersion relations can be solved numerically and the Bernstein modes of order n can be obtained. With one exception (in this case $n = 1$) all Bernstein modes have a cutoff frequency at $k_\perp = 0$ which is equal to a multiple of $|\Omega_{\mathrm{e}}|$. The cutoff of the remaining Bernstein mode occurs at the upper hybrid frequency ω_{uh} (see Fitzpatrick, 2014, Chapter 8.8).

Figure 2.7 shows the first six electron Bernstein modes for different plasma temperatures. Note that only the electrostatic (large $k_\perp$) part of the dispersion relation is shown from $n = 2$ on. A schematic which also shows the behavior at small $k_\perp$ can be found in Boyd and Sanderson (2003, Chapter 7.6). It can be seen from Fig. 2.7 that temperature predominantly influences the Bernstein modes of orders zero and one, i.e. those modes with the lowest frequencies. The high frequency electrostatic modes remain mostly unaffected.

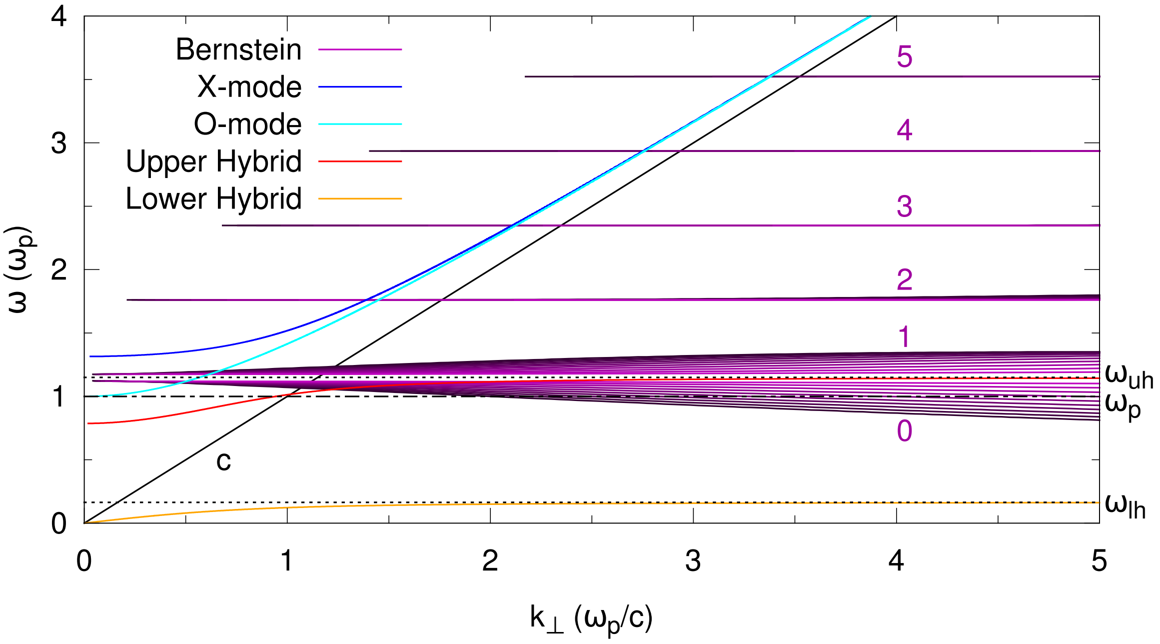

Fig. 2.7: Bernstein modes are additional, perpendicular propagating plasma waves in a warm plasma. Solutions of the dispersion relation of the Bernstein modes of order $n \in \{0, 1, \ldots, 5\}$ are obtained for ten plasma temperatures ($v_{\mathrm{th,e}}/c \in \{0.01, 0.02, \ldots, 0.10\}$). Darker lines refer to higher temperature. The cold plasma dispersion relations for X-, O-, upper, and lower hybrid modes are plotted as a reference. A mass ratio of $m_{\mathrm{p}}/m_{\mathrm{e}} = 10$ has been used.

2.4.2 Wave Damping

As previously indicated, the warm plasma dispersion relations introduce a complex frequency ω_c which includes the damping (or growth) rate Γ as its imaginary part. The damping rate itself can be seen as a function $\Gamma(\boldsymbol{k})$ of the wave vector $\boldsymbol{k}$ which takes on different values depending on the absolute value and the orientation of $\boldsymbol{k}$. Assuming plane waves which oscillate with $\exp(\imath(\boldsymbol{k}\cdot\boldsymbol{r}-\omega_c\,t))$, the imaginary part of ω_c leads to an exponential term which describes the decay of a wave's field amplitude $\delta F(t)=\delta F(t_0)\,\exp(\Gamma\,t)$.

Generally, no damping occurs for superluminal (high frequency) waves (Schlickeiser, 1995; Schlickeiser et al., 1997) or for waves at very large scales, i.e. small wave numbers. With increasing k the wavelength approaches the kinetic scales of the particles in the plasma and damping sets in. For example, in the case of cyclotron damping the typical length scale at which wave-particle interaction becomes possible is given by the Larmor radius. It is important to note that the damping of electromagnetic waves is a collisionless process and that energy dissipation occurs even in a collisionless plasma.

In the following two mechanisms of wave damping will be considered and briefly illustrated: *Landau* and *cyclotron damping*. Both mechanisms are thought to play important roles for the dissipation of field energy at the high-k end of a turbulent cascade of waves. Using the *Landau* and *cyclotron resonance factors* $\zeta_\alpha=\omega/(\sqrt{2}\,k_\parallel\,v_{\mathrm{th},\alpha})$ and $\zeta_\alpha^\pm=(\omega\pm\Omega_\alpha)/(\sqrt{2}\,k_\parallel\,v_{\mathrm{th},\alpha})$, Gary and Nishimura (2004) derive resonance conditions for the Landau and cyclotron resonances:

$$|\zeta_\alpha| \leq 3, \tag{2.85}$$
$$|\zeta_\alpha^\pm| \leq 3. \tag{2.86}$$

Meeting these conditions is a necessary requirement for resonant wave-particle interaction, although Eqs. (2.85) and (2.86) alone are not sufficient to determine whether a wave is damped. From the above equations a more intuitive representation of the resonance conditions in the form of linear dispersion relations can be derived:

$$\omega_\alpha(k_\parallel) = 3\sqrt{2}\,k_\parallel\,v_{\mathrm{th},\alpha}, \tag{2.87}$$
$$\omega_\alpha^\pm(k_\parallel) = |\Omega_\alpha|\pm 3\sqrt{2}\,k_\parallel\,v_{\mathrm{th},\alpha}. \tag{2.88}$$

These frequencies mark the limits of the resonant regime in $k_\parallel$-ω-space and the resonance conditions are

$$\omega(k_\parallel)\leq\omega_\alpha(k_\parallel) \qquad \text{for Landau damping,} \tag{2.89}$$
$$\omega_\alpha^-(k_\parallel)\leq\omega(k_\parallel)\leq\omega_\alpha^+(k_\parallel) \qquad \text{for cyclotron damping.} \tag{2.90}$$

This shows that there is only an upper frequency limit for Landau damping, but a lower as well as an upper frequency limit for cyclotron damping, which are symmetric about the cyclotron frequency of species α.

An interpretation of the resonance conditions above is given by Gary (1993, Chapter 2.2): A particle can only resonate with the electromagnetic fields of a wave if its speed parallel to the wave's direction of propagation is equal (or similar) to the phase speed. The resonance factors ζ_α and $\zeta_\alpha^\pm$ can be seen as the ratio of the wave's parallel phase speed $\omega/k_\parallel$ and the most probable speed $\sqrt{2}\,v_{\mathrm{th},\alpha}$ of a thermal particle of species α. A small ratio means that more particles can be found in the velocity range close to the phase speed, whereas a large ratio denotes that only the high energy tail of the particle distribution can interact with the wave. The resonance conditions denoted by Eqs. (2.85) and (2.86) can therefore be interpreted as an approximation for the fraction of the thermal particle spectrum that must be able to resonate with the wave in order to create a substantial energy transfer.

This interpretation also illustrates why there is no damping in cold plasmas: Since the particles are assumed to be stationary they can never resonate with the waves of finite phase speeds.

Landau Damping

Landau damping was first derived by Landau (1946), who found that a finite damping or growth rate Γ is a direct result of the Vlasov equation. For a Maxwellian velocity distribution Γ is always negative and electromagnetic field fluctuations are damped (Gary, 1993, Chapter 2.2).

An intuitive understanding of Landau damping can be obtained by considering a longitudinal plasma wave, i.e. a wave whose electric field vector oscillates along its direction of propagation. A particle propagating parallel to the wave with a speed close to the phase speed can interact with the electric field. The particle will be accelerated if it is slightly slower than the phase speed and decelerated if it is slightly faster than the phase speed. Due to the shape of the Maxwellian velocity distribution it can be assumed that there are more particles with velocities smaller than the phase speed than there are particles with larger velocities. Therefore, more particles are accelerated by the wave than are decelerated and a net transfer of energy from the wave to the particles is established which results in the damping of the wave.

Although the idea is simple the actual computation of damping rates is a complicated matter and often has to be carried out numerically. For the case of the parallel propagating Langmuir mode an analytic approximation exists (Gary, 1993, Chapter 2.2.1):

$$\Gamma = -\sqrt{\frac{\pi}{8}}\,\frac{k_\mathrm{e}^3}{k^3}\,\frac{\omega^2}{\omega_\mathrm{p,e}}\,\exp\left(-\frac{\omega^2}{2\,k^2\,v_\mathrm{th,e}^2}\right), \tag{2.91}$$

where the real frequency ω is obtained from the dispersion relation of the Langmuir mode, Eq. (2.80). The parameter $k_\mathrm{e} = \omega_\mathrm{p,e}/v_\mathrm{th,e}$ corresponds to the inverse of the electron Debye length, which can be expressed by Eq. (2.2), if only electrons are considered. As an example, the damping rates of the Langmuir mode at different plasma temperatures are shown in the top panel of Fig. 2.8. The exponential term in Eq. (2.91) leads to a fast increase of $|\Gamma|$ with increasing $k_\|$, which quickly results in $\Gamma/\omega < -1$. Therefore, the Langmuir mode is strongly damped and not able to propagate at large $k_\|$.

Parallel propagating waves other than the Langmuir mode are not affected by Landau damping since they are not longitudinally polarized. Oblique and perpendicular propagating low frequency waves, however, are subject to Landau damping. Alfvén and whistler waves are primarily cyclotron damped for parallel and quasi-parallel propagation. However, at increasingly oblique propagation angles Landau damping becomes more and more important, eventually surpassing the effect of cyclotron damping. The case of so-called *kinetic Alfvén waves* (KAWs), i.e. Alfvén waves with high perpendicular wave numbers, is especially interesting and often discussed in the literature (e.g. Hollweg, 1999; Cranmer and van Ballegooijen, 2003; Gary and Nishimura, 2004; Gary and Smith, 2009). Landau damping of KAWs

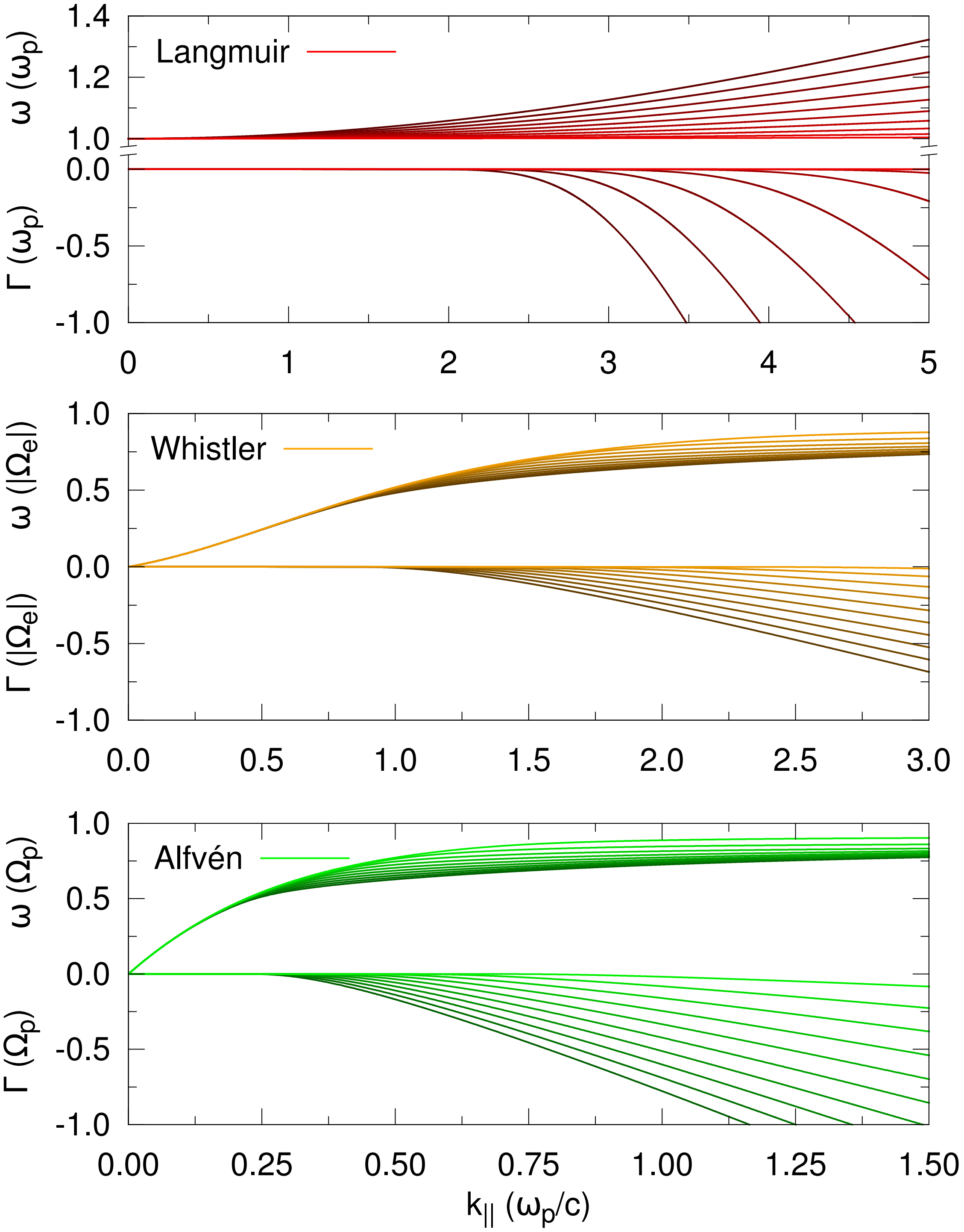

Fig. 2.8: Dispersion relations and damping rates of parallel propagating waves. Lines in different colors represent solutions of the dispersion relations at ten different plasma temperatures ($v_{\mathrm{th,e}}/c \in \{0.01, 0.02, \ldots, 0.10\}$). Darker lines refer to higher temperatures.

is assumed to be an important dissipation mechanism in turbulent media, contributing to plasma heating.

Cyclotron Damping

Similar to the principle of Landau damping the cyclotron damping mechanism is also quickly explained (c.f. Stix, 1958): Charged particles gyrate about a magnetic field $\boldsymbol{B}_0$. The gyration occurs at the cyclotron frequency of the respective particle. If there was a circularly polarized electric field rotating about $\boldsymbol{B}_0$ in the same sense and with the same frequency as the particle, the particle could resonate with the field and be accelerated in a direction perpendicular to $\boldsymbol{B}_0$. However, there is no plasma mode for which this is the case.

In a thermal plasma a particle may have a finite speed along the magnetic field, which is not influenced by its gyration. From the point of view of the particle the frequencies of waves in the plasma are Doppler shifted and, depending on the particle's speed parallel to $\boldsymbol{B}_0$, may be equal to the particle's cyclotron frequency. Therefore, a moving particle can resonate with plasma waves at frequencies other then the cyclotron frequency in the rest frame of the plasma. The faster the particle travels parallel (anti-parallel) to $\boldsymbol{B}_0$, the higher (lower) is its resonant frequency. This is exactly what is stated by the dispersion relation Eq. (2.90).

As this explanation suggests, cyclotron damping only works on circularly polarized waves (or waves with elliptical polarization with a strong transverse field component). Namely only the (quasi-) parallel propagating whistler and Alfvén waves are affected. According to their sense of rotation and their frequency range, whistler waves interact with electrons, whereas Alfvén waves resonate with protons.

For the purely parallel case the damping rates of whistler and Alfvén waves can be obtained from the warm plasma dispersion relation of these waves, Eqs. (2.81) and (2.82). The damping rates Γ for ten different plasma temperatures are shown in the middle and lower panel of Fig. 2.8 as an example. The increase of $|\Gamma|$ with increasing $k_\parallel$ is not as drastic as for the Langmuir mode (top panel of Fig. 2.8). For the parameter sets shown, a relatively wide regime of weak damping can be found in which $-1 < \Gamma/\omega < 0$.

This regime of weak damping is often analyzed, because weakly damped waves can still propagate and are not immediately dissipated. For example, Schlickeiser et al. (1997) derive an analytic approximation for the weak damping limit of whistler and Alfvén waves, which is then used for the discussion of cosmic ray transport. To model the collisionless damping of waves Li et al. (2001) give an analytic expression which describes the damping rate:

$$\frac{\Gamma}{|\Omega_\alpha|} = -m_1 \left(\frac{k\,c}{\omega_{\mathrm{p},\alpha}}\right)^{m_2} \exp\left(-\frac{m_3\,\omega_{\mathrm{p},\alpha}^2}{k^2\,c^2}\right). \tag{2.92}$$

This surprisingly simple function is able to recover the characteristics of the damping rate over a wide range of wave numbers, propagation angles, and plasma betas. Depending on the chosen particle species α, the equation works for the damping of whistler or Alfvén waves at various propagation angles. However, the parameters m_1, m_2 and m_3 cannot be derived from theory, but have to be attained by fitting Eq. (2.92) to measured data or numerically obtained solutions of the exact dispersion relation.

The nature of cyclotron damping leads to an acceleration of particles in the direction perpendicular to the background magnetic field $\boldsymbol{B}_0$, which in turn leads to a preferential heating of the plasma in the perpendicular direction. This so-called cyclotron heating can be used to heat fusion plasmas by generating waves which are quickly dissipated and whose energy is efficiently transferred to the particles (e.g. Stix, 1958). In the low density, collisionless regime of space plasmas cyclotron heating leads to anisotropic temperature profiles, because the particles cannot thermalize due to the lack of collisions. Therefore, it is crucial to understand the cyclotron heating mechanism in order to explain measurements in the solar wind, which show a preferential heating of protons and ions (Marsch and Tu, 2001; Chandran et al., 2010). The influence of cyclotron damping on the high-k end of turbulence spectra is also a recurring topic of discussions (see e.g. Stawicki et al., 2001).

2.5 Plasma Turbulence

Turbulence is a phenomenon which is initially known from hydrodynamics. For sufficiently large Reynolds numbers fluid flows tend to develop turbulent behavior which manifests in the generation of eddies, which then decay into smaller and smaller eddies. The pioneering work of Kolmogorov (1941a,b,c)[16] lead to a first understanding of hydrodynamic turbulence. Theory has been further developed for the magnetohydrodynamic case and it could be shown that Kolmogorov's approach can also be applied to MHD turbulence. This is all the more surprising as – contrary to a classical fluid – an MHD plasma (and therefore MHD turbulence) is not isotropic because of the presence of an ordered magnetic field.

In a plasma, such as the solar wind, so-called *wave turbulence* is assumed at large spatial scales[17], i.e. a form of turbulence which is not driven by the development and decay of eddies, but by the superposition of a variety of plasma waves. The interaction of waves with different field and propagation characteristics leads to turbulent behavior and, by means of nonlinear wave-wave and wave-particle interaction, to an energy cascade from larger to smaller scales. The turbulent cascade comes to a halt at kinetic scales, i.e. in the wave number regime where the waves can resonantly interact with the particles in the plasma and field energy is dissipated in favor of an energy gain of the particles.

This allows for a classification of plasma turbulence into two categories: The first one is the MHD regime, where kinetic effects can be neglected and plasma turbulence behaves more or less like hydrodynamic turbulence. MHD turbulence covers fluctuations at relatively large scales, where energy is injected at the longest wavelengths and transported across the so-called *inertial range* to smaller and smaller scales. The so-called *dissipation range* is excluded from the MHD model, since dissipation effects are kinetic and therefore cannot be treated by the MHD approach.

The second category is called *kinetic turbulence* and also includes the smallest length scales, where the interaction of waves and particles becomes important. Although the wave-particle interactions are not explicitly included in theory, their effect has to be considered by allowing dispersive waves and damping. This regime is generally more complicated and less well understood than MHD turbulence.

Figure 2.9 shows the general picture associated with turbulence. Energy is injected into the system at a large outer scale (small wave numbers k). The energy is transported via

---

[16] At least two of these articles have been translated to English and are readily accessible (Kolmogorov, 1991a,b).

[17] At small kinetic scales different effects may also contribute to turbulence, such as current sheets or magnetic reconnection.

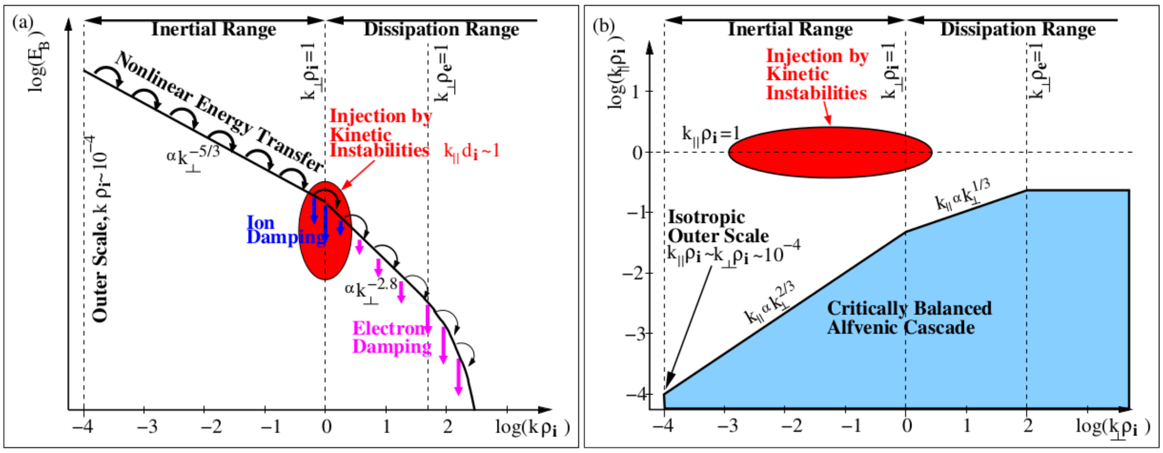

Fig. 2.9: Basic idea of turbulent energy transport: Energy is injected at a large, outer scale and then transported to smaller scales (higher wave numbers k) in the inertial range (left panel). In the kinetic regime the particles can resonate with waves and energy is dissipated, which leads to a steeper spectrum at first and to an abrupt cutoff at even higher wave numbers. The energy transport is not isotropic in wave vector space (right panel) and a cascade to larger perpendicular wave numbers $k_\perp$ is preferred. The length scales d_i, ρ_i, and ρ_e denote the ion inertial length, the ion Larmor radius, and the electron Larmor radius, respectively. The figure is taken from Howes (2015a).

the interaction of waves to smaller spatial scales (larger wave numbers) and the (magnetic) energy spectrum $E_B(k)$ follows a power law distribution (left panel of Fig. 2.9). This is the inertial range. The spectrum steepens as the kinetic regime or *dissipation range* is reached, but energy is still transported to smaller scales. First, only ion effects will start influencing the plasma dynamics, but at even larger wave numbers the electrons can also interact with the plasma waves. This is where the energy spectrum is cut off.

In the injection region the plasma fluctuations are assumed to be isotropic in wave number space. However, depending on the model, a spatial anisotropy of the turbulent energy cascade is expected in the inertial range. This can be motivated by considering turbulence as a result of the interaction of Alfvén waves, where parallel propagating waves do not interact with each other (Sridhar and Goldreich, 1994; Goldreich and Sridhar, 1995). Therefore, the transport of energy to larger perpendicular wave numbers $k_\perp$ is preferred (right panel of Fig. 2.9). This means that more oblique or (quasi-) perpendicular propagating waves are produced than (quasi-) parallel waves. Kraichnan (1965), on the other hand, predicts an isotropic inertial range spectrum. Independent of the model, a change in the power distribution in $k_\|$-$k_\perp$-space is expected as the kinetic regime is reached.

Kinetic plasma instabilities, triggered by temperature anisotropies, might be an additional source of energy for the turbulent cascade. The injection characteristics and the typical length scales or wave number regimes of these instabilities are, however, completely different from the insertion mechanism at the outer scale (see red ellipses in Fig. 2.9).

A recent article by Howes (2015a) names "three fundamental questions", which have to be answered in order to understand space plasma turbulence:

1. "What is the physical mechanism underlying the nonlinear transfer of energy from

large to small scales?”

2. “What are the dominant physical mechanisms responsible for damping the turbulent electromagnetic fluctuation?”
3. “How do coherent structures arise from and/or affect both the nonlinear energy transfer and the dissipation mechanism?”

These three topics are often seen as open questions, although different ideas and theories exist for each one of them. A single consistent model is so far not established, as the individual models often only work in certain regimes.

In the following a brief description of the energy cascade in the inertial range and in the kinetic dissipation range will be given, mainly following the review articles by Howes (2015a,b). However, for the sake of brevity a rigorous derivation of the detailed processes leading to a turbulent cascade will be omitted. The first section, Sect. 2.5.1 below, will consider the inertial range, which can be explained using the MHD formalism. Section 2.5.2 will then discuss the kinetic regime, in which the interaction of waves and particles modifies the energy cascade and leads to dissipation.

2.5.1 Magnetohydrodynamic Turbulence

The ideas of magnetohydrodynamic theory are based on hydrodynamics. In hydrodynamic turbulence energy is injected at an outer scale L and then transported to smaller scales, until a viscous damping sets in at some small scale l_ν. In a setting where the scale l of the hydrodynamic system is smaller than the outer scale, but larger than the dissipation scale, $L \gg l \gg l_\nu$, an *inertial range* exists, where both the effects of driving (i.e. energy input) and damping (i.e. energy dissipation) are negligible. The turbulent cascade is said to be *self-similar* in the inertial range, meaning that no characteristic length scale exists. In this setup Kolmogorov (1941a) found a steady-state description of the turbulent cascade of energy, equivalent to the inertial range depicted in the left panel of Fig. 2.9.

To establish a magnetohydrodynamic model a few alterations of the purely hydrodynamic case are necessary. Fluid turbulence is determined by the turbulence of the velocity field, i.e. kinetic energy. In the MHD case the magnetic energy plays an additional and important role. The length scales at which kinetic and magnetic energy are dissipated may differ. For the kinetic energy viscous dissipation with the length scale l_ν is decisive, whereas for the magnetic energy an additional *resistive dissipation scale* l_μ plays a crucial role. The ratio of these length scales may be described by the *magnetic Prandtl number* $Pr_\mathrm{m} = l_\nu / l_\mu$. For space plasmas the magnetic Prandtl number is small ($Pr_\mathrm{m} < 1$) and viscous effects can typically be neglected.

Due to the existence of an ordered magnetic field, the magnetic fluctuations are not isotropic and different characteristic scales parallel and perpendicular to $\boldsymbol{B}_0$ arise. Additionally, the magnetic field introduces *magnetic tension*, which can act as a restoring force on plasma fluctuations, leading in particular to the emergence of the Alfvén waves. This transforms the vortex-driven hydrodynamic turbulence into the wave-driven magnetohydrodynamic turbulence in a magnetized plasma (Howes, 2015b).

For the MHD approach to be valid four conditions have to be met (Howes, 2015b):

1. The plasma has to be non-relativistic, i.e. the thermal speeds of the individual particle species must be much smaller than the speed of light: $v_{\mathrm{th},\alpha} \ll c$.

2. Particle-particle collisions must be frequent, i.e. the plasma must be strongly collisional, which can be expressed by the ratio of the (proton) mean free path λ_p and the typical length scale l of the turbulent system: $\lambda_\mathrm{p}/l \ll 1$.
3. The length scale of the system is much larger than the kinetic scales, defined by the (proton) Larmor radius $\rho_\mathrm{p} = v_{\mathrm{th},p}/\Omega_\mathrm{p}$: $\rho_\mathrm{p}/l \ll 1$.
4. Only low frequency fluctuations are allowed: $\omega/\Omega_\mathrm{p} \ll 1$.

Assuming the above conditions are met, (incompressible) MHD theory states that turbulence is driven by the nonlinear interaction of counter-propagating[18] Alfvén waves (Iroshnikov, 1963; Kraichnan, 1965)[19]. The dynamics of MHD turbulence is determined by the incompressible MHD equations, which can be written in so-called *Elsasser notation* (Elsasser, 1950):

$$\frac{\partial \boldsymbol{z}^\pm}{\partial t} \mp \left(\boldsymbol{v}_\mathrm{A} \cdot \nabla\right) \boldsymbol{z}^\pm = -\left(\boldsymbol{z}^\mp \cdot \nabla\right) \boldsymbol{z}^\pm - \nabla P/\rho_0, \tag{2.93}$$

$$\nabla \cdot \boldsymbol{z}^\pm = 0. \tag{2.94}$$

Here $\boldsymbol{v}_\mathrm{A} = v_\mathrm{A}\, \boldsymbol{B}_0/B_0$ is the Alfvén velocity vector, $P = p + B^2/(8\,\pi)$ is the total pressure (consisting of thermal and magnetic pressure) and ρ_0 is the mass density. The Elsasser fields $\boldsymbol{z}^\pm = \boldsymbol{u} \pm \boldsymbol{\delta B}/\sqrt{4\,\pi\,\rho_0}$ represent Alfvén waves propagating along or opposite $\boldsymbol{B}_0$ and are expressed via the fluctuating magnetic field $\boldsymbol{\delta B}$ and the fluid velocity $\boldsymbol{u}$. The fluid velocity can be calculated from the drift velocities $\boldsymbol{V}_{\mathrm{d},\alpha}$ and the mass densities ρ_α of the individual particle species: $\boldsymbol{u} = (\boldsymbol{V}_\mathrm{d,p}\,\rho_\mathrm{p} + \boldsymbol{V}_\mathrm{d,e}\,\rho_\mathrm{e})/\rho_0$.

The so-called *Alfvén wave collisions* or nonlinear interactions are described by the first term on the right-hand side of Eq. (2.93): $(\boldsymbol{z}^\mp \cdot \nabla)\,\boldsymbol{z}^\pm$. To estimate the strength of the nonlinear interactions it is convenient to introduce the *nonlinearity parameter* (Howes, 2015a)

$$\chi = \frac{\left|\left(\boldsymbol{z}^\mp \cdot \nabla\right) \boldsymbol{z}^\pm\right|}{\left|\left(\boldsymbol{v}_\mathrm{A} \cdot \nabla\right) \boldsymbol{z}^\pm\right|}. \tag{2.95}$$

Weak MHD Turbulence

In the limit of weak Alfvénic turbulence, $\chi \ll 1$, Sridhar and Goldreich (1994) describe the mechanism which leads to the transport of energy from larger to smaller scales. They consider waves (or wave packages) as quasi-particles and attribute their nonlinear interactions to the aforementioned Alfvén wave collisions, i.e. collisions of wave packages. The lowest order of interaction is a three-wave process, the next higher order includes four waves, and so forth. In principle, all orders of interaction are realized, but the higher order interactions become less and less likely. Therefore, the lowest possible order dominates the turbulent interaction.

According to the picture of quasi-particles Sridhar and Goldreich (1994) discuss Alfvén wave collisions with regard to momentum and energy conservation (in terms of the wave vector $\boldsymbol{k}$ and the frequency ω, respectively). They argue that the three-wave interaction is forbidden in weak Alfvénic turbulence, since the collision of two Alfvén waves would lead

---

[18] In this context "counter-propagating" means that the waves do not necessarily propagate in opposite directions, but that the parallel components of their wave vectors have opposite signs.

[19] For an English translation of Iroshnikov (1963) see Iroshnikov (1964)

to a third wave whose frequency would be zero. This leads to a violation of energy conservation. Therefore, Sridhar and Goldreich (1994) proclaim that weak Alfvénic turbulence is dominated by four-wave interaction, as the interaction process with the lowest possible order. This has become the standard picture for weak turbulence.

Howes and Nielson (2013), however, derive a theory for three wave interaction leading to a perpendicular energy cascade and show numerical proof for their claim (see Nielson et al., 2013). Their approach is formally correct, but the physical implications are highly controversial. A summary of their ideas will be given in the following.

Consider two counter-propagating Alfvén waves with perpendicular polarization, i.e. wave vectors

$$\boldsymbol{k}_1^+ = k_\perp \,\hat{\boldsymbol{x}} - k_\parallel \,\hat{\boldsymbol{z}}, \tag{2.96}$$

$$\boldsymbol{k}_1^- = k_\perp \,\hat{\boldsymbol{y}} + k_\parallel \,\hat{\boldsymbol{z}}, \tag{2.97}$$

where $k_\perp$ and $k_\parallel$ are positive and the background magnetic field points in positive z-direction. The nonlinear interactions of these two waves yield, to lowest order, a purely magnetic wave mode with

$$\boldsymbol{k}_2^{(0)} = k_\perp \,\hat{\boldsymbol{x}} + k_\perp \,\hat{\boldsymbol{y}}. \tag{2.98}$$

Note that this mode has no wave vector component parallel to $\boldsymbol{B}_0$ and, due to the construction of the first (or primary) two Alfvén waves, a frequency $\omega = 2\omega_0$, where ω_0 is the frequency of the initial waves.

To next higher order of the nonlinear interaction the primary waves interact with the newly created secondary wave mode to produce two waves at larger wave numbers:

$$\boldsymbol{k}_3^+ = 2\,k_\perp \,\hat{\boldsymbol{x}} + k_\perp \,\hat{\boldsymbol{y}} - k_\parallel \,\hat{\boldsymbol{z}}, \tag{2.99}$$

$$\boldsymbol{k}_3^- = k_\perp \,\hat{\boldsymbol{x}} + 2\,k_\perp \,\hat{\boldsymbol{y}} + k_\parallel \,\hat{\boldsymbol{z}}. \tag{2.100}$$

Howes and Nielson (2013) claim that this process is the basis for the energy cascade to smaller length scales. A repetition of the two steps (two waves form a third, purely magnetic mode; interaction with the new mode creates further waves at higher k) drives the turbulent cascade to larger perpendicular wave numbers and a strongly anisotropic cascade is produced. The assumption of perpendicularly polarized primary waves maximizes the nonlinear term in the MHD equation, Eq. (2.93), but is not entirely necessary.

The point of criticism raised by Sridhar and Goldreich (1994) and also discussed by Howes (2015a) is the following: The interaction described above satisfies the matching conditions (corresponding to momentum and energy conservation) $\boldsymbol{k}_3^\pm = \boldsymbol{k}_1^\pm + \boldsymbol{k}_2^{(0)}$, $\omega_3 = \omega_1 + \omega_2$, where $\omega_i = k_{\parallel,i}\, v_\mathrm{A}$. However, this implies that $k_{\parallel,2} = 0$, which contradicts the assumption of Alfvén waves. Sridhar and Goldreich (1994) therefore propose a four wave interaction which skips the secondary wave, whereas Howes (2015a) suggests that the three wave interaction is the dominant process if magnetic fluctuations with $k_\parallel = 0$ are “pre-existent” and that four wave interactions are dominant otherwise.

No matter which form of nonlinear interaction is realized, weak MHD turbulence produces a purely perpendicular cascade, where the one-dimensional energy spectrum can be described by a power law. The power law results from the assumption of an energy cascade with a typical time scale which is proportional to the collision rate of Alfvén wave packages of equal length scales. Relating the collision rates of the wave packages to the cascading time scale and the rate of energy injection yields a power law as a steady state solution for the energy spectrum. This approach was not only used by Sridhar and Goldreich (1994), but goes back to the work of Iroshnikov (1963) and Kraichnan (1965).

Strong MHD Turbulence

For a cascade to larger and larger perpendicular wave numbers Sridhar and Goldreich (1994) show that turbulence becomes stronger (in the sense of a faster interaction rate) and eventually can no longer be described by four wave interaction. A regime of *intermediate turbulence* was introduced by Goldreich and Sridhar (1997), which connects weak and strong turbulence and where three wave interactions are dominant. In the case of strong turbulence ($\chi \sim 1$) Goldreich and Sridhar (1995) develop the idea of a *critical balance*, where they express the nonlinearity parameter by the ratio of a linear and nonlinear time scale. The linear time scale is given by a parallel wave number and the Alfvén speed, $\tau^{-1} = k_{\|}\, v_{\mathrm{A}}$, whereas the nonlinear timescale $\tau_{\mathrm{nl}}^{-1} = k_{\perp}\, \delta v_{\perp}$ can be expressed by the perpendicular wave number and the relative perpendicular velocity $\delta v_{\perp}$ of the plasma caused by a fluctuation. With $\chi = \tau/\tau_{\mathrm{nl}} = 1$ an expression for the perpendicular velocity $\delta v_{\perp} = v_{\mathrm{a}}\, k \parallel / k_{\perp}$ follows, which can then be coupled with a condition for the energy cascade. This yields a correlation between the parallel and perpendicular wave number:

$$k_{\|} \propto k_{\perp}^{\kappa}. \tag{2.101}$$

Goldreich and Sridhar (1995) also find that the one-dimensional magnetic energy spectrum $E_B(k_{\perp})$ follows a power law in $k_{\perp}$:

$$E_B(k_{\perp}) \propto k_{\perp}^{\sigma}. \tag{2.102}$$

The exponents κ and σ are model dependent. Goldreich and Sridhar (1995) find $\kappa = 2/3$ and $\sigma = -5/3$, as stated in Fig. 2.9, whereas Kraichnan (1965) or Boldyrev (2006) derive $\kappa = 1/2$ and $\sigma = -3/2$. It is interesting to note that the spectral index of the energy spectrum derived by Goldreich and Sridhar (1995) is the same as the one from hydrodynamic turbulence derived by Kolmogorov (1941a). More importantly, it also matches the observations in the solar wind.

Violation of MHD Conditions

At the beginning of the section four criteria for the applicability of the MHD approach have been stated. While the first condition can be assumed to be satisfied in the solar wind (non-relativistic plasma temperature), the other three conditions can very well be violated. A violation of the third (typical length scale greater than proton Larmor radius) or fourth condition (typical frequencies close to or above the proton cyclotron frequency) lead to an immediate collapse of the MHD model. Here, kinetic effects come into play and a different description of the plasma is needed.

The second condition (strong collisionality), however, can be violated without noticeable effect on Alfvénic turbulence. Even in a weakly collisional or collisionless regime a fluid description of Alfvénic turbulence is still accurate (Strauss, 1976; Schekochihin et al., 2009). Therefore, it is possible to extend the MHD description to scales smaller than the mean free path and to describe the entire inertial range with the same model. Nonetheless, an (at least formal) violation of MHD theory is incurred, which leads to an incorrect representation of compressional waves (e.g. sound waves).

Another critical point of the theory illustrated above is the assumption of incompressibility. This means, that compressional wave modes, such as the fast and slow magnetosonic modes (see Sect. 2.4.1), which cause parallel magnetic field components $\delta B_{\|}$ (i.e. a "compression" of B_0), are excluded from the model. The fast and the slow magnetosonic mode require a kinetic description at all length scales. Both viscous and Landau damping affect these waves at scales of $k_{\|}\,\lambda_{\mathrm{p}} \sim 1$ and $k_{\|}\,\lambda_{\mathrm{p}} \gg 1$, respectively. It can therefore be assumed that the fast and slow magnetosonic modes play only minor roles in space plasma turbulence. Measurements show that the contribution to the total magnetic energy in solar wind turbulence is less than 10%. The influence of compressional wave modes on Alfvénic turbulence can therefore be neglected (see Howes, 2015b, and references therein).

2.5.2 Kinetic Turbulence

In the regime close to or below the proton Larmor radius ρ_{p} kinetic effects set in. On the one hand this leads to dispersive effects, i.e. the linear dispersion relations of the magnetohydrodynamic waves are no longer valid. On the other hand resonant interactions of a large fraction of particles and the electromagnetic fields become relevant, which causes damping of waves and eventually heating of the plasma.

Kinetic Alfvén Wave Turbulence

In the case of Alfvénic turbulence, Howes (2015b) argues that for $k_{\perp}\,\rho_{\mathrm{p}} \leq 1$ the protons decouple from the electromagnetic fluctuations of the Alfvén waves, which leads to a change of the dispersion characteristics of the waves. In this regime the dispersive kinetic Alfvén waves (KAWs) dominate the spectrum. An approximate dispersion relation for KAWs is given by (Schekochihin et al., 2009):

$$\omega = k_{\|}\, v_{\mathrm{A}} \sqrt{1 + \frac{(k_{\perp}\,\rho_{\mathrm{p}})^2}{\beta_{\mathrm{p}} + 2/(1 + T_{\mathrm{e}}/T_{\mathrm{p}})}}, \tag{2.103}$$

where β_{p} is the proton plasma beta, Eq. (2.7), and T_{e} and T_{p} are the electron and proton temperatures. Additional to their dispersive nature KAWs also develop a parallel magnetic field component $\delta B_{\|}$ and are thus compressional waves (Hollweg, 1999).

The nature of KAWs leads to an acceleration of the nonlinear energy transfer to smaller scales (Howes, 2015b). This leads to a break in the energy spectrum at around $k_{\perp}\,\rho_{\mathrm{p}} \sim 1$ and a steepening at larger perpendicular wave numbers (i.e. Howes et al., 2008; Schekochihin et al., 2009, and references therein). The predicted spectral index in the KAW regime ($k_{\perp}\,\rho_{\mathrm{p}} \ll 1$) is $\sigma = -7/3$ if damping is neglected. The concept of critical balance can still be applied, but the wave vector anisotropy is now governed by $k_{\|} \propto k_{\perp}^{1/3}$.

While the prediction for the wave vector anisotropy seems to be accurate, the prediction for the energy spectrum has to be modified due to damping effects. In the solar wind a spectral index of $\sigma = -2.8$ seems to be realized (e.g. Chen et al., 2010), as shown in Fig. 2.9.

Note that cyclotron damping does not contribute significantly to the dissipation of wave energy. Cyclotron damping is in principle possible at frequencies close to the proton cyclotron frequency, but this frequency regime is only reached by quasi-parallel propagating waves.

However, quasi-parallel waves at high enough frequencies are hardly produced in the solar wind due to the anisotropy of the energy cascade in wave vector space.

According to Howes (2015a) the remaining relevant damping mechanisms are *coherent* or *resonant wave-particle interaction*, namely Landau damping of ions and electrons, *stochastic wave-particle interactions*, and the dissipation of energy in *current sheets*. Landau damping is assumed to be a key process (Cranmer and van Ballegooijen, 2003), which is subdivided into two regimes. At length scales around $k_\perp \rho_\mathrm{p} \sim 1$ the proton Landau damping reaches maximum efficiency and introduces the spectral break (indicated by the blue arrows in Fig. 2.9). Electron Landau damping (indicated by pink arrows in Fig. 2.9) sets in slowly and contributes to wave damping over the whole dissipation range of the turbulent cascade. Close to the scales of the electron Larmor radius ($k_\perp \rho_\mathrm{e} \sim 1$) damping increases significantly. This eventually leads to the termination of the turbulent cascade, as energy is removed faster than it can be transported to higher wave numbers.

Stochastic wave-particle interaction may play an important role in strong turbulence, where high amplitudes of the turbulent fluctuations are expected (Howes, 2015a). At sufficiently high amplitudes a proton's orbit may become chaotic and its energy may perform a random walk, caused by stochastic interactions with the electromagnetic fields along the proton's trajectory. In a thermal distribution of protons these stochastic interactions are more likely to increase the energy of one of the many low energy particles than to decrease the energy of one of the fewer high energy particles. Therefore, a net transfer of energy from the electromagnetic fields to the protons results (*stochastic heating*). This mechanism is especially efficient in an environment with low plasma beta (Howes, 2015a). In principle, stochastic electron heating is also possible. However, at the relevant length scales required for the electrons to efficiently interact the energy of the turbulent cascade is typically no longer sufficient to yield a noticeable effect.

Computer simulations, such as the ones by Biskamp and Welter (1989) or Maron and Goldreich (2001), suggest the development of current sheets at small spatial scales as a result of magnetohydrodynamic turbulence. They also find current sheets to be regions where large amounts of field energy are dissipated. Howes (2015a, 2016) promotes the idea that these current sheets are generated by the constructive interference of (kinetic) Alfvén waves. He also identifies Landau damping as the process which finally dissipates the current sheets. Following this theory, current sheets, although being interesting features, can be completely described by the wave turbulence picture in the kinetic regime.

Energy Re-Distribution

When speaking of dissipation, one obvious question arises: Where does the energy go? As total energy is conserved, a loss of energy in the electromagnetic fields must lead to a gain of energy elsewhere.

Consider the total energy W of the plasma, consisting of the energy of the electric and the magnetic field, and the kinetic energy of the particles (Howes, 2015a):

$$W = \int d^3r \left(\frac{|\boldsymbol{E}|^2 + |\boldsymbol{B}|^2}{8\,\pi} + \sum_\alpha \int d^3v \, \frac{1}{2} m_\alpha \, v^2 \, f_\alpha \right), \tag{2.104}$$

where the second term is the kinetic energy $W_{\mathrm{kin},\alpha}$ from Eq. (2.71). With the help of the drift velocity $\boldsymbol{v}_{\mathrm{d},\alpha} = \boldsymbol{\Gamma}_\alpha / n_\alpha$ (see Eq. (2.69)) a *kinetic temperature*

$$T_{\mathrm{kin},\alpha} = \frac{2}{3\,k_{\mathrm{B}}\,n_\alpha} \left(W_{\mathrm{kin},\alpha} - \frac{1}{2}\,n_\alpha\,m_\alpha\,|\boldsymbol{v}_{\mathrm{d},\alpha}|^2 \right) \tag{2.105}$$

for species α can be introduced, which allows to rewrite Eq. (2.104) in the form

$$W = \int d^3r \left(\frac{|\boldsymbol{E}|^2 + |\boldsymbol{B}|^2}{8\,\pi} + \sum_\alpha \left(\frac{1}{2}\,n_\alpha\,m_\alpha\,|\boldsymbol{v}_{\mathrm{d},\alpha}|^2 + \frac{3}{2}\,n_\alpha\,k_{\mathrm{B}}\,T_{\mathrm{kin},\alpha} \right) \right) . \tag{2.106}$$

This equation expresses the total energy of the plasma in three terms (from left to right): electromagnetic energy, kinetic energy of the bulk motion of the plasma, and a mixture of thermal and non-thermal free energy. If the plasma is in thermodynamic equilibrium, the last term contains only thermal energy, as $T_{\mathrm{kin},\alpha} = T_\alpha$. In all other cases free energy is available which may be shifted between the individual terms of Eq. (2.106).

Three processes are mainly relevant for the transfer of energy between the individual terms (Howes, 2015a): Magnetic tension leads to a continuous transfer of field energy from propagating Alfvén waves to the bulk plasma motion and back. This process is periodic and, averaged over time, leads to no energy gain of either waves or bulk plasma. Wave damping, such as cyclotron or Landau damping, transports energy from the electromagnetic fields to the particles, which gain non-thermal free energy. Eventually a temperature anisotropy ($T_\parallel / T_\perp \neq 1$) is caused, which can then trigger plasma instabilities (see e.g. Gary, 1993, Chapter 7). Such instabilities may then lead to a transfer of energy from the particles back to the electromagnetic fields.

In a collisional plasma the effect of thermalization by particle-particle collisions comes into play. Collisions restore thermodynamic equilibrium, i.e. remove free energy and convert it to thermal energy. As thermal energy cannot be reduced without reducing entropy, this energy is no longer available for further interactions and the above mentioned transfer processes may come to a halt.

Generation of Instabilities and Whistler Turbulence

As Howes (2015a,b) points out, plasma instabilities lead to the production of waves in a completely different regime of wave vector space than the original Alfvénic cascade (see Fig. 2.9). These waves typically have larger parallel wave vector components and may even be found in the regime where $k_\parallel / k_\perp > 1$. A recent review by Gary (2015) lists and describes a number of possible instabilities and their effect on the plasma (see also Klein and Howes, 2015). In summary it can be said that kinetic instabilities generate fluctuations at small wavelengths, i.e. large wave numbers. Temperature anisotropies $T_\perp > T_\parallel$ yield quasi-parallel waves, such as proton cyclotron (e.g. Gary and Saito, 2003; Chandran et al., 2010) or whistler waves (e.g. Gary et al., 2014). While proton cyclotron waves are quickly damped and heat the protons (e.g. Moya et al., 2012), whistler waves themselves can start a turbulent cascade which spreads energy to smaller scales and higher frequencies, until electron Landau and electron cyclotron damping set in.

The latter case of whistler turbulence is especially interesting, since energy can be transported to frequencies higher than the proton cyclotron frequency. Simulations suggest that whistler turbulence again leads to an anisotropic cascade in wave vector space, similar to

Alfvénic turbulence. The shape and structure of the energy spectrum is, however, not yet fully understood. It is argued that whistler turbulence might exhibit a steeper power law slope than Alfvénic turbulence in the inertial range and that the steepening of the spectrum in the kinetic dissipation range may be attributed to a transition from Alfvénic to whistler turbulence (Stawicki et al., 2001; Gary and Smith, 2009).

The properties of whistler turbulence have been analyzed in more and more detail over the past years, employing the increasing amount of available computational resources to perform kinetic simulations in two (Gary et al., 2008; Che et al., 2014) and three dimensions (Gary et al., 2012; Chang et al., 2013; Gary et al., 2014; Chang et al., 2015). These studies suggest a steeper energy spectrum than for Alfvénic turbulence, with a spectral index σ in the range between -3.7 and -5.5 and a possible break in the energy spectrum (Chang et al., 2015). Results by Chang et al. (2013) also suggest that the wave vector anisotropy depends on the choice of the plasma beta. A relatively isotropic spectrum is obtained for $\beta \sim 1$, whereas $\beta < 1$ yields an anisotropic cascade which favors the transport of energy to larger $k_\perp$. The anisotropy additionally depends on the energy deployed to the electromagnetic fields of the turbulent whistler waves (Gary et al., 2012).

The whole topic of whistler turbulence – including the cause for its initial generation, the properties of the energy spectrum, and the dissipation processes at large wave numbers – is currently an active field of research. As measurements in the solar wind at the relevant frequencies are very rare, computer simulations are at present the most promising approach to deepen the understanding of kinetic and whistler turbulence.

2.6 Collisionless Transport

Particle transport in a gas is governed by the collisions of the individual particles with each other. A mean free path can be defined and the trajectories of the particles can be assumed to be more or less linear between collisions. A collision then leads to a random change of direction and might also change the particle's energy. In a plasma, however, things are different. Electromagnetic fields play an important role for the transport of charged particles, as their direction of motion and speed not only change during particle-particle collisions, but also along the way in between.

In a collisionless environment the transport of charged particles is entirely dominated by the electromagnetic fields. Since no large scale electric fields exist in a plasma, the ordered background magnetic field plays an important role. Transport along the background field is essentially free, but the particles are bound to the magnetic field lines and in general cannot propagate across the background magnetic field $\boldsymbol{B}_0$. This is often described by introducing a *gyro-* or *guiding center* for a particle, which represents the center of the particle's gyration orbit about the background field. The motion of the particle is then described by a superposition of the motion of the gyro-center (mainly along $\boldsymbol{B}_0$) and the periodic gyration around this center (perpendicular to $\boldsymbol{B}_0$).

With the variety of possible wave-particle interactions non-thermal particle populations may arise from an initially thermal spectrum. Especially the highly energetic particles are of interest. Due to the lack of collisions these particles can travel over large distances without being re-thermalized by interaction with the particles in the thermal part of the spectrum. Their transport characteristics are entirely dominated by collisionless interactions with electromagnetic fields. Magnetic fields can play the role of scattering centers where the particles change their direction of motion. By resonant interactions the particles may be trapped in a certain regime, e.g. in a region close to a shock front where they can be further accelerated.

These processes are crucial for understanding the acceleration and transport of energetic particles in the solar wind. Theoretical frameworks, such as quasi-linear theory (QLT), may be used to derive the behavior of energetic particles. Both the interaction of single particles with electromagnetic fields and the statistical analysis of the phase space evolution of whole particle populations can be studied.

In the following the resonant interaction of (individual) charged particles and magnetic fields will be discussed (Sect. 2.6.2). The focus lies on so-called *pitch angle scattering*, i.e. changes of the particle's propagation angle θ relative to the direction of the background magnetic field $\boldsymbol{B}_0$. Compared to changes of momentum or to spatial diffusion, pitch angle scattering is the fastest and therefore most influential process relevant for particle transport. Theory predicts that a major change of the particle's pitch angle only occurs when the particle is in resonance with the magnetic field of a wave with specific frequency and wave number, whereas non-resonant interactions – on average – do not influence particle transport (so-called *ballistic transport*). Section 2.6.3 then describes particle transport in turbulence. Due to the variety of waves in a turbulent medium a statistical approach has to be chosen here. Before these details will be discussed, a short introduction to QLT is given in Sect. 2.6.1.

2.6.1 Overview of Quasi-Linear Theory Basics

Vlasov Equation and Coordinate System

In the following only the transport of the small number of non-thermal energetic particles in the plasma is considered. As for the (thermal) rest of the particles, the evolution of the distribution function of the particles of interest is governed by the Vlasov equation, Eq. (2.67). However, since the particles of interest are highly energetic, a relativistic representation of the Vlasov equation has to be chosen. While Eq. (2.67) used the particle velocity $\boldsymbol{v}$ as a variable, it is convenient to switch to the momentum $\boldsymbol{p} = \gamma\, m\, \boldsymbol{v}$, where

$$\gamma = \frac{1}{\sqrt{1 - v^2/c^2}} = \sqrt{1 + \frac{p^2}{m^2\, c^2}} \tag{2.107}$$

is the *Lorentz factor*. The resulting *relativistic Vlasov equation* for particles of species α can then be written as (e.g. Schlickeiser, 2003, Chapter 12.1)

$$\frac{\partial f_\alpha}{\partial t} + \frac{\boldsymbol{p}}{\gamma\, m_\alpha} \cdot \frac{\partial f_\alpha}{\partial \boldsymbol{r}} + \dot{\boldsymbol{p}} \cdot \frac{\partial f_\alpha}{\partial \boldsymbol{p}} = S_\alpha(\boldsymbol{r}, \boldsymbol{p}, t), \tag{2.108}$$

where S_α is a source term which is of no particular interest in the following and the time derivative of momentum is given by

$$\dot{\boldsymbol{p}} = q_\alpha \left(\boldsymbol{E}(\boldsymbol{r}, t) + \frac{\boldsymbol{p}}{\gamma\, m_\alpha\, c} \times \boldsymbol{B}(\boldsymbol{r}, t) \right). \tag{2.109}$$

The electric and magnetic fields are defined as in Sect. 2.3.1, i.e. $\boldsymbol{E} = \boldsymbol{\delta E}$ and $\boldsymbol{B} = \boldsymbol{B}_0 + \boldsymbol{\delta B}$ with the background magnetic field $\boldsymbol{B}_0 \,||\, \hat{\boldsymbol{z}}$ and the low amplitude field fluctuations $\boldsymbol{\delta E}$ and $\boldsymbol{\delta B}$.

Under the assumption of low amplitude field fluctuations it is possible to describe the motion of particles by the net motion of their gyro- or guiding center and the periodic rotation about this center. The position of the gyro-center will be denoted by (Schlickeiser, 2003, Chapter 12.1)

$$\boldsymbol{R} = (X, Y, Z) = \boldsymbol{r} + \frac{\boldsymbol{v} \times \hat{\boldsymbol{z}}}{\Omega_\alpha / \gamma}, \tag{2.110}$$

with the position $\boldsymbol{r}$ of the particle, the signed gyrofrequency Ω_α for species α, and the guiding center spatial coordinates

$$\begin{aligned} X &= x + \frac{v\sqrt{1-\mu^2}}{\Omega_\alpha/\gamma} \sin\phi, & (2.111)\\ Y &= y - \frac{v\sqrt{1-\mu^2}}{\Omega_\alpha/\gamma} \cos\phi, & (2.112)\\ Z &= z. & (2.113) \end{aligned}$$

The variables ϕ and $\mu = \cos\theta$ represent azimuth angle and the cosine of the polar angle of the particle's momentum vector:

$$\begin{aligned} p_x &= p\,\cos\phi\,\sqrt{1-\mu^2}, & (2.114)\\ p_y &= p\,\sin\phi\,\sqrt{1-\mu^2}, & (2.115)\\ p_z &= p\,\mu. & (2.116) \end{aligned}$$

The coordinate set describing the motion of the guiding center is then $r_\sigma = (p, \mu, \phi, X, Y, Z)$.

It is worth noting that the polar angle, due to the choice of the coordinate system and the direction of the background magnetic field, is also the *pitch angle* of the particle. Usually the pitch angle is represented by the pitch angle cosine μ, which can be easily expressed by the particle's velocity and the magnetic field vector:

$$\mu = \cos\theta = \frac{\boldsymbol{v} \cdot \boldsymbol{B}_0}{|\boldsymbol{v}|\,|\boldsymbol{B}_0|}. \tag{2.117}$$

The new set of coordinates allows to rewrite the Vlasov equation once more (Schlickeiser, 2003, Chapter 12.1):

$$\frac{\partial f_\alpha}{\partial t} + v\,\mu\,\frac{\partial f_\alpha}{\partial Z} - \Omega_\alpha\,\frac{\partial f_\alpha}{\partial \phi} + \frac{1}{p^2}\,\frac{\partial}{\partial r_\sigma}\left(p^2\,g_{r_\sigma}\,f_\alpha\right) = S_\alpha(\boldsymbol{r}, \boldsymbol{p}, t). \tag{2.118}$$

The variable g_{r_σ} represents the *generalized force term* (Schlickeiser, 2003, Chapter 12.1, Eqs. (12.1.9a-f)) which describes the interaction with the fluctuating electromagnetic fields and is organized in six distinct terms for the six coordinates in r_σ. If these terms are zero one speaks of *undisturbed orbits*, i.e. particle trajectories which are not affected by fluctuating electromagnetic fields.

Derivation of the Fokker-Planck Equation

Next, a statistical approach is chosen to derive the *Fokker-Planck equation* (following Schlickeiser, 2003, Chapter 12.1). The Fokker-Planck equation can be seen as a simplification of the Vlasov equation which describes particle scattering and acceleration as diffusion processes and allows a different and more convenient approach to study changes of the distribution function than the full Vlasov equation. Selecting a particular manifestation of the fluctuating electromagnetic fields and computing the evolution of the particle distribution function according to Eq. (2.118) would not be representative. Instead, an expectation value $\langle f_\alpha(\boldsymbol{r},\boldsymbol{p},t)\rangle = F_\alpha(\boldsymbol{r},\boldsymbol{p},t)$ has to be found by taking the average over an ensemble of distribution functions f_α which are equal at a time t_0, but develop slightly differently for later times t due to the exact nature of the electromagnetic fluctuations entering the generalized force terms g_{r_σ}. Similarly, expectation values for the electromagnetic fields can be found:

$$\langle \boldsymbol{B}(\boldsymbol{r},t)\rangle = \boldsymbol{B}_0, \qquad \langle \boldsymbol{\delta B}(\boldsymbol{r},t)\rangle = 0, \tag{2.119}$$

$$\langle \boldsymbol{E}(\boldsymbol{r},t)\rangle = 0, \qquad \langle \boldsymbol{\delta E}(\boldsymbol{r},t)\rangle = 0. \tag{2.120}$$

The Vlasov equation for the ensemble average F_α can then be written as

$$\frac{\partial F_\alpha}{\partial t} + v\,\mu\,\frac{\partial F_\alpha}{\partial Z} - \Omega_\alpha\,\frac{\partial F_\alpha}{\partial \phi} + \frac{1}{p^2}\,\frac{\partial}{\partial r_\sigma}\left(\langle p^2\, g_{r_\sigma}\, \delta f_\alpha\rangle\right) = S_\alpha(\boldsymbol{r},\boldsymbol{p},t), \tag{2.121}$$

with the deviation of an individual representation of the distribution function from the average $\delta f_\alpha = f_\alpha - F_\alpha$.

The interesting part of Eq. (2.121) is the average over the generalized force terms g_{r_σ} and the fluctuating part of the distribution function δf_α. The time evolution of the latter can be analyzed by subtracting Eq. (2.121) from Eq. (2.118), which yields:

$$\frac{\partial \delta f_\alpha}{\partial t} + v\,\mu\,\frac{\partial \delta f_\alpha}{\partial Z} - \Omega_\alpha\,\frac{\partial \delta f_\alpha}{\partial \phi} = -g_{r_\sigma}\,\frac{\partial F_\alpha}{\partial x_\sigma} - g_{r_\sigma}\,\frac{\partial \delta f_\alpha}{\partial r_\sigma} + \left\langle g_{r_\sigma}\,\frac{\partial \delta f_\alpha}{\partial r_\sigma}\right\rangle \tag{2.122}$$

under the assumption

$$\frac{1}{p^2}\,\frac{\partial}{\partial r_\sigma}(p^2\, g_{r_\sigma}) = 0. \tag{2.123}$$

The next steps are performed under the *quasi-linear approximation*, as described by Jokipii (1966) who built the foundation for quasi-linear theory. The basis for the quasi-linear approximation is the assumption that the fluctuations δE and δB are of small amplitude and that the generalized forces therefore only lead to small perturbations $\delta f_\alpha / F_\alpha \ll 1$ on timescales $t \ll t_F$, where t_F[20] can be written as

$$t_F = F_\alpha \left| g_{r_\sigma}\,\frac{\partial F_\alpha}{\partial r_\sigma}\right|^{-1}. \tag{2.124}$$

Under this assumption the last two terms on the right-hand side of Eq. (2.122) can be neglected, leading to:

$$\frac{\partial \delta f_\alpha}{\partial t} + v\,\mu\,\frac{\partial \delta f_\alpha}{\partial Z} - \Omega_\alpha\,\frac{\partial \delta f_\alpha}{\partial \phi} \simeq -g_{r_\sigma}\,\frac{\partial F_\alpha}{\partial x_\sigma}. \tag{2.125}$$

The above equation can be solved using the method of characteristics. Choosing an unper-

---

[20] The index “F” stands for “force”.

turbed particle orbit in a homogeneous magnetic field as the characteristic, the solution

$$\delta f_\alpha(t) = \delta f_\alpha(t_0) - \int\limits_{t_0}^{t} ds \left(g_{r_\sigma}(r_\nu, s) \, \frac{\partial F_\alpha(r_\nu, s)}{\partial r_\sigma} \right)' \tag{2.126}$$

can be obtained, where the prime means that the expressions inside the brackets have to be evaluated along the undisturbed particle orbit. Further assuming $\langle \delta f_\alpha g_{r_\sigma} \rangle = 0$ the solution Eq. (2.126) can be inserted into Eq. (2.121), which leads to the following equation:

$$\begin{aligned} \frac{\partial F_\alpha}{\partial t} + v\,\mu\,\frac{\partial F_\alpha}{\partial Z} - \Omega_\alpha\,\frac{\partial F_\alpha}{\partial \phi} \;&=\; \frac{1}{p^2}\,\frac{\partial}{\partial r_\sigma} \left\langle p^2\, g_{r_\sigma} \int\limits_{t_0}^{t} ds \left(g_{r_\sigma}(r_\nu, s) \, \frac{\partial F_\alpha(r_\nu, s)}{\partial r_\sigma} \right)' \right\rangle \\ &\quad + S_\alpha(\boldsymbol{r}, \boldsymbol{p}, t). \end{aligned} \tag{2.127}$$

Following the trail of thought described by (Schlickeiser, 2003, Chapter 12.1) the first term on the right-hand side of Eq. (2.127) can be rearranged under the following assumptions: The correlation function $\langle g_{r_\sigma}\, g'_{r_\nu} \rangle$ of the generalized force terms g_{r_σ} and g'_{r_ν} off and on an unperturbed orbit becomes negligible at time intervals $t - s > t_\mathrm{c}$ larger than a correlation time scale t_c. Also, the fluctuations of the derivative $(\partial F_\alpha / \partial r_\nu)'$ along the undisturbed particle orbit is small in the interval $t - s$. Then Eq. (2.127) can be written as

$$\begin{aligned} \frac{\partial F_\alpha}{\partial t} + v\,\mu\,\frac{\partial F_\alpha}{\partial Z} - \Omega_\alpha\,\frac{\partial F_\alpha}{\partial \phi} \;&=\; \frac{1}{p^2}\,\frac{\partial}{\partial r_\sigma} \left(p^2 \left(\int\limits_{0}^{t} ds \,\langle g_{r_\sigma}\, g_{r_\nu}(r_\nu, s) \rangle \right)' \frac{\partial F_\alpha(r_\nu, s)}{\partial r_\nu} \right) \\ &\quad + S_\alpha(\boldsymbol{r}, \boldsymbol{p}, t), \end{aligned} \tag{2.128}$$

where the first term on the right-hand side can again be rewritten (Schlickeiser, 2003, Chapter 12.1):

$$\frac{\partial F_\alpha}{\partial t} + v\,\mu\,\frac{\partial F_\alpha}{\partial Z} - \Omega_\alpha\,\frac{\partial F_\alpha}{\partial \phi} = \frac{1}{p^2}\,\frac{\partial}{\partial r_\sigma} \left(p^2\, D_{r_\sigma r_\nu}\, \frac{\partial F_\alpha}{\partial r_\nu} \right) + S_\alpha(\boldsymbol{r}, \boldsymbol{p}, t), \tag{2.129}$$

with

$$D_{r_\sigma r_\nu}(r_\eta, t) = \Re \int\limits_{0}^{t} d\xi \,\langle g'_{r_\sigma}(t)\, g'_{r_\nu}(t + \xi) \rangle \,. \tag{2.130}$$

Equation (2.129) is the *Fokker-Planck equation* and $D_{r_\sigma r_\nu}$ are the *Fokker-Planck coefficients*.

The Fokker-Planck equation is a diffusion equation which only involves second order correlation functions of the generalized field terms, which have to be integrated along unperturbed orbits. According to Jokipii (1966) these second order correlations are sufficient to describe particle diffusion in phase space, if the quasi-linear approximation is valid (i.e. only small perturbations of the electromagnetic fields). The diffusion coefficients can be further examined analytically, but this procedure will not be discussed here (see e.g. Schlickeiser, 2003, Chapter 12.2.2). Instead, some of the limitations of the quasi-linear theory will be pointed out in the following.

As mentioned earlier one of the basic assumptions of QLT is that the fluctuating fields δB and δE are small compared to B_0. This is a necessary condition for the assumption of unperturbed particle orbits. However, in a turbulent medium the amplitude of the local electromagnetic field may be comparable to the amplitude of the background field (strong turbulence). If this is the case the particle's trajectory can no longer be approximated by an unperturbed orbit. Dupree (1966) shows that QLT can still be applied if the correlation time t_{c} is much smaller than the time scale T at which the particle's trajectory significantly diverges from an unperturbed orbit.

Another problematic property of the model is that particles traveling perpendicular to the background magnetic field are not described correctly. For such particles the pitch angle cosine is $\mu = 0$ and the parallel velocity component becomes zero. Under these circumstances the pitch angle diffusion coefficient $D_{\mu\mu}$ (see Sect. 2.6.2) becomes zero, i.e. the particle can never change its propagation angle relative to $\boldsymbol{B}_0$. The reason for this flaw is that the correlation time t_{c} becomes so large that the initially derived assumptions necessary for the quasi-linear approach are no longer valid. A nonlinear perturbation theory is necessary to overcome this problem (e.g. Völk, 1973; Matthaeus et al., 2003; Shalchi et al., 2004).

Analyzing the applicability of QLT to plasma turbulence Hasselmann and Wibberenz (1970) found that meaningful diffusion coefficients can only be derived if the energy spectrum $E_B(k_\|)$ over the parallel wave number is relatively flat. Assuming a power law distribution the spectral index must not fall below -2 in parallel direction.

Although some shortcomings of QLT are known and improvements and solutions to some of the theory's problems are available, the basic QLT approach will be chosen in the following. This is sufficient for a first insight into the applications of the theory. As more complex problems will be treated numerically later in this work there is no real necessity to describe more advanced theories here.

2.6.2 Resonant Wave-Particle Interaction

Pitch Angle Diffusion Coefficient

In the following the *pitch angle diffusion coefficient* or *pitch angle diffusion* will be discussed in more detail. Pitch angle diffusion describes the scattering of particles off magnetic fields, i.e. wave-particle interaction. Wave-particle scattering can be seen as a resonant interaction, where

$$\omega - k_\| \, v_\alpha \, \mu = n \, \frac{\Omega_\alpha}{\gamma_\alpha} \tag{2.131}$$

is the resonance condition (Schlickeiser, 1989) which relates the properties of the wave (parallel wave number $k_\|$ and frequency ω) to those of the particle (speed v_α, Lorentz factor γ_α, cyclotron frequency Ω_α and pitch angle cosine μ). The parameter $n \in \mathbb{Z}$ describes the order of the resonance.

Wave-particle scattering is caused by the influence of the magnetic field $\boldsymbol{\delta B}$ of the wave on the motion of the particle. This interaction in particular leads to a deviation of the particle's trajectory from the unperturbed orbit and to a change in the parallel component $p_\|$ of the particle's momentum. Following Lee and Lerche (1974), who apply a magnetostatic approach ($\delta E = 0$, $\omega = 0$), the change of $p_\|$ can be expressed by

$$\frac{dp_\|}{dt} = \frac{q_\alpha \, c}{2 \, E_\alpha} \sum_{\pm} (\pm\imath) \, p_\perp \, \delta B_\pm, \tag{2.132}$$

where E_α is the kinetic energy of the particle and $\delta B_\pm = \delta B_x \pm \imath\, \delta B_y$ are the (complex) magnetic fields of a right- (+) or left-handed (−) "Alfvén wave"[21]. The wave vector is assumed to be $\boldsymbol{k} = (k_\perp \cos\psi,\, k_\perp \sin\psi,\, k_\|)$ and the parallel and perpendicular components of the momentum vector can be written as

$$\begin{aligned} p_\| &= p_{\|,0}, && (2.133) \\ p_\pm &= p_x \pm \imath\, p_y = p_\perp \exp\big(\mp \imath(\Phi_0 - \Omega_\alpha\, t/\gamma_\alpha)\big), && (2.134) \end{aligned}$$

where Φ_0 is the initial phase angle of the particle at time t_0. Note that the cyclotron frequency Ω_α is reduced by the Lorentz factor γ_α in the case of relativistic particle speeds.

Using Eq. (2.132) and the definitions of $p_\|$ and $p_\pm$ for the parallel and perpendicular components of the momentum vector the change of the pitch angle cosine can be derived:

$$\frac{d\mu}{dt} = \frac{q_\alpha\, c}{2\, p\, E_\alpha} \sum_\pm (\mp\imath)\, p_{\perp,0} \exp\big(\mp \imath(\phi_0 - \Omega_\alpha\, t/\gamma_\alpha)\big)\, \delta B_\pm. \tag{2.135}$$

By expressing the fluctuations of the magnetic field as Fourier modes

$$\delta B_\pm(\boldsymbol{r}) = \frac{1}{8\,\pi^3} \int d^3\boldsymbol{k}\, \delta B_\pm(\boldsymbol{k}) \exp(\imath\, \boldsymbol{k} \cdot \boldsymbol{r}) \tag{2.136}$$

and rewriting the exponential function in terms of Bessel functions J_n of the first kind Eq. (2.135) can be reformulated (see Lange et al., 2013, Appendix A for details):

$$\begin{aligned} \frac{d\mu}{dt} &= \frac{q_\alpha\, c}{2\, p\, E_\alpha} \sum \pm(\mp\imath)\, p_{\perp,0} \exp(\mp\imath\, \Phi_0)\, \frac{1}{8\,\pi^3} \int d^3\boldsymbol{k}\, \delta B_\pm(\boldsymbol{k}) \sum_n J_n\left(\frac{k_\perp\, v_\perp\, \gamma_\alpha}{\Omega_\alpha}\right) \\ &\quad \cdot \exp\big(-\imath\, n(\Psi - \Phi_0) + \imath\, t(k_\|\, v_{\|,0} \pm \Omega_\alpha/\gamma_\alpha - n\, \Omega_\alpha/\gamma_\alpha)\big). \end{aligned} \tag{2.137}$$

This finally leads to an expression for the pitch angle cosine itself (Lee and Lerche, 1974):

$$\begin{aligned} \mu &= \mu_0 - \frac{q_\alpha\, c}{2\, p\, E_\alpha}\, \frac{p_{\perp,0}}{8\,\pi^3} \int d^3\boldsymbol{k}\, \delta B(\boldsymbol{k}) \sum_n \frac{2\, n\, \Omega_\alpha}{k_\perp\, v_{\perp,0}\, \gamma_\alpha} J_n\left(\frac{k_\perp\, v_{\perp,0}\, \gamma_\alpha}{\Omega_\alpha}\right) \\ &\quad \cdot \exp\big(-\imath\, n(\psi - \Phi_0)\big) \int_0^t dt' \exp\big(\imath\, t'(k_\|\, v_{\|,0} - n\, \Omega_\alpha/\gamma_\alpha)\big). \end{aligned} \tag{2.138}$$

Equation (2.138) describes the time evolution of the pitch angle cosine of a single particle with specific initial conditions (e.g. Φ_0, $v_\|$, $v_\perp$). Lee and Lerche (1974) argue that in a statistical examination of the problem the initial conditions of the particle do not matter. This is also a consequence of the assumptions of QLT: at time scales $t > t_\mathrm{c}$ the particle "forgets" its initial conditions, since the field fluctuations at its current position are no longer correlated with the fluctuations at its starting point. Thus, a statistical approach is possible where only averages of the physical quantities have to be considered. Based on the assumptions $\langle \delta B \rangle = 0$ and $\langle \exp(\imath\, n\, \Phi_0) \rangle = 0$ the ensemble average of the pitch angle cosine must be equal to the initial pitch angle at t_0: $\langle \mu \rangle = \mu_0$. Lee and Lerche (1974) then continue

---

[21] Lee and Lerche (1974) derive their theory in the limit $\omega \ll \Omega_\mathrm{p}$ where left- and right-handed waves can be described by the dispersion relation for Alfvén waves, $\omega = k_\|\, v_\mathrm{A}$.

to define a correlation $\langle \Delta\mu \, \Delta\mu \rangle$ for the change of the pitch angle cosine,

$$\Delta\mu = \mu - \mu_0, \tag{2.139}$$

which allows to derive the pitch angle diffusion coefficient:

$$\begin{aligned} D_{\mu\mu} \;\; &= \;\; \frac{\pi \, q_\alpha^2 \, c^2}{E_\alpha^2} \, (1 - \mu^2) \int d^3\boldsymbol{k} \, P(\boldsymbol{k}) \sum_{n=-\infty}^{\infty} \frac{n^2 \, \Omega_\alpha^2}{k_\perp^2 \, v_\perp^2 \, \gamma_\alpha^2} \\ &\quad \cdot J_n^2 \left(\frac{k_\perp \, v_\perp \, \gamma_\alpha}{\Omega_\alpha} \right) \delta(k_\parallel \, v_\parallel - n \, \Omega_\alpha / \gamma_\alpha), \end{aligned} \tag{2.140}$$

where $P(\boldsymbol{k})$ describes the power spectrum of the fluctuations $\delta\Phi$ of the particles' phase angles Φ (see the original article for details).

The interpretation of the equation for the pitch angle diffusion coefficient can be given as follows: The delta function on the right-hand side of Eq. (2.140) represents the resonance condition[22] and denotes that a particle resonates with "waves that have an integral number of wavelengths in the distance traversed parallel to the ambient field during one gyration about the field" (Lee and Lerche, 1974). The order of the resonance, n, defines the waves which are available for resonance. A resonance of zeroth order ($n = 0$) would mean an interaction with particles which travel parallel to the background magnetic field. Therefore, there is no resonance, since only Alfvén waves are considered in the derivation of $D_{\mu\mu}$ and Alfvén waves do not interact with particles traveling parallel to $\boldsymbol{B}_0$[23]. Resonances of order $n = \pm 1$ mean that particles interact with parallel propagating waves, whereas higher orders ($|n| > 1$) represent interactions with oblique waves, which become less and less important (i.e. the infinite sum over n converges).

Scattering Amplitude

Based on the work of Lee and Lerche (1974) an analytic expression for the pitch angle *scattering amplitude* $\Delta\mu(t)$ was derived by Lange et al. (2013). Their method is interesting for two reasons: first, the resulting expression is analytic and therefore easy to handle; secondly, the scattering amplitude can be directly compared to simulation results.

As mentioned earlier, Lee and Lerche (1974) derive their equations in the magnetostatic limit, where the electric field vanishes and the frequency of the wave is zero. For a single wave this can be interpreted as a transformation into the rest frame of the plasma wave, i.e. a rest frame which is moving at a speed $\boldsymbol{v}_{\mathrm{ph}}$ relative to the rest frame of the bulk plasma. These two rest frames will be called "*wave frame*" and "*plasma frame*" hereafter and quantities in the former will be denoted by a prime, whereas quantities in the latter will be written without prime. In the wave frame, where the particles can only interact with magnetic fields, the energy of the particles is conserved and the only non-vanishing diffusion coefficient is the pitch angle diffusion coefficient $D_{\mu\mu}$ (Schlickeiser, 1994).

The resonance condition, Eq. (2.131), is expressed by

$$-\, k'_\parallel \, v'_\alpha \, \mu' = n \frac{\Omega'_\alpha}{\gamma'_\alpha} \tag{2.141}$$

---

[22] Compared to Eq. (2.131) the frequency ω is neglected here.

[23] Compressional magnetosonic waves may very well interact with parallel propagating particles. This leads to an $n = 0$ resonance, which is called *Cherenkov resonance*.

in the wave frame. Other quantities of importance are the scattering amplitude $\Delta\mu'(t') = \mu'_t - \mu'_0$ (with $\mu'_t := \mu'(t')$) and the mean pitch angle cosine $\bar{\mu}' = (\mu'_t + \mu'_0)/2$ of a single particle in the interval $t - t_0$.

Based on Eq. (2.138) Lange et al. (2013) derive an expression for the scattering amplitude as a function of time:

$$\begin{aligned}\Delta\mu'^{\pm}(\bar{\mu}', t', \Psi'^{\pm}) \;=\; & \frac{\Omega'_\alpha}{\gamma'_\alpha}\frac{\delta B'}{B'_0}\sqrt{1-\bar{\mu}'^2} \\ & \cdot \frac{\cos\left(\Psi'^{\pm}\right) - \cos\left(\left(\pm k'_\parallel\, v'_\alpha\, \bar{\mu}' - \Omega'_\alpha/\gamma'_\alpha\right) t' + \Psi'^{\pm}\right)}{\pm k'_\parallel\, v'_\alpha\, \bar{\mu}' - \Omega'_\alpha/\gamma'_\alpha},\end{aligned} \tag{2.142}$$

where they consider only resonances of the order $|n| = 1$ and choose the phase angle $\Psi'^{\pm}$ in such a way that it maximizes the scattering amplitude (i.e. yields the envelope of all possible solutions):

$$\Psi'^{\pm}(\bar{\mu}', t') = \arctan\left(\frac{\sin\left(\left(\pm k'_\parallel\, v'_\alpha\, \bar{\mu}' - \Omega'_\alpha/\gamma'_\alpha\right) t'\right)}{1 - \cos\left(\left(\pm k'_\parallel\, v'_\alpha\, \bar{\mu}' - \Omega'_\alpha/\gamma'_\alpha\right) t'\right)}\right). \tag{2.143}$$

Due to the limitation to resonances of first order the above equations model only the interaction of particles and (anti-) parallel propagating waves. The superscript signs denote the polarization of these waves, where "+" stands for right-handed and "−" for left-handed waves. To obtain the full set of solutions Eq. (2.142) has to be evaluated using the phase angles Ψ' and $\Psi' + \pi$.

Note that the model for the scattering amplitudes (as well as Lee and Lerche, 1974) assumes *test particles*, i.e. particles which are affected by the electromagnetic fields, but which themselves do not influence the dynamics of the plasma. This assumption is often made when the population of test particles represents only a small fraction of the bulk plasma particles. Contrary to the idea of turbulence Eqs. (2.142) and (2.143) are applied to only a single plasma wave and Eq. (2.142) also describes the scattering amplitude of only a single particle, i.e. the change of the particle's pitch angle $\Delta\mu'$ as a function of the mean pitch angle $\bar{\mu}'$ during the interaction with the magnetic field of the wave. While the shape of $\Delta\mu'(\bar{\mu}')$ is defined by Eq. (2.142), the amplitude depends on the phase angle Ψ'. Choosing Ψ' as defined in Eq. (2.143) yields the maximum possible scattering amplitude, i.e. the change of pitch angle a particle would experience if it had the optimum phase angle relative to the wave. Particles which start the interaction at a different relative phase angle will scatter less efficiently.

In the following a recent adaption of the model of Lange et al. (2013) will be presented, as suggested by Schreiner and Spanier (2015) and fully derived by Schreiner et al. (2017b). The aim of the adaption is to find an analytical representation of the scattering amplitude $\Delta\mu(\mu, t)$ in the plasma frame. This is done by defining transformations between the plasma and the wave frame. With the help of the transformation rules the properties of waves and particles, which are known in the plasma frame, can be expressed in the wave frame. In the wave frame the magnetostatic approximation is valid and Eqs. (2.142) and (2.143) can be used to calculate the scattering amplitude in the wave frame. Finally, the scattering amplitude can be transformed back into the plasma frame.

The idea of this method is very simple and does not require a re-consideration of the basic theory in the framework of QLT. However, the new approach allows to model arbitrary parallel propagating waves. While only non-dispersive Alfvén waves have been assumed in the initial derivation, the method presented below also allows dispersive left- and right-handed waves, such as proton or electron cyclotron waves and whistlers. In principle it is also possible to study the superposition of several waves, because the transformations between rest frames can be carried out for each wave individually. A combined scattering amplitude can then be obtained from the superposition.

The relativistically correct transformations into the wave frame are given by the following equations:

$$\begin{aligned}
t' &= t\,\gamma_{\mathrm{w}}\left(1 - \frac{\mu\, v_\alpha\, v_{\mathrm{ph}}}{c^2}\right), && (2.144)\\
k'_{\|} &= k_{\|}/\gamma_{\mathrm{w}}, && (2.145)\\
\delta B' &= \delta B/\gamma_{\mathrm{w}}, && (2.146)\\
\mu' &= \frac{\mu\, v_\alpha - v_{\mathrm{ph}}}{\sqrt{v_\alpha^2 - 2\,\mu\, v_\alpha\, v_{\mathrm{ph}} + v_{\mathrm{ph}}^2 - \left(1-\mu^2\right) v_\alpha^2\, v_{\mathrm{ph}}^2/c^2}}, && (2.147)\\
v'_\alpha &= \frac{\sqrt{v_\alpha^2 - 2\,\mu\, v_\alpha\, v_{\mathrm{ph}} + v_{\mathrm{ph}}^2 - \left(1-\mu^2\right) v_\alpha^2\, v_{\mathrm{ph}}^2/c^2}}{1 - \mu\, v_\alpha\, v_{\mathrm{ph}}/c^2}. && (2.148)
\end{aligned}$$

Since only parallel propagating waves are considered ($\boldsymbol{v}_{\mathrm{ph}} \parallel \boldsymbol{B}_0$) the amplitude of the background magnetic field and the cyclotron frequency stay constant: $B'_0 = B_0$ and $\Omega'_\alpha = \Omega_\alpha$. The Lorentz factor γ'_α of the particles in the wave frame can be calculated by use of Eq. (2.148). If the phase speed of the wave is also relativistic, the Lorentz factor γ_{W} of the wave has to be considered.

Once the scattering amplitudes have been calculated in the wave frame the results have to be transformed back into the plasma frame. The pitch angle cosine is transformed similarly to Eq. (2.147):

$$\mu = \frac{\mu'\, v'_\alpha + v_{\mathrm{ph}}}{\sqrt{v'^2_\alpha + 2\,\mu'\, v'_\alpha\, v_{\mathrm{ph}} + v_{\mathrm{ph}}^2 - \left(1-\mu'^2\right) v'^2_\alpha\, v_{\mathrm{ph}}^2/c^2}}. \qquad (2.149)$$

The procedure for the scattering amplitude is a bit more complicated, but also straight forward:

$$\begin{aligned}
\Delta\mu^{\pm}(\bar\mu, t) &= \mu_t - \mu_0\\
&= 2\left(\mu_t - \bar\mu\right)\\
&= 2\left(\mu(\mu'_t) - \bar\mu\right)\\
&= 2\Big(\mu\big(\Delta\mu'^{\pm}(\bar\mu, t)/2 + \bar\mu'(\bar\mu)\big) - \bar\mu\Big), && (2.150)
\end{aligned}$$

where Eq. (2.149) is applied to the pitch angle cosine in the wave frame, $\mu'_t = \Delta\mu'/2 + \bar\mu'$, to obtain μ_t.

Note that the particle energy is assumed to be constant in both the wave and the plasma frame. While the kinetic energy is exactly conserved in the wave frame (only elastic scattering at magnetic field fluctuations), this is not the case in the plasma frame. On the one hand there are also electric fields in the plasma frame, on the other hand a particle gains or loses energy when scattering off of moving magnetic fields, as described by Fermi (1949). Therefore, an additional assumption has to be made to ensure the validity of the model.

A change of the energy of the particles can be interpreted as *momentum diffusion*, which is described via the Fokker-Planck coefficients $D_{\mu p}$ and D_{pp}. According to Schlickeiser (1994) these coefficients are of order v_{ph}/c and $(v_{\mathrm{ph}}/c)^2$, respectively, whereas $D_{\mu\mu}$ is of order unity. For $v_{\mathrm{ph}}/c \ll 1$ pitch angle diffusion is still the fastest process and changes in momentum can be neglected. This is only consistent with Eq. (2.62), which implies that the electric field δE of a wave is much smaller than the magnetic field δB if $v_{\mathrm{ph}}/c \ll 1$.

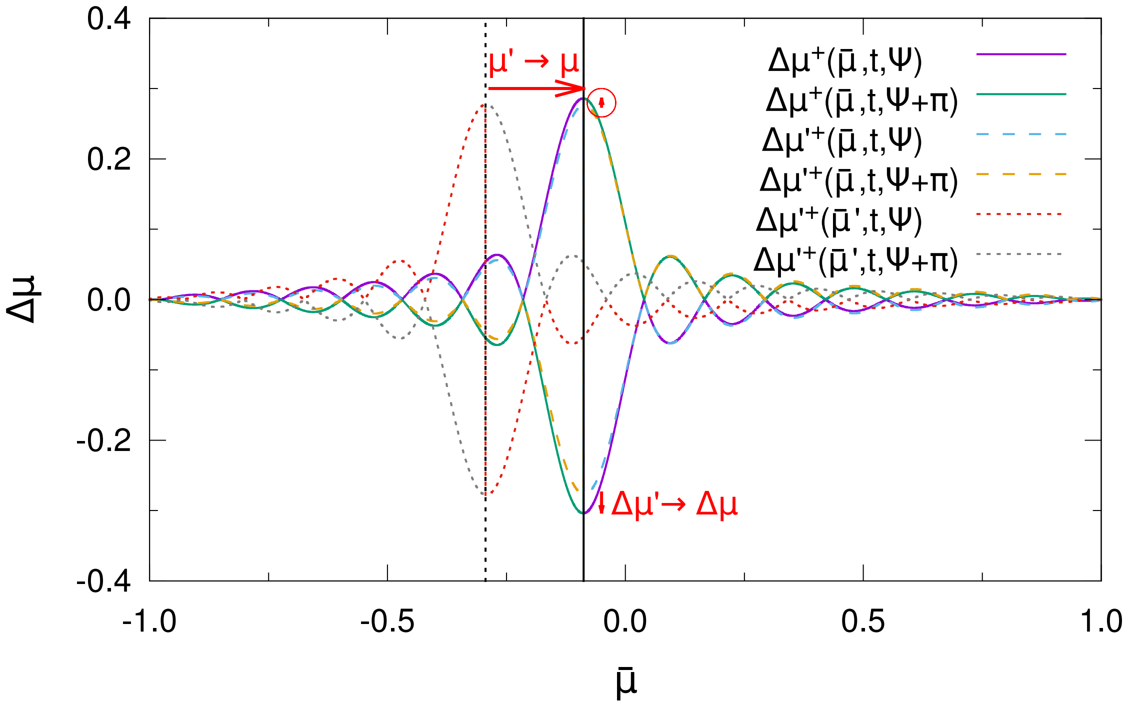

Fig. 2.10: Maximum scattering amplitudes $\Delta\mu$ of electrons during the interaction with right-handed parallel propagating waves. The dotted lines show the predictions by Lange et al. (2013) in the wave frame, Eqs. (2.142) and (2.143). The transformations presented above lead to a shift of the curves along the abscissa (dashed lines), caused by Eqs. (2.144 - 2.148), and to a change of amplitude (solid lines), as the scattering amplitude itself is transformed, Eqs. (2.149) and (2.150). The red arrows indicate these changes. As can be seen by the length of the vertical arrows the scattering amplitudes in the plasma frame are no longer symmetric about $\Delta\mu = 0$. Figure taken from Schreiner et al. (2017b).

The meaning and shape of the scattering amplitude, Eq. (2.142), and the effect of the transformations, Eqs. (2.144 - 2.150), are illustrated in Fig. 2.10. The dotted lines show the scattering amplitude $\Delta\mu'(\bar{\mu}')$ in the wave frame. If Eqs. (2.144 - 2.148) are applied to transform the input quantities t, $k_{\|}$, ω, μ, and v_α, the curves are moved along the abscissa, as can be seen by the dashed curves. At this stage the scattering amplitude in the wave frame, $\Delta\mu'$, is given as a function of the parameters in the plasma frame, which is of course inconsistent. With the help of Eqs. (2.149) and (2.150) this can be fixed, as the scattering amplitude itself is also transformed and $\Delta\mu(\mu)$ in the plasma frame is obtained. However, this last step leads to a slight asymmetry of the scattering amplitude about $\Delta\mu = 0$, as indicated by the red vertical arrows in Fig. 2.10.

The physical interpretation is that the scattering amplitude, and therefore efficiency, is largest at the resonance, i.e. if $\bar{\mu} = \mu_{\rm res}$. The resonant pitch angle cosine $\mu_{\rm res}$ is given by Eq. (2.131) in the plasma frame and by Eq. (2.141) in the wave frame (solid or dashed black vertical line in Fig. 2.10). As can clearly be seen the analytical prediction for the scattering amplitude, Eq. (2.142), recovers the expected behavior and peaks around the resonant pitch angle cosine.

Scattering is inefficient at positions other than $\mu_{\rm res}$. On average, a particle is not affected by the magnetic field fluctuations if it is far away from the resonance. In this regime transport is called *(scatter-) free* or *ballistic*, i.e. without interactions (Trotta and Zimbardo, 2011). However, the smaller side peaks in Fig. 2.10 indicate that non-resonant or "ballistic interactions" (Lange et al., 2013) are possible. These smaller peaks are therefore referred to as *ballistic peaks*.

Note that Fig. 2.10 depicts the *maximum* scattering amplitudes, resulting from the use of the phase angle $\Psi^{\pm}$ given in Eq. (2.143). If a particle with a random relative phase angle to the wave is chosen, this particle may change its pitch angle during an interaction by as much as $|\Delta\mu(\bar{\mu})|$, but smaller values are also possible. Also note that Eq. (2.142) describes the scattering amplitude at a given time $t > t_0$, which is only a snapshot of the evolution of pitch angle scattering. While the resonances stay at constant positions (namely $\mu_{\rm res}$), the ballistic peaks move towards the resonance and become narrower. Their number increases with time.

2.6.3 Particle Transport in Turbulence

Previously the transport of particles in the presence of individual waves has been discussed. However, this situation will hardly be encountered in nature. To describe realistic particle transport a model for particle scattering in a turbulent medium has to be found.

Due to the complexity of the problem a consistent and comprehensive theory is hard to establish. Theory provides useful expectation values and narrows broader questions down to specific physical processes. Computer simulations, however, are as important as analytical theory, because they can address questions which cannot be treated satisfactorily by theory. For example, self-consistent simulations of Gary and Nishimura (2004) probe the scattering of protons across $\mu = 0$ – a process which is only inadequately described by QLT. High amplitude waves (i.e. $\delta B/B_0 \sim 1$) and their effect on momentum diffusion are discussed by Michałek and Ostrowsky (1996), who compare Monte Carlo simulations to QLT predictions. Vainio and Kocharov (2001) also employ the Monte Carlo method to model the transport of energetic protons through self-generated Alfvén waves. The generation or damping of waves by the streaming energetic particles was not considered by the test particle model presented in the previous section.

Theoretical models are also developed (e.g. Schlickeiser, 1989, 1994, who studies transport and acceleration of particles), but often no analytical solutions can be found. This means that either simplifications have to be found (usually involving additional assumptions and a loss of generality) or that the equations finally have to be solved numerically (e.g. Ng and Reames, 1994; Qin et al., 2002; Vainio et al., 2003).

For the case of turbulence in the dispersive range of the low frequency wave modes Steinacker and Miller (1992) and Vainio (2000) have developed models which combine QLT and the full cold plasma dispersion relations. This allows them to derive Fokker-Planck coefficients $D_{\mu\mu}$, $D_{\mu p}$, and D_{pp} as well as mean free paths for particles in dispersive turbulence.

The model is not limited to Alfvénic turbulence, but can also describe whistler turbulence.

While this is certainly interesting and helpful, a full representation of particle transport in turbulent plasmas should be attempted via self-consistent simulations. Following a test particle approach the turbulent background plasma can, for example, be modeled self-consistently with MHD simulations, whereas a sample of test particles is treated kinetically (e.g. Wisniewski et al., 2012; Lange et al., 2013). By statistical analysis of the test particles in the simulations different quantities of interest, such as the Fokker-Planck coefficients, can be derived.

The MHD simulation of course implies that only Alfvénic turbulence in the inertial range can be studied. A more complex picture of turbulence can be obtained using the particle-in-cell (PiC) method, as do Chang et al. (2013, 2015) or Gary et al. (2012, 2014) in their simulations of whistler turbulence. Combining such simulations with a sample of energetic (test) particles leads to a self-consistent picture of particle transport in kinetic turbulence, including dispersion and dissipation effects. Using the detailed particle and field data, which are produced anyway in a PiC simulation, the properties of both the turbulent cascade (such as the spectral index of the magnetic field spectrum) and the energetic particles (diffusion coefficients) can be derived. Methods for analyzing particle statistics are readily available (e.g. Ivascenko et al., 2016) and allow for a meaningful evaluation of simulation data. Results can then be compared to measurements in the solar wind or theoretical models in order to improve both theory and the numerical representation.

3 Numerical Approach

3.1 Simulation Method

3.1.1 How it should be done...

Collisionless plasma dynamics can be entirely described by the combined system of the Vlasov equation, Eq. (2.67) in Sect. 2.4, and Maxwell's equations, Eqs. (2.15 - 2.18) in Sect. 2.3.1. This system of coupled differential equations models the evolution of the phase space density $f_\alpha(\boldsymbol{r}, \boldsymbol{v}, t)$ of particles of species α in its six-dimensional phase space. In principle it is possible to discretize the Vlasov equation and to directly solve it numerically. However, due to the high dimensionality the computational effort for this endeavor is immense. The discretization requires a six-dimensional grid (three dimensions for space and another three for velocity) which leads to high demands on both computing power and memory. A direct numerical treatment of the Vlasov-Maxwell system, although desirable, therefore often collapses due to the excessive demand of computational resources.

Still, Vlasov codes have their advantages over other numerical methods, since they are essentially free from numerical noise and therefore allow for very accurate simulations of physical processes. In fact, if one wanted to achieve a comparably low level of numerical noise with a different method (e.g. a particle-in-cell code), the computational effort would be similar to – or even larger than – the effort for a Vlasov simulation (Büchner, 2007). Especially in lower-dimensional versions Vlasov codes have become more and more common in recent years (e.g. Minoshima et al., 2011).

If only low frequency phenomena are considered the use of a *gyrokinetic code* can be a rewarding alternative (e.g. Görler et al., 2011). The idea of the gyrokinetic approach is to split the fluctuations into a high frequency part (above the electron cyclotron frequency) and a low frequency part. High frequency fluctuations are averaged, whereas the evolution of the remaining low frequency fluctuations can be described by a Vlasov equation for the gyro-centers of the particles. This treatment allows to neglect smallest length scales (e.g. the Debye length) and resolve only the Larmor radius. Compared to a Vlasov code the gyrokinetic approach has the advantage of longer time steps and a relatively coarse spatial grid, which allows for the simulation of larger physical systems. Additionally, one dimension of velocity space is lost due to the reduction of the actual motion of the particles to the trajectories of their gyro-centers.

3.1.2 ...and how it is actually done

Particle-in-Cell

A common alternative to directly discretizing and solving the Vlasov-Maxwell system is the Particle-in-Cell (PiC) method (e.g. Hockney and Eastwood, 1988; Birdsall and Langdon, 2005). The basic idea is to sample the *phase space density* (or particle distribution function) $f_\alpha(\boldsymbol{r}, \boldsymbol{v}, t)$ by use of individual phase space elements. It is assumed that a sufficiently large number N_p of *phase space elements* $f_{\alpha,i}$ represents the original phase space density:

$$\sum_{i=1}^{N_p} f_{\alpha,i}(\boldsymbol{r},\boldsymbol{v},t) \approx f_\alpha(\boldsymbol{r},\boldsymbol{v},t). \tag{3.1}$$

Each phase space sample occupies a small volume in phase space, i.e.

$$f_{\alpha,i}(\boldsymbol{r},\boldsymbol{v},t) = w_i\, S_r\big(\boldsymbol{r}-\boldsymbol{r}_i(t)\big)\, S_v\big(\boldsymbol{v}-\boldsymbol{v}_i(t)\big), \tag{3.2}$$

where w_i is called *macro factor*, describing the statistical weight of the sample, and S_r and S_v are the *form factors*, describing the shape and extent of the phase space sample in real and velocity space.

Contrary to Eulerian Vlasov schemes there is no need for a six-dimensional grid which represents phase space. Instead a three-dimensional grid is provided which only reflects the spatial dimensions of the simulated volume. The grid is populated by phase space elements, which represent the particle density in real space. Velocity space is not completely covered by the phase space samples, but with a large enough number of samples N_p a sufficiently accurate approximation can be reached.

The term “phase space element” or “sample” still sounds rather abstract. However, it can be shown that these elements behave like physical particles. Following Lapenta (2011, Chapter 2.3) a Vlasov equation for the individual phase space samples can be found (for simplicity only in one dimension and non-relativistic):

$$\frac{\partial f_{\alpha,i}}{\partial t} + v_x\,\frac{\partial f_{\alpha,i}}{\partial x} + \frac{q_\alpha\,E_x}{m_\alpha}\,\frac{\partial f_{\alpha,i}}{\partial v_x} = 0. \tag{3.3}$$

The definition Eq. (3.2) can be inserted into Eq. (3.3) and the zeroth moment in velocity can be derived. This leads to a condition for the macro factor:

$$\frac{\partial}{\partial t}\sum_i w_i = 0, \tag{3.4}$$

which states that the sum over all w_i is constant. A common realization of this constraint is to keep the individual w_i constant, meaning that the statistical weight of the individual phase space elements does not change during the simulation. By deriving the first moment in real space an equation is obtained which describes the motion of a phase space sample:

$$w_i\,\frac{\partial x_i}{\partial t} = w_i\,v_i, \tag{3.5}$$

which is equivalent to the equation of motion of a physical particle multiplied by the macro factor. Finally, the first moment in velocity space yields an equation which relates the change in speed v_i to the external force applied by the electric field E_x:

$$w_i\,m_\alpha\,\frac{\partial v_i}{\partial t} = w_i\,q_\alpha\,E_x(x_i). \tag{3.6}$$

This is again equivalent to an equation of motion for a regular particle multiplied by w_i.

The examination of the behavior of phase space elements summarized above suggests that the samples $f_{\alpha,i}$ can be treated just like physical particles of species α. The only difference is the weighting factor w_i, which modifies the mass $m_{\alpha,i} = w_i\, m_\alpha$ and charge $q_{\alpha,i} = w_i\, q_\alpha$ of a phase space sample compared to a physical particle. Therefore, phase space samples are often called *macro particles.* Of course, the treatment of phase space elements as macro particles also works in the more general case with three dimensions, magnetic fields, and relativistic formulation of the equations.

Now that the nature of the phase space samples has become clear, only the description of the electromagnetic fields is missing. As mentioned above the particle-in-cell method uses a grid representing physical space. Each grid cell hosts charge and current densities, which are basically derived from the particles in the cell, as well as the local electric and magnetic fields. Time evolution of the fields can then be done entirely on the grid.

Each particle interacts only with the grid – both to deposit charge and current densities on the grid and to "receive" the electromagnetic fields needed to calculate the Lorentz force. Therefore, no particle-particle interactions are necessary, which reduces the numerical effort from order $\mathcal{O}(N_p^2)$ to $\mathcal{O}(N_p)$. The relatively easy handling of the phase space samples and the linear increase of computational effort with problem size make PiC codes a popular choice (e.g. Fonseca et al., 2002; Cai et al., 2003; Melzani et al., 2013), especially since they recover almost all kinetic effects expected in a collisionless plasma. In the following section, Sect. 3.2, the *ACRONYM* PiC code (Kilian et al., 2012) will be presented in more detail.

Alternative Schemes

The particle-in-cell method is, of course, not the only way to obtain a simplified description of a plasma. Another widely used numerical scheme is the magnetohydrodynamic (MHD) approach (e.g. Goedbloed et al., 2010) for collisional (and therefore thermal) plasmas. The MHD approach assumes that the particle distribution function $f_\alpha(\boldsymbol{r}, \boldsymbol{v}, t)$ can be characterized by its statistical moments in velocity space. Typically the first two moments are considered, which simplifies the Boltzmann equation and yields a system of new equations referred to as *MHD equations.* The MHD equations can be solved numerically using finite volume methods and the plasma is generally treated as fluid.

The downside of MHD simulations is that all kinetic effects are neglected due to the absence of actual particles. A deviation of the particle distribution function from the thermodynamic equilibrium is not possible, which is equivalent to the assumption that the simulated plasma is collisional. Large scale developments in a magnetized plasma can therefore be recovered by MHD, but care has to be taken when phenomena at scales smaller than the mean free path of the particles are considered. Close to kinetic scales, e.g. the Larmor radius of the particles, the MHD model breaks down. However, MHD codes have proven to be well-suited for studying the large scale Alfvénic turbulence in the solar wind (e.g. Lange and Spanier, 2012; Beresnyak, 2014).

Between the kinetic (PiC) and the fluid (MHD) representation of a plasma in numerical simulations a variety of hybrid models exist. For example, it is possible to model one particle species as a fluid (e.g. the electrons) and another species as kinetic particles (e.g. the protons), to recover kinetic effects of the latter species without the additional effort of simulating the former species in detail (e.g. Franci et al., 2015a; Franci et al., 2015b). Hybrid codes therefore may recover more physical processes than MHD codes, whereas they are (ideally) less computationally expensive than PiC simulations. The interested reader may be referred to Kilian et al. (2017), who discuss different kinetic and hybrid approaches and their influence on the development of plasma waves in the simulation. For the analysis of small populations of test particles and their reaction to the surrounding bulk plasma the method of so-called *test particle MHD* can be employed. Here the bulk plasma is modeled by an MHD simulation, whereas the test particle population consists of a number of individual particles which are treated fully kinetic (e.g. Lange et al., 2013). However, this method is not entirely self-consistent, as the test particles cannot influence the bulk plasma.

3.2 The ACRONYM PiC Code

The *ACRONYM* particle-in-cell code (Kilian et al., 2012) has been developed at the University of Würzburg over the past years (Burkart et al., 2010; Ganse, 2012; Kilian, 2015; Kempf, 2016). ACRONYM – *Advanced Code for Relativistic Objects, Now with Yee-lattice and Macro particles* – is a fully relativistic, explicit[24], electromagnetic PiC code which can be operated with one, two, or three spatial dimensions. Electromagnetic fields and particle velocities are always treated as three-dimensional vectors, independent of the number of spatial dimensions simulated (so-called *1d3v*, *2d3v*, or *3d3v* simulations).

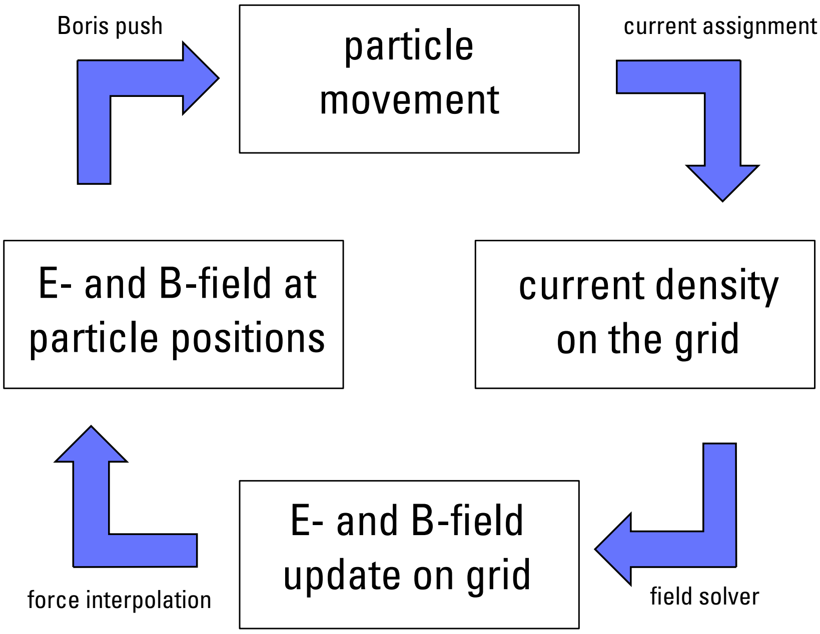

Fig. 3.1: Subroutines of a time step: From the motion of the particles the current density is calculated and interpolated to the grid. Field quantities are updated via Maxwell's equations and then interpolated to the positions of the particles. Finally, the particles' velocities and positions are updated according to the Lorentz force exerted by the electromagnetic fields. Figure according to Ganse (2012).

A schematic of the different subroutines carried out in each time step is shown in Fig. 3.1. These routines, as well as the general setup of the grid and the treatment of the macro particles will be briefly summarized below. The descriptions mostly follow Kilian (2015, Chapter 5), who presents the most comprehensive characterization of the features currently available in the ACRONYM code.

---

[24] An alternative *implicit* code based on ACRONYM and the work of Petrov and Davis (2011) is discussed in Kempf et al. (2013).

3.2.1 Discretized Grid

The basis for the treatment of the electromagnetic fields is the grid, consisting of individual grid cells which each host the local electric and magnetic field vectors $\boldsymbol{E}$ and $\boldsymbol{B}$, the local current density vector $\boldsymbol{j}$, and the local charge density ρ. The grid is set up using a so-called *Yee scheme* (Yee, 1966), which can be interpreted as two sub grids which are offset by half a cell relative to each other. One sub grid hosts the electric field, the other the magnetic field, as indicated in Fig. 3.2. The advantage of this method is that each component of the electric (magnetic) field is surrounded by four components of the magnetic (electric) field. Moreover, the surrounding field components all point in directions perpendicular to the direction of the field component in the center. This allows for a simple and fast calculation of the a-component of the curl $(\nabla \times \boldsymbol{E})_a$ of the electric field at the position of the relevant component B_a of the magnetic field and vice versa. The importance of this advantage is obvious, since Maxwell's equations require the calculation of the curl of both fields and have to be solved at each grid point in each time step.

In principle it is possible to choose freely if the electric field is located at the edges and the magnetic field at the face centers of the grid cells or the other way round. However, the variant chosen in the ACRONYM code and depicted in Fig. 3.2 brings along certain advantages for the representation of conducting boundaries in the simulation (see Kilian, 2015, Chapter 5.2.6). Labeling the current cell with the numerical coordinates (i, j, k) the x-component of the electric field is located half way along the edge towards grid cell $(i + 1, j, k)$, i.e. at $(i + \frac{1}{2}, j, k)$. The corresponding component of the current density is deposited at the same place, which is again convenient for the computation of Maxwell's equations. Shifted by half a cell width in each direction relative to E_x the x-component of the magnetic field is located at $(i, j + \frac{1}{2}, k + \frac{1}{2})$. Scalar quantities, such as the charge density, can be stored directly at (i, j, k).

3.2.2 Time Evolution of the Electromagnetic Fields

With the field and current density vectors deployed on the grid the time evolution of the electromagnetic fields can be calculated. Looking at Maxwell's equations, Eqs. (2.15-2.18), it can be seen that only two equations are directly affected by time evolution. The choice of the Yee scheme for the spatial discretization of the fields ensures that the other two equations, (2.15) and (2.16), are satisfied at all time steps in the simulation (disregarding small numerical errors), if they were satisfied at the beginning of the simulation. Equations (2.17) and (2.18) have to be slightly rewritten in order to be solved numerically using a *Finite-Differences Time-Domain* (*FDTD*) method:

$$\frac{\partial \boldsymbol{B}}{\partial t} = -c\, \boldsymbol{\nabla} \times \boldsymbol{E}, \tag{3.7}$$

$$\frac{\partial \boldsymbol{E}}{\partial t} = c\, \boldsymbol{\nabla} \times \boldsymbol{B} - 4\pi\, \boldsymbol{j}. \tag{3.8}$$

Time is discretized in individual *time steps* of length Δt. The maximum length of a time step is limited by the *Courant-Friedrichs-Lewi* or *CFL condition* (Courant et al., 1928), which basically states that the time step must be shorter than the time required by the fastest signal to propagate across one grid cell (see Eqs. (3.14) and (3.15) below). Labeling the current time step with t and the next consecutive step with $t + 1$ the time derivative of

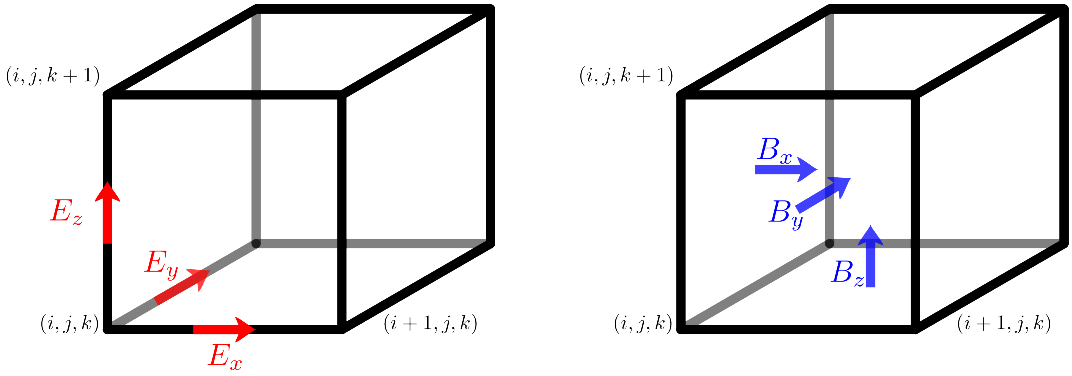

(a) electric field **(b)** magnetic field

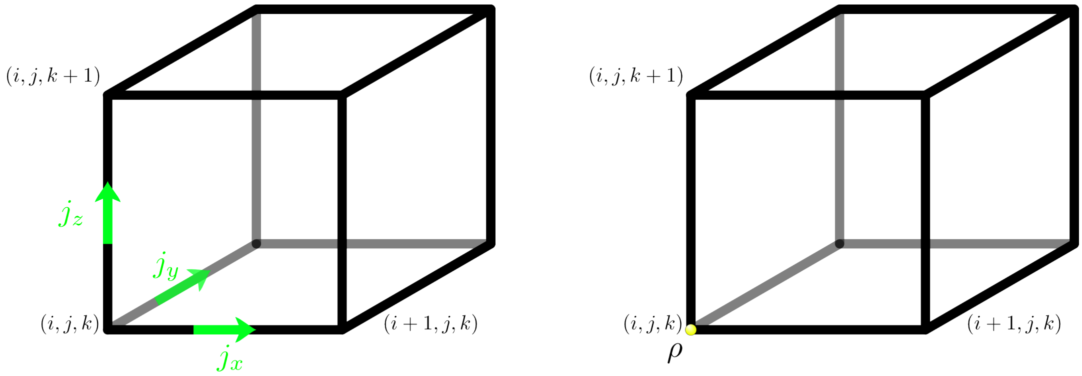

(c) current density **(d)** charge density

Fig. 3.2: Positions of the field and current density vectors and the charge density inside a grid cell according to the Yee scheme. Components of the electric field vector $\boldsymbol{E}$ point along the edges of the cell and are located in the middle of each edge (panel a). The components of the magnetic field vector $\boldsymbol{B}$ are shifted by half a cell width in each direction relative to the electric field. This means that the components of $\boldsymbol{B}$ are face centered, as depicted in panel b). The current density vector $\boldsymbol{j}$ is treated like the electric field and its components also point along the edges of the cell (panel c). The charge density ρ is scalar and can simply be stored at the origin of the cell. Figures taken from Kilian (2015).

the electric field can be approximated by

$$\frac{\partial \boldsymbol{E}}{\partial t} \simeq \frac{\boldsymbol{E}^{t+1} - \boldsymbol{E}^{t}}{\Delta t}. \tag{3.9}$$

The time derivative of the magnetic field can be reformulated in the same manner. To solve the coupled differential equations for the electric and magnetic fields, it is convenient to calculate the magnetic field with an offset of $\Delta t/2$ relative to the electric field, corresponding to a *leap frog* scheme in time. This yields the update rules for the magnetic and electric field, derived from Eqs. (3.7) and (3.8):

$$\begin{aligned} \boldsymbol{B}^{t+\frac{1}{2}} &= \boldsymbol{B}^{t-\frac{1}{2}} - c\,\Delta t\,\nabla \times \boldsymbol{E}^{t}, && (3.10)\\ \boldsymbol{E}^{t+1} &= \boldsymbol{E}^{t} \quad + c\,\Delta t\,\nabla \times \boldsymbol{B}^{t+\frac{1}{2}} - 4\,\pi\,\Delta t\,\boldsymbol{j}^{t+\frac{1}{2}}. && (3.11) \end{aligned}$$

The length of the time step Δt and the further discretization of the spatial derivatives in the above equations then depend on the exact nature of the field solver that is employed. Kilian (2015, Chapter 5.2.5) lists a number of different field solvers which are implemented in ACRONYM. For the sake of brevity only the most basic scheme will be presented here, namely the Yee scheme, which was mentioned in the previous section and which is also the standard method in the ACRONYM code.

As an example the curl of the electric field is considered. Starting with the x-component of the curl the derivatives are replaced with central differences. The x-component of the curl of the electric field at the numerical coordinate $(i, j+\frac{1}{2}, k+\frac{1}{2})$ would be

$$(\nabla \times \boldsymbol{E})_{x,(i,j+\frac{1}{2},k+\frac{1}{2})} \simeq \frac{E_{z,(i,j+1,k)} - E_{z,(i,j,k)}}{\Delta x} - \frac{E_{y,(i,j,k+1)} - E_{y,(i,j,k)}}{\Delta x}, \tag{3.12}$$

where Δx is the edge length of a grid cell or the *grid spacing*. The other components of the curl can be calculated equivalently. Note that the individual components are located at the face centers of the grid cell and point (anti-) parallel to the components of the magnetic fields, which was the reason for the initial construction of the Yee lattice.

In a similar manner the curl of the magnetic field can be computed:

$$(\nabla \times \boldsymbol{B})_{x,(i+\frac{1}{2},j,k)} \simeq \frac{B_{z,(i,j,k)} - B_{z,(i,j-1,k)}}{\Delta x} - \frac{B_{y,(i,j,k)} - B_{y,(i,j,k-1)}}{\Delta x}, \tag{3.13}$$

where the components of the curl of the magnetic field are positioned at the same place as the corresponding component of the electric field.

Inserting Eqs. (3.12) and (3.13) into Eqs. (3.10) and (3.11) yields the update rules for the electric and magnetic fields (see Ganse, 2012, Chapter 4.2.1). This method is second order accurate and conserves the divergence of the magnetic field, i.e. if $\nabla \cdot \boldsymbol{B} = 0$ was satisfied at the beginning it will stay like this for the rest of the simulation. The maximum length of the time step is (Vay et al., 2011)

$$\Delta t_{\mathrm{Yee}} < \sqrt{\frac{1}{3}}\,\frac{\Delta x}{c}, \tag{3.14}$$

where the speed of light c is assumed to be the maximum velocity at which signals (i.e. waves or particles) can propagate.

The Yee scheme is simple to understand and implement. It is therefore used as the default in the ACRONYM code. However, it is not perfect and leads to nonphysical dispersion relations for wave modes propagating parallel to one of the grid axes. For large wave numbers, i.e. small wavelengths, the group velocity decreases and is reduced to zero when the wavelength is of the order of the grid spacing. This phenomenon is discussed in more detail by Vay et al. (2011) and Kilian (2015), who also give a modified dispersion relation which matches the simulated dispersion characteristics. Waves propagating along the space diagonal are not affected by this effect, which leads to an artificially introduced anisotropy in space.

More complex field solvers can be developed to make the simulation more accurate. Methods of higher order, as well as the *nonstandard finite differences* (*NSFD*) schemes by Cole (2002) and Kärkkäinen et al. (2006) are available, but will not be discussed here (see Vay et al., 2011; Kilian, 2015). Especially the NSFD schemes are interesting. A method named *CK5* (after Cole, 2002; Kärkkäinen et al., 2006), which uses not only four, but 36 field components with different weighting to compute the curl of a field, is optimized towards an isotropic representation of field propagation. Compared to the Yee scheme this method is slightly more expensive in terms of numerical effort, but in exchange the time step may be longer:

$$\Delta t_{\mathrm{CK5}} < \sqrt{\frac{5}{6}}\,\frac{\Delta x}{c}. \tag{3.15}$$

3.2.3 Form Factors

The current density $\boldsymbol{j}$ enters Eq. (3.8) as a source term. Therefore it must be obtained from the motion of the individual macro particles and stored on the grid. For doing so it is important to define which particles will contribute to the current density in a given grid cell. This is done with the help of the *form factor*, introduced in Eq. (3.2).

Consider a macro particle as a cloud of physical particles. The form factor then describes the extent of the cloud and the particle density profile therein. If the cloud overlaps one or more grid points then these grid points will be affected by the macro particle. The shape and size of the form factor therefore also determine the accuracy of the calculation of the current densities.

Hockney and Eastwood (1988) discuss three common form factors, namely *nearest grid point* (*NGP*), *cloud in cell* (*CIC*), and *triangular shaped cloud* (*TSC*). With the NGP method the macro particle is represented by a delta function in space. It only affects one grid cell, i.e. if the particle leaves one cell and enters another a sharp, discontinuous decrease or increase of the current densities in both cells is caused. The discontinuities in the current density lead to a high level of noise in the electromagnetic fields (see e.g. Ganse, 2012, Chapter 4.3 for example simulations). Also, the particles are essentially quadratic in shape, which leads to a loss of isotropy, because a movement of the particle parallel to one of the grid axes affects the grid differently than a movement in a diagonal direction, as Kilian (2015, Chapter 5.2.2) points out.

The CIC form factor – as introduced by Birdsall and Fuss (1997), for example – models the macro particle as a cloud with constant particle density and the volume of one grid cell. The macro particle can overlap with up to two cells along each of the grid axes. These cells are affected by the particle and the contribution to the current density in each cell scales linearly with the overlap. Compared to NGP the numerical noise drops by one order of magnitude, because jumps in the current density due to a particle propagating into a neighboring cell are flattened.

A cloud with a width of two grid cells and a triangular density profile is described by the TSC scheme. The density is zero at the edges of the cloud and linearly increases towards the center. A macro particle with a TSC form factor overlaps three grid cells along each axis. The contribution to the current density in a cell changes smoothly with the fraction of the particle overlapping the cell. This can be modeled with a *weighting function* which is composed of three parabolic parts. The TSC form factor improves energy conservation in the simulation and is often employed in PiC codes as a compromise of numerical accuracy and computational effort.

Form factors describe the shape of the macro particle, whereas the contribution of a particle to the current density in each cell is defined by the weighting function. Mathematically the weighting function is the convolution of the form factor (describing the macro particle) and a rectangle function (describing the volume of the grid cell). Starting from NGP, the next higher form factor has always the shape of the weighting function of the previous one (see figures in Kilian, 2015, Chapter 5.2.2). In principle, this procedure can be repeated to obtain more complex form factors than TSC. However, this quickly increases the computational effort, whereas the numerical accuracy improves only slowly. Therefore, a balance between accuracy and effort has to be found (in the case of the ACRONYM code the TSC scheme is used by default).

The form factor is needed twice: First, the current density has to be collected from the particles and interpolated onto the grid. Secondly, the electromagnetic fields at different grid points have to be interpolated to the positions of the particles to calculate the Lorentz force. Birdsall and Fuss (1997) note that nonphysical self-forces (e.g. particles being accelerated by their own electric field) can be avoided, if the same form factor is used for both the interpolation of the current density onto the grid and the interpolation of the electromagnetic fields to the position of the particle. If different form factors are employed in the two interpolation steps, the field strengths may increase exponentially, if a lower order form factor is used for current deposition than for field interpolation. In the opposite case the electromagnetic fields will perform harmonic oscillations, which is much less fatal for the simulation (Hockney and Eastwood, 1988).

3.2.4 Current Deposition

To calculate the current density created by a moving particle, the macro particle's velocity can be multiplied by its charge. Then the current has to be weighted according to the form factor S of the macro particle and deposited on the affected grid points (Kilian, 2015, Chapter 5.2.4):

$$\boldsymbol{j}\big(\boldsymbol{R}_{(i,j,k)}\big) = \sum_n w_n \, q_\alpha \, \boldsymbol{v}_n \, S\big(\boldsymbol{r}_n - \boldsymbol{R}_{(i,j,k)}\big), \tag{3.16}$$

where $\boldsymbol{R}_{(i,j,k)}$ are the coordinates of the grid point and $\boldsymbol{r}_n$ are the coordinates of the macro particle n with velocity $\boldsymbol{v}_n$, macro factor w_n, and charge q_α according to its species α. This procedure is depicted in panel a) of Fig. 3.3.

The problem of this method is that the resulting current density on the grid does not satisfy the continuity equation, leading to the generation of nonphysical electric fields. In principle, this can be avoided by solving Poisson's equation in each time step to correct the electric field. However, it is also possible to resort to a more complex scheme for the deposition

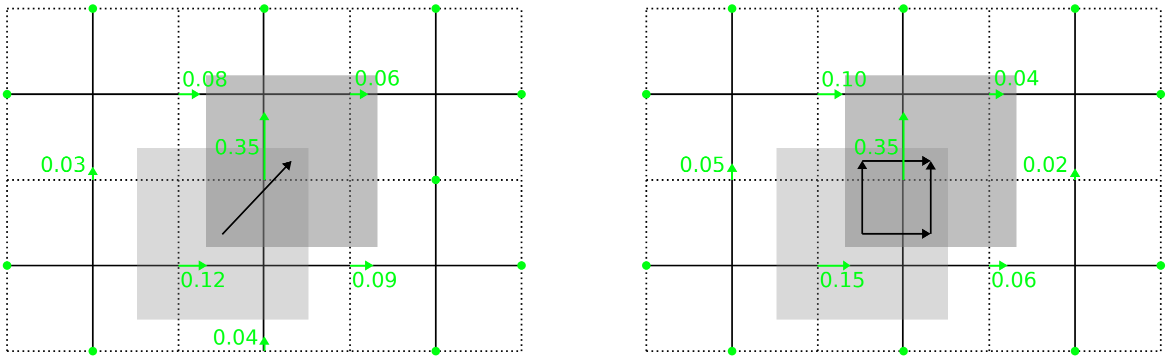

(a) naive method **(b)** method of Esirkepov (2001)

Fig. 3.3: A particle with a certain form factor (gray area) moves through the grid. The borders of the cells are denoted by solid lines, cell centers are connected by dotted lines. In a naive approach to calculate the current density on the grid the direct path between the start and end point of the particle is chosen (panel a). The current is simply calculated from the charge and the velocity of the particle. A more accurate representation of the current density can be obtained by use of the method of Esirkepov (2001), which splits the motion of the particle into components parallel to the grid axes (panel b). Figures taken from Kilian (2015, Chapter 5.2.4).

of the current density on the grid. By default, the ACRONYM code uses the method of Esirkepov (2001), which is briefly summarized below. A much more detailed presentation of the method of Esirkepov (2001), which is (unlike the original publication) mostly consistent with the nomenclature in this work, can be found in Kilian (2015, Chapter 5.2.4).

The method is based on the assumption that the form factor (or the weighting factor) can be decomposed into distinct parts for the different components of the position vector:

$$S(\boldsymbol{r}) = S(r_x)\, S(r_y)\, S(r_z). \tag{3.17}$$

This is the case for all form factors named in Sect. 3.2.3. The current density in each cell is then calculated from the displacement of the charge in the cell between time steps t and $t+1$. The displacement can be obtained from the difference of the shape functions (Ganse, 2012):

$$\begin{aligned} S(\boldsymbol{r}^{t+1}) - S(\boldsymbol{r}^{t}) &= S(r_x^{t+1},\, r_y^{t+1},\, r_z^{t+1}) - S(r_x^{t},\, r_y^{t},\, r_z^{t}) \\ &= S(r_x^{t+1},\, r_y^{t}, r_z^{t}) - S(r_x^{t},\, r_y^{t},\, r_z^{t}) \\ &\quad + S(r_x^{t+1},\, r_y^{t+1}, r_z^{t}) - S(r_x^{t+1},\, r_y^{t},\, r_z^{t}) \\ &\quad + S(r_x^{t+1},\, r_y^{t+1}, r_z^{t+1}) - S(r_x^{t+1},\, r_y^{t+1},\, r_z^{t}). \end{aligned} \tag{3.18}$$

As can be seen from Eq. (3.18) the charge displacement is decomposed into three components parallel to the three grid axes. This also leads to a decomposition of the current density into its components parallel to the axes, as depicted in panel b) of Fig. 3.3, which can be interpreted as splitting the particle's trajectory into a set of three axially parallel lines. The final result is independent of the chosen order of the lines (i.e. the two paths depicted in

Fig. 3.3 b) are equivalent).

3.2.5 Particle Propagation

As for the electric and magnetic fields a leap frog scheme in time is used, which means that the position of a particle is known at time t and updated to time $t+1$, but the velocity used for the update is calculated at time $t+\frac{1}{2}$. With the velocity known at time $t-\frac{1}{2}$ and the Lorentz force $\boldsymbol{F}$, right-hand side of Eq. (2.14), the update rule can be written as

$$\boldsymbol{v}^{t+\frac{1}{2}} = \boldsymbol{v}^{t-\frac{1}{2}} + \Delta t\, \boldsymbol{F}^t / m_\alpha, \tag{3.19}$$

where m_α is the mass of a particle of species α. Suppose the electromagnetic fields are known at time t, the velocity vector must also be known at the same time to calculate the vector product $\boldsymbol{v} \times \boldsymbol{B}$ which enters the Lorentz force. The required velocity can be approximated by

$$\boldsymbol{v}^t = \frac{1}{2}\big(\boldsymbol{v}^{t+\frac{1}{2}} + \boldsymbol{v}^{t-\frac{1}{2}}\big), \tag{3.20}$$

which can be inserted into Eq. (3.19) to yield:

$$\boldsymbol{v}^{t+\frac{1}{2}} = \boldsymbol{v}^{t-\frac{1}{2}} + \frac{\Delta t\, q_\alpha}{m_\alpha} \left(\boldsymbol{E}^t + \frac{\boldsymbol{v}^{t+\frac{1}{2}} + \boldsymbol{v}^{t-\frac{1}{2}}}{2\,c} \times \boldsymbol{B}^t \right). \tag{3.21}$$

The equation above can be solved according to the method suggested by Boris (1970), as described by Penn et al. (2003). This so-called *Boris push* does not push the particle along a straight line between the positions at time t and $t+1$, but splits the movement into two linear parts and one rotation as shown in panel a) of Fig. 3.4. The update of the velocity vector is performed in velocity space, where the acceleration due to the electric field is calculated at first. Half of the acceleration is applied to the velocity vector, corresponding to the acceleration a particle would experience during half a time step. Then the effect of the magnetic field is considered, which rotates the velocity vector without leading to further acceleration. Finally, the other half of the calculated acceleration is applied to the velocity vector, corresponding to the force exerted by the electric field in the second half of the time step.

A graphical representation of the calculations needed for this update scheme are depicted in panel b) of Fig. 3.4. The quantities shown in the figure are defined as follows:

$$\boldsymbol{v}^- = \boldsymbol{v}^{t-\frac{1}{2}} + \frac{\Delta t\, q_\alpha}{2\, m_\alpha}\boldsymbol{E}, \tag{3.22}$$

$$\boldsymbol{\Omega} = \frac{\Delta t\, q_\alpha}{2\, m_\alpha\, c}\boldsymbol{B}, \tag{3.23}$$

$$\boldsymbol{t} = \frac{2\,\boldsymbol{\Omega}}{1 + \boldsymbol{\Omega}\cdot\boldsymbol{\Omega}}, \tag{3.24}$$

$$\boldsymbol{v}' = \boldsymbol{v}^- + \boldsymbol{v}^- \times \boldsymbol{\Omega}, \tag{3.25}$$

$$\boldsymbol{v}^+ = \boldsymbol{v}^- + \boldsymbol{v}' \times \boldsymbol{t}, \tag{3.26}$$

$$\boldsymbol{v}^{t+\frac{1}{2}} = \boldsymbol{v}^+ + \frac{\Delta t\, q_\alpha}{2\, m_\alpha}\boldsymbol{E}. \tag{3.27}$$

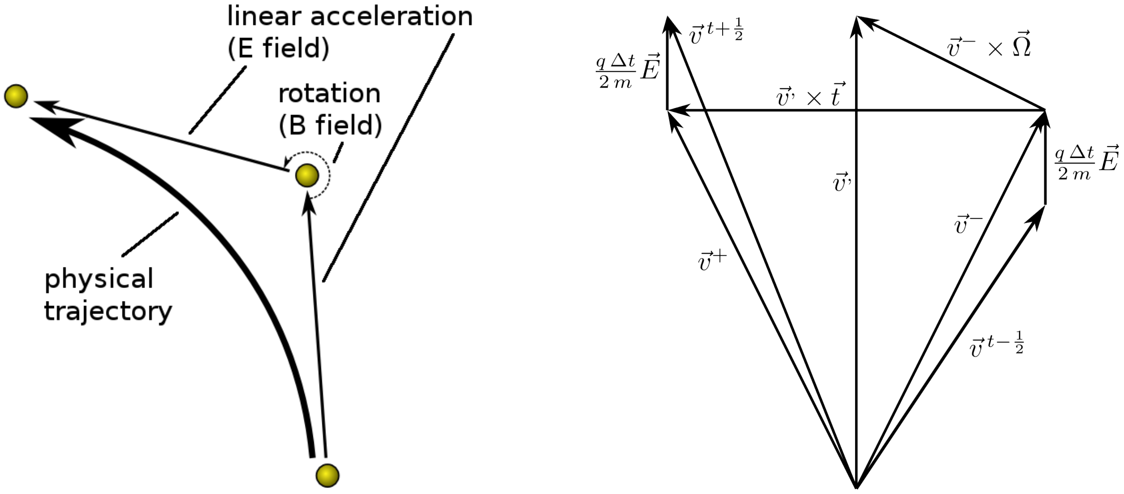

(a) velocity update

(b) exact calculation scheme

Fig. 3.4: The velocity update is performed in three steps, as seen in panel a): First, a linear acceleration phase resolves the effect of the electric field over half of a time step. Then the velocity vector is rotated, depending on the magnetic field. Finally, a second linear acceleration during the second half of the time step is applied. Panel b) depicts the exact update procedures suggested by Boris (1970). The quantities shown are defined in the text. Figures taken from Ganse (2012, Chapter 4.2.2) and Kilian (2015, Chapter 5.2.4).

The Boris push is a very efficient and accurate method to update the velocities of the particles. It is also numerically stable. Increasing the length of the time steps, the modeling of particle gyration becomes less and less accurate and finally undergoes a transition into an adiabatic drift motion. For sufficiently short time steps no problems are encountered. Vay (2008) shows that the Boris push yields accurate solutions even in the case of relativistic particles. However, above a Lorentz factor of $\gamma \sim 1000$ additional corrections are required.

The update of the particle position is simple compared to the update of the velocity:

$$\boldsymbol{r}^{t+1} = \boldsymbol{r}^{t} + \boldsymbol{v}^{t+\frac{1}{2}}\,\Delta t. \tag{3.28}$$

3.2.6 Numerical Limitations

The PiC method is very versatile, because it is basically capable of modeling all physical processes in a collisionless plasma. This is not done by introducing equations which describe macroscopic effects directly, but by correctly reproducing the behavior of individual particles on a microscopic level. All large scale phenomena, like plasma waves, shock fronts, current sheets, etc., emerge from the microphysics of the particles. The treatment of the particles is based only on electromagnetic interactions with the fields, as described above, and therefore relatively robust and fail-safe.

However, to correctly recover the microphysics of the plasma the microscopic or *kinetic length scales* have to be resolved. This means that the grid spacing is of the order of the

Debye length λ_D. In fact, larger cells lead to numerical instabilities (Hockney and Eastwood, 1988) which result in the heating of the plasma until the Debye length matches the cell size. The time step is coupled to the grid spacing via the CFL condition and thus is of the order of λ_D/c, which is a rather small number, considering that λ_D is typically of the order of a few meters in the solar wind (Koskinen, 2011, Chapter 1.2)[25].

These properties become even more problematic if low frequency waves are considered. Such waves typically have long wavelengths, which means that a large simulation box is required anyway. Additionally, a large number of time steps is needed in order to resolve the frequencies of these waves in Fourier space or to allow for a noticeable propagation of the wave during the simulated time. The simulation of low frequency waves is still possible and PiC codes model these waves very accurately. However, it is a very expensive endeavor and one might consider the use of a different numerical scheme, such as the Darwin approximation (Fang et al., 2009) or a hybrid approach (see Kilian et al., 2017, for a comparison of these approaches).

The short length of the time step and the small size of the grid cells allows to simulate plasma volumes which are negligible compared to the extent of the solar wind. Therefore, periodic boundary conditions are often employed in order to represent the fact that the simulated volume is surrounded by plasma with the same physical properties[26]. While this is convenient and simple to implement, it leads to a discretization of the available wavelengths in the simulation. The periodic boundary conditions enforce a periodicity of the electromagnetic field fluctuations, which means that only such waves are realized whose wavelengths correspond to integer fractions of the length of the simulation box along the direction of wave propagation. Wave modes are therefore represented by a finite number of individual waves with discrete wave numbers and frequencies. While these individual waves follow the correct dispersion relations, the energy distribution is not necessarily reproduced physically correct (see Ganse, 2012, Fig. 4.6 for an example).

The discretization of the wave modes requires the simulation box to be sufficiently large in order to achieve a reasonable resolution of wave number space. At the same time the number of particles per cell ("ppc" – "particles per cell") also has to be sufficiently large. One problem is the coverage of velocity space: While the macro particles have a finite size in real space, they are delta-shaped in velocity space (e.g. Birdsall and Langdon, 2005). The phase space density is therefore not continuous and can be interpreted as a number of particle beams, which lead to the excitation of electromagnetic waves, as described by Ganse (2012, Chapter 4.4.1). These electromagnetic waves are the constituents of the permanent background of electromagnetic noise.

A second problem arises from the spatial distribution of the macro particles. As mentioned in Sect. 3.2.3, a moving particle may cause strong fluctuations of the current density (and therefore of the electromagnetic fields) when it enters another cell. By employing large numbers of particles the fluctuations are evened out, which decreases the nonphysical noise in the fields. The field energy of the shot noise created by the macro particles is inversely proportional to the number of macro particles per cell. Therefore, a reduction of the noise level is always connected to a significant increase of the computational cost, which – to first order – is directly proportional to the number of particles in the simulation.

---

[25] However, the choice of an implicit PiC scheme allows for longer time steps (see Kilian, 2015; Kempf, 2016, Chapters 5.5 and 4.5, respectively).

[26] Conducting or absorbing boundaries are also implemented in ACRONYM, as described by Kilian (2015, Chapter 5.2.6).

3.2.7 Parallelization

PiC simulations can rarely be carried out on just a single computer. Due to the high requirements for both memory and processing power, larger machines with multiple CPUs or clusters of computers have to be used. The code has to run in parallel on several CPUs and the individual threads carrying out the computations have to be interconnected to allow for communication. Finally, the results of the simulation have to be written to hard disk, which is also done in parallel, since each thread holds only the information about its part of the simulation. It is a science in its own regard to optimize the parallelization of the code and to allow it to run efficiently even on large supercomputing systems with thousands or tens of thousands of CPUs. In the following a brief overview of a few characteristic features of ACRONYM related to its parallelization is given.

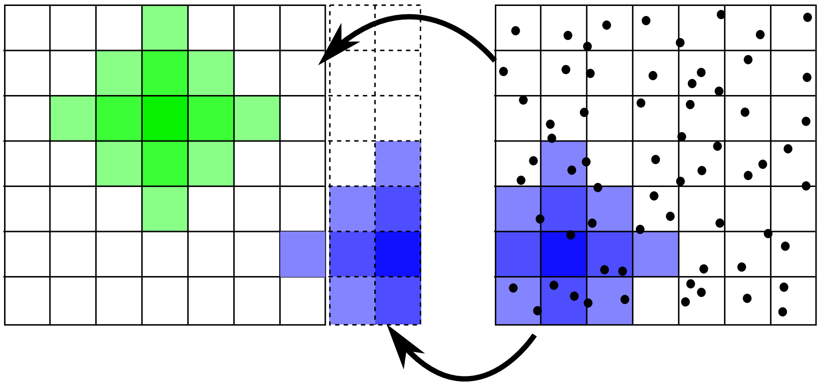

Fig. 3.5: At the beginning of each time step particles that leave a domain are transferred to a neighboring domain. Ghost cells are established at the edges of each domain and initialized with copies of the neighboring domain's electromagnetic fields. Figure taken from Ganse (2009, Chapter 2.1).

Luckily the simulated volume can be subdivided into different smaller domains, since no part of the update routine in each time step requires knowledge of particle positions or field configurations at every point on the grid. Particle and field updates are performed using only local input, where "local" refers to a volume of only a few cells in each direction (typically of the order of the width of the form factor). Therefore, it is possible to compute one time step in a given domain without input from other domains. To correctly treat the boundaries of each domain a number of *ghost cells* is added to that domain, as seen in Fig. 3.5. These ghost cells are supplied with copies of the electromagnetic fields of the neighboring domain. The width of the frame of ghost cells around each domain is determined by the width of the form factor. Ghost cells ensure that particles at the edge of a domain experience the correct Lorentz force generated by the surrounding fields.

Between two time steps neighboring domains may exchange particles that have left one domain and entered another. This is the most critical step when it comes to performance, because the different threads have to communicate and exchange particle data. However, each thread only has to communicate with its direct neighbors, i.e. no global or all-to-all communication is required. Therefore each thread has to transfer data to or receive data from only up to 26 other threads, independent of the total number of threads participating in the simulation. In the ACRONYM code the communication is carried out using the *Message*

Passing Interface (*MPI*).

In certain intervals (or at the end of the simulation) output may be written to hard disk. Particle output is written in parallel using MPI-IO, which leads to a very basic or "raw" data structure, but which can be done very efficiently in terms of output throughput. Other quantities are treated differently. Mainly for diagnostic purposes a simple text output can be written. This output format presents a summary of global quantities, such as total energy, field energy, kinetic energy of the particles, etc., which are calculated directly during runtime and stored as one line of text per output time step.

More complicated quantities, such as the three dimensional field vectors in each grid cell, are written to a single file using the HDF5 library (see Kilian, 2015, Chapter 5.6.4 for details). Different threads can access the output file in parallel and write their part of the data. The HDF5 file contains a pre-defined structure, which basically represents the field data as three-dimensional matrices. This allows for an efficient and intuitive post-processing of the simulation data.

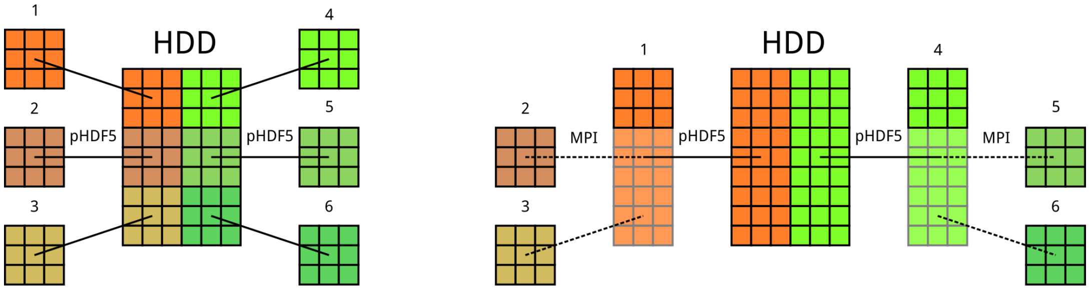

Fig. 3.6: The original output scheme for the electromagnetic fields used in the ACRONYM code had each thread write its own data in parallel to a single HDF5 file (left side). With a number of individual threads in the order of a few thousand this lead to performance losses. A different implementation of the field output has therefore been introduced, where dedicated threads first collect data from neighboring threads and then write the accumulated data to disk. The reduced number of threads accessing the output file in parallel leads to a higher overall throughput of data. Figure according to Kempf (2016, Chapter 4.4).

It has proven to be more efficient to define threads dedicated to field output which then collect field data from surrounding threads before writing to disk (Kempf, 2016, Chapter 4.4). This results in less threads which try to access the HDF5 file in parallel. Previously each thread wrote its own part of the data, but this lead to severe performance problems if several thousand threads were involved. A graphical representation of the old and new output schemes is shown in Fig. 3.6.

A common way to measure the performance of a PiC code is a *weak scaling test*, where the problem size (i.e. the size of the simulation box and the number of macro particles) is increased with the number of parallel threads. Performance can then be measured in particle updates per second, since the computational cost of a simulation mostly depends on the number of particles multiplied by the number of time steps. A high number of particle updates per second is a measure for fast and efficient computation, whereas a linear increase of the updates per second with the number of parallel threads indicates the optimal scaling behavior, i.e. efficient parallelization. ACRONYM has been used on several supercomputing systems and has proven to be well-suited for running on thousands of cores (see e.g. Kempf, 2016, Chapter 4.3).

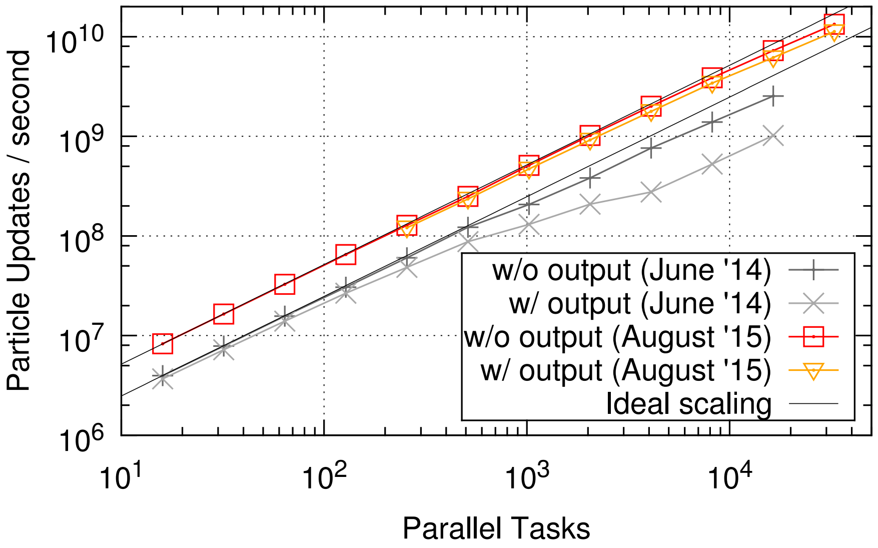

Fig. 3.7: Weak scaling of the ACRONYM code on the SuperMUC system. Test runs with and without field output are shown for two different test periods. During the earlier test period the old output scheme was still in use, which lead to a significant loss of performance if output is enabled (gray lines). With the new routine introduced by Kempf (2016) output is no longer a bottleneck (red and orange lines). The additional performance gain by a factor of two compared to the earlier tests is due to a different choice of the compiler.

Most of the simulations presented in the work at hand have been carried out on the SuperMUC system, the supercomputer hosted by the Leibniz-Rechenzentrum (LRZ) in Garching near Munich (Germany). A scaling graph depicting the performance of ACRONYM on this system is shown in Fig. 3.7. It can be seen that the current version of ACRONYM (scaling tests labeled with “August ’15”) closely follows the ideal scaling behavior, showing noticeable deviations only when more than 10000 parallel threads are employed. The influence of the new output scheme becomes obvious when the orange and the light gray line are compared. Additionally to the improved output an overall boost of performance could be achieved by switching to a different compiler, which increased the number of particle updates per second by a factor of two.

3.3 Extensions to ACRONYM

In the previous section a short overview of the ACRONYM PiC code was given. However, this only described the standard code. For the physical problems addressed in this work some alterations have been made and extensions or additional tools have been developed. These will be described in the following.

3.3.1 Wave Excitation

Initializing a simulation with a thermal particle population leads to the excitation of all possible plasma waves. This is on the one hand caused by grid effects and on the other hand by the relatively small number of macro particles, which leads to noticeable fluctuations in the electromagnetic fields. These fluctuations then relax into physically allowed waves. Waves are generated over the whole frequency and wave number range, with the exception of strongly damped waves which are immediately damped or drowned in particle noise.

If no additional features, e.g. particle beams, are initialized, the simulated plasma establishes an equilibrium state after a few plasma cycles $\tau_\mathrm{p} = 1/\omega_\mathrm{p}$ and no energy is shifted between particles and waves. The spectra $E_E(\omega)$ and $E_B(\omega)$ of the electric and magnetic field energy mainly follow a $1/\omega$ gradient up to very high frequencies where the spectra flatten due to the numerical noise level.

While this can be seen as a “natural background” of waves in a thermal plasma, it does not allow to study the interaction of individual waves and particles or the generation of a turbulent spectrum consisting of Alfvén or whistler waves, for example. Therefore, an additional mechanism to excite specific waves is desirable. Of course, waves can be excited via plasma instabilities which are triggered by a temperature anisotropy (e.g. Gary et al., 2014) or by particle beams (e.g. Che et al., 2014; Skender and Tsiklauri, 2014). However, this method is not very precise in the sense that no single wave with a specific wave number or frequency can be excited directly. Plasma instabilities always yield a spectrum of several waves with different intensities, wave numbers and angles of propagation.

An alternative method is the direct initialization of electromagnetic fields which correspond to the fields of a specific plasma wave. This method has been implemented previously for parallel propagating waves (Schreiner, 2013; Schreiner and Spanier, 2014). The code has then been rewritten to allow for arbitrary directions of wave propagation. This allows to initialize single waves for the detailed study of wave-particle interaction or sets of waves with different wave vectors which form the seed population for a turbulent cascade (e.g. Gary and Saito, 2003; Gary et al., 2012; Chang et al., 2015). The procedure used to excite specific waves during the initialization of the simulation is described in the following.

As mentioned in Sect. 3.2.6, only a finite number of different wave numbers is available in a simulation with periodic boundaries. Therefore, a wave is primarily selected by choosing a suitable wave vector. The wave vector is split into its three components (in a three-dimensional simulation) and each component has to be chosen such that an integer multiple of the corresponding wavelength matches the edge length of the simulation box in the respective direction. It is convenient to introduce the *numerical wave number* k_num:

$$k_\mathrm{num} = \frac{k\,L}{2\,\pi} = \frac{L}{\lambda}, \tag{3.29}$$

where k, L and λ are the wave number, edge length and wavelength (parallel to one axis of the simulation box) in physical units. The numerical wave number therefore is a measure for the wavelength relative to the size of the simulation box which is independent of the physical setup of the simulation.

After all three components of the wave vector and the direction of the background magnetic field are set, the polar and azimuth angles θ and ϕ of the wave vector can be calculated. The general dispersion relation, Eq. (2.39), can then be solved numerically, which produces ten solutions for the frequency ω. Five solutions are negative and therefore discarded immediately, while the other five correspond to solutions on the five dispersion surfaces depicted in Fig. 2.1. The desired frequency is determined by an additional input parameter which selects the correct dispersion surface for the wave that is being initialized.

With the wave vector in polar coordinates and the correct frequency, the polarization state of the wave can be obtained. Equations (2.48) and (2.49) determine the polarization of the electric field by calculating the magnitude of two components of the electric field vector $\boldsymbol{\delta E}$ of the wave relative to the third component. The polarization of the magnetic field vector $\boldsymbol{\delta B}$ is derived via Eq. (2.50), which also yields the ratio $\delta E/\delta B$ of the amplitudes of the electric and the magnetic field. Note that only relative field quantities have been obtained yet. The absolute physical amplitudes are set by another input parameter, which defines either the energy density of the electric or the magnetic field. The components of the field vectors are scaled according to this parameter after their relations towards each other have been set up.

So far the electric and magnetic field vectors $\boldsymbol{\delta E}(\boldsymbol{k},\, \omega)$ and $\boldsymbol{\delta B}(\boldsymbol{k},\, \omega)$ are complex quantities in Fourier space. To obtain real quantities in physical space Eqs. (2.47) and (2.51) are used, where the position vector $\boldsymbol{r}$ is discretized according to the position of the grid cells in the simulation box and the time t is set to zero. This yields spatial fluctuations of the electric and magnetic fields, which are then deployed on the grid.

Note that the initialization method only yields spatial information about the field structure, while information about frequency or the direction of propagation is lost. This has to be compensated by performing an initial adjustment of the particles' velocities before the simulation starts. The electromagnetic fields of the wave influence the motion of the particles, as expressed by Eqs. (2.52 - 2.54). Similar to the electromagnetic fields, a real velocity can be obtained by multiplying the complex velocity vector by $\exp(\imath\, \boldsymbol{k} \cdot \boldsymbol{r})$ and taking the real part of the result. Here, $\boldsymbol{r}$ is the position of the particle. The resulting velocity is added to the random thermal velocity vector of that particle. This step is crucial, because otherwise a series of waves with equal wave numbers, but different polarizations and frequencies may be excited (see Appendix A for an example).

The complete procedure mimics a situation in which a plasma wave is already established in the simulated plasma volume. Within a few plasma cycles an equilibrium state is reached and the wave is conserved over the whole simulation, if it is not damped, or otherwise removed or modified (i.e. by wave-wave interactions). If several waves are desired, the procedure can be repeated with a different wave vector. The resulting electromagnetic fields which are initialized are the superposition of the fields of the individual waves. Similarly, the velocity boost is performed according to the sum of the individual boost velocities for each wave.

As the method described above relies on cold plasma theory, mainly two limitations have to be considered. First, the perturbations, i.e. the amplitudes of the waves, have to be small compared to the background magnetic field B_0. If this is not the case additional wave structures are produced with frequencies and wave numbers corresponding to higher harmonics of the original excitation. Secondly, cold plasma theory does not include wave damping and altered dispersion relations of wave modes near the resonances (see Fig. 2.8). Close to the resonances in a cold plasma the particle velocities resulting from Eqs. (2.52 - 2.54) quickly diverge and lead to strongly relativistic particles. In the current version of ACRONYM this can only be avoided by not exciting waves close to the resonance. Weakly damped waves, however, can be initialized, although their dispersion relation in a warm plasma differs from the cold plasma prediction. An excitation with a slightly offset frequency quickly relaxes into a physically allowed state, i.e. the correct wave in a warm plasma.

3.3.2 Test Particle Populations

In order to study wave-particle scattering, a specific initialization of a test particle population is prepared. By default ACRONYM allows for three particle species (protons, electrons and positrons) and two populations (*background* and *jet*) which can consist of all possible combinations of the particle species. While the background population usually represents a thermal plasma of electrons and protons (or a pair plasma) the jet population is intended to host particles which stream relative to the rest frame of the background plasma. This allows for the simulation of streaming instabilities, for example.

The modified version of ACRONYM used in this work keeps the background population as it is, but changes the characteristics and initialization of the jet population (hereafter referred to as *test particle population*). The new particle population represents a small fraction of the non-thermal energetic particles. This is modeled by reducing the macro factor of the test particles to one. By doing so the test particles have no noticeable influence on the background plasma, even if the ratio of numerical particles $N_\mathrm{t}/N_\mathrm{bg}$ in the test and the background particle population is of the order of unity.

Test particles are initialized as a mono-energetic population, i.e. the particles have the same absolute speed, but their direction of motion is chosen randomly. The speed is calculated from the resonance condition using one of the excited waves in the plasma (see previous section). Solving Eq. (2.131) for the speed of a particle of species α yields:

$$v_\alpha = \left| \frac{k_\parallel\, \omega\, |\mu_\mathrm{res}| \pm |\Omega_\alpha| \sqrt{k_\parallel^2\, \mu_\mathrm{res}^2 + (\Omega_\alpha^2 - \omega^2)/c^2}}{k_\parallel^2\, \mu_\mathrm{res}^2 + \Omega_\alpha^2/c^2} \right| , \tag{3.30}$$

where μ_res is the desired resonant pitch angle cosine. The sign in the numerator changes depending on the polarization of the wave, its direction of propagation, and the particle species[27].

The directions of motion of the bulk of the test particles are chosen at random, using the speed calculated from Eq. (3.30), a random polar angle cosine μ, and a random azimuth angle ϕ. This yields an isotropic distribution of the velocity vectors in μ-ϕ-space. It is convenient to choose an isotropic distribution in $\mu = \cos\theta$ (instead of θ), because the analysis of pitch angle scattering relies on the pitch angle cosine and not on the pitch angle itself.

A fraction of the test particle population is not initialized as described above, but is given a parabolic distribution of polar angle cosines. This is done by assigning

$$\mu = A\,(R + B)^{1/3} - C \tag{3.31}$$

to the particles, where R is a random number between zero and one and A, B, and C are parameters describing the shape of the parabola. The parabolic distribution is required for one of the analysis tools used to study pitch angle scattering (see Sect. 3.4.1). Ivascenko et al. (2016) suggest the use of a half-parabola, i.e. $A = 2$, $B = 0$, $C = 1$ (see Fig. 3.8). However, the implementation in the ACRONYM code also allows for different parameters. The resulting angular distribution of the entire test particle population is, therefore, not entirely isotropic.

The technique described above to create a population of energetic test particles for the

---

[27] In fact, the code just calculates both velocities v_α^+ and v_α^- and checks which one is correct by inserting them into the resonance condition. This avoids a more complicated case-by-case analysis.

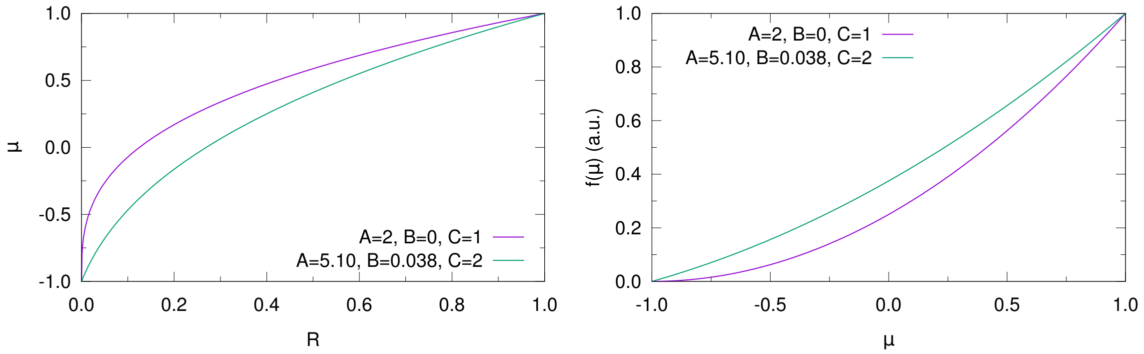

Fig. 3.8: A fraction of the test particle population has their pitch angle cosines assigned according to a parabolic distribution. The left panel shows the assigned pitch angle cosine μ as a function of the random number $R \in [0, 1]$, which is used to generate the distribution. The curves in the left panel follow Eq. (3.31) and employ two sets of parameters A, B, and C, as indicated. The right panel depicts the resulting particle distribution $f(\mu)$ as a function of μ. The purple lines employ the parameters suggested by Ivascenko et al. (2016), whereas the green curves show a possible alternative implementation which can be used in the ACRONYM code. Note that the derivative $df(\mu)/d\mu \neq 0$ over the whole range of pitch angle cosines in the latter case, whereas it becomes zero at $\mu = -1$ when the parameters of Ivascenko et al. (2016) are used.

study of wave-particle scattering was designed for a single plasma wave in the simulation. However, it can also be applied to simulations with several plasma waves. The test particle speed is then calculated using the wave number and frequency of the first plasma wave specified in the simulation's input file.

Especially for the use with simulations of turbulence, another initialization strategy has been implemented. It is expected that turbulence develops from the initial conditions of the simulation, i.e. from a small set of seed waves which interact and start the turbulent cascade. This process takes time and it may be desired to wait until a turbulent cascade is established before the transport of energetic test particles can be studied. Therefore an optional deployment of test particles at later times in the simulation has been introduced. The particles are created at a time step which can be specified in the input file for the simulation and the initialization itself is carried out as described earlier. They can then be tracked for the rest of the simulation.

To efficiently store and post-process the test particle data a new output format has been established. Test particle output is written to HDF5 files and includes the ID number of each test particle (for the tracking of individual particles), the three velocity components and the three components of the local magnetic field at the particle's position in each output time step. The information gathered in the test particle output files could also be obtained from the regular particle and field output, which store (among others) the positions and velocities of all particles and the field configuration in each grid cell, respectively. However, the full particle and field output is more extensive than the test particle output. Therefore, the reduced test particle output is much more efficient both in terms of output performance and disk space requirements. This allows for a higher number of output time steps, i.e. a better time resolution of the test particle data.

Two smaller problems arise from the method of test particle initialization: First, in the current version of the code the test particle speed is determined from the properties of a plasma wave and an input parameter μ_{res}, the latter specifying the resonant pitch angle cosine. It is not possible to define a test particle speed or energy directly, which may be inconvenient in some cases. However, if a specific energy is desired, the matching μ_{res} can be calculated manually from the resonance condition Eq. (2.131) and used as the required input parameter for the simulation. The possibility to directly select a particle energy via a new input parameter is planned for a future version of the code.

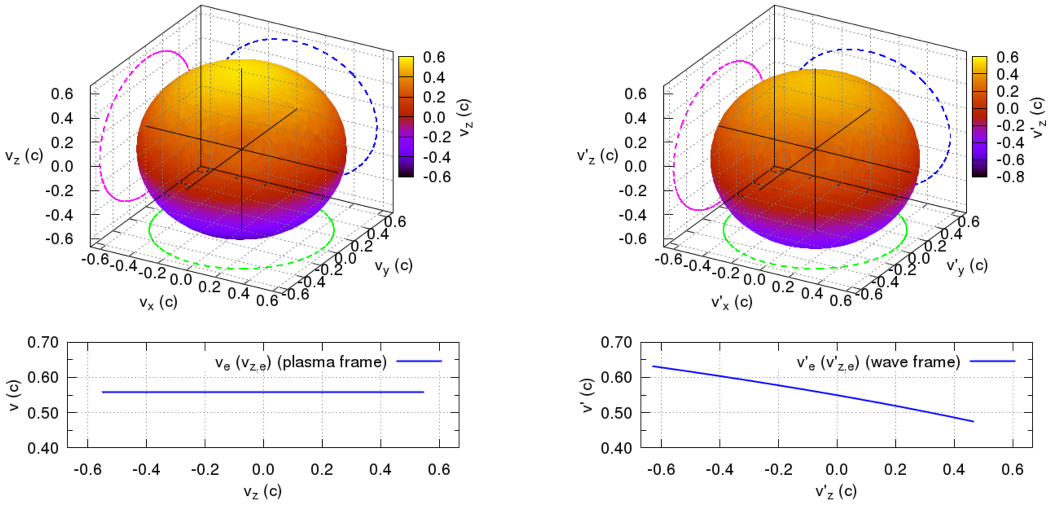

(a) plasma frame

(b) wave frame

Fig. 3.9: Test particle velocity distributions in the rest frames of the plasma (left) and the wave (right). A mono-energetic distribution is initialized in the plasma frame. Boosting into the rest frame of a wave propagating parallel to the background magnetic field $\boldsymbol{B}_0 \,||\, \hat{\boldsymbol{z}}$ results in an energy distribution which becomes a function of the pitch angle cosine μ'. The velocity distribution is boosted anti-parallel to $\boldsymbol{B}_0$, as can be seen in the panels on the right. In the bottom panels the speed $v = |\boldsymbol{v}|$ in the plasma frame ($v' = |\boldsymbol{v}'|$ in the wave frame) is plotted as a function of the parallel velocity component $v_z = v\,\mu$ ($v'_z = v'\,\mu'$).

Secondly, the test particles are initialized as a mono-energetic population in the rest frame of the plasma. If wave-particle scattering is analyzed in the rest frame of the wave, as described in Sect. 2.6.2, the particle population is not mono-energetic in the respective rest frame, as shown in Fig. 3.9. This means that the scattering amplitude in the rest frame of the wave, Eq. (2.142), implicitly becomes a function of the test particle energy $E'_{\mathrm{t}}(\mu')$ which depends on the pitch angle cosine μ'. This is not a problem in itself, but it should be noted anyway.

3.3.3 Magnetostatic Test Particle Code

Especially for the problem of wave-particle scattering a test particle code has been derived from ACRONYM (see Schreiner et al., 2017b, Sect. 3.2). The idea behind this simplified version of the code is to model a system which is as close as possible to the assumptions of the magnetostatic test particle approach described in Sect. 2.6.2.

The test particle code does not include a field solver, i.e. the electromagnetic fields which are initialized at the beginning persist throughout the whole simulation. If a single plasma wave is initialized, this can be seen as being in the rest frame of the wave, where the spatial field fluctuations do not change with time. The electric field is removed, as a transformation into the rest frame of the wave would lead to a vanishing electric field of the wave. The setup for the test particle simulations can therefore be described as "magnetostatic", since only magnetic fields are present, which experience no variations in time.

Because of the absence of a field solver the particles cannot influence the electromagnetic fields. Therefore, the thermal population forming the background plasma can be omitted. As a side effect the initialized magnetic field is not affected by fluctuations caused by the particles, i.e. there is no background noise.

The only particle population which is still of interest consists of the energetic test particles. These particles can propagate through the simulation box and are affected by the magnetic field. Wave-particle scattering is therefore possible, although there is no back reaction of the particles on the wave. The usual test particle output can be written to disk to evaluate the simulations and to study pitch angle scattering.

Artificial Wave Propagation

As an additional option it is possible to include moving waves in a test particle simulation. In this case the setup is not assumed to model the rest frame of the wave, but the rest frame of the thermal plasma. The magnetic and electric fields of the wave (or several waves) are initialized at the beginning of the simulation.

The field solver and the thermal population of particles are omitted, whereby the wave cannot propagate self-consistently. However, it is possible to propagate the wave manually, using the cold plasma predictions for the frequency and the phase speed. For doing so the electric and magnetic fields are deployed on the grid in each time step according to Eqs. (2.47) and (2.51), respectively.

3.4 Analysis Tools

A standard set of analysis tools is available for the ACRONYM code. These tools are mainly meant for the post-processing of simulation data, such as computing the spectral energy densities of the different components of the electromagnetic fields or deriving the plasma temperature from the velocity histograms of the particle data. With the new features introduced in the previous section and with some of the questions in mind, which will be addressed in this work, it is necessary to expand the set of standard tools. In the following two new procedures for the processing of field and test particle data are presented.

3.4.1 Pitch Angle Scattering

Pitch angle scattering is studied by analyzing the behavior of a test particle population (see Sect. 3.3.2). As stated earlier a test particle output format has been established which stores relevant information about the test particles. Each particle has a unique ID number, which makes it possible to track the particle throughout the simulation and to compare a particle's velocity and pitch angle at different points in time.

While the velocity of each particle is stored directly, the pitch angle has to be calculated during post processing. With the velocity $\boldsymbol{v}$ and the local magnetic field $\boldsymbol{B}_{\text{local}}$ at the particle's position the pitch angle can be calculated in two ways. The definition which is typically used describes the pitch angle as the angle between the particle's direction of motion and the background magnetic field $\boldsymbol{B}_0$, as denoted by Eq. (2.117). If not denoted otherwise this definition is used in the work at hand.

As an alternative definition one could define the angle between $\boldsymbol{v}$ and $\boldsymbol{B}_{\text{local}}$, which yields

$$\mu_{\text{local}} = \frac{\boldsymbol{v} \cdot \boldsymbol{B}_{\text{local}}}{|\boldsymbol{v}|\,|\boldsymbol{B}_{\text{local}}|}, \tag{3.32}$$

for the cosine of a *local pitch angle*. This definition might be interesting in the case of high amplitude plasma waves, where $\delta B/B \sim 1$ and the concept of an ordered magnetic field becomes invalid.

Scattering amplitudes of the individual particles can be expressed by Eq. (2.139), where the change of the pitch angle $\Delta\mu(t)$ is expressed as the difference of the pitch angles $\mu(t)$ at the current point in time and μ_0 at the beginning of the simulation. Similarly, a mean pitch angle $\bar{\mu}(t) = (\mu(t) + \mu_0)/2$ can be defined for each particle. These quantities can be calculated for all particles at each output time step. Collecting the data of the individual particles in bins of $\bar{\mu}$-$\Delta\mu$-phase space allows to study the behavior of the test particle population statistically. The binned data can be plotted as a scatter plot which then shows the particle density in $\bar{\mu}$-$\Delta\mu$-phase space. The shape of the particle distribution in phase space can be directly compared to the predictions of the analytical model described in Sect. 2.6.2. This is useful to evaluate simulation results and to check for deviations of simulation data from the predictions of the simplified QLT model, which might hint at physical processes in the simulation which are not recovered in the model.

The analysis tools needed are relatively simple and fail-safe. Basically one only needs to sort the test particle data and build histograms, which are then plotted together with the analytical predictions discussed in Sect. 2.6.2 [28]. The same procedure can also be used to investigate momentum scattering.

Alternatively the statistical properties of the test particle population can also be used to derive the pitch angle scattering coefficient $D_{\mu\mu}$. For doing so the pitch angle cosines have to be calculated and the particle data has to be sorted in a one-dimensional histogram to obtain the particle number per pitch angle bin for each time step. The pitch angle diffusion coefficient can then be computed using the methods described by Ivascenko et al. (2016), which will be briefly outlined below.

One requirement for the use of the methods of Ivascenko et al. (2016) is that the particle distribution $f(\mu)$ and its derivative with respect to μ are nonzero over the whole range of pitch angle cosines, i.e. $f(\mu) \neq 0$ and $df(\mu)/dt \neq 0$. Therefore, the parabolic pitch angle distribution has been implemented for the initialization of test particles, as described in Sect. 3.3.2.

The diffusion coefficient is calculated from a simplified Fokker-Planck equation, Eq. (2.129), where pitch angle diffusion is assumed to be the only relevant diffusion process:

$$\frac{\partial f_\alpha}{\partial t} - \frac{\partial}{\partial \mu} D_{\mu\mu} \frac{\partial f_\alpha}{\partial \mu} = 0. \tag{3.33}$$

---

[28] Finding the correct analytical model is the most tricky part here.

This equation can be rewritten to yield

$$\frac{\partial f_\alpha(\mu,t)}{\partial t} = \left(\frac{dD_{\mu\mu}(\mu)}{d\mu}\right)\frac{\partial f_\alpha(\mu,t)}{\partial \mu} + D_{\mu\mu}(\mu)\,\frac{\partial^2 f_\alpha(\mu,t)}{\partial \mu^2}, \tag{3.34}$$

which can be solved numerically for $D_{\mu\mu}$ after discretizing μ and t. To reduce the noise and recover the relevant features in the resulting $D_{\mu\mu}$ Ivascenko et al. (2016) suggest to smooth the data via low-degree polynomial fits using the method of Savitzky and Golay (1964).

The second method described by Ivascenko et al. (2016) is based on integrating Eq. (3.33) over μ, which yields the pitch angle current j_μ:

$$\int_{-1}^{\mu} \mu\,\frac{\partial f_\alpha(\mu,t)}{\partial t} = D_{\mu\mu}(\mu)\,\frac{\partial f_\alpha(\mu,t)}{\partial \mu} = -j_\mu. \tag{3.35}$$

The diffusion coefficient is then obtained by dividing j_μ by $\partial f_\alpha / \partial \mu$.

Both methods do not rely on QLT assumptions, i.e. on the assumption of $\delta B/B_0 \ll 1$. However, since the change of the particle distribution is analyzed in pitch angle space, a noticeable change of $f_\alpha(\mu)$ is required for the methods to yield results. The effect of waves with very low amplitudes, which cause particle scattering, but do not lead to a change of $f_\alpha(\mu)$, should therefore be studied with different methods, such as the calculation of a running diffusion coefficient (Ivascenko et al., 2016).

3.4.2 Measuring Damping Rates

The interaction of plasma waves and particles leads to a transfer of energy in certain wave number and frequency regimes. Resonances of waves and particles cause the damping of waves and an increase of the particle energy, leading to plasma heating. While these processes can be described theoretically and damping rates can be calculated from the dispersion relations in warm plasmas (see Sect. 2.4.2) it is also interesting to investigate whether wave damping is correctly modeled in the simulations. To do so the effect of wave damping has to be quantified and extracted from simulation data. However, other than the frequency or wave number, which can be obtained directly by Fourier transforming field data in space and time, the damping rate cannot be recovered so easily.

The different contributions to the total energy content of the simulation are calculated during runtime and can be stored in regular output intervals. The time evolution of the energy composition then can give first hints at the physical processes in the simulation. However, it is generally not possible to distinguish between different processes or to relate a change in field energy to the damping of a specific wave mode, for example.

In the following a method is described which allows to extract the damping rate of individual waves from the dispersion relations obtained from the field data of a simulation. This method is similar to the procedure described by Koen et al. (2012), who measure the growth rates of different wave modes in a simulation of plasma instabilities triggered by the interaction of several populations of electrons. Their technique is based on the energy density $W(k,\omega)$ of the electromagnetic fields in Fourier space, which allows them to relate features in k-ω-space to specific wave modes. An equivalent approach is used by Schreiner et al. (2017a) for the study of cyclotron damped Alfvén and proton cyclotron waves. This approach is summarized below.

Test Simulation Setup

For a more demonstrative description of the procedure to obtain the damping rate two example simulations are set up. These three-dimensional simulations use the ACRONYM PiC code and the method to excite plasma waves described in Sect. 3.3.1. Both simulations employ the parameter set provided in Tables 3.1 and 3.2. The difference between the simulations lies in the excitation of waves: The first simulation contains five excited waves at odd numerical wave numbers $k_\mathrm{num} \in \{1, 3, 5, 7, 9\}$ along the dispersion relation of the Alfvén branch, the second simulation contains the same number of waves, but at even $k_\mathrm{num} \in \{2, 4, 6, 8, 10\}$. This way it can be checked if the energy of each wave is confined in the respective wave number bin in the dispersion plots (see Fig. 3.10). Similar to the numerical wave number which was introduced in Eq. (3.29) a numerical frequency can be defined:

$$\omega_\mathrm{num} = \frac{\omega\, T}{2\,\pi}, \tag{3.36}$$

where $T = N_t\,\Delta t$ is the physical duration simulated and N_t is the number of time steps with length Δt in the simulation. The advantage of k_num and ω_num is that the values of these quantities directly reflect the position of the respective wave number or frequency bin in the dispersion plots (i.e. $\omega_\mathrm{num} = 0$ refers to the lowest frequency bin).

$\omega_\mathrm{p,e}\,(\mathrm{rad\ s^{-1}})$	$\lvert\Omega_\mathrm{e}\rvert\,(\omega_\mathrm{p,e})$	$v_\mathrm{th,e}\,(c)$	$\delta B\,(B_0)$
$2.00 \cdot 10^{8}$	$4.40 \cdot 10^{-1}$	$5.00 \cdot 10^{-2}$	$5.00 \cdot 10^{-3}$

Table 3.1: Physical parameters for the example simulations: plasma frequency $\omega_\mathrm{p,e}$, cyclotron frequency Ω_e, and thermal speed $v_\mathrm{th,e}$ of the electrons, as well as the amplitude δB of the waves' magnetic fields.

$N_\parallel\,(\Delta x)$	$N_\perp\,(\Delta x)$	$N_t\,(\Delta t)$	$\Delta x\,(c\,\omega_\mathrm{p,e}^{-1})$	$\Delta t\,(\omega_\mathrm{p,e}^{-1})$	$m_\mathrm{p}\,(m_\mathrm{e})$	ppc
1200	64	50000	$3.53 \cdot 10^{-2}$	$2.04 \cdot 10^{-2}$	40.0	128

Table 3.2: Numerical parameters for the example simulations: number of cells $N_\parallel$ and $N_\perp$ in the directions parallel and perpendicular to the background magnetic field, number of time steps N_t, grid spacing Δx, time step length Δt, (artificial) proton mass m_p, and ppc, i.e. the number of particles (electrons and protons combined) per cell.

Measuring Procedure

To be able to obtain the damping rates of the excited waves the electromagnetic fields in the simulations have to be Fourier transformed in time and space. An example of one of the resulting dispersion relations is shown in Fig. 3.10 a). As can be seen the frequency regime of the Alfvén / proton cyclotron mode is hardly resolved. However, the energy of the excited waves is located at the expected positions (darker spots at odd k_num along the bottom of the image).

Figure 3.10 a) contains data from the whole simulation, i.e. all time steps have been considered. Therefore, the resulting energy distribution in k-ω-space can be seen as a time

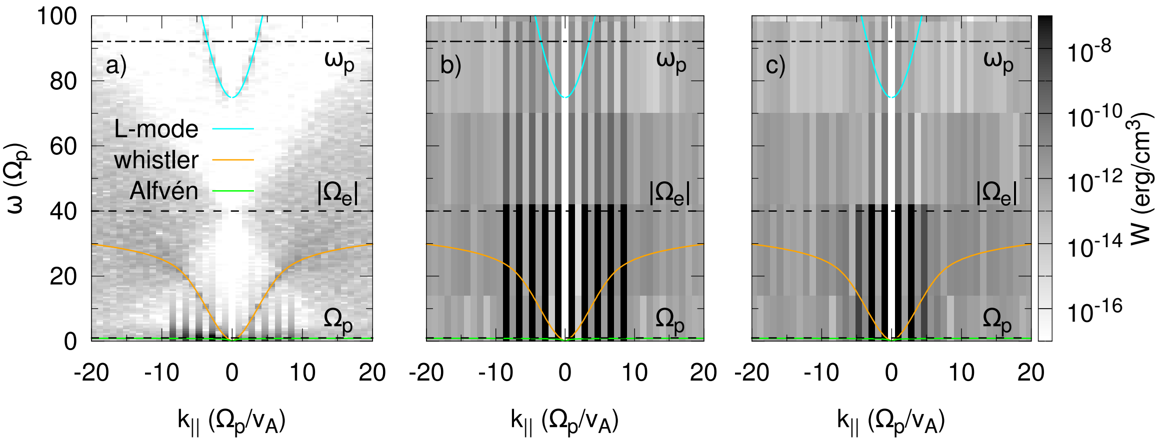

Fig. 3.10: Dispersion plots obtained from the data of a component of the magnetic field perpendicular to $\boldsymbol{B}_0$. The left panel contains data from the whole simulation, the center and right panels show Fourier transformed data from a shorter interval in time (i.e. less time steps). While this drastically reduces the frequency resolution, it yields insights into the time evolution of the energy density: The excited waves (dark spots at odd k_{num}) contain large amounts of energy at the beginning of the simulation (center), but lose energy over time due to cyclotron damping. This results in noticeably less field energy towards the end of the simulation (right). Note that only five waves at positive $k_\parallel$ have been excited. However, since the frequencies of the waves are not resolved, the energy density of the waves is mapped to the lowest frequency bin $\omega_{\mathrm{num}} = 0$. This refers to static field fluctuations, so all information about the propagation of the waves is lost and the waves are depicted both at positive and negative $k_\parallel$. The increased energy density in other frequency bins (e.g. $\omega_{\mathrm{num}} = 1$) is caused by the windowing function used for the Fourier transformation. Figure according to Schreiner et al. (2017a).

average over the entire simulated time span. Similarly, averages over shorter periods of time can be obtained by selecting only the field data from the respective time steps. Fourier transforming the field data from a shorter interval of time leads to a reduced frequency resolution in the dispersion plots. This can be seen in Fig. 3.10 b) and c), where intervals of equal lengths at the beginning and at the end of the simulation have been used. Although the frequency resolution in these images does not allow to distinguish wave modes, the energy of the excited waves is still located in the correct wave number bins[29].

However, with the loss of frequency resolution one gains insight into the time evolution of the energy distribution. Whereas the energy density of the excited waves is high at the beginning (Fig. 3.10 b), it has significantly decreased towards the end of the simulation (Fig. 3.10 c). By separating the simulation data into intervals of equal length and Fourier transforming the data from each interval one can obtain a time line of the energy density in k-ω-space. The energy density of each excited wave can be determined by selecting the appropriate wave number bin, which yields the energy density $W(k, t)$ as a function of the wave number and time. Note that the total energy density of the electric and magnetic

---

[29] The broadening in frequency space is a result of the windowing function used for the Fourier transformation in time and is not related to the physical properties of the waves of the simulation.

fields has to be calculated by adding up the energy densities of all the different components of both fields.

For a decaying wave a time dependent amplitude $A(t)$ is expected:

$$A(t) \propto \exp(\Gamma\, t), \tag{3.37}$$

which leads to a decay of the energy density:

$$W(t) \propto A^2(t) \propto \exp(2\,\Gamma\, t), \tag{3.38}$$

where Γ is the *damping rate*. The energy density measured from the simulation data is expected to behave as described by Eq. (3.38). The damping rate of a wave can therefore be obtained by fitting an exponential function to the data.

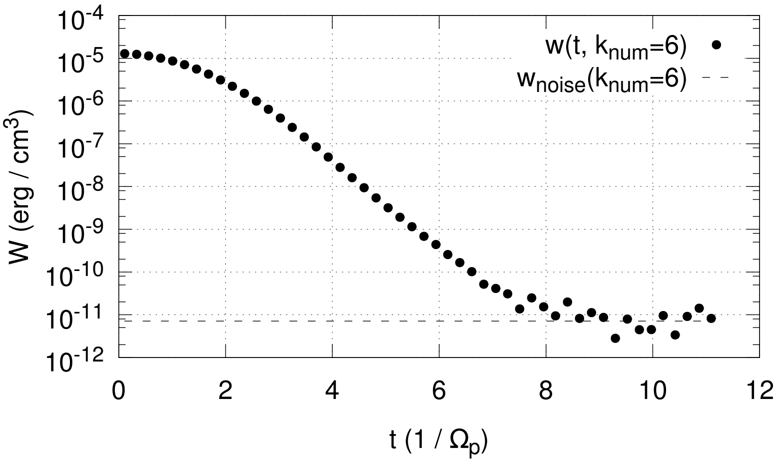

Fig. 3.11: Time evolution of the energy density W of a single damped wave. The energy of the wave begins to decrease slowly, but establishes the expected exponential decay after a few proton cyclotron time scales. The exponential decay comes to a halt when the level of the background noise is reached (dashed line) and no further energy can be extracted from the wave. Figure taken from Schreiner et al. (2017a).

However, this is not exactly the case, as Fig. 3.11 shows. Three distinct phases exist: At the beginning of the simulation the energy of the damped wave decays slower than expected. This regime transits into a phase of exponential decay, as expected from theory. Finally, the energy density of the damped wave reaches the level of the background noise in the simulation. At this point no further energy is extracted and the energy density stays at a constant level (with small fluctuations).

By selecting only the interval in which the energy density decays exponentially an exponential fit can be applied to the data (see Fig. 3.12 a). This step has to be repeated for all excited waves in both simulations to obtain the damping rates $\Gamma(k_\parallel)$ of each wave. The damping rates can then be plotted over the parallel wave number $k_\parallel$ and compared to the predictions of warm plasma theory using Eqs. (2.81) and (2.82). This is shown in Fig. 3.12 b) for the data from the example simulations. To better compare the measured damping rates $\Gamma(k_\parallel)$, which are only obtained at distinct wave numbers, to the theoretical prediction a fit can be applied to the data. Li et al. (2001) suggest a relatively simple analytical function with three fit parameters, which has already been introduced in Eq. (2.92) in Sect. 2.4.2. This fit is also presented in Fig. 3.12 b).

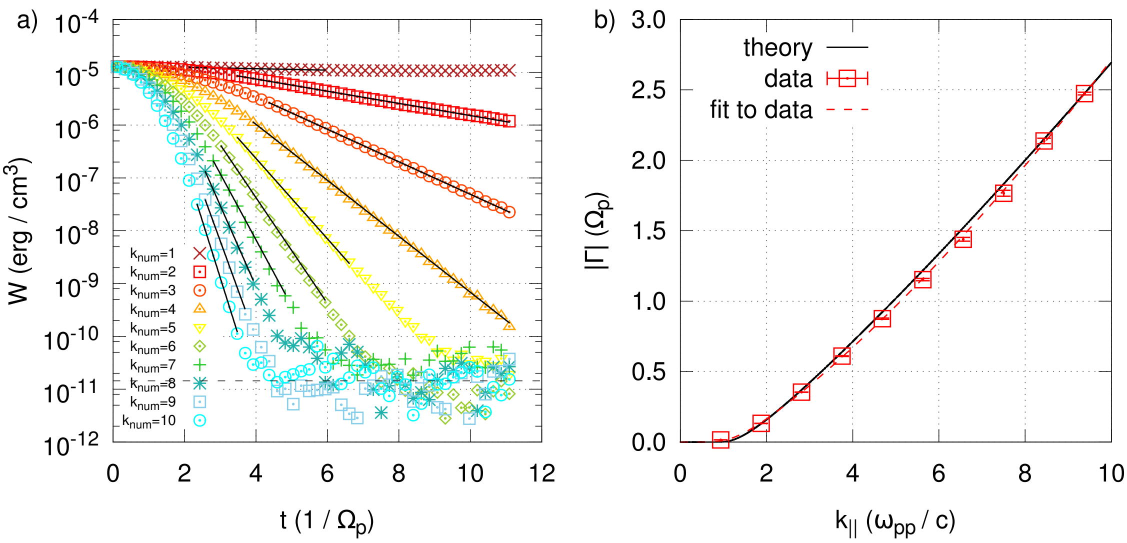

Fig. 3.12: The left panel depicts the time evolution of the energy densities of the ten excited waves in the two test simulations. Solid black lines show the exponential fits to the data of the individual waves. The dashed black line marks the level of the background noise. The damping rates of the different waves, which are derived from the exponential fits, are plotted over the parallel wave number in the right panel. Error bars represent statistical errors from the fits and are hardly visible in most cases. The solid black line shows the predicted damping rate from warm plasma theory, whereas the dashed red line is a fit to the data according to the model of Li et al. (2001). Figure taken from Schreiner et al. (2017a).

The demonstration of the method to measure damping rates from simulation data shows that it is not necessary to resolve the frequencies of the damped waves. The results which are obtained from the measurements and are presented in Fig. 3.12 show good agreement with the theoretical prediction. Schreiner et al. (2017a) also show that a different method, namely the fitting of Lorentzian profiles to the energy density $W(\omega)$ in frequency space, yields significantly worse results if applied to the same data. The method described above is therefore a helpful tool to investigate wave damping in a simulation, since it mainly relies on measuring the energy density in a specific wave number bin instead of a frequency bin. This is an important advantage, since the frequencies of low frequency waves which are affected by damping are typically not well resolved in PiC simulations.

4 Results

4.1 Observation of Cyclotron Damping in PiC Simulations

As pointed out in Sect. 2.5, the damping of waves is an important element of the kinetic regime of plasma turbulence. Kinetic processes and the onset of damping lead to a steepening of the turbulent energy cascade and, ultimately, to its exponential cutoff. In order to simulate turbulence self-consistently, it is therefore unavoidable to consider wave damping and its effect on the plasma. Knowing the length scales on which damping occurs helps to estimate what the turbulent cascade will look like (e.g. in terms of its extent in wave number space) and which parameters have to be chosen for a simulation to recover a certain regime (i.e. parts of the inertial range and the transit into the dissipation range).

Damping is also of interest if the transport of energetic particles is considered. Particles of a given energy can only interact with waves in specific frequency and wave number regimes. The resonance condition provided by Eq. (2.131) states that high energy particles can interact with waves at smaller frequencies and wave numbers, whereas low energy particles can only resonate with waves at higher frequencies, which are often in the dispersive or dissipative regime of the wave's dispersion relation. To make sure that particles can actually resonate with a wave it is therefore important to consider if the wave is damped, as strong damping might lead to the decay of the wave before a resonant interaction can take effect (see e.g. Schreiner and Spanier, 2014, Fig. 2).

It is often claimed that PiC codes are able to recover all physical phenomena in a collisionless plasma, especially including kinetic effects such as wave damping. However, none of the physical processes are actually included in a PiC code in the sense that they are directly implemented or modeled by specific equations. They all result from the self-consistent simulation of electromagnetic interactions of individual particles. It is therefore necessary to investigate if physical phenomena, which emerge from the collective behavior of the whole particle population, are represented physically accurate, or if they are distorted by numerical effects.

In the following a study is presented which analyzes cyclotron damping of low frequency waves in detail. Cyclotron damping can be easily modeled using parallel propagating, circularly polarized waves, namely Alfvén / proton cyclotron waves and whistler / electron cyclotron waves. As the names suggest, these waves each interact only with one particle species. Thus, damping can be evaluated in two ways: First, the loss of electromagnetic field energy can be measured. Secondly, a gain of kinetic energy of a single particle species can be observed.

At least some mechanism which damps parallel propagating waves near the cyclotron frequencies of electrons and protons is found in PiC simulations. The spectral energy distributions $E_{E_\perp}(k_\parallel, \omega)$ and $E_{B_\perp}(k_\parallel, \omega)$ of the electric and magnetic field components perpendicular to the background magnetic field $\boldsymbol{B}_0$, i.e. the transverse field components of a parallel wave, clearly show the dispersion relations of the Alfvén and whistler branches. However, these branches do not extend to the respective cyclotron frequencies of electrons and protons, but already vanish at lower frequencies, as shown in Fig. 4.1 for the whistler mode. The frequencies at which the branches vanish coincide with the borders of triangular shaped regions with higher energy density. These regions can be accurately described by the resonance condition for cyclotron damping provided by Gary and Nishimura (2004), as presented in Eqs. (2.86) and (2.90). This suggests that cyclotron damping is, at least qualitatively, realized in PiC simulations.

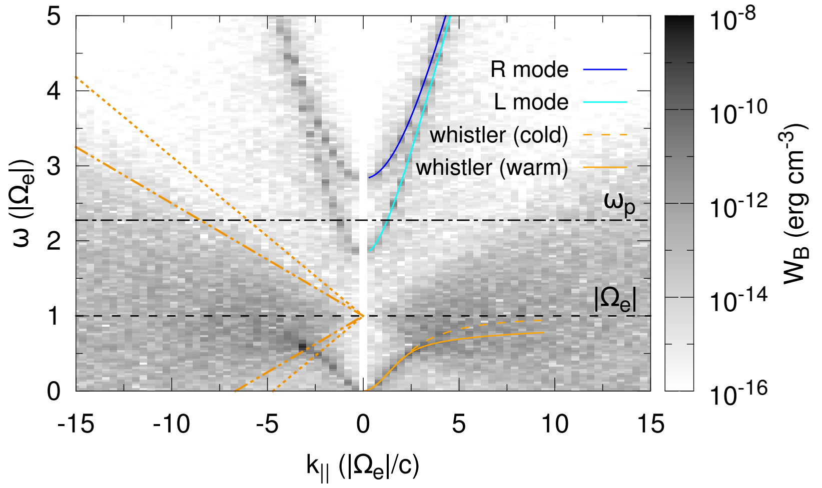

Fig. 4.1: Spectral energy distribution $W_{B_\perp}(k_\parallel, \omega)$ of one of the perpendicular components of the magnetic field, corresponding to the transverse magnetic field of parallel propagating waves. The high frequency R- and L-modes are recovered and follow the cold plasma dispersion relation. In the low frequency regime ($\omega < |\Omega_\mathrm{e}|$) the whistler branch is resolved, whereas the Alfvén branch is not visible due to its low frequency. Because of the finite plasma temperature the whistler branch follows the warm plasma dispersion relation, which deviates from the cold plasma prediction. The whistler branch vanishes due to cyclotron damping in the dark, triangularly shaped regimes around $|\Omega_\mathrm{e}|$. The borders of the dark regions are marked by the dotted and dash-dot-dotted lines on the left side of the plot. These lines represent the resonance condition for cyclotron damping from Eq. (2.90) (dotted lines) or an adaption thereof, where the slope corresponds to $3\,k_\parallel\,v_\mathrm{th,e}$ instead of $\sqrt{2}\,3\,k_\parallel\,v_\mathrm{th,e}$ (dash-dot-dotted lines). The latter is in better agreement with the simulation. The dark spot, where the whistler branch intersects the dash-dot-dotted line, represents an excited, weakly damped wave. Figure according to Schreiner et al. (2017a).

For the following quantitative study, which is mainly a reproduction of the results of Schreiner et al. (2017a), the Alfvén branch has been chosen. These waves at lowest frequencies are hardly resolved in the spectral energy distributions which can be obtained from a typical PiC simulation. An accurate comparison of their dispersion relation in the simulation and the theoretical prediction is therefore often not possible. However, despite the additional challenge of under-resolved frequencies, it is possible to measure the damping rates Γ of Alfvén and ion cyclotron waves using the method described in Sect. 3.4.2. Thus, the properties of the wave can be analyzed in terms of $\Gamma(k_\parallel)$ and compared to predictions from warm plasma theory.

Different numerical setups are considered, where the focus lies on the dimensionality of the simulation. Due to the high computational effort of PiC simulations, two- or even one-dimensional setups are often favored, if permitted by the physical problem. Therefore, it is interesting to investigate if the dimensionality of the simulation influences wave dissipation. Furthermore, several sets of physical input parameters for the simulations are considered.

4.1.1 Detailed Study of 3D Simulations

Simulation Setup

Cyclotron damping is studied by exciting several parallel propagating, circularly polarized waves with different parallel wave numbers $k_\parallel$. Waves are chosen to be left-handed, i.e. resonating with the thermal protons in the simulation. The initialization follows the method described in Sect. 3.3.1 and the precise setup of the simulations is the same as the one in the example, which was briefly described in Sect. 3.4.2. The physical and numerical parameters are summarized in Tables 4.1 and 4.2. These tables are the same as Tables 3.1 and 3.2 in Sect. 3.4.2, and are reprinted here for easier reference.

$\omega_{\mathrm{p,e}}\,(\mathrm{rad\ s^{-1}})$	$\lvert\Omega_{\mathrm{e}}\rvert\,(\omega_{\mathrm{p,e}})$	$v_{\mathrm{th,e}}\,(c)$	$\delta B\,(B_0)$
$2.00 \cdot 10^{8}$	$4.40 \cdot 10^{-1}$	$5.00 \cdot 10^{-2}$	$5.00 \cdot 10^{-3}$

Table 4.1: Physical parameters for the simulations of cyclotron damping: plasma frequency $\omega_{\mathrm{p,e}}$, cyclotron frequency Ω_{e}, and thermal speed $v_{\mathrm{th,e}}$ of the electrons, as well as the amplitude δB of the waves' magnetic fields.

$N_\parallel\,(\Delta x)$	$N_\perp\,(\Delta x)$	$N_t\,(\Delta t)$	$\Delta x\,(c\,\omega_{\mathrm{p,e}}^{-1})$	$\Delta t\,(\omega_{\mathrm{p,e}}^{-1})$	$m_{\mathrm{p}}\,(m_{\mathrm{e}})$	ppc
1200	64	50000	$3.53 \cdot 10^{-2}$	$2.04 \cdot 10^{-2}$	40.0	128

Table 4.2: Numerical parameters for the simulations of cyclotron damping: number of cells $N_\parallel$ and $N_\perp$ in the directions parallel and perpendicular to the background magnetic field, number of time steps N_t, grid spacing Δx, time step length Δt, (artificial) proton mass m_{p}, and ppc, i.e. the number of particles (electrons and protons combined) per cell.

Waves are excited at ten different parallel wave numbers, which are expressed by the numerical wave number k_{num} introduced in Eq. (3.29). Like in the example simulations described in Sect. 3.4.2, two simulations with the same setup are prepared, where one simulation contains waves at odd $k_{\mathrm{num}} \in \{1,\ 3,\ 5,\ 7,\ 9\}$ and the other contains waves at even $k_{\mathrm{num}} \in \{2,\ 4,\ 6,\ 8,\ 10\}$ to allow for a visible separation of waves in the plots of the spectral energy distribution in Fourier space.

However, for the detailed study presented here, not only two simulations are carried out. The initial conditions of each simulation rely on a random distribution of the thermal particles both in real and velocity space[30]. By chance, any such random distribution might lead to atypical results. Therefore, a simulation should, in principle, be repeated several times with different seeds for the random number generators which determine the particle distribution. For this study a total of twelve simulations are set up, six each for wave excitation

---

[30] The spatial distribution is isotropic, but the particles' velocities follow a Maxwellian distribution.

at odd and even k_{num}. The simulations use the same parameters (those defined in Tables 4.1 and 4.2), but each pair consisting of one "odd" and one "even" simulation has a unique seed parameter for the random number generators.

This set of simulations will be referred to as set A, the subsets of simulations with odd and even k_{num} are denoted by A_1 and A_2, respectively. Energy densities derived from the spectral energy distributions of the individual simulations can be averaged over the six simulations of each subset. This also allows to derive a meaningful value of the numerical noise level in the energy spectrum.

The damping rates of the waves are measured according to the method described in Sect. 3.4.2. This requires that the simulation data is subdivided into several intervals in time to allow for the computation of the spectral energy density at several points in time during the simulation (i.e. the time line of the spectral energy density). The time resolution of the evolution of the spectral energy density depends on the number and length of these intervals. Shorter intervals yield a higher time resolution, but worse spectral resolution, whereas longer intervals lead to the opposite behavior. To test whether the choice of the interval length t_{int} has any influence on the obtained values of the damping rate several interval lengths are realized. Each simulation is analyzed with three values of $t_{\mathrm{int}} \in \{1000,\, 3000,\, 5000\}\, \Delta t$, where Δt is the length of a single time step. Expressed in proton cyclotron time scales these interval lengths correspond to $t_{\mathrm{int}}\, \Omega_{\mathrm{p}} \in \{0.22,\, 0.67,\, 1.12\}$.

Temperature Analysis

Before the damping rates are measured it is also worthwhile to look at the evolution of the particle distribution. As mentioned earlier, it is expected that the dissipated field energy is transferred to the protons, as only the protons resonate with the left-handed waves. More specifically, the cyclotron resonance leads to an acceleration of particles perpendicular to the background magnetic field $\boldsymbol{B}_0$, thus triggering temperature anisotropy. Since the plasma simulated by a PiC code is collisionless, the temperature anisotropy is not reduced by particle-particle collisions and should be conserved even after all waves have been completely dissipated.

To monitor the temperature of the plasma, the full particle data has to be considered. Particle data is stored only a few times per simulation, since the incurring amount of data is huge. By producing histograms from the velocity data of the individual particles, the temperatures T_{e} and T_{p} of the electrons and the protons can be derived. It is also possible to calculate the parallel and perpendicular temperatures $T_{\|,\alpha}$ and $T_{\perp,\alpha}$ for each particle species α.

The time evolution of the global electron and proton temperatures, as well as the parallel and perpendicular temperatures are presented in Fig. 4.2. Obviously the electron temperature is not affected by the cyclotron damping of left-handed waves, as expected. There is no anisotropy in the electron temperature. The situation is different for the protons, however. The global proton temperature T_{p} is higher than the electron temperature T_{e} over the whole time. In fact, Fig. 4.2 shows that the simulations are initialized with an increased global temperature of the protons and anisotropy in the proton temperature. This is caused by the mechanism used to excite plasma waves, which performs an initial boost of the particles' velocities, according to the electromagnetic fields of the initialized waves (see Sect. 3.3.1). Since the protons strongly couple to the Alfvén and ion cyclotron waves, their velocities are noticeably boosted, especially at wave frequencies close to the proton cyclotron frequency,

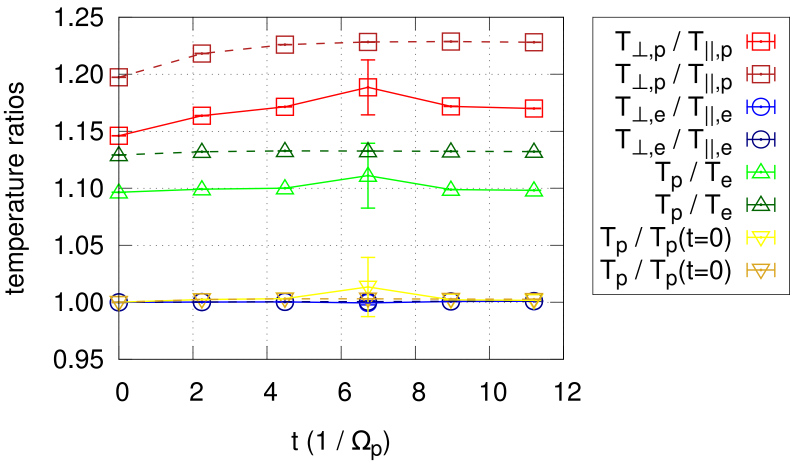

Fig. 4.2: Characteristics of the global temperatures T_e and T_p of electrons and protons, as well as the temperatures $T_{\|,\alpha}$ and $T_{\perp,\alpha}$ parallel and perpendicular to $\boldsymbol{B}_0$ for both species. The temperatures (and their standard errors) are derived from the averaged particle data of the simulations of sets A_1 and A_2 separately. Lighter colors and solid lines refer to A_1, whereas darker colors and dashed lines correspond to A_2. Figure according to Schreiner et al. (2017a).

as Eqs. (2.52) and (2.52) suggest. Therefore, the anisotropies in the simulations of set A_2 are stronger, as these simulations contain waves at higher frequencies than the simulations in set A_1. Over the course of the simulated time the anisotropy increases, as more and more field energy is dissipated and the protons gain perpendicular speed. The energy transfer from the waves to the particles slows down after a few proton cyclotron time scales, as is expected from an exponential decay of the waves, and the temperature anisotropy becomes constant. However, the increase of the global temperature of the protons is negligible.

Examples of the parallel and perpendicular velocity spectra of electrons and protons in one simulation are provided in Appendix B. These spectra show that the parallel and perpendicular velocity distributions of the protons can be approximated by Gaussian distributions. However, systematic deviations from the Gaussians show the influence of wave damping. Interestingly, the parallel velocity spectrum indicates that particles are accelerated parallel to $\boldsymbol{B}_0$. This might be explained by momentum conservation, i.e. the momentum of the parallel propagating waves is transferred to the particles while the wave decays. Unfortunately, this is only a conjecture so far, since a quantitative analysis of the particle data did not allow for an unambiguous conclusion: the signal to noise ratio simply is too small. To lesser extent the electrons show a similar behavior.

Damping Rates

The averaged field data from sets A_1 and A_2 is analyzed as described in Sect. 3.4.2[31]. The procedure is repeated three times for the three different interval lengths mentioned

---

[31] For a more detailed description of the averaging of simulation data and the production of the standard errors see Schreiner et al. (2017a, Sect. 5.1.2).

earlier, $t_{\mathrm{int}} \in \{1000,\, 3000,\, 5000\}\,\Delta t$. To compare the measured damping rates Γ to theory, the warm plasma prediction is calculated from Eqs. (2.81) and (2.82). However, as was shown above, the effective proton temperature and the temperature anisotropy differ between simulations A_1 and A_2. Therefore, two theoretical curves for the damping rate $\Gamma_{\mathrm{theory}}(k_\parallel)$ are computed, using the parameters from Table 4.1 and the proton temperature $T_{\mathrm{p},1} = 1.10\,T_{\mathrm{e}}$ ($T_{\mathrm{p},2} = 1.13\,T_{\mathrm{e}}$) and anisotropy $T_{\perp,\mathrm{p},1} = 1.15\,T_{\parallel,\mathrm{p},1}$ ($T_{\perp,\mathrm{p},2} = 1.20\,T_{\parallel,\mathrm{p},2}$) for set A_1 (A_2). These values approximate the temperature configurations in the simulations, but do not match them completely, since the temperature changes over the course of the simulation, as Fig. 4.2 illustrates.

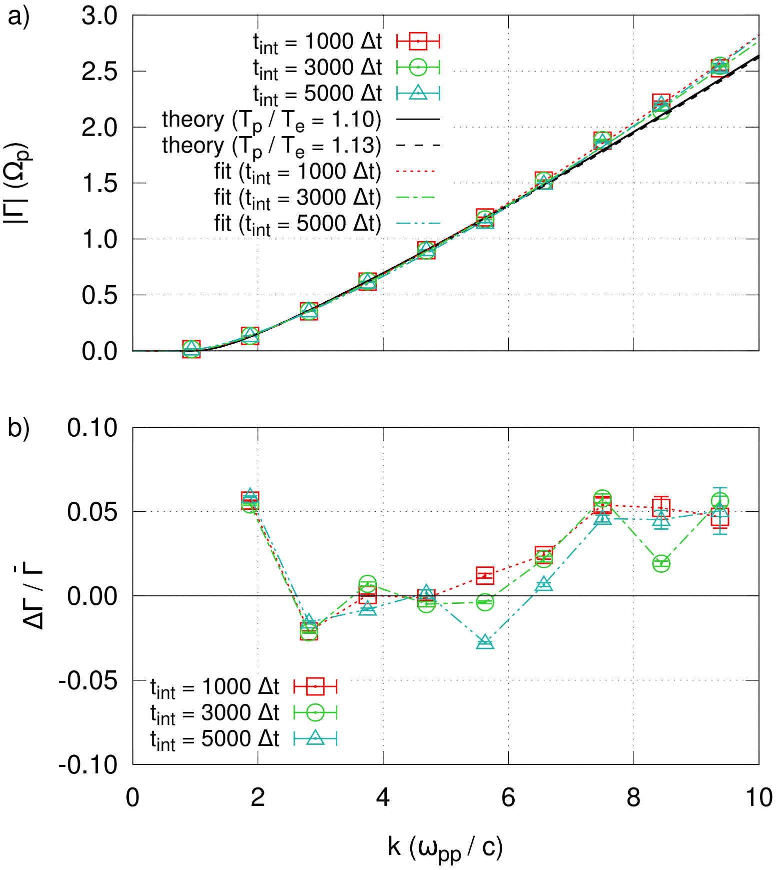

Fig. 4.3: The measured and theoretical damping rates as functions of the parallel wave number are presented in panel a). The simulation data has been analyzed with three different interval lengths t_{int}, as indicated. Fits to the data are produced using Eq. (2.92). Panel b) shows the deviation of the measured damping rate from theory, indicating a good overall agreement with a maximum deviation of about 5%. Figure taken from Schreiner et al. (2017a).

The measured and theoretical damping rates are plotted as functions of the parallel wave number $k_\parallel$ in Fig. 4.3 a). It can be seen that the difference between the two theoretical models for the damping rate (with different temperature settings) is only marginal. Similarly, the measured data points do not exhibit any signs which indicate the different proton temperatures. The choice of the interval length t_{int} has no significant influence on the obtained damping rates. The main difference that arises from the different choices of t_{int} is the time resolution of the evolution of the waves' energy densities and, therefore, the number of data points which can be included in the exponential fit that yields the damping rate. This is illustrated in Appendix B.

Fits to the measured data are provided using Eq. (2.92). The resulting curves closely follow the theoretical predictions up to $k_\parallel c/\omega_{\text{p,p}} \approx 7$, then they deviate in agreement with the measured data.

It needs to be said that besides the apparent agreement of the measured and predicted values in Fig. 4.3 there is one significant problem. The measured damping rate for the lowest wave number, $k_{\text{num}} = 1$, exceeds the theoretical prediction by two orders of magnitude. Because the absolute value of the damping rate at this wave number is so low, this massive discrepancy cannot be seen in the plot. The time evolution of this wave's energy density exhibits a steep slope at the beginning of the simulation, where the damping rate was measured. However, towards the end of the simulation the slope becomes significantly flatter and is in better agreement with the theoretical prediction (see Appendix B for details). The reason for the fast dissipation of energy in the early phase of the simulation is unclear. The data for $k_{\text{num}} = 1$ will not be considered in the following.

Figure 4.3 b) depicts the measurement's deviation $\Delta\Gamma/\bar{\Gamma}$ from the theoretical prediction, where

$$\frac{\Delta\Gamma}{\bar{\Gamma}} = \frac{\Gamma_{\text{sim}} - \Gamma_{\text{theory}}}{0.5\,(\Gamma_{\text{sim}} + \Gamma_{\text{theory}})}. \tag{4.1}$$

The overall agreement of the measured data with the predictions is very good, exhibiting deviations by only up to 5% at the lowest[32] and the three highest wave numbers. For the majority of data points a deviation of less than 2% is found, which is in the range of the deviation between the theoretical predictions for the different temperatures at the beginning and the end of the simulation.

4.1.2 Effects of Reduced Dimensionality

ACRONYM is available in 1d3v, 2d3v and 3d3v configurations, meaning that the particle velocities and field vectors will always be three-dimensional, whereas the number of resolved spatial dimensions can be varied between one and three. In principle, cyclotron damping of a parallel propagating wave can be studied with only one spatial dimension to resolve the wave parallel to its direction of propagation. This leads to spatial and temporal fluctuations of the electromagnetic fields, which are required. Particles with a resonant parallel velocity can resonantly interact with the fields and gain energy by being accelerated perpendicular to the propagation of the wave.

However, the perpendicular motion of the particles is not or at least only partially reproduced in a one- or two-dimensional setup. Consequently, the gyration of the particle about the background magnetic field is not recovered in real space, but only in velocity space (since all three components of the velocity vector are kept). The question is whether this has any influence on the damping process itself or the rate of energy transfer from the electromagnetic fields to the particles. In the following the simulations from Sect. 4.1.1 are repeated in two- or one-dimensional setups to investigate this question.

---

[32] The lowest wave number is $k_{\text{num}} = 2$, since the wave at $k_{\text{num}} = 1$ is not considered.

2D Simulations

Following the naming of the three-dimensional simulations the twelve two-dimensional simulations are grouped in two subsets B_1 and B_2, including waves at odd and even k_{num}. The results from these simulations are presented in Fig. 4.4, which shows the damping rate $\Gamma(k_{\|})$ and the deviation of the measurements from the theoretical prediction as functions of the parallel wave number in panels a) and b).

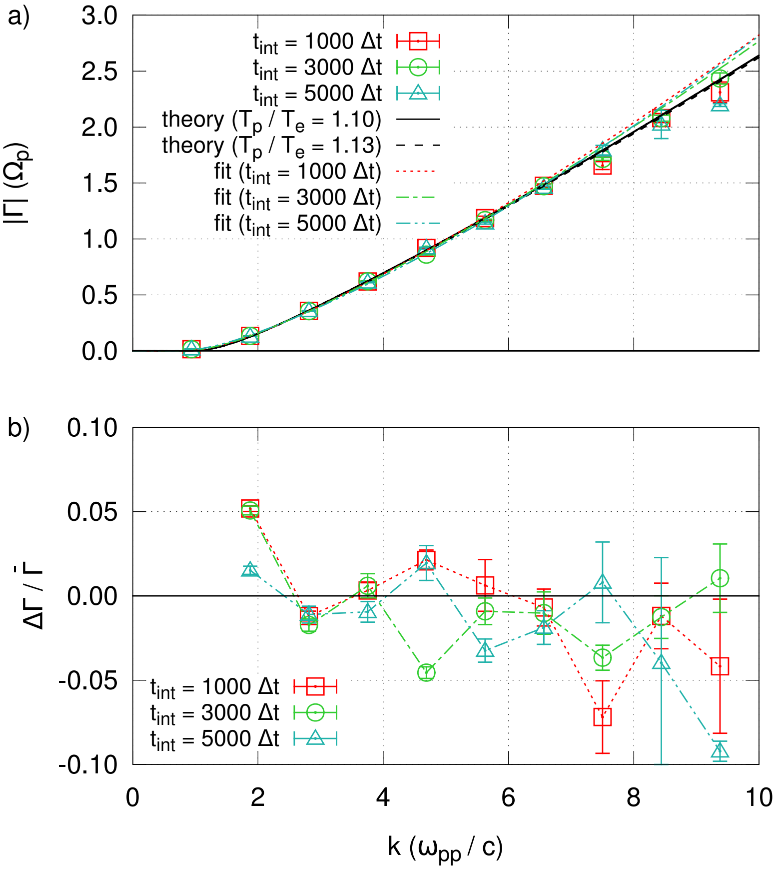

Fig. 4.4: The measured damping rates from simulations of sets B_1 and B_2 and the theoretical predictions from warm plasma theory are shown in panel a) as functions of the parallel wave number. Two theoretical curves are shown, according to the different temperature settings in the two subsets (same as in Fig. 4.3). Fits to the data are produced using Eq. (2.92). Panel b) shows the deviation of the measured damping rate from theory according to Eq. (4.1). Figure according to Schreiner et al. (2017a).

Other than for the three-dimensional simulations, the measured damping rates from the two-dimensional simulations underestimate damping at high wave numbers. At least for the interval lengths $t_{\mathrm{int}} = 1000\,\Delta t$ and $t_{\mathrm{int}} = 5000\,\Delta t$ there is a trend in the deviation from theory depicted in Fig. 4.4 b), which suggests that the measurement becomes less accurate with increasing k. This can be explained by the time evolution of the energy densities of the waves, which are shown in Appendix B: The numerical noise level in the two-dimensional simulations is about two orders of magnitude higher than in the three-dimensional simulations, thus making the exponential fits to the data less accurate, because fewer data points are available. This predominantly affects the strongly damped waves.

However, the overall deviation of measurement and theory is still mainly below 5%. It can be expected that cyclotron damping is recovered correctly in the simulation, although it is more difficult to accurately measure the damping rates due to the increased numerical noise.

1D Simulations

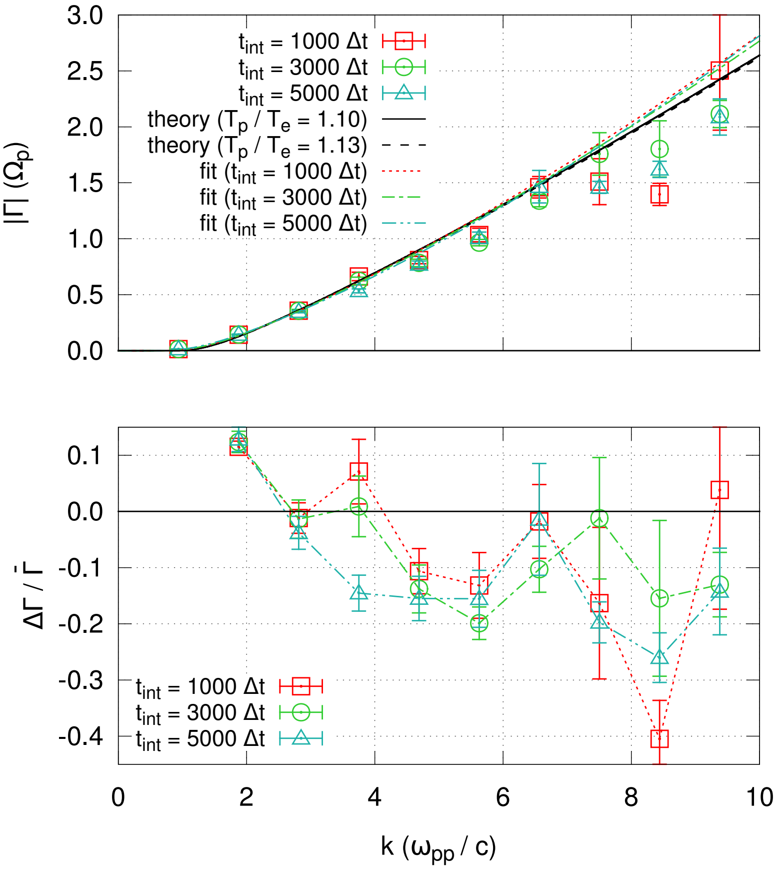

Fig. 4.5: The measured damping rates from simulations of sets C_1 and C_2 and the theoretical predictions from warm plasma theory are shown in panel a) as functions of the parallel wave number. Two theoretical curves are shown, according to the different temperature settings in the two subsets (same as in Fig. 4.3). Fits to the data are produced using Eq. (2.92). Panel b) shows the deviation of the measured damping rate from theory according to Eq. (4.1). Figure according to Schreiner et al. (2017a).

The situation becomes significantly worse when one-dimensional simulations (subsets C_1 and C_2) are considered. The measured damping rates are shown in Fig. 4.5 a). It can be seen that the data points deviate from the theoretical curves and systematically underestimate the (expected) damping rates. The relative deviation of measurements and theory is depicted in Fig. 4.5 b) and exhibits a downward trend similar to the one seen in Fig. 4.4 b). However, the deviation reaches up to 40% here and the majority of data points lies between 10% and 20% below the expected rates. In this respect the results from the one-dimensional simulations differ from the previously presented results, because no wave number regime exists for which an acceptable agreement of theory and measurements can be found.

Also note the large standard errors shown in Fig. 4.5 a). However, even within the error bars there is hardly any agreement of measurements and theory. The errors lie between 5% and 10% of the damping rates obtained from the simulations and show that the uncertainties of the measurements are also large compared to the results from the two- and three-dimensional simulations.

The reason for this can be found by looking at the time profiles of the energy densities of the waves, which are included in Appendix B. The numerical noise level is increased by another two orders of magnitude compared to the two-dimensional simulations (i.e. four orders of magnitude relative to the three-dimensional simulations). This makes it hard to find reliable exponential fits to the data and therefore diminishes the quality of the final results.

4.1.3 Reduction of the Computational Cost by Other Means

Should it not be possible to reduce the dimensionality of a simulation for some reason, there are other means of lowering the computational effort. Two possibilities immediately come to mind: First, the number of particles per cell can be reduced, thus increasing the macro factor of the numerical particles and potentially diminishing the coverage of phase space. Secondly, the size of the simulation box can be reduced to a minimum. The latter is a somewhat artificial point in the discussion of cyclotron damping of parallel propagating waves, since it was already shown that the two spatial dimensions perpendicular to the background magnetic field $\boldsymbol{B}_0$ can (in principle) be entirely neglected. However, for other physical setups this might not be the case.

In the following two additional sets of twelve simulations each will be discussed. Both sets employ the parameters presented in Tables 4.1 and 4.2, except for the changes described below. The twelve simulations of each set consist of two subsets, which will be labeled by indices “1” and “2” as described in Sect. 4.1.1. Plasma waves are excited according to the same scheme as used for the previously discussed simulations.

The first series of simulations presented in this section is set D, which is characterized by a reduced number of particles per cell: Instead of 128 particles a minimum of only four numerical particles (two electrons and two protons) per cell is chosen. The second series of simulations, set E, again uses 128 particles per cell, but has the number of cells in both directions perpendicular to $\boldsymbol{B}_0$ reduced to eight (instead of 64). This not only reduces the total number of particles in the simulation, but it also means that the proton Larmor radius is no longer recovered, since it exceeds the widths of the simulation box. The particles can still gyrate, however, due to the periodic boundary conditions.

Note that the results presented below have not been published previously, other than the results shown in Sects. 4.1.1, 4.1.2 and 4.1.4.

Reduction of the Particle Number per Cell

The simulations of series D are analyzed according to the method described in Sect. 3.4.2 and results are depicted in Fig. 4.6. The measured damping rates follow the expected theoretical curves (see Sect. 4.1.1), as Fig. 4.6 a) shows. Compared to the data presented in Fig. 4.3 the standard errors are larger here. The reduction of the number of particles per cell (from 128 ppc to 4 ppc) increases the numerically caused field fluctuations (due to the smaller number of phase space samples), thus leading to more noticeable deviations between the individual simulations of set D.

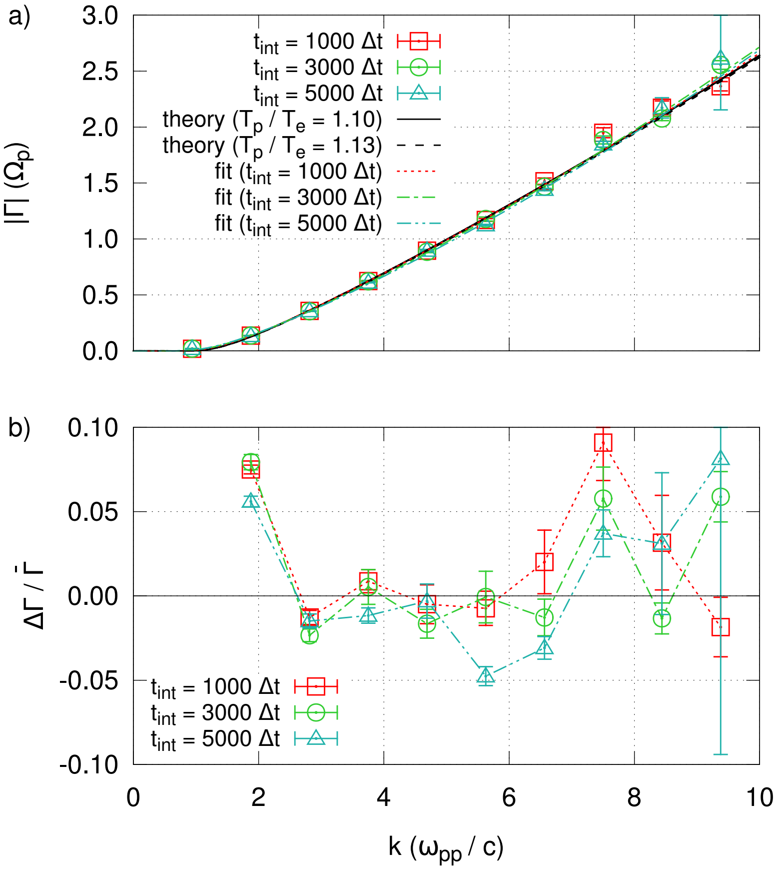

Fig. 4.6: The measured damping rates from simulations of sets D_1 and D_2 and the theoretical predictions from warm plasma theory are shown in panel a) as functions of the parallel wave number. Two theoretical curves are shown, according to the different temperature settings in the two subsets (same as in Fig. 4.3). Fits to the data are produced using Eq. (2.92). Panel b) shows the deviation of the measured damping rate from theory according to Eq. (4.1).

The fits applied to the measured $\Gamma(k_{\|})$ can hardly be distinguished from the theoretical curves. The damping rates obtained from the simulations are in almost perfect agreement with theory in the regime $2 < k_{\|}\, c/\omega_{\mathrm{p}} < 7$ (see Fig. 4.6 b). Only for high wave numbers the deviations from theory grow to up to 10%. However, these deviations are still covered by the standard errors of the measured data.

In terms of accuracy the data from the simulations of series D is comparable to that of the two-dimensional simulations (set B) discussed in Sect. 4.1.2. Even the numerical noise level of the electromagnetic fields is of the same order of magnitude, as can be seen in the figures in Appendix B. This suggests that the noise level not only depends on the number of particles per cell, but also on the total number of particles in the simulation, which is almost equal in the simulations of sets B and D (within a factor of two). Compared to the one-dimensional simulations (set C) the simulations from series D contain 128 times more particles.

Reduction of the Number of Grid Cells

The number of grid cells in the simulations of series E is reduced by decreasing the edge length perpendicular to the background magnetic field $\boldsymbol{B}_0$. Instead of $N_\perp = 64\,\Delta x$, as stated in Table 4.2, only eight cells are used. Note that the simulations of series E are still three-dimensional and that they again use 128 particles per cell.

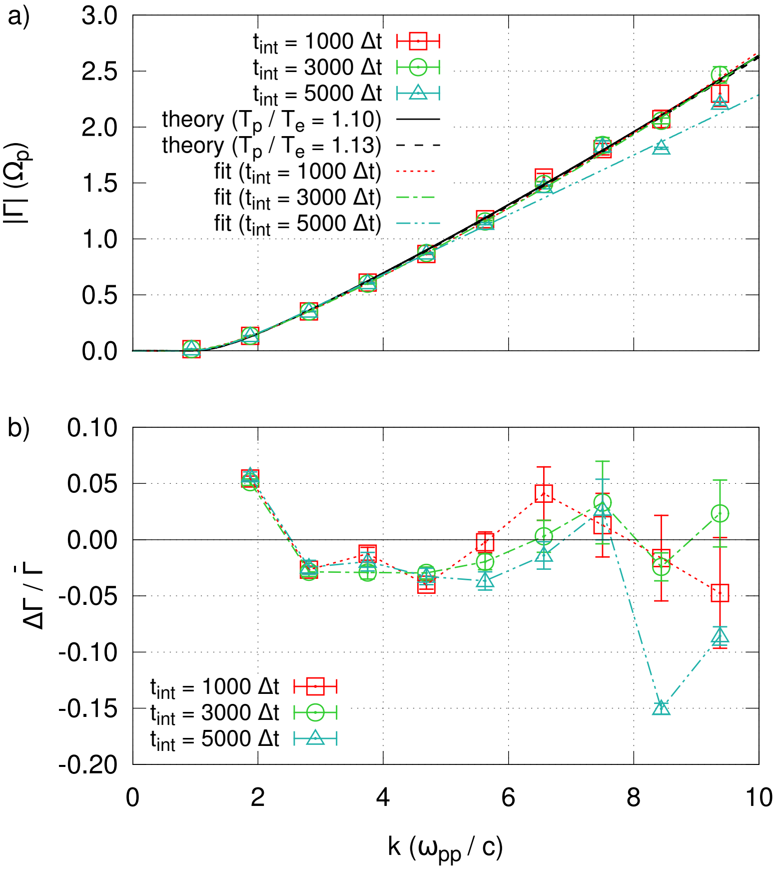

Fig. 4.7: The measured damping rates from simulations of sets E_1 and E_2 and the theoretical predictions from warm plasma theory are shown in panel a) as functions of the parallel wave number. Two theoretical curves are shown, according to the different temperature settings in the two subsets (same as in Fig. 4.3). Fits to the data are produced using Eq. (2.92). Panel b) shows the deviation of the measured damping rate from theory according to Eq. (4.1).

Analysis of the data from subsets E_1 and E_2 yields the damping rates which are depicted in Fig. 4.7 a). Besides two data points which were obtained using $t_{\text{int}} = 5000\,\Delta t$, the measured damping rates are in good agreement with the theoretical expectations. This is also supported by the relative deviation of measurement and theory, shown in Fig. 4.7. Most measured damping rates deviate by less than 5% from the expectations.

The damping rates for $k_{\text{num}} = 9$ and $k_{\text{num}} = 10$ measured with $t_{\text{int}} = 5000\,\Delta t$ are obtained from an exponential fit to three data points only (see Appendix B). The main problem is that the first of the three data points might still be in the regime where the energy density $W(t)$ decreases sub-exponentially, whereas the last data point is already very close to or within the energy regime of the numerical noise. This makes the exponential fits unreliable and potentially leads to an underestimation of damping.

As was already the case for the simulations with a reduced number of particles per cell, the standard errors derived for the measured data are larger than in the reference simulations discussed in Sect. 4.1.1. This again suggests more pronounced fluctuations between the individual simulations of series E, caused by the smaller number of numerical particles. The total particle count in the simulations is the same as for the two-dimensional simulations described in Sect. 4.1.2 (series B). Thus, the numerical noise level of the electromagnetic fields is expected to be similar to that in the two-dimensional simulations. This is actually the case, as can be seen in the plots of the time evolution of the field energy density provided in Appendix B.

The results of this part of the study are especially interesting, since the Larmor radius of the thermal protons is not covered by the extent of the simulation box. One might argue that this leads to nonphysical effects, because (due to the periodic boundaries) a gyrating proton encounters the same field configuration over and over again along its path of gyration. However, this does not seem to be the case.

4.1.4 Variation of Physical Parameters

The last part of the extended study of cyclotron damping in PiC simulations covers six simulations with different physical parameter sets. Other than the previously discussed sets of simulations, these six simulations each represent a single example. There are no repetitions of simulations with altered seed parameters for the random number generators. There are also no pairs of simulations with the same setup, but different wave numbers for the excited plasma waves. The six simulations from this series will be named F_i, with $i \in \{1, 2, 3, 4, 5, 6\}$.

The simulations of series F use the numerical parameters given in Table 4.2[33], but sets of physical parameters which are summarized in Table 4.3. These parameters are based on Table 4.1, but for each simulation either the background magnetic field B_0, the plasma frequency ω_{p}, or the temperature (in terms of the thermal velocity $v_{\text{th,e}}$ of the electrons) is changed. Note that a change of the plasma frequency or the temperature also leads to changes of the grid spacing and the length of a time step. In order to characterize the different simulations without having to repeat the full set of three physical parameters, the plasma beta is also included in Table 4.3. The plasma beta is defined by Eq. (2.7).

Because the previously shown results have indicated that the interval length t_{int} has only a minor effect, the simulations of series F are analyzed only once, using $t_{\text{int}} = 1000\,\Delta t$.

---

[33] Except for simulation F_3, which employs twice as many time steps, i.e. $N_t = 10^5$.

simulation	$\omega_{\mathrm{p,e}}\,(\mathrm{rad\,s^{-1}})$	$\lvert\Omega_{\mathrm{e}}\rvert\,(\omega_{\mathrm{p,e}})$	$v_{\mathrm{th,e}}\,(c)$	β	$\Delta x\,(c\,\omega_{\mathrm{p,e}}^{-1})$	$\Delta t\,(\omega_{\mathrm{p,e}}^{-1})$
F_1	$2.0 \cdot 10^{8}$	$2.64 \cdot 10^{-1}$	0.05	0.144	$3.53 \cdot 10^{-2}$	$2.04 \cdot 10^{-2}$
F_2	$2.0 \cdot 10^{8}$	$8.79 \cdot 10^{-1}$	0.05	0.013	$3.53 \cdot 10^{-2}$	$2.04 \cdot 10^{-2}$
F_3	$2.0 \cdot 10^{8}$	$4.40 \cdot 10^{-1}$	0.02	0.008	$1.41 \cdot 10^{-2}$	$8.16 \cdot 10^{-3}$
F_4	$2.0 \cdot 10^{8}$	$4.40 \cdot 10^{-1}$	0.10	0.207	$7.04 \cdot 10^{-2}$	$4.06 \cdot 10^{-2}$
F_5	$5.0 \cdot 10^{7}$	1.76	0.05	0.003	$3.53 \cdot 10^{-2}$	$2.04 \cdot 10^{-2}$
F_6	$5.0 \cdot 10^{8}$	$1.76 \cdot 10^{-1}$	0.05	0.323	$3.53 \cdot 10^{-2}$	$2.04 \cdot 10^{-2}$

Table 4.3: Physical and numerical parameters for the simulations of series F: plasma frequency ω_{p}, electron cyclotron frequency Ω_{e}, thermal speed of the electrons $v_{\mathrm{th,e}}$, plasma beta β, grid spacing Δx, and time step length Δt.

The theoretical predictions for the damping rates of Alfvén / proton cyclotron waves are calculated individually for each simulation from Eqs. (2.81) and (2.82). Note that no temperature anisotropy is inserted into Eq. (2.82) and that $T = T_{\mathrm{e}} = T_{\mathrm{p}}$ is assumed. This is most likely not the case in the simulations, but it allows easier handling of the data, since no temperature analysis has to be performed for each simulation.

The simulations each include five excited Alfvén / proton cyclotron waves with numerical wave numbers $k_{\mathrm{num}} \in \{1,\ 3,\ 5,\ 7,\ 9\}$. The data is analyzed following the procedure described in Sect. 3.4.2 and the resulting damping rates are depicted in Fig. 4.8 a) together with predictions from warm plasma theory and the damping rates obtained from the simulations of set A (see Sect. 4.1.1). It can be seen that the normalized damping rate $|\Gamma|/\Omega_{\mathrm{p}}$ at a given wave number $k\,c/\omega_{\mathrm{p}}$ is lowest in the plasma with the lowest plasma beta. The measured data mainly follows the expected theoretical curves, although it is striking that most data points lie below the predictions.

Looking at the relative deviations $\Delta\Gamma/\bar{\Gamma}$ in Fig. 4.8 b), it can be seen that the relative deviation of the data from simulations with $\beta > 0.1$ is mainly below 10%. Although the relative deviation exceeds that of the previously presented three-dimensional simulations of series A, the results are generally satisfactory. Larger deviations are to be expected, since the data from the simulations discussed here is not averaged over several runs. The fact that the measured rates fall short of the expected ones is also not surprising, because the normalized damping rates are very high, i.e. $|\Gamma|/\Omega_{\mathrm{p}} > 1$. Thus, the waves are strongly damped and the exponential fits to the field data are not very reliable, as was argued for previous simulations as well.

However, the situation is different for the simulations with very low plasma beta. Figure 4.8 b) shows that the measurements deviate from theory by up to 40%. For the smallest wave number, $k_{\mathrm{num}} = 1$, the deviation is even worse in simulation F_5. Here, $\Delta\Gamma/\bar{\Gamma} = 1.63$ is found. Together with the overestimated damping rate at $k_{\mathrm{num}} = 1$ in simulation F_3, this suggests that very weak damping rates are also difficult to measure. This corresponds well with the findings for a weakly damped wave discussed in Sect. 4.1.1 and in Appendix B.

To better understand why the measured damping rates lie below the expected values in simulations with low plasma beta, simulation F_5 is analyzed in more detail. The time evolution of the electromagnetic field energy densities of the five different waves is shown in Fig. 4.9 a). It can be seen that, after an initial period of slower decay, an exponential

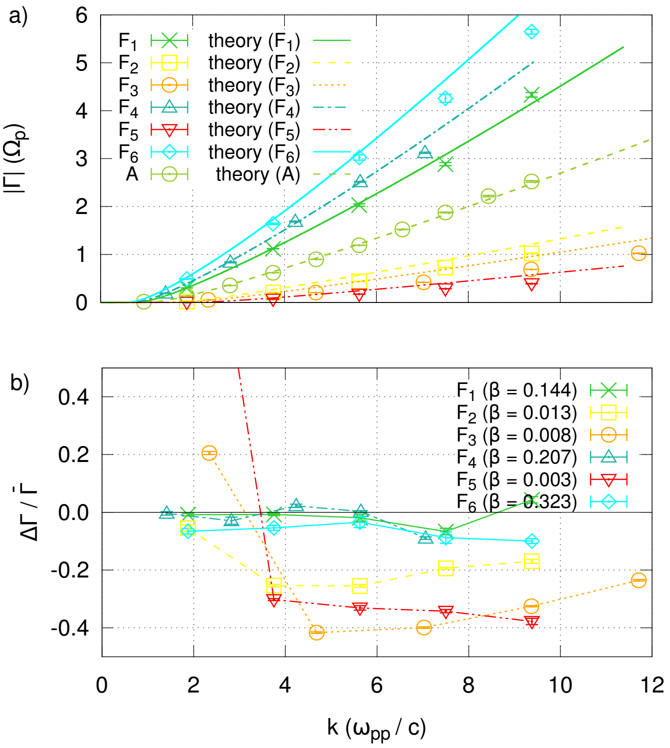

Fig. 4.8: The measured damping rates from the six simulations of series F are depicted in panel a) together with the corresponding predictions from warm plasma theory. An interval length $t_{\mathrm{int}} = 1000\,\Delta t$ was used for the analysis of the simulation data. Panel b) shows the relative deviations of the measured rates from theory. It can be seen that the measurements become inaccurate in the case of very small plasma betas. Note that the data point at $k_{\mathrm{num}} = 1$ is not shown for simulation F$_5$ because of its large value of $\Delta\Gamma/\bar{\Gamma} = 1.63$. Figure according to Schreiner et al. (2017a).

decrease develops. After a few proton cyclotron time scales (more precisely, after different times for the different waves) the slope changes again, becoming less steep. The exponential decay resumes, but with a changed damping rate.

As indicated by the solid and dotted black lines along the data points in Fig. 4.9 a), an “early” and a “late” exponential fit can be applied (results from the early fits are provided in Fig. 4.8). The resulting damping rates are depicted in Fig. 4.9 b) together with the warm plasma prediction. While the early measurement yields damping rates below the theoretical values, the late measurements exhibit even smaller damping rates. Unfortunately, the reason for the observed kink in the time evolution of the energy density is absolutely unclear. With the current set of simulations it cannot be said whether the kink has any physical implication or if it is a numerical artifact. Future studies addressing this question could start by varying the initial energy density of the excited wave in order to see whether the kink appears at a specific energy density or rather at a specific point in time. The influence of the number of particles per cell (and thus the amplitude of the numerical noise) could also be investigated. If the kink appears at a specific energy level above the numerical noise, it is most certainly related to numerical effects.

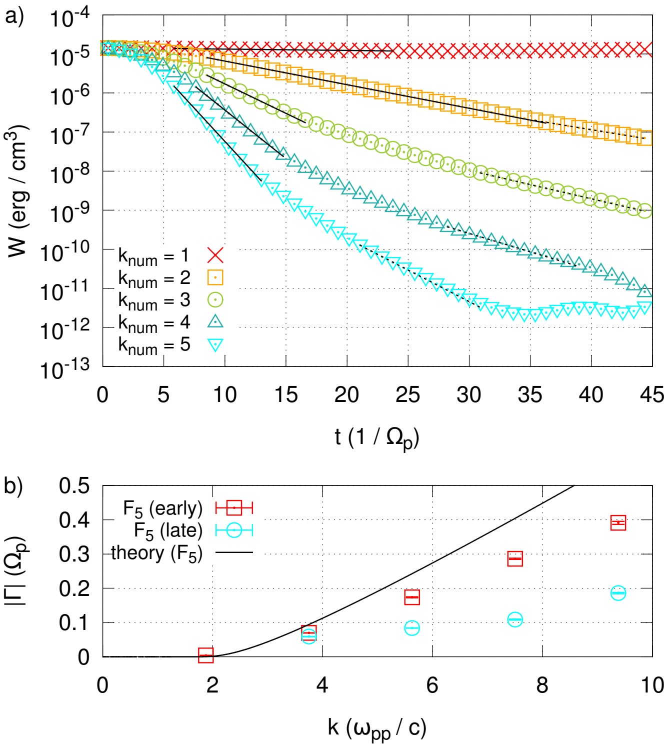

Fig. 4.9: The energy densities of the five excited waves in simulation F_5 are plotted over time in panel a). The time lines show that (after a short initial phase) an exponential decay of the electromagnetic energy of the waves sets in. At later times the slope of the curves changes and establishes an exponential decay with a different damping rate. The numerical noise level has not been measured explicitly, but can be expected to be located in the interval $10^{-12} < W_{\text{noise}} < 10^{-11}$. Exponential fits to the data can be applied at early (black, solid lines) and late times in the simulation (black, dotted lines). The damping rates resulting from the fits are depicted in panel b) and labeled accordingly. Figure according to Schreiner et al. (2017a).

The reason why the simulations of plasmas with very small betas produce damping rates which are too small could also not be found so far. A more extended study, as suggested above, could also help to solve this problem.

4.1.5 Résumé

In the previous sections the method to extract damping rates from simulation data, which was introduced in Sect. 3.4.2, was applied to simulations of cyclotron damped waves. The numerical study was focused on the effect of numerical parameters, such as the number of macro particles in the simulation, or the dimensionality of the simulation box, on the representation of cyclotron damping. Since a dissipation process, which reduces the energy of plasma waves in certain regimes of k-ω-phase space, was previously found in plots of the spectral energy distribution of the electromagnetic fields, the main question is not if, but how accurate cyclotron damping is modeled by a PiC code.

In a first series of three-dimensional simulations the general possibility of obtaining reliable measurements of the damping rates of individual waves was investigated (see Sect. 4.1.1). It could be shown that electromagnetic field energy is dissipated and transferred to the particles, leading to an increase of the perpendicular temperature $T_{\perp,\mathrm{p}}$ of the protons, as expected from the decay of left-handed, parallel propagating proton cyclotron waves. Using the method described in Sect. 3.4.2, the damping rates of the different waves in the simulation could be measured. While a good overall agreement of the results with the theoretical expectations could be achieved, two problems were identified: First, weakly damped waves behave different than expected, as they exhibit fast dissipation of energy in the first few proton cyclotron time scales and return to the expected slow, exponential decay later. Secondly, the damping rates of strongly damped waves are systematically underestimated.

The first of the two problems is most likely a result of the initialization of the excited waves. The reason for the initial fast decay of field energy is not entirely clear. However, since all excited waves show unexpected behavior at the very beginning of the simulations (i.e. a slow transit into exponential decay), it is assumed that the initialization of the waves does not result in a "natural" state of the warm plasma. This can be expected, since the excitation is based on cold plasma theory, but warm plasma effects are studied here. As was shown in Sect. 2.4.1 the frequency of a wave of a given wave number is lower in a warm plasma than in a corresponding cold plasma. Therefore, the electromagnetic fields of the damped proton cyclotron waves are modeled inaccurately during initialization. Furthermore, the initial particle boost (see Sect. 3.3.1 and Appendix A) overestimates the particles' boost velocities, which are also based on the cold plasma approximation. Close to the cyclotron resonances Eqs. (2.52) and (2.53) yield very high speeds which should not occur in a warm plasma. The initialization process implemented in ACRONYM, therefore, is not optimal for the excitation of damped plasma waves.

The second problem mentioned above concerns the method of extracting the damping rates from the electromagnetic field data itself. The measurement is based on the exponential fits to the time evolution of the field energy of a given wave. These fits are only meaningful and accurate if a sufficient number of data points can be included. Due to the finite level of numerical background noise in the simulations, only a small number of data points are available in the regime of exponential decay of strongly damped waves. Therefore, strong damping is difficult to handle and requires a high initial signal to noise ratio, i.e. a high energy density of the damped wave at the beginning of the simulation and a very low numerical noise level.

Section 4.1.2 discussed the influence of a reduced dimensionality of the simulation box on the modeling and measurement of cyclotron damping. The results obtained from the one- and two-dimensional simulations are less accurate than those from the three-dimensional simulations presented in Sect. 4.1.1. However, this is primarily due to the increased noise level in the low dimensional simulations, which hinders the measurement of damping rates via exponential fits to the time evolution of energy densities. No evidence is found for a principle problem with the physically correct representation of cyclotron damping in low dimensional PiC simulations. It is expected that more accurate results could be obtained with a higher number of particles per cell. However, if the particle count has to be increased anyway, it might be worth considering a simulation in higher dimensionality.

In the simulations presented in Sect. 4.1.3 the number of numerical particles per cell or the extent of the simulation box perpendicular to the background magnetic field have been reduced. While these simulations are still three-dimensional, they include far less macro particles in total than the simulations discussed in Sect. 4.1.1. Thus, phase space is sampled less accurately and a higher level of numerical noise is caused. However, the mechanism of cyclotron damping still works in the simulations, although the quality of the measurements of the damping rates is diminished. It is interesting to note that cyclotron damping is still modeled physically correct if the extent of the simulation box is smaller than the Larmor radius of the protons.

While all simulations in Sects. 4.1.1, 4.1.2, and 4.1.3 are based on the same set of physical parameters, different parameter sets have been used for the simulations in Sect. 4.1.4. The analysis of these simulations has shown that damping in simulations with small plasma betas behaves differently from expectations: Not only are the measured damping rates not in agreement with the warm plasma predictions; the time evolution of the energy densities of the excited plasma waves also shows that energy is dissipated exponentially over a few proton cyclotron time scales until damping slows down and proceeds with a different rate. An explanation of this observation could so far not be found.

At this stage it would be very interesting to investigate wave damping with different codes. A comparison of several numerical schemes, similar to the studies of Kilian et al. (2017) or Told et al. (2016), would definitely be worthwhile.

4.2 Resonant Wave-Particle Scattering

Before resonant wave-particle scattering is considered in a turbulent medium, it is important to investigate the interaction of particles and individual waves under controlled conditions. This can be seen as a pilot study for subsequent, more complex simulations. With the theoretical framework provided in Sect. 2.6.2, the interaction of particles and a single wave can be studied. This simple setup can be realized in a PiC simulation as well, using the mechanism for wave excitation presented in Sect. 3.3.1 and the initialization method for a test particle population that was introduced in Sect. 3.3.2.

Using only a single, parallel propagating wave and a mono-energetic population of test particles, different questions can already be addressed: Which particle species can undergo resonant scattering with which kind of waves? How does the energy of test particles influence their scattering behavior? How well can the analytical theory describe the interaction of particles and waves with finite amplitudes? Does the model break down when the amplitude is increased? Can momentum diffusion (which is not described by the analytical model described in Sect. 2.6.2) be neglected, or does it have a noticeable impact on particle scattering in a fully kinetic, electromagnetic simulation?

In the case of only parallel propagating waves it is also possible to include two or more excited waves in a single simulation to study their effect on particle scattering. The direction of propagation parallel to the background magnetic field $\boldsymbol{B}_0$ is important here, since (anti-) parallel propagating waves cannot interact with each other. Therefore, no energy cascade is established, as would be the case in a turbulent medium. The waves simply propagate through the simulation box unaltered, which makes a theoretical description and comparisons between theory and numerical results easier.

By addressing the above mentioned aspects it is possible to validate the numerical method using setups which are well-described by theory. After validation, it is also possible to test the limits of the theoretical description in physical regimes where the validity of basic assumptions of the theory is questionable. The following sections will give an overview over the studies of resonant wave-particle interaction in a simplified setup and present the answers to some of the questions raised above.

4.2.1 Early Work, Theory and Simulation Setup

As a starting point for the investigation of resonant wave-particle scattering with a kinetic PiC code the interaction of protons and Alfvén waves was chosen. First simulations were based on the work of Lange et al. (2013) and could reproduce resonant scattering of energetic protons and Alfvén waves in accordance with both MHD simulations and QLT predictions (Schreiner and Spanier, 2014). While these first tests can be seen as a validation of the numerical approach, they also point to two specific problems: First, the analytical model suggested by Lange et al. (2013) is inaccurate and does not yield a description of the scattering amplitude $\Delta\mu(\mu)$ over the whole interval $-1 \leq \mu \leq 1$. Secondly, PiC codes are ill-suited to simulate the time and length scales required to model proton scattering off of low frequency Alfvén waves.

The problem with theory can be identified by considering the derivation of the analytical predictions for the scattering amplitude $\Delta\mu(\mu)$. Equations (2.142) and (2.143) have been derived in the magnetostatic limit or in the rest frame of the plasma wave. However, in the simulations of both Lange et al. (2013) and Schreiner and Spanier (2014) the bulk plasma is at rest and the waves are moving through the simulation box, i.e. the simulations describe the rest frame of the plasma. The model equations therefore have to be transformed between the two rest frames. Lange et al. (2013) provide the following transformations:

$$\mu' = \mu - \frac{v_{\mathrm{ph}}}{v_\alpha}, \tag{4.2}$$

$$v'_\alpha = v_\alpha, \tag{4.3}$$

where primed and unprimed quantities are given in the rest frames of the wave and the plasma, respectively. While these transformations yield acceptable results if the phase speed of the wave is much smaller than the speed of the energetic test particles, $v_{\mathrm{ph}} \ll v_\alpha$, it can immediately be seen that they are never entirely correct. Equation (4.2) maps the pitch angle cosine μ in the plasma frame into an interval $(-1 - v_{\mathrm{ph}}/v_\alpha) \leq \mu' \leq (1 - v_{\mathrm{ph}}/v_\alpha)$ in the wave frame, which differs from the interval in which the (pitch angle) cosine is mathematically defined.

The simple transformations cause deviations between numerical results and analytical theory, which become obvious if $v_{\mathrm{ph}} \ll v_\alpha$ is violated (see Schreiner and Spanier, 2014, Fig.2). Therefore, the new and correct transformations have been derived and presented in Sect. 2.6.2, Eqs. (2.144 - 2.150). The advantage of the new transformations – besides from being physically correct – is in particular the possibility to model the interaction of particles and dispersive waves. As can be seen from the resonance condition, Eq. (2.131), lower particle velocities are required to resonate with (dispersive) waves at higher frequencies. The ratio v_{ph}/v_α, therefore, potentially grows with increasing frequency and decreasing particle energy, so that the use of the simple transformations leads to larger and larger errors.

The numerical problem arising from the simulation of Alfvén waves, namely the immense amount of computational resources required, has a very simple solution: Do not simulate non-dispersive Alfvén waves with PiC codes! Alfvén waves and protons have been chosen to be able to compare PiC simulations to the results from MHD simulations by Lange et al.

(2013). This helped to validate the code, but essentially the PiC method is a bad choice for this problem. Hybrid codes, which treat electrons as a fluid, would be a better means to conduct simulations in the low frequency regime of Alfvén waves.

To make the study regarding proton scattering complete, the ACRONYM code was used to model proton scattering off of whistler waves. A few proof of concept simulations were carried out to check whether protons can resonate with whistler waves at frequencies up to the proton cyclotron frequency. This is, in fact, the case (see Appendix C). However, the proton energies required to interact with dispersive whistler waves are so low, that test particles interact with the thermal background plasma. These test particles can hardly be called "energetic" and random scattering off of thermal fluctuations becomes an important factor determining the transport characteristics of the protons.

The more interesting simulations are those of energetic electrons and whistler waves. The PiC method is well-suited for simulating the relevant time and lengths scales. Furthermore, the process of electron scattering off of whistler waves is also relevant in the solar wind. Dispersive waves, such as whistlers, are expected to strongly influence the transport of energetic electrons. Only electrons at highest energies (in the range of more than a few MeV) will resonate with non-dispersive waves, whereas the electrons become resonant with dispersive waves at lower energies.

In the following, only electron scattering will be considered. As stated at the beginning of Sect. 4.2, a variety of questions can be addressed by simple simulations of mono-energetic test particles and individual plasma waves. For this purpose several studies have been carried out (Schreiner et al., 2017b), which will be presented here.

The setups for the different simulations are relatively similar and will therefore all be described together below. Parameters which are subject to change are listed in Table 4.4, whereas those parameters, which stay constant for all simulations, will be explained in the text. All simulations are carried out using the 2d3v version of ACRONYM, i.e. two spatially resolved dimensions, but fully three-dimensional velocity and field vectors. For the modeling of parallel propagating waves two spatial dimensions are sufficient[34]. The simulations are labeled "Sj", where "S" stands for "scattering" and j is an integer number identifying a single simulation.

The numerical parameters are the same for all simulation (except for S13 and S17). These parameters include the number of cells in parallel and perpendicular direction, $N_\parallel = 4096$ and $N_\perp = 128$, the grid spacing $\Delta x = 1.29 \cdot 10^{-3}\, c/\omega_\mathrm{p}$, and the length of a time step $\Delta t = 7.46 \cdot 10^{-4}/\omega_\mathrm{p}$. The box size is chosen such that the wavelength λ of the excited parallel propagating whistler wave corresponds to the length of the simulation box $L_\parallel = \lambda = N_\parallel\, \Delta x$. The width of the box, $L_\perp = N_\perp\, \Delta x$, is about twice the Larmor radius ρ_e of thermal electrons. Recovering the Larmor radius ρ_p of the protons is not necessary and would also hardly be possible with reasonable computational effort, since the natural mass ratio $m_\mathrm{p}/m_\mathrm{e} = 1836$ is used and $\rho_\mathrm{p}/\rho_\mathrm{e} = \sqrt{m_\mathrm{p}/m_\mathrm{e}}$. The number of test electrons, which are tracked for the study of wave-particle interaction, is $N_\mathrm{e} = 1.0 \cdot 10^6$.

Two larger simulations are performed (S13 and S17), which feature twice the number of grid cells in parallel direction, $N_\parallel = 8192$, and a total number of test electrons $N_\mathrm{e} = 2.1 \cdot 10^6$.

The physical parameters for the thermal background plasma in the simulations are inspired

---

[34] One-dimensional simulations would also be able to recover the desired plasma waves. However, previous tests have shown that one-dimensional simulations tend to produce numerical artifacts when it comes to resonant scattering.

simulation (code)	B_0 (G)	$k_\parallel$ ($\lvert\Omega_\mathrm{e}\rvert/c$)	ω ($\lvert\Omega_\mathrm{e}\rvert$)	δB (B_0)	v_e (c)	E_kin (keV)	μ_res	μ'_res
S1 (PiC)	0.20	50.6	0.58	0.02	0.063	1.0	-0.13	-0.30
S2 (PiC)	0.20	50.6	0.58	0.02	0.099	2.5	-0.082	-0.20
S3 (PiC)	0.20	50.6	0.58	0.02	0.20	10.5	-0.039	-0.10
S4 (PiC)	2.00	5.06	0.58	0.02	0.56	105	-0.088	-0.28
S5 (PiC)	2.00	5.06	0.58	0.02	0.72	226	-0.031	-0.19
S6 (PiC)	2.00	5.06	0.58	0.02	0.86	495	0.017	-0.12
S7 (PiC)	2.00	5.06	0.58	0.02	0.95	1052	0.053	-0.068
S8 (PiC)	2.00	5.06	0.58	0.04	0.56	105	-0.088	-0.28
S9 (PiC)	2.00	5.06	0.58	0.08	0.56	105	-0.088	-0.28
S10 (PiC)	2.00	5.06	0.58	0.16	0.56	105	-0.088	-0.28
S11 (PiC)	2.00	5.06	0.58	0.32	0.56	105	-0.088	-0.28
S12 (PiC)	2.00	5.06,	0.58	0.02	0.56	105	-0.088	-0.28
		-5.06	0.58	0.02			0.088	0.28
S13 (PiC)	2.00	2.53,	0.23,	0.08,	0.56	105	-0.40	-0.54
		5.06,	0.58,	0.04,			-0.088	-0.28
		0.76,	0.76,	0.02,			-0.017	-0.19
		0.85	0.85	0.01			0.0033	-0.15
S14 (test part.*)	2.00	5.06	0.58	0.02	0.56	105	-0.088	-0.28
S15 (test part.)	2.00	5.06	0.58	0.02	0.56	105	-0.088	-0.28
S16 (test part.)	2.00	5.06,	0.58	0.02	0.56	105	-0.088	-0.28
		-5.06	0.58	0.02			0.088	0.28
S17 (test part.)	2.00	2.53,	0.23,	0.08,	0.56	105	-0.40	-0.54
		5.06,	0.58,	0.04,			-0.088	-0.28
		0.76,	0.76,	0.02,			-0.017	-0.19
		0.85	0.85	0.01			0.0033	-0.15

Table 4.4: Physical parameters for the simulation of electron scattering: background magnetic field B_0, parallel wave number $k_\parallel$, frequency ω and magnetic field amplitude δB of the excited waves, speed v_e and kinetic energy E_kin of the test electrons, and resonant pitch angle cosines μ_res and μ'_res in the plasma and the wave frame, respectively. Simulations S14 through S17 are carried out using the magnetostatic test particle code described in Sect. 3.3.3. *Note that S14 uses the mechanism for artificial wave propagation in a test particle simulation.

by Vainio et al. (2003), who provide a model for solar wind parameters as a function of the distance to the Sun. As a starting point a distance of 2.6 solar radii is chosen[35]. The model yields the plasma temperature $T^{\mathrm{model}} = 2.0 \cdot 10^6\,\mathrm{K}$, the plasma frequency $\omega_{\mathrm{p}}^{\mathrm{model}} = 6.4 \cdot 10^7\,\mathrm{rad/s}$, and the background magnetic field $B_0^{\mathrm{model}} = 0.20\,\mathrm{G}$. These parameters are adapted to optimize the setup of the simulations in terms of the required computational resources. The temperature is decreased to $T = 2.0 \cdot 10^4\,\mathrm{K}$ and the plasma frequency is increased to $\omega_{\mathrm{p}} = 1.5 \cdot 10^8\,\mathrm{rad/s}$. Adjusting the temperature expands the frequency regime available for the excitation of undamped waves, whereas the increase of the plasma frequency leads to a more convenient grid spacing and time step length. The magnetic field is kept for some simulations (S1, S2, S3 and S14) and multiplied by a factor of ten for all others (see Table 4.4). The temperature T and magnetic field B_0 can be translated to the electron thermal speed $v_{\mathrm{th,e}} = 1.83 \cdot 10^{-3}\,c$ and the electron cyclotron frequency $|\Omega_{\mathrm{e}}| = 2.34 \cdot 10^{-2}\,\omega_{\mathrm{p}}$ for S1, S2, S3 and S14 or $|\Omega_{\mathrm{e}}| = 2.34 \cdot 10^{-1}\,\omega_{\mathrm{p}}$ for the rest of the simulations.

Table 4.4 lists the remaining physical parameters, such as the parallel wave number $k_{\|}$ and the frequency ω of the excited waves, the waves' amplitudes δB, and the test electrons' speed v_{e} and equivalent kinetic energy E_{kin}. Additionally, the expected resonant pitch angle cosines μ_{res} and μ'_{res} in the plasma and the wave frame are calculated from the respective resonance conditions, Eqs. (2.131) and (2.141), and are included in the table. The table is organized in several blocks of simulations, separated by horizontal lines. Each block lists simulations which can be assigned to a specific part of the numerical study presented in the following sections. The first block contains three simulations with low energy electrons and low background magnetic field, whereas the second block includes high energy electrons in simulations with increased magnetic field. Both sets of simulations will be discussed in Sect. 4.2.2. The third block represents the study of different amplitudes of the excited waves, which is presented in Sect. 4.2.4. The two simulations listed in the fourth block contain more than one wave and are analyzed in Sect. 4.2.5. A few simulations have been carried out using the magnetostatic test particle code described in Sect. 3.3.3. The parameters for these simulations are denoted in the last block of Table 4.4. However, there is no specific section which deals with these simulations. They are used for comparison with self-consistent, fully electromagnetic simulations and are therefore discussed together with their respective PiC simulation.

4.2.2 Study of Test Electron Energy

With a first series of simulations in the systematic study of the resonant scattering of electrons and whistler waves, the influence of the particle energy is investigated. Particle energies are varied between $E_{\mathrm{kin}} \simeq 1\,\mathrm{keV}$ and $E_{\mathrm{kin}} \simeq 1\,\mathrm{MeV}$, where the electrons in the range $1\,\mathrm{keV} \leq E_{\mathrm{kin}} \leq 10\,\mathrm{keV}$ are denoted “low energy electrons” (simulations S1, S2, and S3) and those in the range $100\,\mathrm{keV} \leq E_{\mathrm{kin}} \leq 1\,\mathrm{MeV}$ are named “high energy electrons” (S4 through S7).

To track wave-particle scattering in the simulations the scattering amplitude $\Delta\mu(\bar{\mu})$ is considered. As described in Sect. 3.3.2, the test electron data can be processed to obtain the pitch angle cosines $\mu(t)$ of the particles at time t. Comparing the current pitch angle cosine to μ_0 at the beginning of the simulation yields the change of the pitch angle $\Delta\mu(t) = \mu(t) - \mu_0$,

---

[35] This choice was made mainly for reasons of numerical convenience. However, assuming the existence of plasma waves and the occurrence of wave-particle interaction in a region close to the Sun also seems reasonable.

i.e. the scattering amplitude, and the mean pitch angle cosine $\bar{\mu}(t) = (\mu(t)+\mu_0)/2$. Using the data of all particles to create histograms, the scattering amplitude $\Delta\mu(\bar{\mu}, t)$ can be directly compared to the analytical prediction from Eqs. (2.142) and (2.143) – after these equations have been transformed into the plasma frame, of course.

It is not expected that the change of the electron energy leads to major qualitative changes in the shape and time evolution of the scattering amplitudes. However, it is a simple test which helps to verify both theory and simulation.

Low Energy Electrons

To give an overview of the evolution of pitch angle scattering in terms of the scattering amplitude, the data from the first simulation, S1, is shown in Fig. 4.10. The three panels illustrate time evolution of the scattering amplitude over the 10^6 time steps in the simulation, equivalent to a physical time span of $t\,|\Omega_\mathrm{e}| = 17.5$. As can be seen in both the simulation data and the analytical prediction, the resonance develops around the expected resonant pitch angle cosine μ_res. Over time the resonance peak becomes taller and narrower, as do the ballistic side peaks. New ballistic peaks propagate from the edges, i.e. $\bar{\mu} = \pm 1$, towards the resonance, thus increasing the total number of ballistic peaks with time.

While theory predicts the further growth of the amplitude of the resonance peak, the simulation data shows that the peak height is actually limited. It has reached its maximum in panel c) of Fig. 4.10, but theory and simulation noticeably depart from each other in panel b) already. However the shape, peak height and position of the smaller ballistic peaks is modeled perfectly by the analytical description.

The red arrows in panels a) and b) of Fig. 4.10 mark the predicted height of the resonance peak for positive and negative $\Delta\mu$. Arrows are omitted in panel c), because the predicted amplitudes are outside of the plot range. It can be seen that the prediction is slightly asymmetric, as mentioned in Sect. 2.6.2. Simulation data, however, does not seem to follow this prediction and is symmetric about $\Delta\mu = 0$.

Finally, the data in panel c) exhibits a narrow, dark line at the center of the resonance peak and at the centers of the two neighboring ballistic peaks. These lines, indicating a higher particle density in $\bar{\mu}$-$\Delta\mu$-phase space, broaden with time and replace the structures they were initially formed in. This substructure inside the individual peaks is not recovered by the analytical model, which only predicts the maximum scattering amplitude.

Figure 4.11 shows a comparison of the scattering amplitudes obtained from the simulations S1, S2, and S3 at time $t_2\,|\Omega_\mathrm{e}| = 10.5$. Except for deviations regarding the amplitude of the resonance peak, the analytical model describes the data well for all three electron energies. Since the excited whistler wave has the same wave number and frequency in all three simulations, but the particle energy changes, a change of the resonant pitch angle cosine can be observed. In this case, the resonant pitch angle cosine moves towards $\bar{\mu} = 0$ with increasing particle energy.

Comparing the different panels of Fig. 4.11, one also finds that the resonance peak becomes narrower with increasing electron energy. However, this is only an effect of the chosen abscissa: The resonance peak has a constant width in terms of $v_{\|,\mathrm{e}} = v_\mathrm{e}\,\bar{\mu}$, independent of the absolute value of v_e.

The number of ballistic peaks increases with energy, which can again be explained with the choice of the abscissa. Assuming that the width of the ballistic peaks is also the same in terms of $v_{\|,\mathrm{e}}$ for all three simulations, then there is simply more room for ballistic peaks

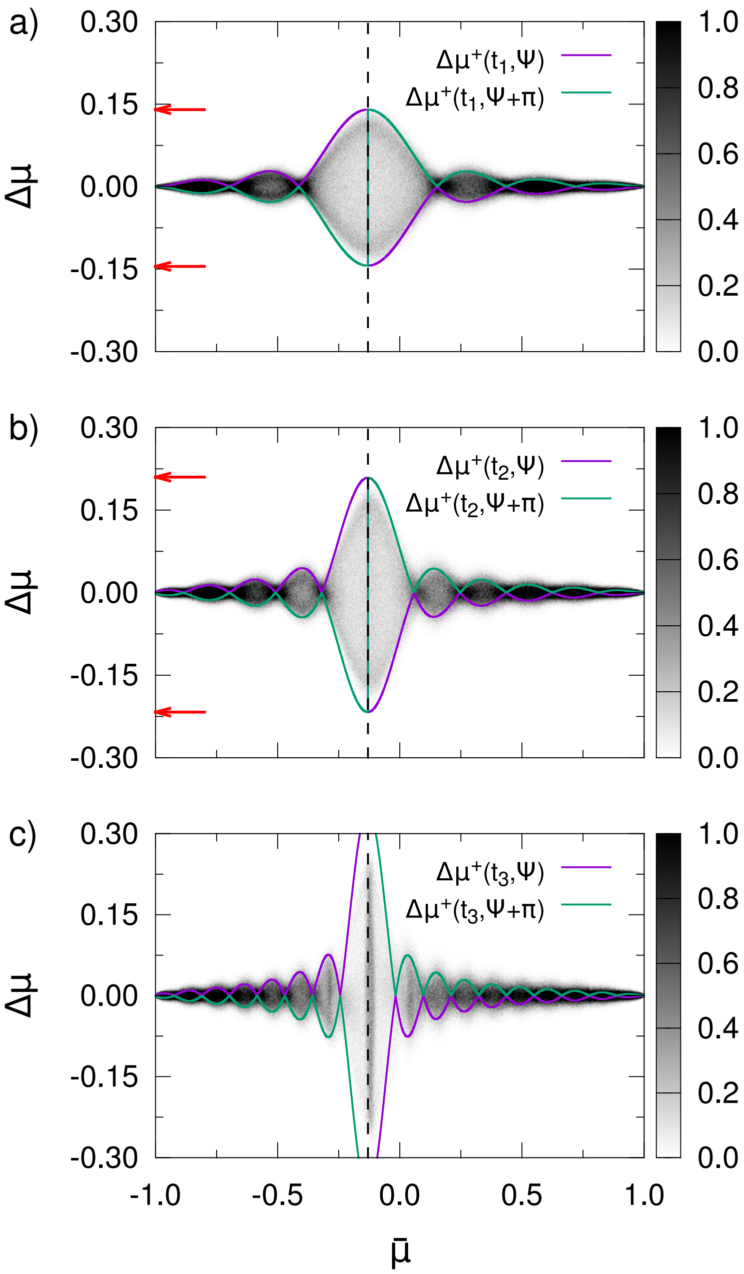

Fig. 4.10: Test electron data from simulation S1 presented as scatter plots in $\bar{\mu}$-$\Delta\mu$-phase space at different points in time in the simulation: $t_1\,|\Omega_\mathrm{e}| = 7.0$ (panel a), $t_2\,|\Omega_\mathrm{e}| = 10.5$ (panel b), and $t_3\,|\Omega_\mathrm{e}| = 17.5$ (panel c). The simulation data (in gray scale, normalized to $10^{-4}\,N_\mathrm{e}$) is compared to the maximum scattering amplitude $\Delta\mu(\bar{\mu}, t)$ obtained from theoretical considerations (solid, colored lines). The dashed, vertical line marks the position of the expected resonant pitch angle cosine μ_res. Red arrows show the predicted amplitude of the resonance peaks for positive and negative $\Delta\mu$ and hint at the slight asymmetry which was mentioned in Sect. 2.6.2. Figure taken from Schreiner et al. (2017b).

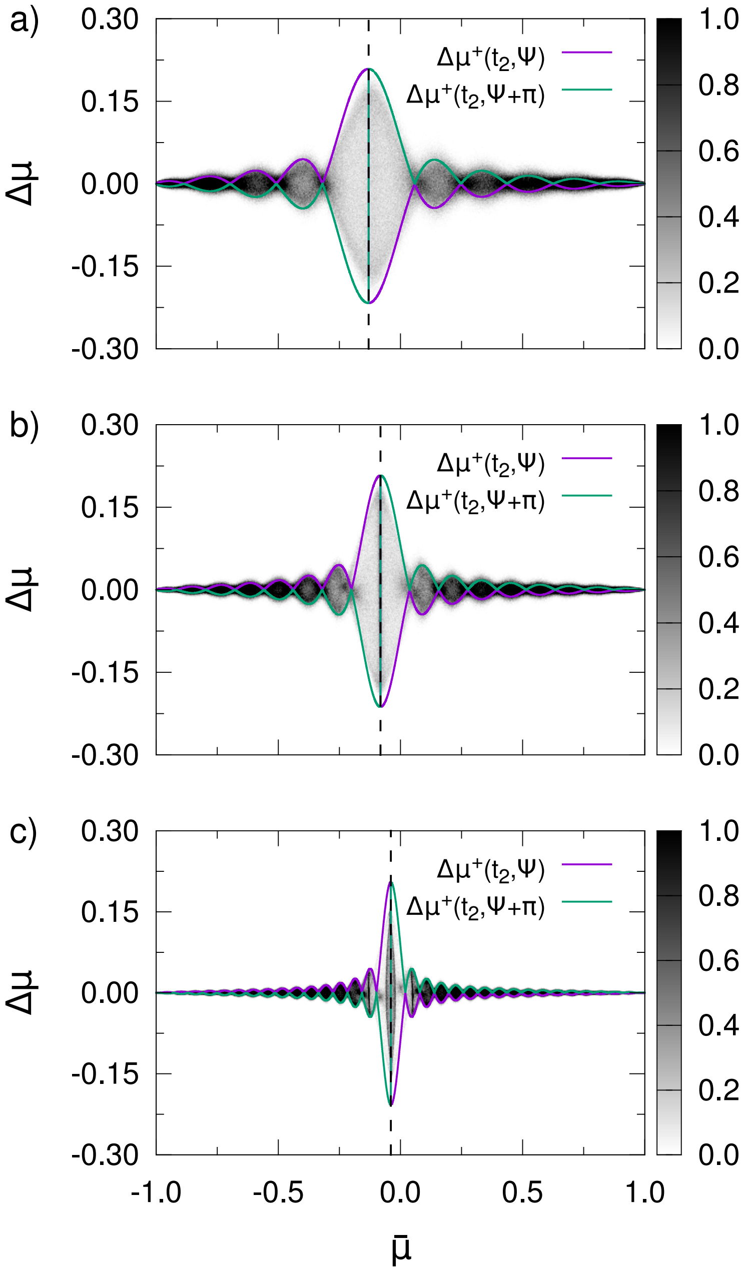

Fig. 4.11: Scatter plots of test electron data in $\bar{\mu}$-$\Delta\mu$-phase space for the three simulations of low energy electrons: S1 (panel a, same as Fig. 4.10 b), S2 (panel b), and S3 (panel c). The plots present the data at one point in time, $t_2\,|\Omega_\mathrm{e}| = 10.5$, and compare it to analytical predictions (solid, colored lines). The dashed, vertical lines mark the positions of the resonant pitch angle cosines μ_res. The color coding of the data is the same as in Fig. 4.10. Figure taken from Schreiner et al. (2017b).

if v_{e} is larger.

Apart from the number of ballistic peaks the three scatter plots in the different panels of Fig. 4.11 also differ in the substructures of the peaks. In panel a) there is no noticeable substructure visible inside the resonance peak, whereas a dark line at $\bar{\mu} = \mu_{\mathrm{res}}$ can be seen in panel b). Panel c) shows a broadened dark substructure inside the resonance peak, which is about to replace the fading outer shape of the resonance. These observations suggest that the time evolution of resonant scattering is slightly faster for higher electron energies.

High Energy Electrons

In the next set of simulations, S4 through S7, the high energy electrons are considered. Note that the background magnetic field B_0 is increased by a factor of ten compared to the previously discussed simulations. This also increases the frequency ω of the excited wave and the cyclotron frequency $|\Omega_{\mathrm{e}}|$ by the same factor. The evolution of wave-particle scattering proceeds on electron cyclotron time scales. Thus, the evolution can now be observed on shorter physical times (in terms of seconds) than for the previous simulations. This also means that the simulations need to cover fewer numerical time steps.

Figure 4.12 depicts test particle data from the four simulations S4 through S7 in panels a) through d). The scattering amplitudes are shown at $t_2\,|\Omega_{\mathrm{e}}| = 10.5$, i.e. at a stage which is comparable to the plots in Fig. 4.11. The parameters for the waves are the same in all four simulations, but the energy of the electrons changes. As mentioned for the case of low energy electrons, this leads to different positions of the resonance in the different simulations, as can be seen in Fig. 4.12, where the dashed lines mark μ_{res} in the different panels.

According to the explanation given previously, the width of the resonance peak (and the widths of the ballistic peaks) decreases with increasing electron energy, as expected. The height, shape, and positions of the peaks (resonance and ballistic) are recovered by the analytical model. However, other than for the low energy electrons, no substructure is visible inside any of the resonance peaks in Fig. 4.12.

One interesting, although expected feature in the plots in Fig. 4.12 is that the height $\Delta\mu_{\mathrm{res}} := \Delta\mu(\mu_{\mathrm{res}})$ of the resonance peak depends on the particle energy. From the analytical model for the scattering amplitude, Eq. (2.142), it is expected that the peak height scales with the inverse of the test electrons' Lorentz factor, i.e. $\Delta\mu_{\mathrm{res}} \propto 1/\gamma_{\mathrm{e}}$. This relation is confirmed by the simulations, as Table 4.5 shows. Table 4.5 lists the amplitudes of the resonance peaks $\Delta\mu_{\mathrm{res},j}$ and the Lorentz factors $\gamma_{\mathrm{e},j}$ for the simulations Sj ($j \in \{5, 6, 7\}$) relative to $\Delta\mu_{\mathrm{res},4}$ and $\gamma_{\mathrm{e},4}$ in simulation S4.

j	$\Delta\mu_{\mathrm{res},j} \,/\, \Delta\mu_{\mathrm{res},4}$	$\gamma_{\mathrm{e},4} \,/\, \gamma_{\mathrm{e},j}$
5	0.85	0.84
6	0.63	0.61
7	0.41	0.40

Table 4.5: Comparison of the amplitudes $\Delta\mu_{\mathrm{res}}$ of the resonance peaks and the test electrons' Lorentz factors γ_{e} for simulations S4 through S7. The data from simulations Sj, with $j \in \{5, 6, 7\}$, are given relative to simulation S4.

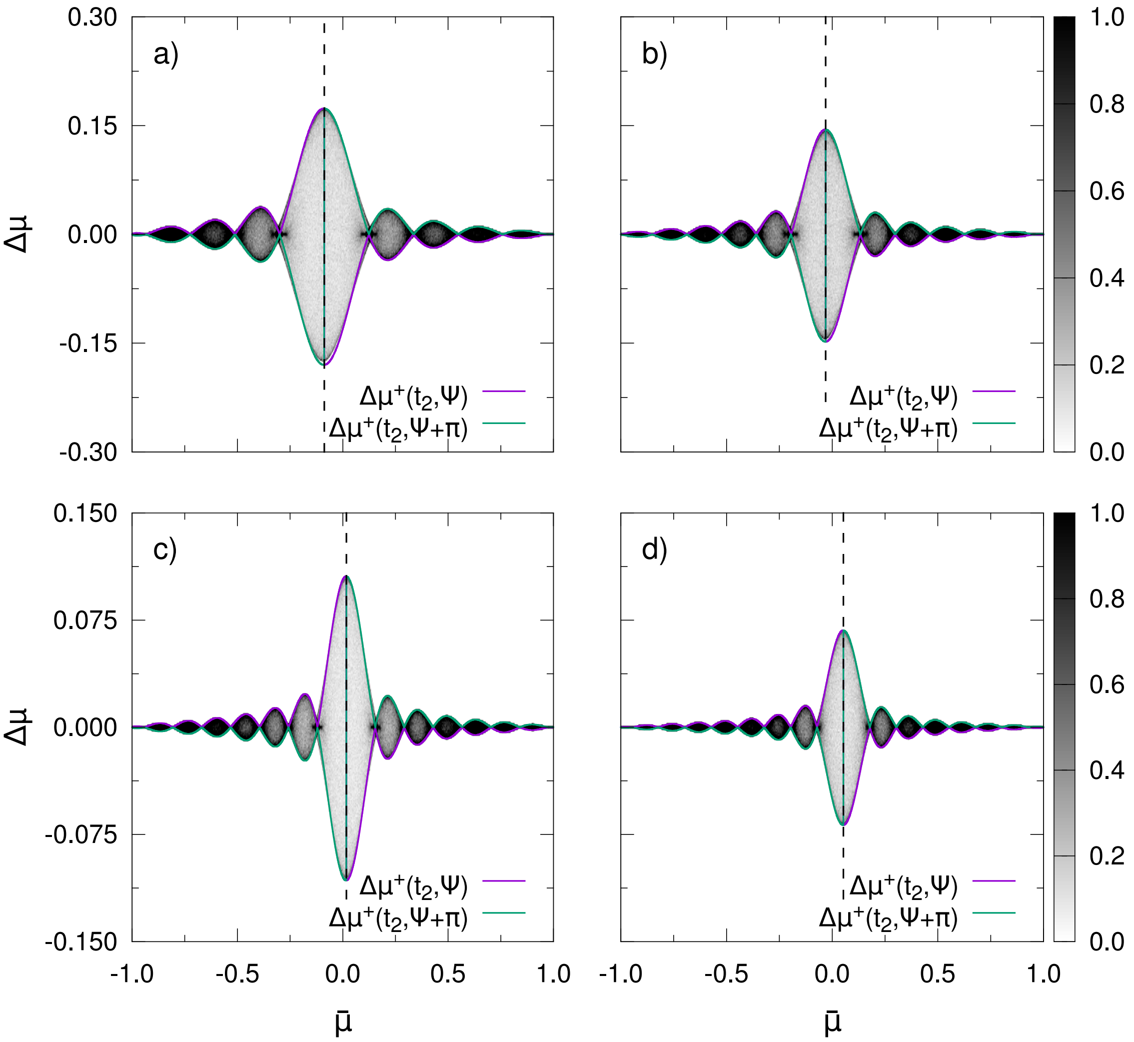

Fig. 4.12: Test particle data from simulations S4 through S7 (panels a through d) is presented in the form of scatter plots in $\bar{\mu}$-$\Delta\mu$-phase space for time $t_2\,|\Omega_\mathrm{e}| = 10.5$. Solid, colored lines show the predictions for the maximum scattering amplitude according to the analytical model presented in Sect. 2.6.2. Dashed vertical lines mark the resonant pitch angle cosines μ_res. The color coded simulation data represents particle density and is normalized to $10^{-4}\,N_\mathrm{e}$, with the total number of test particles N_e. Figure taken from Schreiner et al. (2017b).

4.2.3 Verification of Theoretical Assumptions

So far the results of the PiC simulations are in good agreement with the theoretical model, although the model has been derived using the magnetostatic approximation. It might therefore be interesting to compare full PiC simulations to similar simulations carried out with the simplified test particle code described in Sect. 3.3.3. Differences between the results of the magnetostatic simulations and those of the PiC simulations would hint at additional processes influencing wave-particle scattering in the self-consistent PiC simulations.

The second question, which is addressed in this section, is whether the assumption that pitch angle scattering is the fastest diffusion process is actually valid in the PiC simulation. Pitch angle scattering is therefore compared to momentum scattering of the test electrons, i.e. changes of their energy over time.

Magnetostatic Simulations

Simulation S4 (105 keV electrons) is chosen as a reference setup. Two additional simulations, S14 and S15, are prepared which both use the same setup, but are carried out with different simulation codes. Simulation S14 uses the test particle code from Sect. 3.3.3 with the mechanism for artificial wave propagation. This simulation emulates the full PiC simulation in the sense that the energetic electrons encounter a moving wave with electromagnetic fields that vary with time and space. However, the field fluctuations caused by the thermal background plasma are omitted. The purely magnetostatic code (without wave propagation) is used for simulation S15. This is to be interpreted as a simulation in the rest frame of the plasma waves, i.e. the moving electrons see a static magnetic field, which only exhibits spatial fluctuations. Again, there is no background plasma.

The analytical predictions for the maximum scattering amplitude are calculated in the rest frame of the plasma for simulations S4 and S14, i.e. transforming Eqs. (2.142) and (2.143) by the use of Eqs. (2.144 - 2.150). Since simulation S15 is performed in the rest frame of the wave, Eqs. (2.142) and (2.143) can be applied directly. The theoretical curves are plotted together with the simulation data in Fig. 4.13, where panels a), b), and c) show data from S4, S14, and S15, respectively. The analytical model matches the numerical results in all three cases.

The resonant pitch angle cosine μ_{res} is the same in simulations S4 and S14, as can be seen in Fig. 4.13 a) and b). The data from both simulations exhibits the same features regarding the position and number of ballistic peaks, the amplitude and (non-existent) substructure of the resonance peak, and the general particle density in phase space. As expected, the data from simulation S15 exhibits a different shape of the particle distribution in phase space.

In Fig. 4.13 c) the resonance is shifted compared to panels a) and b), according to the resonance condition in the wave frame, Eq. (2.141). The distribution of the ballistic peaks is also different, in accordance with the analytical theory. Like for the simulations in the plasma frame, there is no substructure inside the resonance peak and the qualitative picture of the phase space density is similar to the results of the other two simulations.

The similarity of the numerical results from the simulations in different rest frames and with different codes and the overall agreement of simulation data and analytical theory suggests that the scattering behavior of energetic particles is well-described by the model. Although the model initially neglects a finite frequency ω and the electromagnetic field δE of the wave, it can be successfully applied to the non-magnetostatic case. The dynamical electromagnetic fields in the PiC simulation do not seem to cause additional effects which are not recovered by the model described in Sect. 2.6.2.

Momentum Diffusion

In the magnetostatic case the particles only interact with magnetic fields, obviously. Therefore they do not change their energy, since scattering off of static fluctuations of the magnetic field only changes the direction of the velocity $\boldsymbol{v}_{\mathrm{e}}$, but not its magnitude. This situation changes in the case of a propagating wave, since the scattering process is not energy-

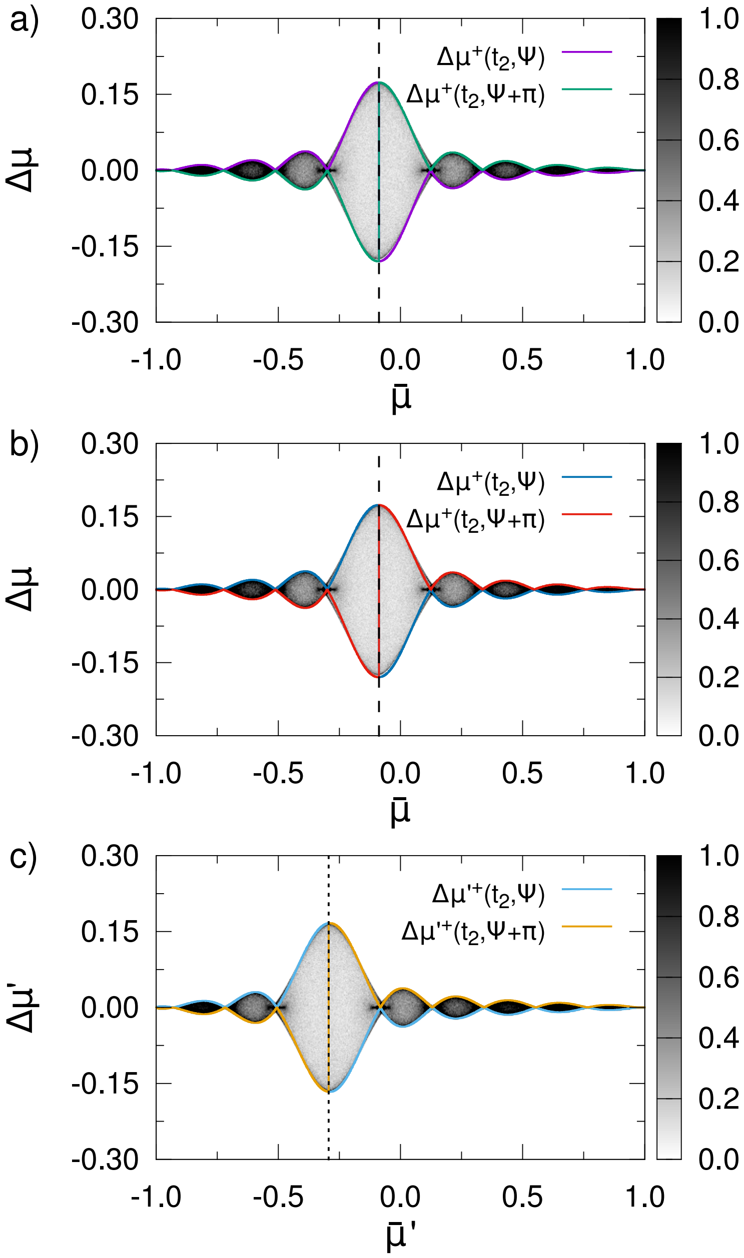

Fig. 4.13: Test electron data from simulations S4 (panel a), S14 (panel b), and S15 (panel c) for time $t_2\,|\Omega_\mathrm{e}| = 10.5$. The scatter plots in panels a) and b) show the particle density in $\bar{\mu}$-$\Delta\mu$-phase space in the rest frame of the plasma, whereas the plot in panel c) depicts the phase space density in the rest frame of the wave ($\bar{\mu}'$ and $\Delta\mu'$). The colored lines show the analytical predictions for the maximum scattering amplitude in the plasma (panels a and b) and in the wave frame (panel c), according to the (transformed) Eqs. (2.142) and (2.143). Dashed and dotted vertical lines mark the positions of μ_res and μ'_res, respectively. Color coding is the same as in Fig. 4.12. Figure taken from Schreiner et al. (2017b).

conserving in the plasma frame (although it is in the wave frame). According to the picture of particle scattering off of moving magnetic fields suggested by Fermi (1949), the particles may gain energy in a "head-on collision" ($\boldsymbol{v}_\mathrm{e} \cdot \boldsymbol{v}_\mathrm{ph} < 0$), while they lose energy in an "overtaking collision" ($\boldsymbol{v}_\mathrm{e} \cdot \boldsymbol{v}_\mathrm{ph} > 0$). Additionally, the electric field of the wave may play a role, although the amplitude of the electric field is small compared to the amplitude of the magnetic field, according to Eq. (2.62).

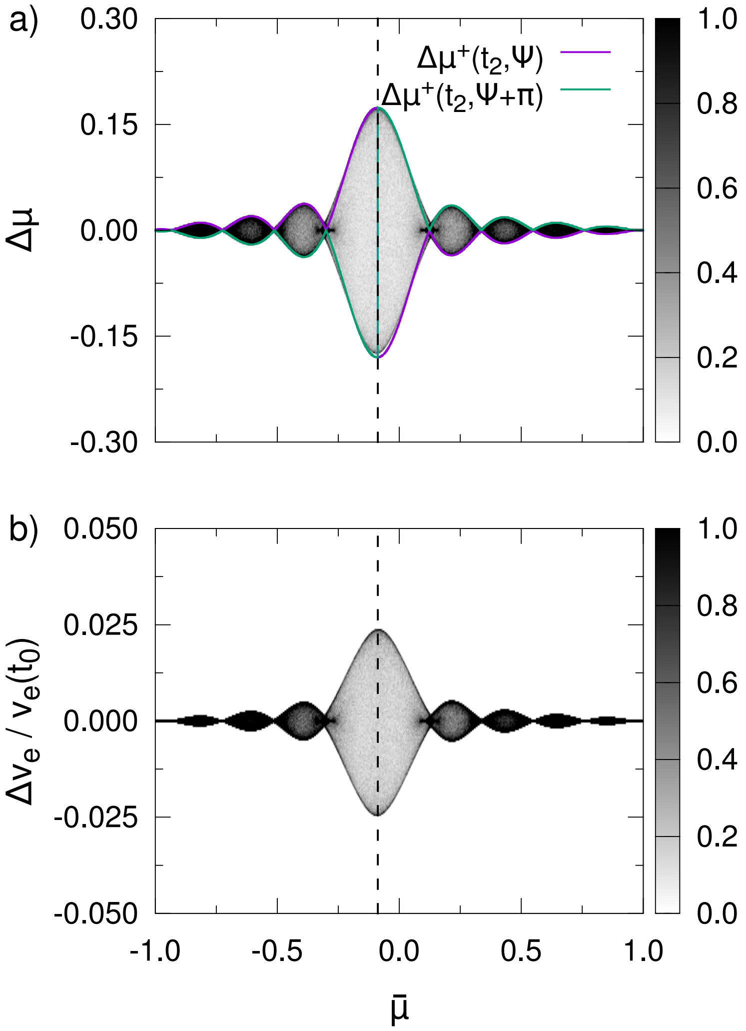

Fig. 4.14: Scatter plots showing test electron data from simulation S4. Panel a) is the same as panel a) in Fig. 4.12 and shows the scattering amplitude $\Delta\mu$ as a function of $\bar{\mu}$, together with the analytical predictions. Panel b) shows the change of the particles' speeds Δv_e relative to the speed $v_\mathrm{e}(t_0)$, which is the same for all particles at the beginning of the simulation. Both panels show data from time step $t_2\,|\Omega_\mathrm{e}| = 10.5$ and have the color coded particle density normalized to $10^{-4}\,N_\mathrm{e}$. The vertical dashed lines mark the position of the resonance, i.e. μ_res. Figure taken from Schreiner et al. (2017b).

Simulation S4 is therefore analyzed with respect to fluctuations of the test electrons' energies. Similar to the scatter plot of the particle density in $\bar{\mu}$-$\Delta\mu$-phase space, a scatter plot in $\bar{\mu}$-Δv_e-space can be obtained from the simulation data. This is shown in Fig. 4.14, which compares pitch angle scattering (panel a) to momentum scattering (panel b). The change of momentum is represented by the relative change of the particles' speeds $\Delta v_\mathrm{e}(t)/v_\mathrm{e}(t_0)$, where $\Delta v_\mathrm{e}(t) = v_\mathrm{e}(t) - v_\mathrm{e}(t_0)$.

As can be seen from Fig. 4.14, the changes of the particles' speeds Δv_e follow a similar pattern as the changes of their pitch angle cosines if plotted as a function of $\bar{\mu}$. This can be explained by considering the energy E_kin and momentum $\boldsymbol{p}_\mathrm{e}$ of a particle in the rest frames of the plasma and the wave. Using the Lorentz transformation of the kinetic energy, the energy of the particle in the wave frame can be expressed by

$$E'_\mathrm{kin} = \gamma_\mathrm{w}\, E_\mathrm{kin} - \gamma_\mathrm{w}\, v_\mathrm{ph}\, p_{\|,\mathrm{e}}, \tag{4.4}$$

where v_ph and γ_w are the phase speed of the parallel propagating wave and the respective Lorentz factor. Since the energy of the particle is conserved in the wave frame, i.e. $\Delta E'_\mathrm{kin} = 0$, the change of the particle's energy in the plasma frame can be written as

$$\Delta E_\mathrm{kin} = v_\mathrm{ph}\, \Delta p_{\|,\mathrm{e}}. \tag{4.5}$$

The change of the parallel component of the particle's momentum can be expressed by the respective quantities in the wave frame, which yields

$$\Delta E_\mathrm{kin} = \gamma_\mathrm{w}\, v_\mathrm{ph}\, \Delta p'_{\|,\mathrm{e}} = \gamma_\mathrm{w}\, v_\mathrm{ph}\, p'_\mathrm{e}\, \Delta\mu'. \tag{4.6}$$

This means that the change of a particle's kinetic energy in the plasma frame is a function of the change of its pitch angle $\Delta\mu'$ in the wave frame. The latter is given by Eq. (2.142), which implies that ΔE_kin is a function of $\bar{\mu}$ that is proportional to the pitch angle scattering amplitude.

The particles' speeds change by up to 2.5% in the example simulation characterized by Fig. 4.14. The relative change of their pitch angle cosine is much larger, indicating that pitch angle scattering is faster and more efficient than momentum scattering. This was one of the preconditions for the derivation and use of the analytical model described in Sect. 2.6.2.

4.2.4 Study of Wave Amplitude

The numerical approach has been validated by running several simulations with setups in accordance with the assumptions of QLT. Since no unexpected deviations of simulation results and analytical theory have been found, it can be assumed that resonant wave-particle interaction is modeled physically accurate in PiC simulations. Therefore, such simulations can now be used to test the limits of QLT, using setups in which the assumptions of QLT are no longer valid.

In the following a series of simulations (S8 through S11) is discussed, in which the amplitude ΔB of the magnetic field of the excited whistler wave is increased step by step. The simulations are based on the reference setup of S4, with changes as indicated in Table 4.4. Results of the simulations are shown in Fig. 4.15 for time $t_2\,|\Omega_\mathrm{e}| = 10.5$ together with the predictions of the analytical model.

Looking at the scatter plots in Fig. 4.15 two main differences between the individual panels are obvious: First, the amplitudes of the resonance and the ballistic peaks increase

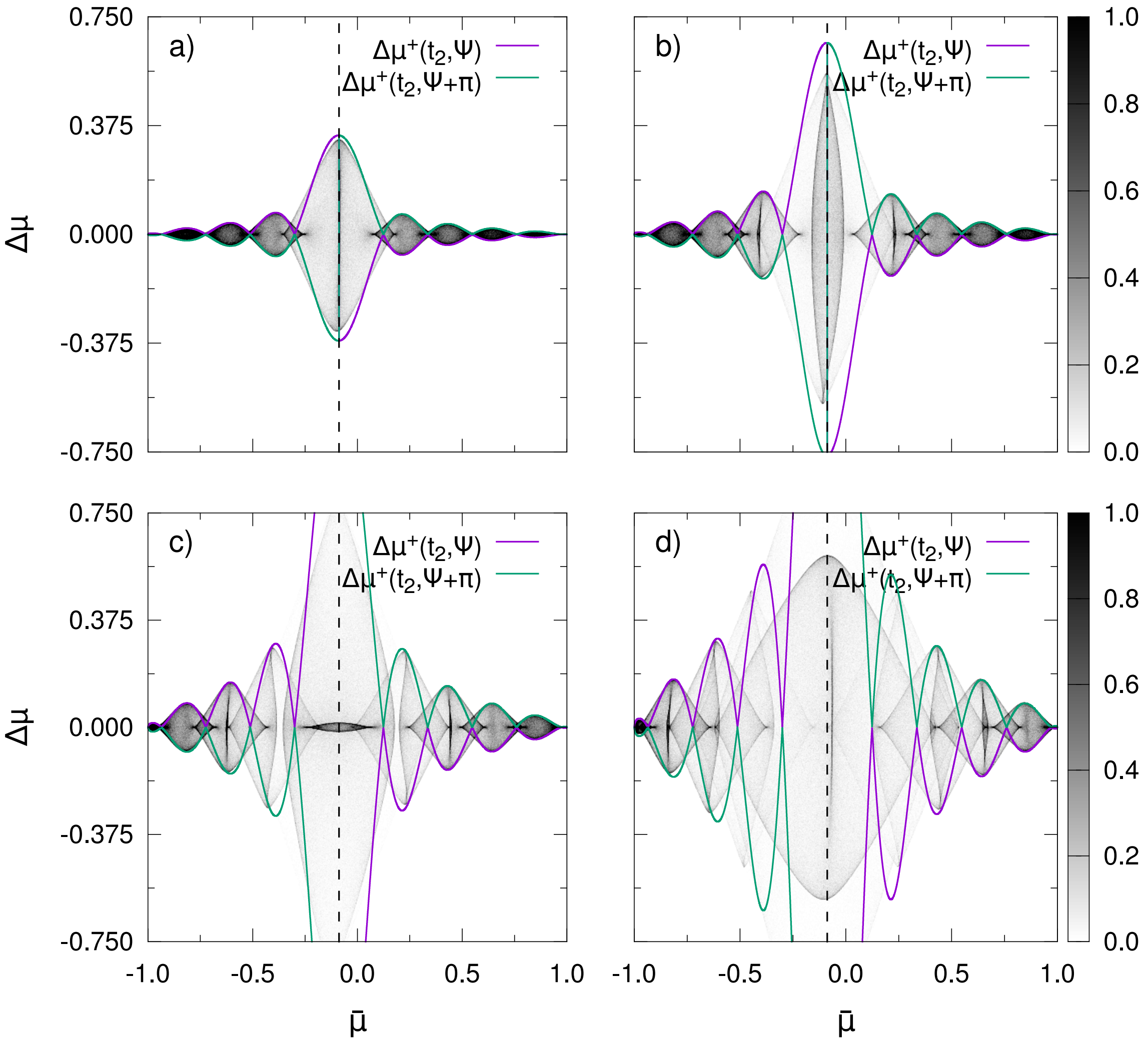

Fig. 4.15: Scatter plots showing the interaction of energetic electrons and whistler waves with different amplitudes. The four panels a) through d) include data from simulations S8 through S11, where the amplitude δB of the magnetic field of the wave is increased step by step. Color coding represents the particle density normalized to $10^{-4}\,N_\mathrm{e}$ and colored lines mark the predicted maximum scattering amplitude. Note that wave numbers and frequencies of the plasma waves, as well as the electron energies are the same in all simulations, resulting in a resonant pitch angle cosine μ_res which is also equal in all setups (as indicated by the vertical, dashed lines). Figure taken from Schreiner et al. (2017b).

from panel a) to d). This is expected and in accordance with Eq. (2.142), which predicts that $\Delta\mu \propto \delta B/B_0$. Secondly, the substructure of the peaks changes with the amplitude δB of the wave's magnetic field. As mentioned earlier, the analytical model does not yield predictions for the particle density in phase space. Therefore, the shape and evolution of substructures can only be studied by numerical simulations.

The ballistic peaks (where $\Delta\mu$ is relatively small) are well-described by the theoretical model concerning their amplitudes and positions. However, especially panel d) of Fig. 4.15

shows an important deviation between theory and numerical results: While the model predicts that the scattering amplitude drops to zero between two neighboring ballistic peaks, it is always finite in the simulation. Considering the substructure of the ballistic peaks it seems that neighboring peaks overlap, producing an envelope which differs from the predicted maximum scattering amplitude.

The shape and amplitude of the resonance peaks are not recovered by the analytical model, as would be expected since the assumptions of a small magnetic field amplitude δB and small changes $\Delta\mu$ of the pitch angle become violated. With increasing amplitude of the resonance peak the asymmetry of the analytical prediction also becomes more pronounced (see especially Fig. 4.15 b). The simulation data is in accordance with the expected resonant pitch angle cosine μ_{res}. Although the position of the substructure inside the resonance peak in panel d) deviates from the dashed line, the maximum peak amplitude can be found at the predicted μ_{res}.

4.2.5 Interaction with Several Waves

In a first attempt to study the interaction of energetic electrons and several waves, two simulations containing two waves each have been carried out. Simulation S12 is a full PiC simulation, whereas S16 uses the magnetostatic test particle code. Both simulations are based on the setup of simulation S4, as can be seen in Table 4.4. The two waves in each simulation have the same frequency and wavelengths, but propagate in opposite directions. Thus, according to the resonance conditions in the plasma and the wave frame, Eqs. (2.131) and (2.141), two resonances are expected which lie symmetrically on opposite sides of $\bar{\mu} = 0$.

To be able to compare the simulation results with the analytical model, it is assumed that the scattering amplitudes caused by the individual waves can be superposed to obtain a total scattering amplitude $\Delta\mu_{\text{total}}$. In the magnetostatic simulation this is achieved by adding up the scattering amplitudes $\Delta\mu'_j$ of the two waves ($j \in \{1, 2\}$):

$$|\Delta\mu'_{\text{total}}(\bar{\mu}')| = |\Delta\mu'_1(\bar{\mu}')| + |\Delta\mu'_2(\bar{\mu}')|. \tag{4.7}$$

The resulting curve is assumed to be the envelope of the particle distribution in $\bar{\mu}'$-$\Delta\mu'$-phase space. A similar approach is chosen for the PiC simulation. However, the scattering amplitudes $\Delta\mu_j(\mu)$ caused by the individual waves have to be calculated separately using the transformations between rest frames, Eqs. (2.144 - 2.150), which are different for the two waves. Care has to be taken when these scattering amplitudes are summed up to form the total scattering amplitude, since $\Delta\mu$ is not symmetric about zero in the plasma frame. However, by the use of piece-wise defined functions it is possible to obtain an analytical function which maintains the asymmetry and describes the total scattering amplitude.

These predictions for $\Delta\mu_{\text{total}}$ and $\Delta\mu'_{\text{total}}$ are shown in Fig. 4.16 together with the test electron data from simulations S12 and S16. The figure depicts the time evolution of the particle density in phase space both in the PiC and the magnetostatic simulation (panels on the left and right, respectively). In the magnetostatic case the analytical approximation describes the data very well over the whole interval of time. The shapes and amplitudes of the resonance and ballistic peaks are reproduced accurately and the simulation data exhibits the expected symmetric shape.

The data from the PiC simulation, however, deviates from the model prediction. While the deviation is not visible at the beginning of the simulation (Fig. 4.16 a), it becomes

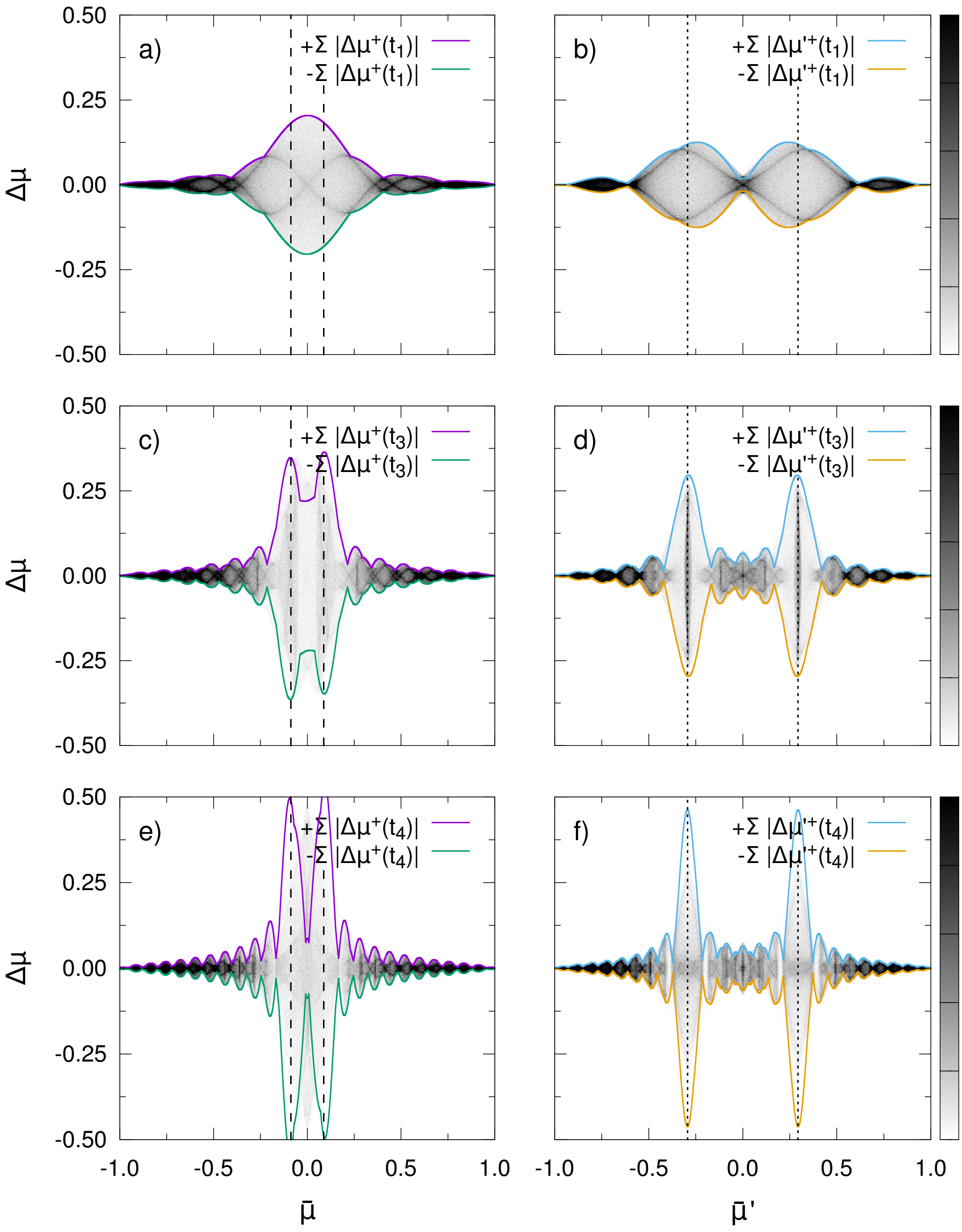

Fig. 4.16: Electron scattering off of two counter-propagating whistler waves with the same frequency and wavelength in a PiC simulation (S12, left panels) and in a magnetostatic simulation (S16, right panels). The particle distribution in phase space and the expected maximum scattering amplitudes are shown at three points in time: $t_1\,|\Omega_\mathrm{e}| = 7.0$ (panels a and b), $t_3\,|\Omega_\mathrm{e}| = 17.5$ (panels c and d), and $t_4\,|\Omega_\mathrm{e}| = 28.0$ (panels e and f). The positions of the resonances in the PiC and in the magnetostatic simulation are marked by the dashed and dotted lines, respectively. The particle density is normalized to $10^{-4}\,N_\mathrm{e}$. Figure taken from Schreiner et al. (2017b).

obvious at later times (Fig. 4.16 b and c). The resonance peaks are closer to $\bar{\mu} = 0$ than expected and merge into a single peak at $\bar{\mu} = 0$ towards the end of the simulation (panel c). This seems to be an effect of the proximity of the two resonances rather than of the PiC simulation, since similar behavior can also be observed in a magnetostatic simulation with a different setup which produces resonances closer to $\bar{\mu}' = 0$ (not shown here). This finding suggests that the assumption of a total scattering amplitude $\Delta\mu_{\text{total}}$, which can be obtained from a superposition of individual $\Delta\mu_j$, is not generally valid.

To further investigate the interaction of particles and several waves, two more simulations including four waves each have been carried out. From the setup of the PiC simulation S13 and the corresponding magnetostatic simulation S18, listed in Table 4.4, it can be seen that the four waves propagate in the same direction, but have different wavelengths, frequencies, and amplitudes. This was meant to emulate a very simple "spectrum" of waves, leading to resonances at different pitch angle cosines.

The results of simulations S13 and S18 are presented in Fig. 4.17. As an estimate for the scattering amplitude a superposition $\Delta\mu_{\text{total}}$ (or $\Delta\mu'_{\text{total}}$ in the magnetostatic case) has been calculated from the scattering amplitudes which are expected for the individual waves. Figure 4.17 shows that the approximated analytical prediction matches the maximum scattering amplitude, but not the shape of the particle distribution in phase space. This is the case for both the PiC (plasma frame) and the magnetostatic simulation (wave frame). While the ballistic scattering at positive $\bar{\mu}$ (or $\bar{\mu}'$) is described relatively well by theory (as expected, since $\Delta\mu$ is small), the resonance peaks are not. The model predicts a structure which indicates the signatures of the individual resonances with the different waves. However, the simulation data presents a different picture: The particle distribution forms only one large "blob" in phase space and no structures can be found which resemble the expected resonance peaks. The electron distributions in both the PiC and the magnetostatic simulations exhibit substructures, mainly forming nearly vertical lines at different pitch angle cosines. One of these lines matches the position of the leftmost resonance, the others, however, do not.

To further analyze the simulations in a more statistical manner the pitch angle diffusion coefficient $D_{\mu\mu}$ is calculated for simulation S13. As a first approximation $D_{\mu\mu}$ is derived from the approximated analytical model using the so-called *running diffusion coefficient* (e.g. Lange et al., 2013, Eq. (24)):

$$D_{\mu\mu} \sim \frac{(\Delta\mu)^2}{2\,\Delta t}, \tag{4.8}$$

where $\Delta t = t - t_0$ is the interval of time from the beginning of the resonant interaction at t_0 to the current point in time t. For the change of the pitch angle, $\Delta\mu$, the approximated function labeled "$+\sum|\Delta\mu^+(t_2)|$" in Fig. 4.17 is inserted into the above equation. The resulting diffusion coefficient as a function of $\bar{\mu}$ is depicted in Fig. 4.18.

Additionally, the pitch angle diffusion coefficient is derived directly from the test electron data, using the "diffusion equation fitting method" presented by Ivascenko et al. (2016) (see Sect. 3.4.1 for a brief description). The obtained $D_{\mu\mu}$ is also shown in Fig. 4.18 and exhibits two main features or peaks, which are not recovered by the approximated running diffusion coefficient. However, although the $D_{\mu\mu}$ derived with the method of Ivascenko et al. (2016) has a different shape than the approximated running diffusion coefficient, the maximum amplitude is almost the same in both cases. The tallest peak is located at the position of maximum scattering amplitude in Fig. 4.17 a), as would be expected. The second most

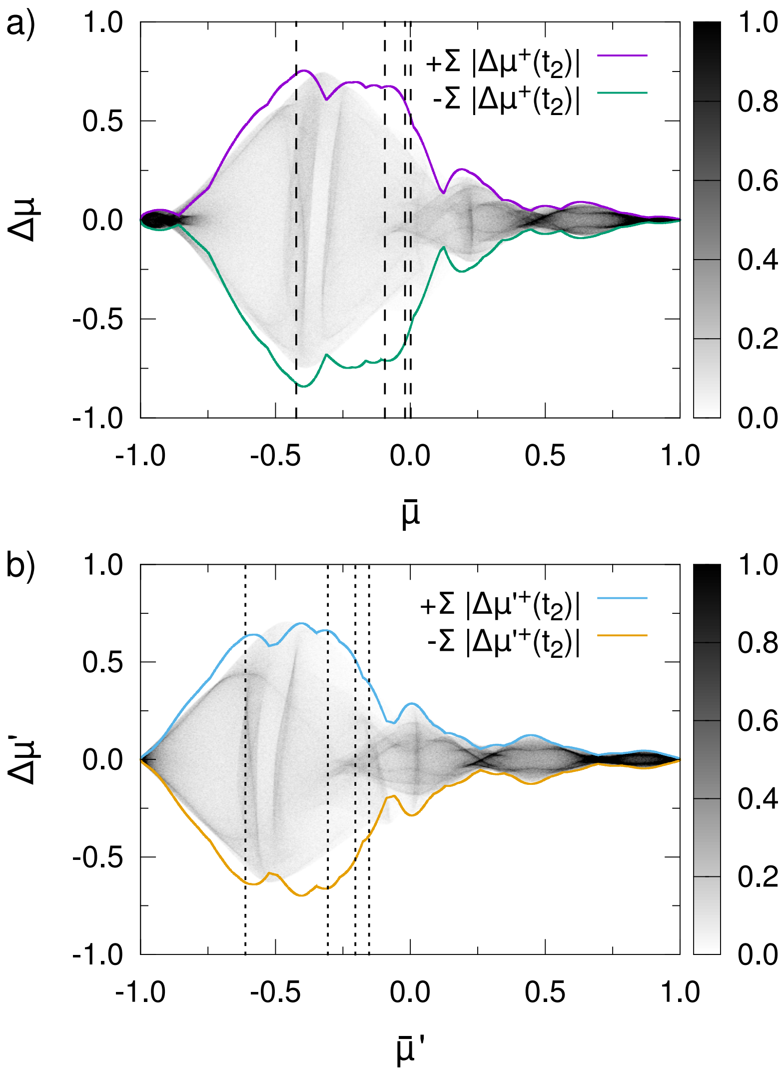

Fig. 4.17: Electron densities in pitch angle phase space for two simulations including four different whistler waves at time $t_2\,|\Omega_\mathrm{e}| = 10.5$. Panel a) shows the data from a full PiC simulation, whereas panel b) presents the results of a magnetostatic simulation. The solid, colored lines are approximated analytical predictions for the maximum scattering amplitude. The positions of the individual resonances with the different waves are indicated by the black dashed and dotted lines in the plasma and the wave frame, respectively. The color coding is the same as in Fig. 4.16. Figure taken from Schreiner et al. (2017b).

prominent peak lies at the position of one of the expected resonances, which is interesting, since it can hardly be guessed from the scatter plot in Fig. 4.17 a). Negative results for $D_{\mu\mu}$ are, of course, physically impossible and can be caused by numerical instabilities. The instabilities do not affect the rest of the data.

It would be interesting to compare the pitch angle diffusion coefficient, which was found from analyzing the simulation data, to a more accurate theoretical model. However, the well-established models, such as the one by Steinacker and Miller (1992), do not consider

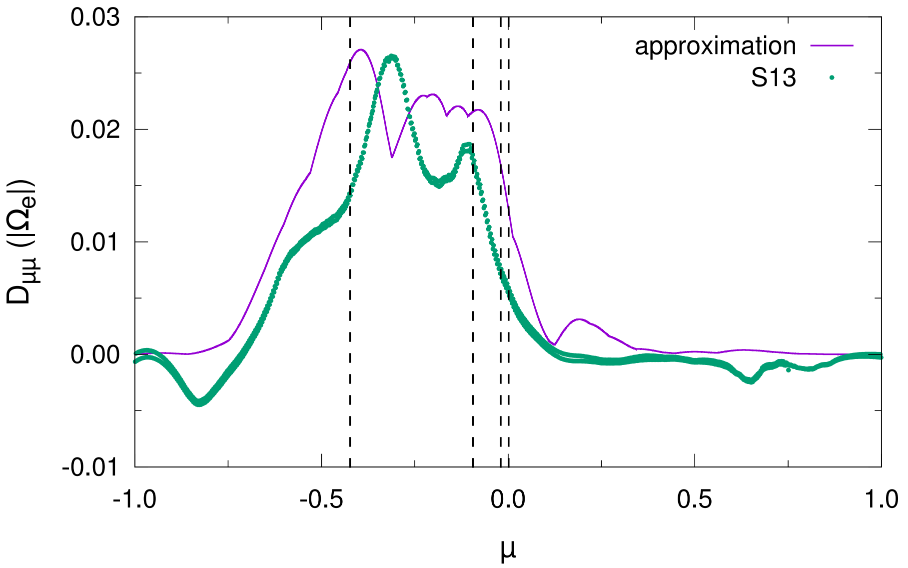

Fig. 4.18: Pitch angle diffusion coefficients $D_{\mu\mu}$ derived from the approximated analytical model (purple line) and calculated from the simulation S13's test electron data using the method of Ivascenko et al. (2016) (green dots, negative results are numerical artifacts). Note that the green dots alternate between two slightly different solutions (especially seen around $\mu = -1$), which is an effect of the numerical method. The data is analyzed for time $t_2 \, |\Omega_\mathrm{e}| = 10.5$. The dashed vertical lines mark the resonant pitch angle cosines μ_res for the interaction with the four individual whistler waves included in S13. Figure taken from Schreiner et al. (2017b).

individual waves, but continuous spectra of multiple waves with different frequencies and wave numbers. Applying such a model to the setup of simulation S13, for example, only yields a $D_{\mu\mu}$ which mainly consists of delta-shaped peaks at the positions of the individual resonances. Besides the question whether such a shape is physically plausible, it is also not well-suited to describe the simulation data.

4.2.6 Analysis of Particle Trajectories

To gain some deeper understanding of the scattering processes which lead to the various shapes of the particle densities in the scatter plots presented in the previous sections, the trajectories of individual test electrons are studied. A random set of test electrons is chosen from a simulation. To track their movement in phase space two quantities are calculated for each particle: The change of the particle's pitch angle cosine between two consecutive output time steps $\Delta\tilde{\mu} = \mu(t_n) - \mu(t_{n-1})$ is obtained from the difference of the pitch angles $\mu(t_n)$ and $\mu(t_{n-1})$ in the n-th and the $(n-1)$-th time step. Similarly the mean pitch angle cosine $\tilde{\mu} = (\mu(t_n) + \mu(t_{n-1}))/2$ can be calculated. Plotting $\Delta\tilde{\mu}$ as a function of $\tilde{\mu}$ yields the trajectory of the particle in phase space.

Figure 4.19 shows the trajectories of 50 test electrons in simulations S4, S9, S11, and S12 (panels a through d) over an interval $\Delta T \, |\Omega_\mathrm{e}| = 70.0$, corresponding to 80 output time steps. As can be seen from Table 4.4, the test electrons in all four simulations have a kinetic energy of $E_\mathrm{kin} = 105\,\mathrm{keV}$. The amplitude of the excited plasma wave is increased

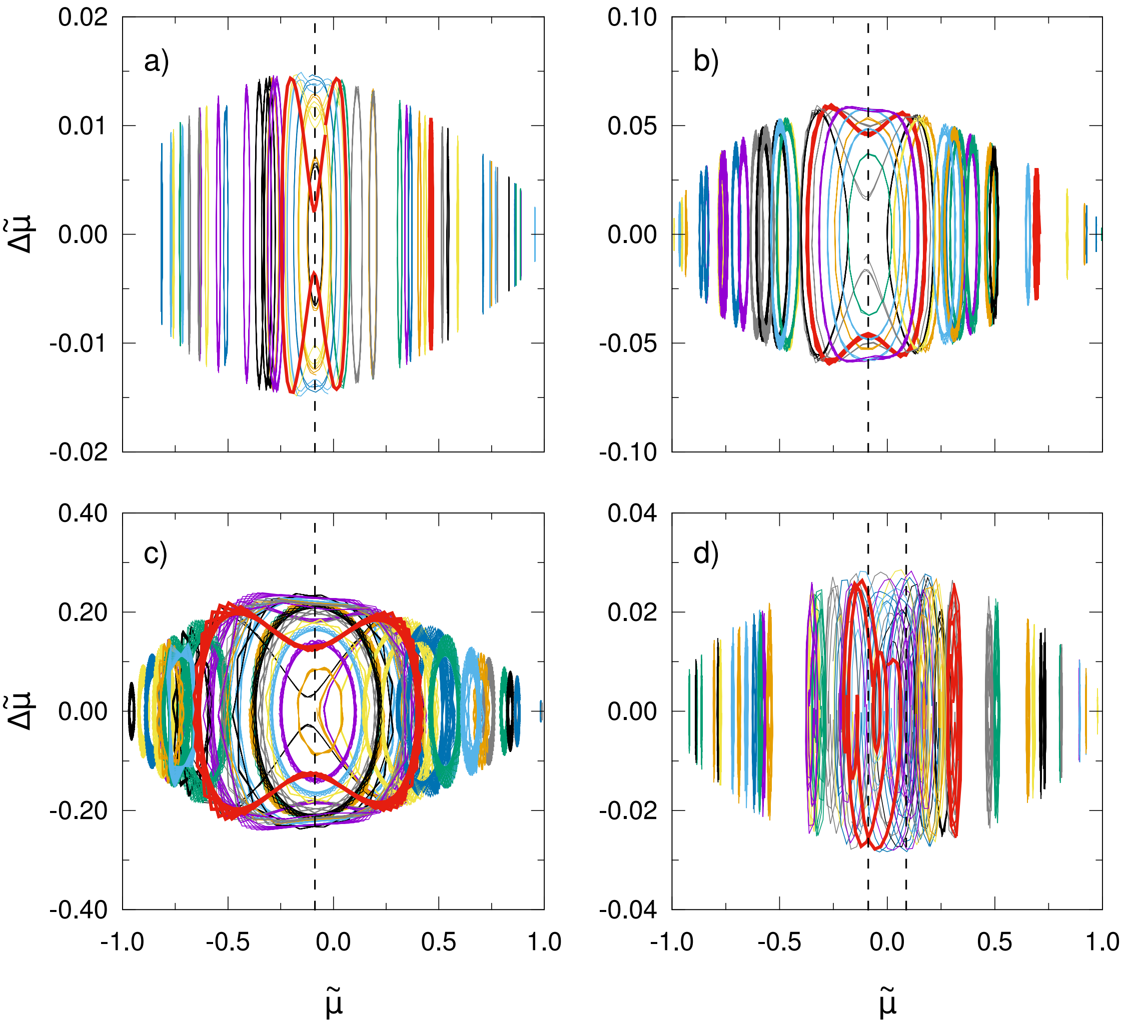

Fig. 4.19: The phase space trajectories of 50 randomly chosen particles from simulations S4 (panel a), S9 (panel b), S11 (panel c) and S12 (panel d) are presented. Dashed, vertical lines mark the positions of resonant pitch angle cosines, the ordinate and abscissa show the change of the pitch angle cosine $\Delta\tilde{\mu}$ between two consecutive output time steps and the mean pitch angle cosine $\tilde{\mu}$ in this interval. The colored lines represent the trajectories of individual particles. Trajectories marked in red are discussed in the text. Figure taken from Schreiner et al. (2017b).

from $\delta B/B_0 = 0.02$ (S4, see Sect. 4.2.2) over $\delta B/B_0 = 0.08$ to $\delta B/B_0 = 0.32$ (S9 and S11, see Sect. 4.2.4). Simulation S12 contains two counter-propagating waves, as discussed in Sect. 4.2.5.

The scattering of electrons and whistler waves was well-described by the analytical model for simulations S4 and S9, whereas the results of S11 and S12 deviated from the prediction. However, it can be seen in Fig. 4.19 that the trajectories of single particles do not differ qualitatively for simulations S4, S9 and S11 (panels a through c). Most particles propagate along closed orbits in phase space, which have an elliptical shape. Far away from the resonant pitch angle cosine μ_{res} the ellipses are very narrow in terms of $\tilde{\mu}$, as can be seen in Fig. 4.19 panels a) and b) on the example of the ellipses at $\tilde{\mu} \sim 0.5$ or $\tilde{\mu} \sim 0.7$, respectively, which are marked in red. Closer to the resonance the ellipses broaden and also gain amplitude (along $\Delta\tilde{\mu}$). Some of the particles run on elliptical trajectories around μ_{res}, whereas some other particles' trajectories have a different shape. There are trajectories around μ_{res} which seem to be formed from the coalescence of two ellipses, which merge at the resonant pitch angle cosine (see the red curves in Fig. 4.19 a), b) and c) near μ_{res}). Overall, the particles' trajectories in simulations S4, S9 and S11 appear to be deterministic instead of diffusive.

The more interesting case is simulation S12, including two whistler waves. Figure 4.19 d) shows the narrow, elliptical trajectories far away from the resonances, which can also be found in the other simulations. However, closer to the two resonances the picture changes. There are curves with an overall elliptical shape, which seem to be criss-crossed by the particle's trajectory several times in a random manner (see the trajectory marked in red near $\tilde{\mu} \sim 0.3$). The other red line (in the interval $-0.25 < \tilde{\mu} < 0.1$) in Fig. 4.19 d) shows the trajectory of a particle which encounters the resonances. This particle does not follow a closed orbit in phase space, but travels along a spiral, which allows it to scatter from the position of one resonance to the other resonance. It can be assumed that this is the signature of micro-physical diffusion.

In the previous sections it could be seen that the analytical model from Sect. 2.6.2 yields a reasonable description of the interaction of particles and a single wave. The test electrons in the simulations exhibit QLT-like behavior when interacting with a wave, i.e. the particle distribution in phase space broadens and shows the expected pitch angle scattering amplitudes. However, the analysis of the phase space trajectories of individual particles proves that the particles propagate along closed orbits. This observation is not in agreement with the idea of pitch angle diffusion.

Sudan and Ott (1971) describe the interaction of particles and a single whistler wave in a way which explains the closed orbits in phase space. They argue that the field fluctuations caused by the wave can be seen as a series of potential wells along the direction in which the wave propagates. Electrons can then become trapped inside these potential wells. An equation of motion for the electrons in the rest frame of the wave is derived by Sudan and Ott (1971), which can be written as

$$\frac{dv'_{\parallel\,\mathrm{e}}}{dt'} = \frac{\delta B'}{B_0} \frac{|\Omega_{\mathrm{e}}|}{\gamma'_{\mathrm{e}}} \sin(k'_{\parallel}\, z'\, t + \phi'), \tag{4.9}$$

if the wave propagates parallel to $\boldsymbol{B}_0 \,||\, \hat{\boldsymbol{z}}$. Here, z' is the spatial coordinate along the direction of the wave's propagation, ϕ' is the azimuth angle of the particle, and $v'_{\parallel\,\mathrm{e}}$ and γ'_{e} are the particle's parallel velocity component and Lorentz factor. Equation (4.9) describes an effective potential which is fluctuating in space, thus creating the aforementioned potential wells. Particles with a parallel speed $v'_{\parallel\,\mathrm{e}} = \Omega_{\mathrm{e}}/(\gamma'_{\mathrm{e}}\, k'_{\parallel})$ become trapped in the potential wells and can only oscillate back and forth along the wave in a limited range. However, this speed is the same as the one obtained from the resonance condition in the wave frame, Eq. (2.141). Thus, resonant interaction of particles and a single wave corresponds to an effective trapping of the particles, which prevents diffusion. Non-resonant particles hardly interact with the wave and can escape the potential wells.

The oscillation of trapped particles inside the potential wells can be described in terms of their parallel speed. According to Sudan and Ott (1971) the parallel speed of a trapped electron lies in the interval

$$\Delta v'_{\parallel\,\mathrm{e}} \approx 2^{3/2} \sqrt{\frac{\delta B'}{B_0} \, \frac{\Omega_\mathrm{e}}{\gamma'_\mathrm{e}} \, \frac{v'_\mathrm{e}\,(1-\mu'^2)^{1/2}}{k'_\parallel}}, \tag{4.10}$$

which can be divided by v'_e to yield an interval $\Delta\tilde{\mu}_\mathrm{trap}$ in pitch angle space. Inserting $\mu' = \mu'_\mathrm{res}$ and $v'_\mathrm{e} = v'_\mathrm{e}(\mu')$ into Eq. (4.10) allows to calculate the interval width at the position of the resonant pitch angle cosine. After the results have been transformed into the plasma frame, they can be directly compared to the width (along $\tilde{\mu}$) of the ellipses centered around μ_res in panels a), b), and c) of Fig. 4.19. For the three panels the values $\Delta\tilde{\mu}_\mathrm{trap} = \{0.23,\, 0.46,\, 0.93\}$ can be obtained, which are in good agreement with the maximum widths of the particle trajectories in Fig. 4.19. These findings support the claim that no pitch angle diffusion occurs if only a single plasma wave is available for scattering. Resonant particles become trapped in potential wells created by the fields of the wave and follow closed orbits in phase space, whereas non-resonant particles are not affected by trapping effects (i.e. ballistic transport). Pitch angle diffusion only arises from the interactions of particles and several waves, as can be seen in Fig. 4.19 d).

4.2.7 Résumé

In the previous sections the interaction of energetic electrons and whistler waves has been studied. PiC simulations have been compared to the analytical model of Lange et al. (2013) derived in the framework of magnetostatic QLT, which was presented in Sect. 2.6.2. If the preconditions for the validity of the QLT approach are met by the setup for the simulation, the results match the model predictions very well. This can be seen as a validation of the simulation results.

In Sect. 4.2.3 it was shown that momentum diffusion occurs in the PiC simulations. However, the change of the particles' energies is relatively small and pitch angle scattering can be seen as the fastest, most influential process.

Simulations with increased amplitudes δB of the magnetic field of the excited whistler wave have been studied in Sect. 4.2.4 and compared to the analytical model. As expected, the model is not able to reproduce the simulation results if δB becomes large compared to the background magnetic field B_0. However, the model still yields a surprisingly good approximation of the simulation results, at least reproducing the amplitudes and positions of the ballistic peaks.

The analytical model was derived for the interaction of particles and a single wave. Although it was expected that the model can be extended to reproduce the scattering characteristics of particles and several waves, this is not generally the case. The simulations in Sect. 4.2.5 show that a correct total scattering amplitude can only be obtained if the resonant pitch angle cosines μ_res for the individual waves are far apart from each other. Especially in the case of simulation S12, where four waves are included, the analytical model fails completely and cannot reproduce the shape of the particle distribution in phase space.

The most interesting result of the extended study of wave-particle interaction in the simplified setup with only one wave is that no micro-physical diffusion occurs. Although the particle distribution in phase space develops according to the QLT predictions, the trajectories of the individual test electrons are closed orbits in pitch angle phase space. This is consistent with the idea of Sudan and Ott (1971), who argue that the wave creates a series of potential wells, which are able to trap particles. They derive that resonant particles become trapped and are only able to oscillate inside their respective potential wells, which prevents diffusion. Non-resonant particles can escape the potential wells and propagate more or less along undisturbed orbits, which is comparable to the idea of ballistic transport.

These findings imply that several waves with different wave numbers and frequencies are required for pitch angle diffusion. Sect. 4.2.5 shows that two counter-propagating waves are already sufficient to cause diffusion, as can be seen when looking at the particle trajectories in Fig. 4.19 d). More complex simulations, including a whole spectrum of (turbulent) waves, are expected to exhibit stronger diffusion processes. Here it might also be possible to apply more advanced theoretical models, such as those by Steinacker and Miller (1992) or Vainio (2000), to describe the simulation results. The pitch angle diffusion coefficient $D_{\mu\mu}$ or the particles' mean free path could then be derived from the simulation data and compared to model predictions.

The interaction of particles and dispersive waves is harder to handle by theory than the interaction with non-dispersive waves. In the latter case it is possible to derive a model in the rest frame of the waves, since they all have the same phase speed. This is, however, not possible for dispersive waves, which have different phase speeds at different frequencies and wave numbers. Therefore, the full dispersion relations of the relevant plasma waves have to be coupled to the equations needed to derive resonant interactions. This is done by Steinacker and Miller (1992) and Vainio (2000). With the transformations between rest frames, which are presented in Sect. 2.6.2, the full dispersion relations are implicitly coupled to the model of Lee and Lerche (1974) and its advancement by Lange et al. (2013), as well.

Although the model of Lange et al. (2013) describes the behavior of single particles, it can also be used to derive properties of a whole particle population. As can be seen in the scatter plots, which have been shown in the previous sections, the analytical prediction for the maximum scattering amplitude $\Delta\mu$ can be interpreted as the envelope of the particle distribution in phase space. The exact phase space distribution can then be sampled by the use of a large number of test particles in a kinetic simulation. The simulations discussed in this work have revealed that the particle distribution is not homogeneous in phase space, but that there are density fluctuations which follow distinct patterns. These patterns, however, are not predicted by the analytical model.

It can therefore be argued that self-consistent simulations of large numbers of particles offer a new and different perspective of wave-particle interaction. Since additional effects, such as temperature, which are often neglected in theory, can be easily included in numerical models, simulations can improve and extend the understanding of complex physical processes, such as the wave-particle resonance and pitch angle scattering. Numerical studies including a spectrum of different waves, such as Gary and Saito (2003), are therefore a viable next step.

4.3 Kinetic Turbulence

As a further topic of this thesis, simulations of kinetic turbulence will be discussed. In Sect. 2.5.2 the theoretical understanding of turbulence in the kinetic regime was summarized. While there is some knowledge about the processes in the dispersive or dissipative range of the spectrum, many details are still unclear, making it difficult to find a suitable model on which simulations can be based.

For the work at hand a focus on whistler turbulence has been chosen. However, this is not meant to imply that kinetic Alfvén waves (KAWs) should be excluded as constituents of the turbulence spectrum in the kinetic regime. While simulations of KAWs would be technically feasible, a PiC code would not be the best choice for this endeavor. The frequencies of KAWs are too low to be resolved with reasonable computational effort. Whistler waves, on the other hand, allow for much more convenient simulations. However, numerical convenience is not the only reason for choosing whistler waves. Observations clearly show that fluctuations above the proton cyclotron frequency can be found in the solar wind. These fluctuations cannot be explained by kinetic Alfvén waves and are therefore assumed to be whistler waves.

The study of whistler turbulence will be subdivided into three sections, beginning with a validation of the code by comparing results from test simulations to existing work known from literature. The second part contains new simulations and focuses on the spectral energy distribution. Lastly, the transport of energetic electrons in turbulence will be discussed.

4.3.1 Validation

The numerical setups described by Gary et al. (2008) and Gary et al. (2012) are chosen as test problems for the validation of simulations of whistler turbulence. The former specify a two-dimensional PiC simulation of decaying whistler turbulence, and the latter discuss a series of three-dimensional simulations otherwise using the same setup. Both articles give very detailed descriptions of the physical and numerical parameters used and the exact initial conditions of their simulations, which serves as an excellent basis for the reproduction of their numerical experiments.

Setup and Analysis Methods

A summary of the physical and numerical parameters used in simulations T1 and T2 (“T” denotes “turbulence”) can be found in Tables 4.6 and 4.7. The two simulations are based on the setups of one of the three-dimensional simulations from Gary et al. (2012) (T1) and the two-dimensional version thereof presented in Gary et al. (2008) (T2). They will both be discussed in more detail in the following.

$\omega_{\mathrm{p,e}}\,(\mathrm{rad\ s^{-1}})$	$\lvert\Omega_{\mathrm{e}}\rvert\,(\omega_{\mathrm{p,e}})$	$v_{\mathrm{th,e}}\,(c)$	$\delta B^2/B_0^2$	β
$1.966 \cdot 10^8$	0.447	0.10	0.10	0.20

Table 4.6: Physical parameters for simulations T1 and T2: plasma frequency $\omega_{\mathrm{p,e}}$, cyclotron frequency Ω_{e}, and thermal speed $v_{\mathrm{th,e}}$ of the electrons, the sum δB^2 of the squares of the magnetic field amplitudes of the individual waves, and the plasma beta β. Note that the ratio $\delta B^2/B_0^2$ is defined as the parameter ϵ_0, which is used to reference the different simulations in Gary et al. (2012).

Both simulations employ the natural mass ratio and are initialized using the method for wave excitation described in Sect. 3.3.1. The three-dimensional simulation T1 includes initial waves at 150 different positions in (discretized) wave number space, whereas the two-dimensional simulation T2 contains 42 excited waves. The layout of the initial waves in wave number space is explained below and sketched in Fig. 4.20 for the two-dimensional setup.

In the two-dimensional case the background magnetic field $\boldsymbol{B}_0$ points in z-direction and the simulation box covers the x-z-plane. Three waves are excited at the three lowest pos-

simulation	$N_{\parallel}\,(\Delta x)$	$N_{\perp}\,(\Delta x)$	$N_t\,(\Delta t)$	$\Delta x\,(c\,\omega_{\mathrm{p,e}}^{-1})$	$\Delta t\,(\omega_{\mathrm{p,e}}^{-1})$	ppc
T1	512	512	$2.0 \cdot 10^4$	0.10	0.05	128
T2	1024	1024	$1.0 \cdot 10^5$	0.10	0.05	128

Table 4.7: Numerical parameters for simulations T1 and T2: number of cells $N_{\parallel}$ and $N_{\perp}$ in the directions parallel and perpendicular to the background magnetic field $\boldsymbol{B}_0$, number of time steps N_t, grid spacing Δx, time step length Δt, and ppc, i.e. the number of particles (electrons and protons combined) per cell. Note that T1 is a three-dimensional simulation where $N_{\perp}$ describes the box size in both directions perpendicular to $\boldsymbol{B}_0$.

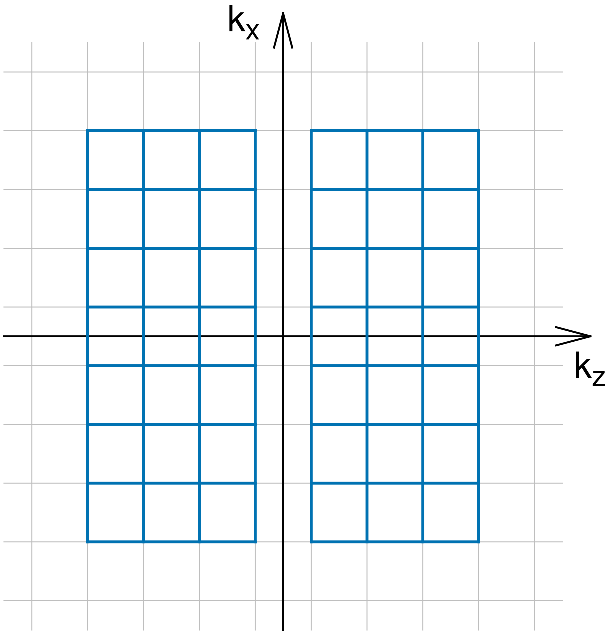

Fig. 4.20: Schematic representation of two-dimensional wave number space. The discretized wave vectors are represented by the gray boxes, the axis mark the directions parallel (k_z) and perpendicular (k_x) to the background magnetic field $\boldsymbol{B}_0$ in the case of a two-dimensional simulation. For the simulation of decaying turbulence in two dimensions, a set of 42 initial waves is excited, where each wave occupies one position on the grid. These positions are indicated by the blue boxes, in accordance with the setup specified by Gary et al. (2008).

sible purely parallel wave numbers. Another three are initialized with opposite direction of propagation, i.e. anti-parallel to $\boldsymbol{B}_0$. The rest of the waves is organized in four blocks, one in each quadrant of the x-z-plane in k-space. Each block consists of a three by three matrix of wave numbers, starting with the lowest possible (finite) values of $k_{\parallel}$ and $k_{\perp}$.

In the three dimensional case the setup for the excited waves is similar. However, instead of limiting the excited waves to the x-z-plane, the block layout is also applied to the y-z-plane and the two planes defined by the z-direction and the two diagonals of the x-y-plane. This increases the total number of initialized waves to 150. A more detailed description, including the values of the respective wave numbers, can be found in Gary et al. (2012).

The excited waves are initialized with equal amplitudes and a random phase angle. The total magnetic energy density of the initial waves is set to 10% of the energy density of the background magnetic field. As indicated in Table 4.6, this can be expressed by $\delta B^2/B_0^2 = 0.1$, where $\delta B^2 = \sum_j \delta B_j^2$ and j is used to index the individual waves.

To analyze the simulations, the spectra of the magnetic energy density $E_B = |\boldsymbol{B}^2(\boldsymbol{k})|/(8\,\pi)$ in wave number space are considered. A two-dimensional energy spectrum, i.e. $E_B(k_\parallel,\, k_\perp)$, can be obtained by Fourier transforming the field data and integrating over the angle ϕ in the x-y-plane to obtain the perpendicular coordinate $k_\perp$. The parallel direction is equivalent to the z-direction. Similarly, a one-dimensional spectrum $E_B(k)$ can be obtained by integrating over the angle θ in the $k_\parallel$-$k_\perp$-plane. Additional one-dimensional spectra $E_B(k_\parallel)$ and $E_B(k_\perp)$ are obtained by integrating $E_B(k_\parallel,\, k_\perp)$ over $k_\perp$ and $k_\parallel$, respectively.

Gary et al. (2012) suggest further methods for analysis, such as tracking the total magnetic energy of the plasma waves and the kinetic energy of the particles (i.e. the temperature) over time. However, this is omitted here for brevity.

3D Simulation

Figure 4.21 shows the distribution of the magnetic energy in $k_\parallel$-$k_\perp$-space. The two panels show data from simulation T1 at two points in time: Panel a) depicts the initialized energy distribution, which is concentrated at small wave numbers, whereas panel b) presents the spectrum of the fully developed turbulence after half of the simulation. Note that the data in each panel is taken from a single time step, which does not allow to deduce the exact direction of propagation, although the angle θ between the wave vector $\boldsymbol{k}$ and $\boldsymbol{B}_0$ can be derived. In particular, it cannot be distinguished between propagation parallel or anti-parallel to $\boldsymbol{B}_0$. Thus, θ is confined to the range $0 \leq \theta \leq \pi/2$.

The spectra in Fig. 4.21 are produced using all components of the magnetic field. Thus, the signature of the background field can be seen as a red spot at $k_\parallel = k_\perp = 0$. Panel a) depicts the initial energy distribution of the excited waves. Note that there is more energy in the oblique waves than in the purely parallel waves, since the integration over the azimuth angle ϕ implies that several oblique waves are mapped to the same bin and their energy contents are summed up. In Fig. 4.21 b) the block structure of the initially excited waves can still be seen, although the energy has decreased especially at higher $k_\perp$. The spectrum shows the expected wave number anisotropy: Energy is transported preferentially to larger $k_\perp$, whereas the cascade to higher $k_\parallel$ is slower and shorter.

The two-dimensional energy spectrum in Fig. 4.21 b) is qualitatively in good agreement with the spectra shown in Gary et al. (2012, Fig. 3), although their spectra are shown for a higher initial energy density of the waves[36].

One-dimensional magnetic energy spectra are shown in Fig. 4.22. Panel a) depicts the energy $E_B(k)$ as a function of the absolute of the wave vector at different points in time during simulation T1. Again, the initial configuration of the excited waves is seen in a narrowly confined region. At later times the spectrum extends to larger k, spanning more than one order of magnitude in wave number and approximately seven orders of magnitude in energy. In accordance with the simulations discussed by Gary et al. (2012), a steady state is established after an interval of roughly $t\,|\Omega_\mathrm{e}| \approx 100$. After this time the spectral slope

---

[36] Note that they plot $k_\perp$ on the abscissa and $k_\parallel$ on the ordinate. They also seem to be able to retrieve information about the exact direction of the wave vector, although they do not state how this is done.

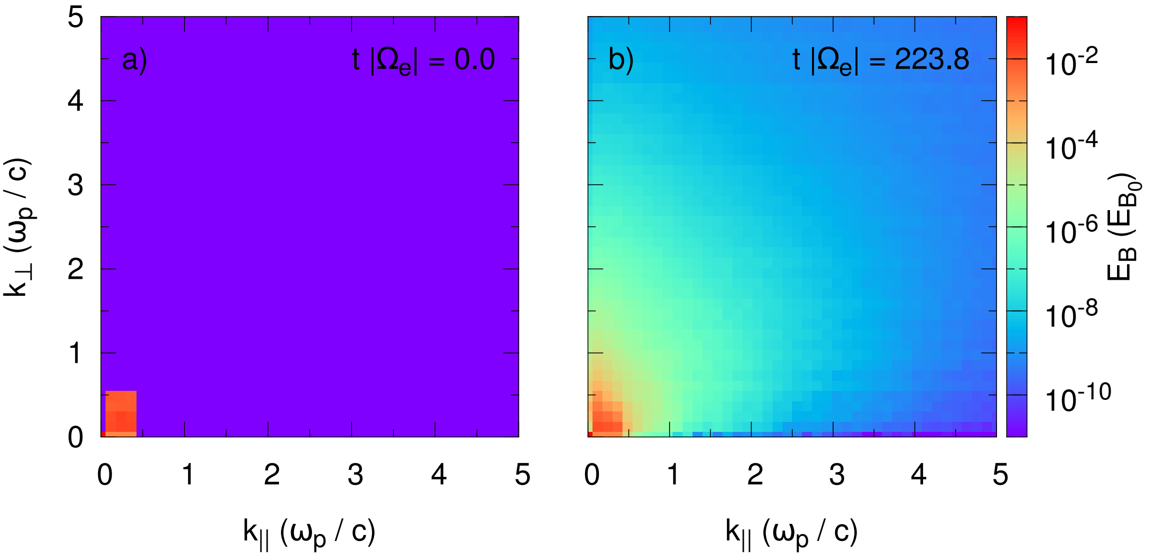

Fig. 4.21: Distribution of the magnetic energy E_B in wave number space at two points in time during simulation T1. The energy is normalized to the energy E_{B_0} of the background magnetic field. Panel a) shows the energy distribution at the beginning of the simulation, where only a few initial waves are excited at small wave numbers. Panel b) depicts the fully developed spectrum after half of the simulation. An anisotropic cascade is developed, which preferentially transports energy to higher perpendicular wave numbers.

hardly changes. However, since the turbulence is only decaying, i.e. not driven by a constant energy input, the overall energy level drops slightly towards later time steps.

As can be seen in Fig. 4.22 a) the energy reaches a minimum around $k\,c/\omega_\mathrm{p} \approx 8$. At larger k the energy increases again and forms a plateau at even larger wave numbers. This indicates that the regime above $k\,c/\omega_\mathrm{e} \approx 8$ is dominated by numerical noise, which increases with time. The increase can be partly attributed to the rising temperature of the plasma due to the decaying waves (see Gary et al., 2012, Fig. 1 b), leading to a higher level of thermal fluctuations. However, numerical effects most likely also contribute to the rise of the noise level at high k. It is therefore advisable to analyze the energy spectra only up to the wave number of the minimum energy.

Panel b) of Fig. 4.22 shows the magnetic energy density as a function of the parallel and perpendicular component of the wave vector. The distinction between $k_\|$ and $k_\perp$ is helpful, since the transport of energy in wave number space is anisotropic, as Fig. 4.21 b) depicts. In the literature it is also common to only discuss the perpendicular energy spectrum $E_B(k_\perp)$, which makes it necessary to produce these kinds of spectra. The energy distribution is assumed to follow a power law, as discussed in Sect. 2.5:

$$E_B(k_\|) \propto k_\|^{\sigma_\|}, \tag{4.11}$$

$$E_B(k_\perp) \propto k_\perp^{\sigma_\perp}. \tag{4.12}$$

As an example, the spectral indices $\sigma_\|$ and $\sigma_\perp$ are derived from a power law fit to the data for one point in time, as presented in Fig. 4.22 b). For the parallel spectrum a constant

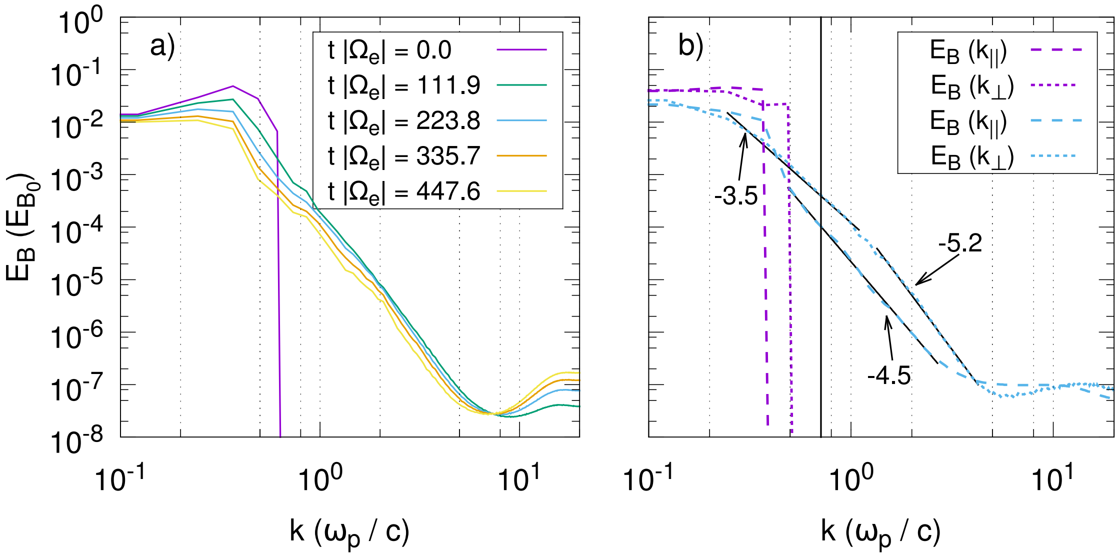

Fig. 4.22: One-dimensional energy spectra obtained from the magnetic field data of simulation T1. The magnetic energy E_B is shown as a function of the absolute of the wave vector $k = |\boldsymbol{k}|$ in panel a). The different lines represent spectra obtained at different points in time during the simulation. In panel b) the magnetic energy is shown as function of both $k_{\|}$ and $k_{\perp}$ for two points in time: $t\,|\Omega_{\mathrm{e}}| = 0.0$ (purple lines) and $t\,|\Omega_{\mathrm{e}}| = 223.8$ (blue lines). Power law fits are applied to these spectra (black lines) to obtain the spectral indices indicated by the three numbers in the plot. The vertical black line close to $k\,c/\omega_{\mathrm{p}} \approx 0.7$ marks the minimum parallel wave number at which cyclotron damping is expected. The energies in both panels are normalized to E_{B_0}, the energy of the background magnetic field.

slope over the whole range of parallel wave numbers can be found, resulting in $\sigma_{\|} = -4.5$. This is interesting, because cyclotron damping of parallel propagating waves sets in around $k\,c/\omega_{\mathrm{p}} \approx 0.7$, indicated by the vertical black line in Fig. 4.22 b). However, the onset of cyclotron damping does not seem to have an effect on the spectrum.

Contrary to the parallel spectrum, the perpendicular spectrum $E_B(k_{\perp})$ exhibits a break around $k_{\perp}\,c/\omega_{\mathrm{p}} = 1$, in agreement with the results of Gary et al. (2012) and observational data by Alexandrova et al. (2009) and Sahraoui et al. (2009, 2010). The spectral indices $\sigma_{\perp} = -3.5$ before and $\sigma_{\perp} = -5.2$ after the break are similar to those obtained by Gary et al. (2012, Fig. 4)[37]. According to Saito et al. (2008), the spectral break and the steepening at higher wave numbers can be attributed to nonlinear Landau damping of obliquely propagating whistler waves. However, this has not been explicitly tested for simulation T1.

2D Simulation

The two-dimensional simulation T2 can be analyzed in the same way as T1. Figure 4.23 shows the two-dimensional energy distribution in wave number space at early (panel a) and late times (panel b) during the simulation T2. The energy distribution is shown for the same point in time in Fig. 4.21 b) and Fig. 4.23 a) for simulations T1 and T2, respectively. In direct

---

[37] Unfortunately, Gary et al. (2012) do not provide parallel spectra.

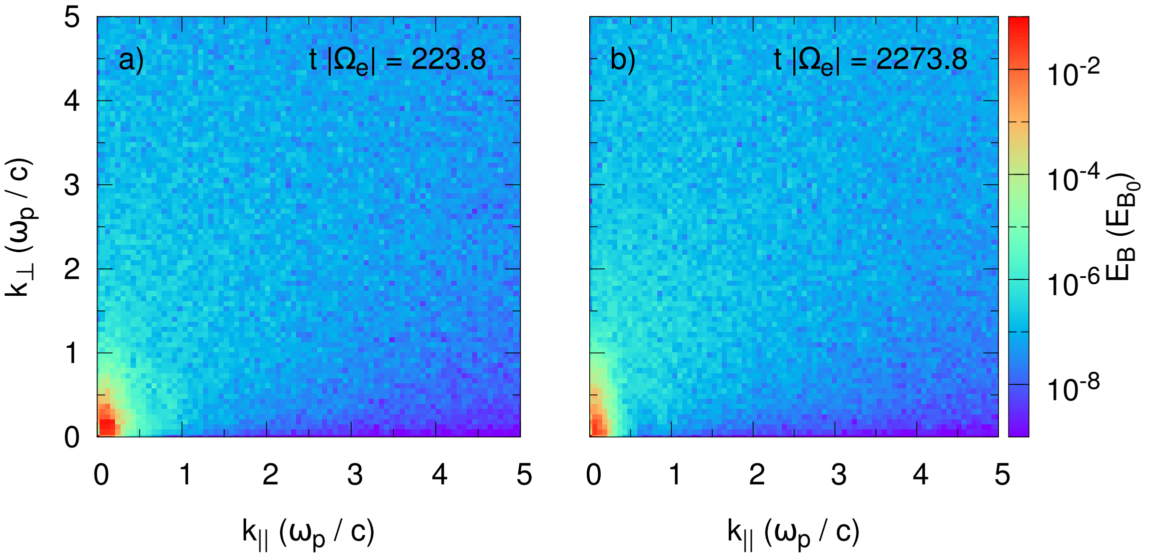

Fig. 4.23: Magnetic energy distribution in wave number space at two points in time. The data is taken from simulation T2 and the energy is normalized to E_{B_0}, the energy of the background magnetic field. Panel a) shows the energy distribution at a relatively early stage of the simulation (for direct comparison to Fig. 4.21 b), whereas panel b) contains data from the end of the simulation. The anisotropic energy distribution can be seen in both panels.

comparison it can be seen that the energy spectrum stretches out to higher wave numbers in the three-dimensional simulation. The turbulence spectrum is confined to a smaller region of relatively small wave numbers in the two-dimensional case, since the numerical noise level drowns the turbulent fluctuations[38]. Panel b) of Fig. 4.23 shows the energy spectrum at the end of the simulation. The anisotropy of the spectrum is clearly visible. It can also be seen that the total energy of the turbulent fluctuations has decreased due to dissipation processes.

A plot similar to Fig. 4.23 is provided by Gary et al. (2008, Fig. 3), with their panel b) representing the same point in time as panel a) here. The shape and extent of the magnetic field fluctuations at small wave numbers are comparable in both plots. However, Gary et al. (2008) show no example for the late time development of the spectrum.

The one-dimensional spectra are presented in Fig. 4.24, similar to Fig. 4.22 for the three-dimensional case. The most significant difference between the spectra obtained from T1 and T2 is that the numerical noise in the two-dimensional simulation drowns the spectrum above $k\,c/\omega_\mathrm{p} \sim 1$. The energy distribution $E_B(k)$ becomes completely flat in the interval $2 \leq k\,c/\omega_\mathrm{p} \leq 6$, as can be seen in Fig. 4.24 a). At higher wave numbers the energy level rises again, similar to the results of T1. Apart from the noise background the energy distribution seems to follow a power law at small wave numbers and the energy level decreases with time. It can also be seen that the spectrum becomes flatter with time, suggesting that a steady state has not been reached at $t\,|\Omega_\mathrm{e}| = 223.8$. Data from other time steps than those shown in Fig. 4.24 allows to estimate that the steady state is reached after about 400 to 500 electron

---

[38] Note that the lower boundary of the energy range depicted in Fig. 4.23 lies two orders of magnitude above that of Fig. 4.21.

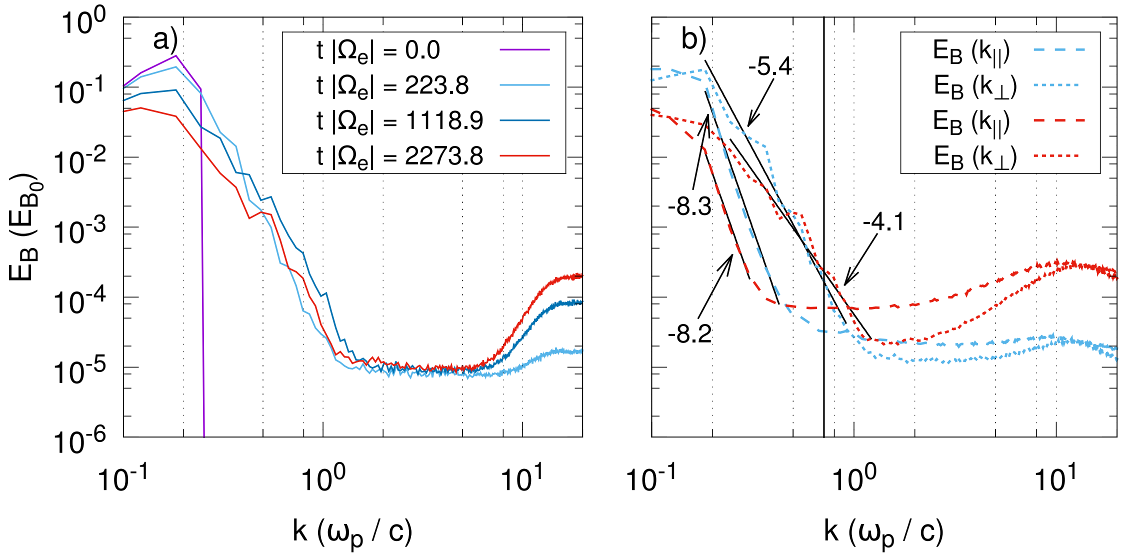

Fig. 4.24: One-dimensional energy spectra normalized to the energy E_{B_0} of the background magnetic field. Panel a) depicts the magnetic energy $E_B(k)$ as a function of the absolute of the wave vector at different times during simulation T2. In panel b) the energy is plotted over the parallel and perpendicular wave numbers separately. The data is taken from the same time steps of the simulation as the data in Fig. 4.23. Power law fits are indicated by the black lines, the respective spectral indices are denoted by the numbers in the plot. The vertical black line near $k\,c/\omega_\mathrm{e} \approx 0.7$ marks the onset of cyclotron damping of parallel propagating waves.

cyclotron time scales. This is different from the three-dimensional simulation T1, where the steady state was reached after about one hundred electron cyclotron time scales.

The flattening of the spectrum over time can also be seen in Fig. 4.24 b), where $E_B(k_\|)$ and $E_B(k_\perp)$ are shown. The splitting of the energy spectrum in its parallel and perpendicular part reveals that the energy distribution is dominated by the perpendicular cascade, which extends to roughly $k_\perp\,c/\omega_\mathrm{e} = 1$. Perpendicular spectral indices are measured as $\sigma_\perp = -5.4$ at an early stage of the simulation and $\sigma_\perp = -4.1$ towards the end. The parallel spectrum on the other hand is limited to a smaller range of wave numbers and exhibits a steep slope with indices $\sigma_\| = -8.3$ at early times and $\sigma_\| = -8.2$ at late times. It can also be seen that especially the parallel spectrum is cut short by the increased noise level at late times in the simulation.

Although this is not shown here, the spectral index $\sigma_\|$ is also variable over time. The parallel spectrum flattens slightly in the early phase of the simulation and becomes steeper again later. However, due to the few data points constituting the power law slope, it is difficult to say whether a steady state is produced at some point in time, since changes with physical origin cannot be clearly distinguished from numerical or statistical fluctuations.

Gary et al. (2008, Fig. 2) also show parallel and perpendicular spectra. The spectral indices derived from T2 are similar to those given by Gary et al. (2008) for the point in time shown in their Fig. 2, although the parallel spectrum in T2 seems to be steeper. It is worth noting that their spectra show the energy distribution only up to $k_{\|,\perp}\,c/\omega_\mathrm{p} \approx 1$, so that a potential background of numerical noise at higher wave numbers would not be seen.

Generally it can be assumed that simulation T2 is in agreement with the simulation presented by Gary et al. (2008). The properties of the spectra are comparable, although the parallel spectrum in T2 seems to be a bit steeper and therefore extends over a smaller range of parallel wave numbers, before the noise background sets in. Compared to the three-dimensional simulation T1, the perpendicular spectrum from T2 does not exhibit a break, which might be due to the fact that the spectrum is effectively cut off at $k\,c/\omega_{\mathrm{p}} \approx 1$. At this wave number the numerical background noise becomes dominant in T2, whereas the perpendicular spectrum obtained from T1 steepens and extends to higher wave numbers.

Further Remarks

The results of the first two test simulations presented above show satisfactory agreement with the expectations. Both two- and three-dimensional setups produce a power law spectrum of the magnetic energy as a function of the wave number. The parallel spectra are steeper than the perpendicular ones, which hints at the evident anisotropy in wave number space (see Figs. 4.21 and 4.23).

The magnetic energy data from the three-dimensional simulation T1 exhibits a break and a steepening of the spectral slope at high perpendicular wave numbers. This is, however, not recovered in the two-dimensional simulation, because the numerical noise dominates the relevant wave number regime.

The contribution of numerical noise at high wave numbers to the parallel and perpendicular spectra $E_B(k_\parallel)$ and $E_B(k_\perp)$ can be reduced. Bear in mind that the one-dimensional spectra $E_B(k_\parallel)$ and $E_B(k_\perp)$ are produced from the spectral energy distribution $E_B(k_\parallel,\, k_\perp)$ in two dimensions by integrating over $k_\perp$ and $k_\parallel$, respectively. Thus, numerical noise at high perpendicular (parallel) wave numbers contributes to the parallel (perpendicular) spectrum over the whole range of parallel (perpendicular) wave numbers. Consider the parallel spectrum $E_B(k_\parallel)$. To reduce the contribution of noise, the orthogonal (i.e. perpendicular) wave number range has to be restricted, thus simply cutting off the regions at high wave numbers where the noise becomes dominant. Similarly, the perpendicular spectrum can be improved by restricting the parallel wave number range. It seems to be a good choice to select only one third of the available parallel and perpendicular wave numbers for further analysis and the production of the energy spectra. Appendix D explains in more detail, how limiting the perpendicular or parallel wave number range helps to improve the quality of the parallel and perpendicular spectra. If not stated otherwise, the reduced spectra, i.e. spectra which are obtained from a limited range of wave numbers, will be presented in the following.

The numerical grid in the simulations of Gary et al. (2008, 2012) barely resolves the Debye length λ_{D}. With $\Delta x = \lambda_{\mathrm{D}}$ being the limit for numerical accuracy, it is interesting to test whether a better resolution of the Debye length might improve the results of the simulations. A test simulation has been prepared, which is based on the physical parameters from Table 4.6, but employs different numerical parameters. The results are presented in Appendix D. They show that there is no qualitative difference between the spectra obtained from simulation T2 and counterpart T2b with higher spatial resolution.

The comparison of Figs. 4.22 and 4.24 clearly shows that the spectra have different slopes depending on the dimensionality of the simulation. For the perpendicular spectrum this can be explained by a more efficient energy transport in the three-dimensional simulation. Plasma waves with various directions of propagation in the perpendicular plane can be generated, whereas this is not possible in the two-dimensional setup. Therefore, more energy can be transported towards higher perpendicular wave numbers in the three-dimensional simulation, explaining the flatter perpendicular spectrum. A similar argumentation also holds for obliquely propagating waves. Since such obliquely propagating waves also contribute to the energy distribution in the parallel spectrum, $E_B(k_\parallel)$ is also expected to be flatter in the three-dimensional case, which is confirmed by the simulations.

4.3.2 Turbulence Spectra

A variety of simulations with different physical and numerical setups were carried out in order to investigate the spectral properties of whistler turbulence. The basic idea is to resolve several wave numbers in both the undamped and the damped regime of the whistler mode. This should allow to see differences in the spectral slope or the anisotropy in both regimes.

To resolve the relatively large spatial scales of the undamped regime, large simulation boxes are required. Thus, it was decided to restrict the investigations to two-dimensional setups, since the computational effort for a parameter study in three dimensions is currently unacceptable. If a suitable set of parameters is found, a corresponding three-dimensional simulation can still be conducted.

However, despite best efforts and extended analytical studies in advance of the numerical experiments, most simulations were unsuccessful or at least yielded unexpected results. In the following, a few of the encountered problems will be named and briefly described. For the sake of brevity, the results of only five simulations will be discussed. These simulations, T3 through T7, are characterized by the physical and numerical parameters listed in Tables 4.8 and 4.9. The setups are meant to simulate decaying turbulence with a set of 42 initially excited whistler waves, which are prepared according to the description in Sect. 4.3.1.

simulation	$\omega_{\mathrm{p,e}}$ (rad s^{-1})	$\lvert\Omega_{\mathrm{e}}\rvert$ ($\omega_{\mathrm{p,e}}$)	$v_{\mathrm{th,e}}$ (c)	$\delta B^2/B_0^2$	β
T3	$8.000 \cdot 10^7$	0.660	0.03	0.10	$8.3 \cdot 10^{-3}$
T4	$8.000 \cdot 10^7$	0.660	0.04	0.10	$1.5 \cdot 10^{-2}$
T5	$8.000 \cdot 10^7$	0.660	0.05	0.10	$2.3 \cdot 10^{-2}$
T6	$1.966 \cdot 10^8$	0.447	0.10	0.10	$2.0 \cdot 10^{-1}$
T7	$1.966 \cdot 10^8$	0.447	0.05	0.10	$5.0 \cdot 10^{-2}$

Table 4.8: Physical parameters for simulations T3 through T7: plasma frequency $\omega_{\mathrm{p,e}}$, cyclotron frequency Ω_{e}, and thermal speed $v_{\mathrm{th,e}}$ of the electrons, the sum δB^2 of the squares of the magnetic field amplitudes of the individual waves, and the plasma beta β. Note that the physical parameters for T6 are the same as for simulations T1 and T2, listed in Table 4.6.

Problems Encountered

To illustrate the unexpected problems encountered in the simulations of whistler turbulence, the three simulations T3, T4, and T5 are analyzed in the following. As can be seen in Tables 4.8 and 4.9, the simulations employ similar sets of parameters. While the box size, the plasma frequency ω_{p}, and the magnetic field B_0 stay the same, the temperature is

simulation	$N_{\|\|}\,(\Delta x)$	$N_\perp\,(\Delta x)$	$N_t\,(\Delta t)$	$\Delta x\,(c\,\omega_{\mathrm{p,e}}^{-1})$	$\Delta t\,(\omega_{\mathrm{p,e}}^{-1})$	ppc
T3	8192	8192	$1.2 \cdot 10^5$	$2.1 \cdot 10^{-2}$	$1.2 \cdot 10^{-2}$	256
T4	8192	8192	$5.0 \cdot 10^4$	$2.8 \cdot 10^{-2}$	$1.6 \cdot 10^{-2}$	256
T5	8192	8192	$1.2 \cdot 10^5$	$3.5 \cdot 10^{-2}$	$2.0 \cdot 10^{-2}$	256
T6	2048	2048	$1.0 \cdot 10^5$	$7.0 \cdot 10^{-2}$	$4.1 \cdot 10^{-2}$	256
T7	2048	2048	$1.0 \cdot 10^5$	$3.5 \cdot 10^{-2}$	$2.0 \cdot 10^{-2}$	256

Table 4.9: Numerical parameters for the two-dimensional simulations T3 through T7: number of cells $N_{||}$ and $N_\perp$ in the directions parallel and perpendicular to the background magnetic field, number of time steps N_t, grid spacing Δx, time step length Δt, and ppc, i.e. the number of particles (electrons and protons combined) per cell.

changed, leading to different plasma betas β and a different grid spacing Δx and time step length Δt.

With 8192 cells both along the parallel and the perpendicular direction a total of 4096 individual parallel and perpendicular wave numbers are available[39]. However, most of these wave numbers lie in the damped regime, where the waves are dissipated by either Landau or cyclotron damping. To obtain an estimate of the number of undamped waves in the simulation, cyclotron damping is considered. Using the dispersion relation of the parallel propagating whistler mode, $n^2 = R$ as stated by Eq. (2.45), and the condition for cyclotron resonance, Eq. (2.88), the minimum resonant wave number k_c can be calculated. This number then allows to determine how many numerical wave numbers below k_c are included in a specific simulation. In the case of simulation T3, 50 parallel wave numbers in the undamped regime are resolved. Assuming a similar number of perpendicular wave numbers below the onset of Landau damping[40], it can be estimated that the turbulence spectrum comprises roughly 50 wave numbers in the undamped regime and may then extend to higher k in the dissipative range. The setups for T4 and T5 are similar, however with slightly fewer possible waves in the undamped regime: 37 and 30, respectively.

Relating the number of grid cells (roughly 8000) to the number of waves contributing to the turbulence spectrum (roughly 80) shows that even the waves in the dissipation range can still be considered to have long wavelengths compared to the physical scale of the grid resolution. Thus, a lot of numerical effort is put into the simulation of small scale fluctuations, which play no part in the physical processes of interest. To reduce the numerical cost of these simulations, it has been tested whether the grid spacing can be rescaled. By use of a numerical parameter the grid spacing Δx of a simulation can be altered, neglecting the requirement to resolve the Debye length λ_D. The length of the time step Δt is also changed accordingly, to maintain the CFL condition. Thus, it is possible to increase both Δx and Δt, thereby reducing the computational effort of the simulation.

While, in principle, only small scale phenomena are neglected and the physics on larger scales remains accurate, an increase of Δx above λ_D leads to numerical heating. Numerical

---

[39] The number of independent wave numbers is half the number of grid cells, since the direction of propagation cannot be recovered for single time steps. Thus, the data is symmetric about $k = 0$, which makes all data at negative k redundant.

[40] The exact number could be calculated, using the resonance condition for Landau damping, Eq. (2.87), and the dispersion relation for oblique waves. However, to obtain a first estimate, this effort is not necessary.

heating increases the particle energy, and thus the plasma temperature, until the Debye length matches the grid spacing again. On short time scales, this numerical heating process may not be noticeable. However, on the time scales required to establish a spectrum of turbulent waves, the temperature increase cannot be neglected. In a number of test simulations (not shown here) it was found that rescaling the grid spacing unfortunately does not present a viable option to reduce the computational effort for turbulence simulations.

Besides the difficulties of finding numerical parameters which allow for simulations with reasonable computational effort, the choice of the physical parameters is also not trivial. As indicated above, the parameters for simulations T3, T4, and T5 were selected because they allow for a relatively wide range of wave numbers in the undamped regime. From the analysis of the previous simulations, especially T1 and the spectrum presented in Fig. 4.22, it is expected that the magnetic energy distribution follows a power law spectrum in wave number space. A spectral break at the wave number corresponding to the onset of dissipation and a steepening of the spectrum at higher k may also be anticipated. However, this is not the case, as Fig. 4.25 shows.

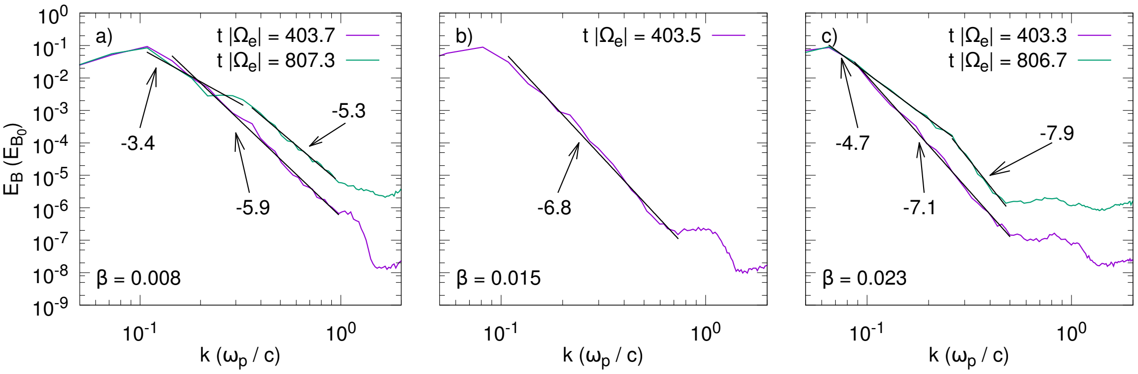

Fig. 4.25: Magnetic energy distribution $E_B(k)$ as a function of the wave number k for simulations T3 (panel a), T4 (panel b), and T5 (panel c). Black lines indicate power law behavior with a spectral index as denoted by the numbers in the figure. At intermediate times (purple lines) the energy distribution follows an unbroken power law at small wave numbers, which ends in a flat plateau. The energy level of the plateau is above the numerical noise floor. A steep cutoff is assumed to indicate the onset of dissipation at high k. Data at later times in the simulation is available for T3 and T5 (green lines). Both spectra show a break which could not be related to a specific wave number. At high k a noticeable increase of the noise level can be seen.

The three panels a) through c) of Fig. 4.25 correspond to simulations T3, T4 and T5, respectively, and show the magnetic energy density $E_B(k)$ as a function of the wave number k. At intermediate times during the simulations ($t\,|\Omega_\mathrm{e}| = 403.7$) all three spectra exhibit a power law slope, which extends from the small wave numbers of the initially excited waves to higher k. The onset of dissipation is expected at $k\,c/\omega_\mathrm{p} \approx \{1.8,\, 1.6,\, 1.5\}$ for T3, T4, and T5. However, instead of a power law spectrum up to these wave numbers, a different behavior is found. In all three simulations the power law slope ends at a smaller wave number than expected and transitions to a short “plateau”, where the spectrum is entirely flat. The energy level of this plateau lies above the numerical noise limit, which can be clearly seen at larger k, where the magnetic energy drops steeply towards the noise floor. The final cutoff is located approximately where the onset of dissipation is expected.

Besides the unexpected plateau at the high-k end of the power law spectrum, the time evolution of the energy distribution at small wave numbers is also unanticipated. Field data at a later point in time is available for simulations T3 and T5 and presented in Fig. 4.25 (green lines). While the magnetic field energy initially follows an unbroken power law, a spectral break appears at later times. Thus, the spectrum is separated into a flatter part at smallest k and a steeper regime after the break. It is also worth noting that none of the spectral indices found at late times matches those at the earlier point in time.

Additional information on the power law spectra is presented in Appendix D, where also the parallel and perpendicular spectra are shown. It can be seen that the energy transport is very anisotropic, clearly preferring the perpendicular direction. The anisotropy increases with decreasing plasma beta, in accordance with simulations by Chang et al. (2013). This can be seen in the two-dimensional energy spectra depicted in Fig. 4.26.

The two-dimensional energy distribution $E_B(k_\parallel, k_\perp)$ in wave number space also gives another impression of the plateau seen in Fig. 4.25. The three panels of Fig. 4.26 again correspond to simulations T3 through T5. At smallest wave numbers they show the initially excited waves, surrounded by less and less energetic waves towards higher wave numbers. This marks the power law regime of the spectra presented in Fig. 4.25. The low wave number region of the spectrum is embedded in a halo of constant energy which corresponds to the plateau in $E_B(k)$. The halo seems to be almost entirely isotropic, exhibiting a smaller energy density only in the quasi-parallel direction. The magnetic energy spectrum from simulation T3 (Fig. 4.25 a) also contains a cloud-like structure at oblique wave numbers, which is missing in the other two simulations.

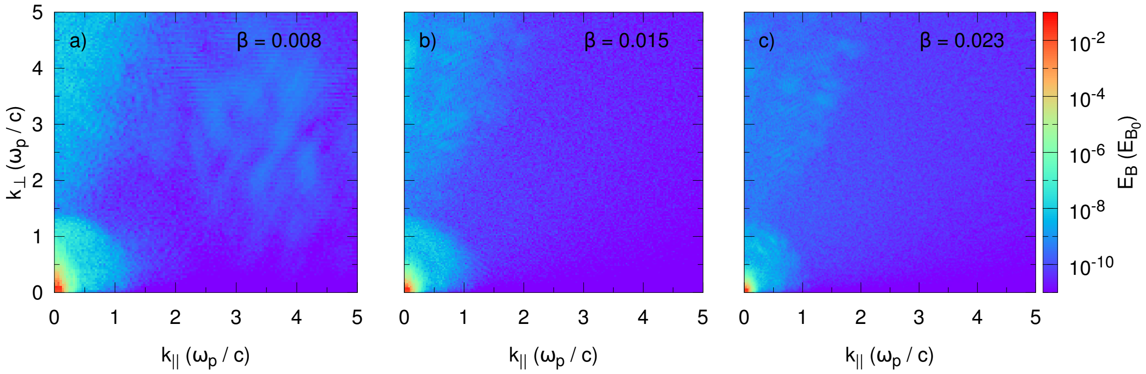

Fig. 4.26: Distribution of the magnetic field energy in two-dimensional wave number space for simulations T3 (panel a), T4 (panel b), and T5 (panel c). Data is shown for times $t\,|\Omega_e| = \{403.7,\, 403.5,\, 403.3\}$ in the three simulations, to allow for a comparison with the one-dimensional spectra in Fig. 4.25. The two-dimensional energy distribution exhibits the anisotropic turbulent cascade at small wave numbers, which is surrounded by an almost isotropic halo of constant energy. At large perpendicular wave numbers additional structures can be observed.

Considering the apparent anisotropy of the power law regime, which can be clearly seen in Fig. 4.26, it can be assumed that the process responsible for the generation of the halo is not related to the turbulent cascade. The energy distribution in the turbulent cascade favors the transport to higher perpendicular wave numbers, which is not the case in the halo.

Although similar halo structures were found in several simulations with different numerical and physical setups, their origin remains unclear.

Similarly, the origin of the structures at large perpendicular wave numbers, which can be seen in all three panels of Fig. 4.26, could not be explained. A deposition of energy at large perpendicular wave numbers was observed in various simulations. Wide-stretched structures in wave number space were found, whose shape ranged from the triangular shape seen in Fig. 4.26 to more elliptical "blobs". With the data currently available it cannot be said whether these structures are of physical or of numerical origin. Frequent output of the electromagnetic fields might be helpful for producing plots of the energy density in k-ω-space. This might allow to relate the observed structures to specific frequencies, thus offering clues to physical processes related to the generation of these structures.

Although further investigations might be interesting and worthwhile, they have not been carried out as part of this work, since the aim of the turbulence simulations is to find a suitable setup to analyze the transport of energetic particles. With the computational cost of the simulations and the limited amount of available resources in mind, repetitions of the previous simulations were omitted. However, a more detailed analysis of field data from a simulation with more frequent output time steps might be an interesting project for the future. It is worth noting that so far only two-dimensional simulations were performed and that it is unclear, whether the structures described above also occur in a three-dimensional setup. Unfortunately, the computational requirements for a three-dimensional setup of this size (8192 grid cells in each direction) exceeds the available resources by far.

Well-proven Setup

With the unforeseen results of many of the simulations of whistler turbulence, a more reliable setup was chosen to investigate particle transport. The physical parameters used by Gary et al. (2008, 2012) produce repeatable results even if the numerical parameters are changed. They have therefore been chosen as the basis for the simulations of particle transport. In the following, two two-dimensional simulations, T6 and T7, are discussed, which employ an adaption of the setup described by Gary et al. (2008).

Simulation T6 uses the same physical parameters as T1 and T2 (see Sect. 4.3.1), but a larger simulation box and more particles per cell, thus increasing the spatial resolution and reducing the numerical noise. The same numerical setup is employed in T7. However, the physical parameters are slightly altered. Compared to T6 a lower plasma temperature and therefore a lower plasma beta are chosen. The detailed parameter sets can be found in Tables 4.8 and 4.9.

Figure 4.27 shows the perpendicular spectra $E_B(k_\perp)$ of the magnetic field energy from simulations T6 (panel a) and T7 (panel b). Other than the spectrum obtained from simulation T2 (see Fig. 4.24), these spectra both exhibit a break. At small perpendicular wave numbers the magnetic energy distribution follows a power law with spectral index $\sigma_\perp = \{-3.1, -3.0\}$ for T6 and T7, respectively. After the break the spectra steepen, and significant differences between both simulations become obvious in the different spectral indices.

The numerical noise level in simulation T7 is about one order of magnitude lower than in T6, which allows an energy cascade to higher wave numbers. This can be explained by the lower plasma temperature in T7, leading to less kinetic energy of the particles and therefore less fluctuations in the electromagnetic fields. The flatter spectrum in T7 (after the break; compared to T6) agrees with results from Chang et al. (2013), who report a more efficient

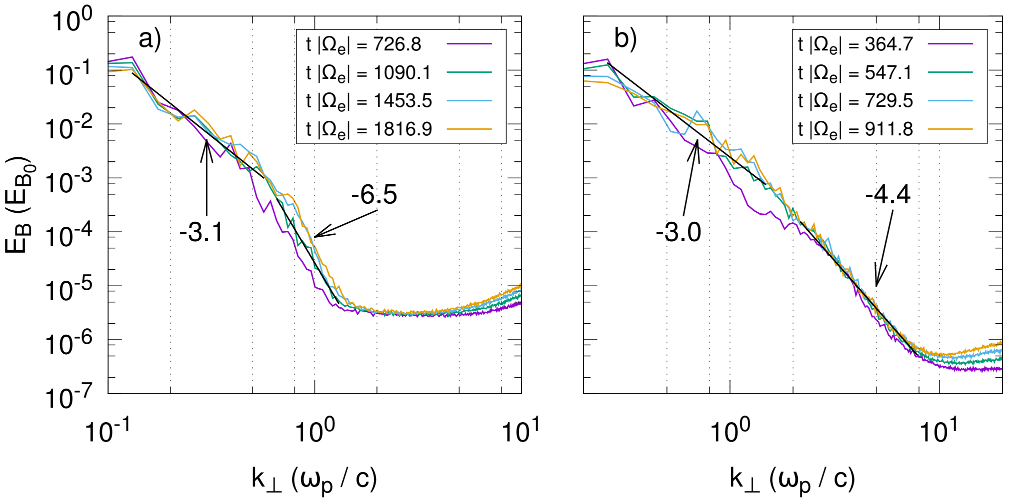

Fig. 4.27: Magnetic field energy distribution $E_B(k_\perp)$ over the perpendicular wave number $k_\perp$ for simulations T6 (panel a) and T7 (panel b). The data is obtained at four different points in time in the two simulations, as indicated in the key. At the earliest time steps shown the spectra reach their steady states. Later in the simulations, the shapes of the spectra hardly change. Power law fits to the data in panels a) and b) are indicated by the black lines at times $t\,|\Omega_\mathrm{e}| = \{1090.1,\, 547.1\}$, respectively. The spectral indices are denoted by the numbers in the plot.

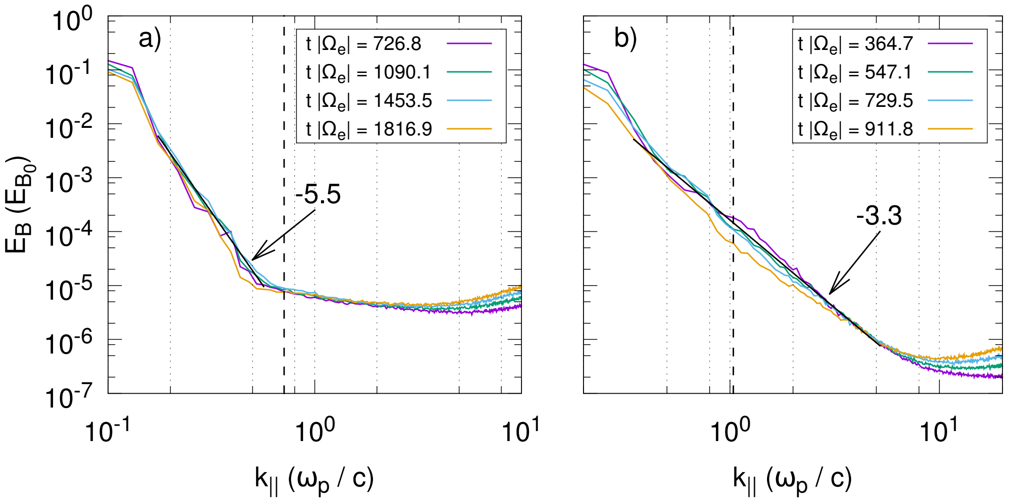

Fig. 4.28: Magnetic field energy distribution $E_B(k_\parallel)$ over the parallel wave number $k_\parallel$ for simulations T6 (panel a) and T7 (panel b). The data is obtained at four different points in time in the two simulations, as indicated in the key. The spectra reach their steady state at the earliest time steps shown. Power law fits to the data in panels a) and b) are indicated by the black lines at times $t\,|\Omega_\mathrm{e}| = \{1090.1,\, 547.1\}$, respectively. The spectral indices are denoted by the numbers in the plot. The dashed, vertical lines mark the expected onset of cyclotron damping for purely parallel propagating waves.

perpendicular energy transport with decreasing plasma beta β.

Chang et al. (2013) also observe stronger anisotropy in simulations with lower β. However, this is not supported by the data from simulations T6 and T7. The parallel spectra $E_B(k_\parallel)$ are depicted in Fig. 4.28. In both cases the parallel spectra do not contain a break and are steeper than the perpendicular spectra at small wave numbers. For T6 the parallel spectrum reaches the noise level approximately at the position where cyclotron damping is assumed to set in (Fig. 4.28 a). Figure 4.28 b), however, shows that the parallel spectrum in simulation T7 extends to wave numbers in the damped regime. The slope does not change at the transition into the dissipation range and is flatter than the slope in the perpendicular spectrum at corresponding $k_\perp$. Thus, the parallel energy transport is assumed to dominate at large wave numbers. Unfortunately, the turbulent cascade reaches the numerical noise level prior to that.

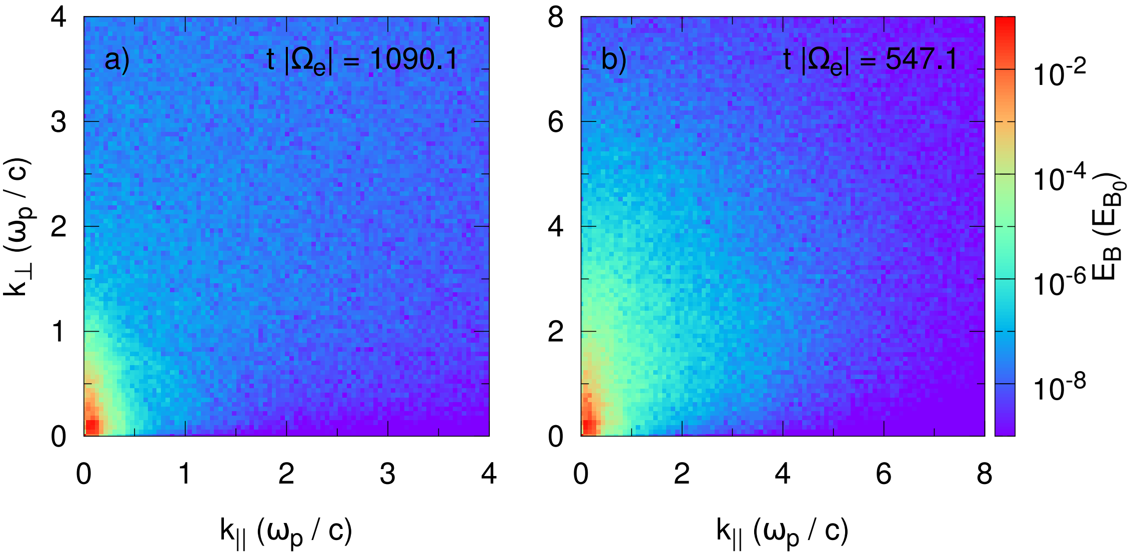

Fig. 4.29: Two dimensional magnetic field energy distribution in wave number space for simulations T6 (panel a) and T7 (panel b). Note the different scales on the axis of both panels.

The energy distribution $E_B(k_\parallel, k_\perp)$ in two-dimensional wave number space supports the claim that parallel energy transport becomes important in simulation T7, as Fig. 4.29 shows. Panel b) depicts the distribution of magnetic field energy in simulation T7. Although hardly any (quasi-) parallel waves are produced above $k_\parallel \, c/\omega_\mathrm{p} \approx 1$ (where cyclotron damping sets in), this critical parallel wave number can be passed at higher $k_\perp$. At small wave numbers, however, the perpendicular cascade clearly dominates. In simulation T6 the situation is different, as Fig. 4.29 a) shows. The perpendicular cascade at small wave numbers is similar to S7, as expected, but at larger $k_\perp$ there is hardly any energy transport to higher parallel wave numbers, in agreement with the spectra in Figs. 4.27 and 4.28.

4.3.3 Particle Transport

Using the setups of simulations T6 and T7, the transport of energetic electrons in kinetic turbulence is studied. In the following, the exact parameters for the test particle energy distribution are presented and the method used to analyze the outcome of the simulations is explained. The goal of the analysis is to obtain pitch angle diffusion coefficients $D_{\mu\mu}$ from the particle data and compare them to a theoretical model.

Setup and Analysis

In simulations T6 and T7 decaying whistler turbulence is simulated, as was shown in the previous section. As can be seen in the magnetic energy spectra presented in Figs. 4.27 and 4.28, a steady state in terms of the power law slope of the spectral energy distribution is established after a given time in each of the two simulations[41]. As soon as this stage of the simulation is reached, a population of energetic test electrons can be injected. The test electrons are initialized as described in Sect. 3.3.2, i.e. as a mono-energetic population with a parabolic distribution $f(\mu)$ of pitch angle cosines $\mu = \cos\theta$ (see Eq. (3.31)).

Simulations T6 and T7 are configured such that a checkpoint is saved at a point in time where the energy spectrum has reached its steady state. The simulations can then be restarted from this checkpoint and test electrons can be injected after the restart. This technique allows to employ a new set of test electron parameters for each restart. Thus, several simulations of particle transport can be set up with minimum computational effort, since the time until the steady state of the turbulent cascade is reached has to be simulated only once.

The time step for the checkpoint and subsequent restart is chosen to be $t\,|\Omega_\mathrm{e}| = 726.8$ for T6 and $t\,|\Omega_\mathrm{e}| = 364.7$ for T7. Simulations T6 and T7 represent the setups of the background plasma, as defined in Tables 4.8 and 4.9. For each of these two setups six test electron configurations are prepared. The simulations are labeled according to the physical setup (T6 or T7) followed by a letter referring to the test particle configuration ("a" through "f"). The parameters of the test particles can be found in Table 4.10 and describe the test electron speed v_e and kinetic energy $E_\mathrm{kin,e}$.

simulation	Tja	Tjb	Tjc	Tjd	Tje	Tjf
$v_\mathrm{e}\,(c)$	0.546	0.862	0.941	0.979	0.999	0.999
$E_\mathrm{kin,e}\,(\mathrm{eV})$	$1.0 \cdot 10^5$	$5.0 \cdot 10^5$	$1.0 \cdot 10^6$	$2.0 \cdot 10^6$	$1.0 \cdot 10^7$	$1.0 \cdot 10^7$

Table 4.10: Test electron characteristics for the simulations of particle transport: test electron speed v_e and corresponding kinetic energy $E_\mathrm{kin,e}$. The individual simulations (letters "a" through "f") are based on the simulations of kinetic turbulence Tj, with $j \in \{6, 7\}$, which are described in Sect. 4.3.2 (Tables 4.8 and 4.9). Note that simulations Tje and Tjf employ the same test electron energies. However, they differ in the way the test electron distribution is initialized (see text).

The test electron energy is increased from simulation T6a (T7a) to T6e (T7e). Simulation T6f (T7f) uses the same particle energy as T6e (T7e), but a different parabolic angular distribution of the particles: Here the particle density $f(\mu)$ increases with increasing μ, while in the other simulations it decreases with increasing pitch angle cosine. This change

---

[41] Since decaying turbulence is simulated, the total energy decreases with time. The "steady state" therefore does not imply that the spectral energy distribution is constant over time, but rather that the shape of the distribution does not change qualitatively.

in the pitch angle distribution allows to check for systematic errors in the particle data, as will be described below.

The test particle data is analyzed as described in Sect. 3.4.1. At specific output intervals the velocity vector $\boldsymbol{v}_\mathrm{e}$ of each test particle and the local magnetic field $\boldsymbol{B}$ at the particle's current position are written to disk. This allows to compute the particles' pitch angles in the local magnetic field configuration at a given time via Eq. (3.32). The particles can then be binned according to their pitch angle cosines to obtain the particle distribution $f(\mu, t)$ in pitch angle space at time t. Using the "diffusion equation integration method" of Ivascenko et al. (2016) it is then possible to derive the pitch angle diffusion coefficient $D_{\mu\mu}(\mu, t)$ at each output time step.

To compare the numerical results to theory, the model of Shalchi and Schlickeiser (2006) has been chosen. Using the framework of quasi-linear theory, they derive an expression for the pitch angle diffusion coefficient in plasma turbulence. Their model is special in the sense that they explicitly consider steep energy spectra with spectral indices $-4 \leq \sigma \leq -2$. The model distinguishes between Alfvénic and fast mode turbulence and equations for $D_{\mu\mu}$ are presented for both cases. While the whistler wave turbulence simulated in T6 and T7 is obviously not composed of Alfvén waves, the Alfvénic model is still chosen in the following. The reason for this choice is that fast mode turbulence relies on compressional waves, which occur mainly at high perpendicular wave numbers. However, considering the steepness of the energy spectra found in T6 and T7, it can be assumed that only a few wave modes at small wave numbers dominate the interactions with the energetic particles. For these waves the assumption of high perpendicular wave numbers, and thus compressibility, does not hold. Instead, their electromagnetic field configuration behaves "Alfvénic", i.e. the fields are mostly transverse and circularly polarized.

In the following, the model equations and parameters from Shalchi and Schlickeiser (2006) will be briefly described. There are two expressions for $D_{\mu\mu}$, depending on the ratio of the pitch angle cosine μ and the parameter $\epsilon = v_\mathrm{A}/v_\mathrm{e}$:

$$D_{\mu\mu} = \frac{\pi\,(s-1)\,v_\mathrm{e}\,\rho_\mathrm{e}^{s-2}\,k_\mathrm{min}^{s-1}\,\delta B^2}{2\,{}_2F_1(\frac{s}{2}+1, 1, \frac{2}{3}, 1-\Lambda)\,B_0^2}\,\epsilon^{s-1}\left(\frac{1}{2}+\frac{4\,\zeta(s+1)}{\pi}\right) \quad \text{for } \mu < \epsilon, \tag{4.13}$$

$$D_{\mu\mu} = \frac{\pi\,(s-1)\,v_\mathrm{e}\,\rho_\mathrm{e}^{s-2}\,k_\mathrm{min}^{s-1}\,\delta B^2}{2\,{}_2F_1(\frac{s}{2}+1, 1, \frac{2}{3}, 1-\Lambda)\,B_0^2}\,\mu^{s-1}\,\left(1-\mu^2\right)\left(\frac{1}{2}+\frac{4\,\zeta(s+1)}{\pi}\right) \quad \text{for } \mu > \epsilon. \tag{4.14}$$

Here the Riemann zeta function $\zeta(s+1)$ and the hypergeometric function ${}_2F_1(\frac{s}{2}+1, 1, \frac{2}{3}, 1-\Lambda)$ are used. The parameter s is the absolute of the spectral index, i.e. in the notation of the work at hand $s = |\sigma|$, which is assumed to be between two and four. The Larmor radius of the test electrons is denoted by ρ_e, the minimum wave number k_min describes the beginning of the turbulent cascade in wave number space, $\delta B^2/B_0^2$ denotes the magnetic energy of the turbulent fluctuations relative to the background magnetic field and Λ is the anisotropy parameter defined by Lerche and Schlickeiser (2001, Eq. (1)). An anisotropy parameter smaller (larger) than one means that perpendicular (parallel) energy transport is preferred in the turbulent cascade.

The spectral index s and the anisotropy parameter Λ are not predicted by the model. They might be obtainable by analyzing the turbulent spectrum in the simulation. However, for the current study they are assumed to be free parameters, which can be tweaked in order to fit the model to the data.

Pitch Angle Diffusion Coefficients

The test particle simulations are analyzed as described above. The energetic electrons are tracked for several electron cyclotron time scales and the resulting pitch angle diffusion coefficients $D_{\mu\mu}$ are presented in Figs. 4.30 and 4.31 for data based on the setup of T6 and T7, respectively. Time is measured as the interval Δt from the time of the injection of the particles to the current time step.

The results of both sets of simulations, one based on T6, the other based on T7, do not differ qualitatively, as would be expected from the two setups. The only difference between the physical parameters for T6 and T7 is the plasma temperature, which has no direct influence on the test electrons. Although the magnetic energy spectrum differs at high wave numbers (see Fig. 4.27), the distribution of magnetic energy at small wave numbers is very similar. As the explanations below will show, this low wave number regime represents the dominant influence on particle transport. Thus, the two sets of simulations will be discussed simultaneously in the following.

Although particle data can be obtained for an arbitrary number of time steps, the interval which can be used for the analysis is still limited. The method of Ivascenko et al. (2016) critically depends on the particle distribution $f(\mu)$ in pitch angle space. In order for the method to work, the initial distribution must be slightly disturbed, but the perturbations must not be too strong. This leaves only a brief period of time for the optimal efficiency of the method.

Figures 4.30 a) and 4.31 a) show the typical behavior of the derived $D_{\mu\mu}$ over time. Shortly after the injection of the test electrons the perturbations of $f(\mu)$ are small, resulting in a low amplitude of $D_{\mu\mu}$ (purple lines). With increasing time the amplitude grows and reaches a maximum (green and blue lines). At later times the amplitude decreases again, as the perturbations become too strong and the method becomes unreliable (orange lines). The other panels of the two figures show the time evolution until the maximum amplitude of $D_{\mu\mu}$ is reached for other test electron energies.

Although the turbulent cascade is assumed to be symmetric about $\mu = 0$, the panels of Figs. 4.30 and 4.31 show an obvious asymmetry in the pitch angle diffusion coefficients derived from the test electron data. The amplitude of $D_{\mu\mu}$ is generally larger for $\mu < 0$. While the energy spectrum itself is isotropic in μ, one could argue that the polarization of the waves' magnetic fields relative to the direction of the background magnetic field B_0 is different (i.e. the plasma physics definition of the polarization). This should, however, not have an influence on the scattering behavior of the test electrons, as can be seen in Fig. 4.16, where resonant scattering of energetic electrons and two counter-propagating waves is shown. Despite the opposite polarization of the waves (in the plasma physics notation) the resulting scattering amplitudes are symmetric about $\mu = 0$.

The main reason for the asymmetry found in Figs. 4.30 and 4.31 is that the parabolic distribution $f(\mu)$ of the test particles implies that there are more test electrons at negative pitch angle cosines (except for simulations T6f and T7f). Therefore, the particle statistics is more reliable for negative μ and the method of Ivascenko et al. (2016) produces more accurate diffusion coefficients. While $D_{\mu\mu}$ can also be calculated for $\mu > 0$, it is more prone to errors and statistical fluctuations play a more important role, as Fig. 4.32 indicates. However, small scale statistical fluctuations can be suppressed by use of a Savitzky-Golay-filter, as suggested by Ivascenko et al. (2016).

Especially for early time steps it can be seen that $D_{\mu\mu}$ is found to diverge at $\mu = 1$. This

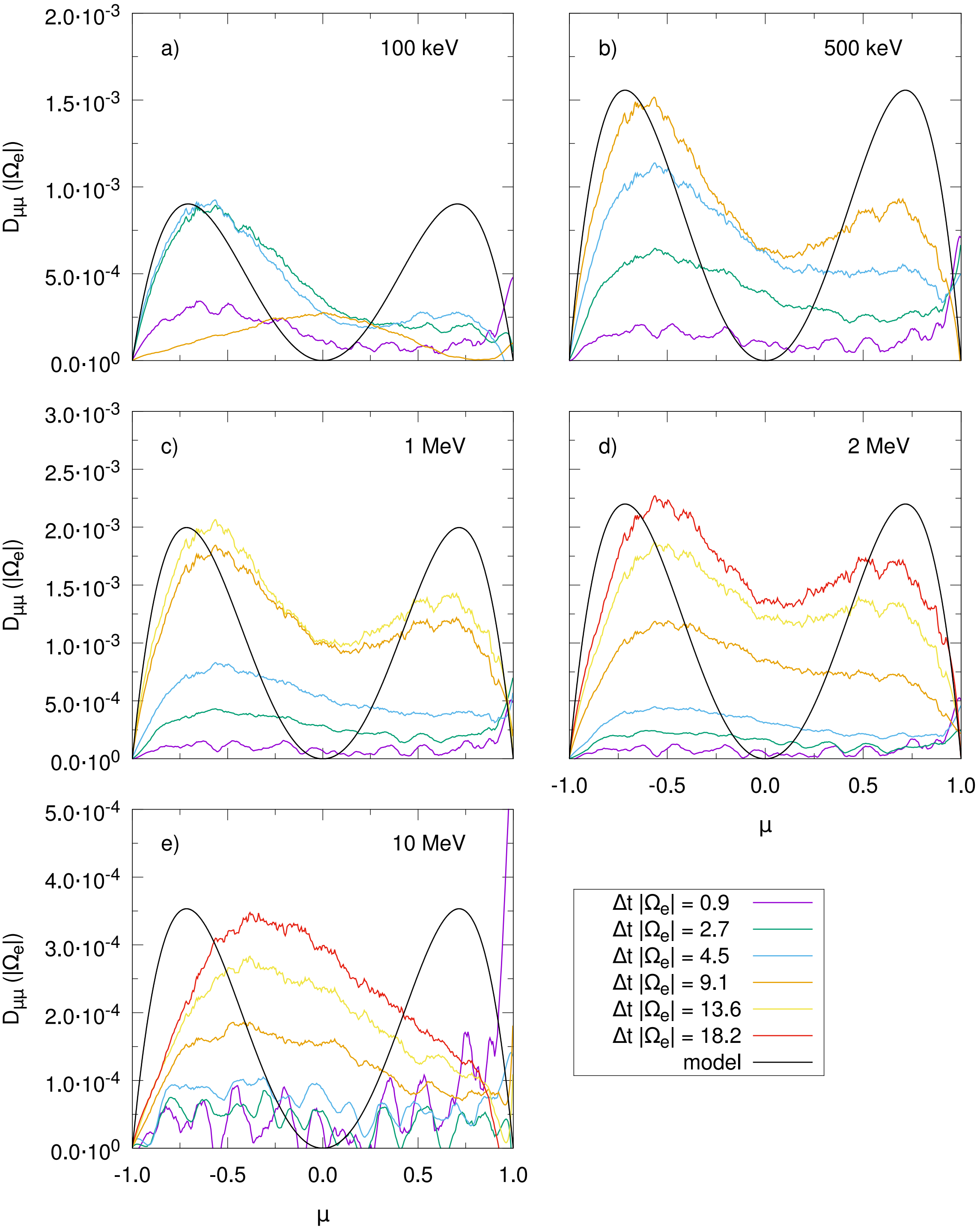

Fig. 4.30: Pitch angle diffusion coefficients $D_{\mu\mu}$ for test electrons with different energies as indicated in the individual panels. Panels a) through e) refer to simulations T6a through T6e. The colored lines denote the diffusion coefficients derived from the simulation data at various times. The black lines follow the model predictions of Shalchi and Schlickeiser (2006) with the parameters indicated in Table 4.11.

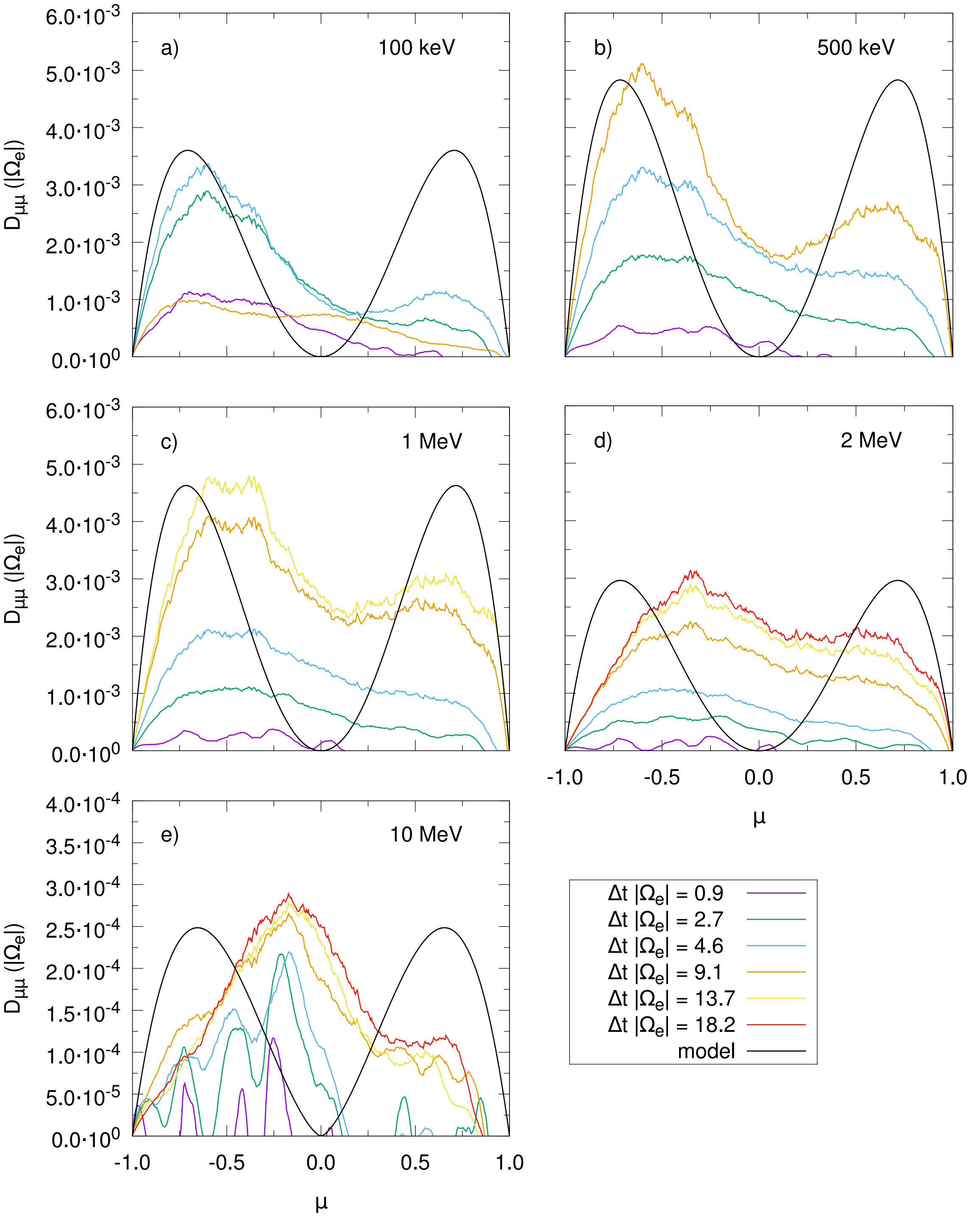

Fig. 4.31: Pitch angle diffusion coefficients $D_{\mu\mu}$ for test electrons with different energies as indicated in the individual panels. Panels a) through e) refer to simulations T7a through T7e. The colored lines denote the diffusion coefficients derived from the simulation data at various times. The black lines follow the model predictions of Shalchi and Schlickeiser (2006) with the parameters indicated in Table 4.11.

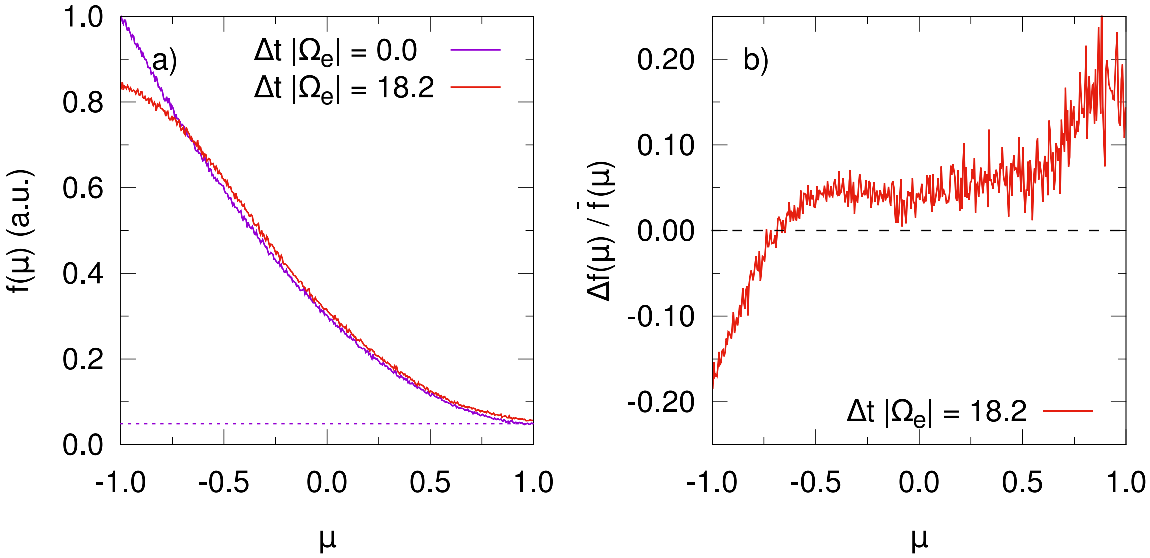

Fig. 4.32: Test electron distribution in pitch angle space. Panel a) shows the initial distribution $f(\mu)$ at the time of the injection of the test electrons ($\Delta t = 0$) and at a later time in simulation T6c. The relative deviation $\Delta f / \bar{f}$ of the distributions at these two time steps is depicted in panel b). The deviation is defined as the difference of the two distributions over their mean value. It can be seen that statistical fluctuations become more significant for larger μ.

is, of course, not a physical effect. At $\mu = 1$ the derivative of the initial parabolic distribution $f(\mu)$ becomes (almost) zero. In this case, the method of Ivascenko et al. (2016) becomes numerically unstable.

Another numerical effect causes $D_{\mu\mu}$ to become negative. This can be seen in various panels of Fig. 4.31 for early times. Negative solutions are most likely related to statistical fluctuations in the particle distribution, which drown the signal at early times, when the physically motivated perturbations of $f(\mu)$ are still developing.

Besides these flaws, the derived pitch angle diffusion coefficients appear reasonable. They develop a (more or less) symmetric shape about $\mu = 0$, indicating that neither direction is preferred. This is expected from the setup of the turbulence simulations T6 and T7, which employ a symmetric layout of initial waves and therefore should produce turbulent cascades which are symmetric in μ[42].

An interesting observation is that the pitch angle diffusion coefficients grow in amplitude with the particle energy increasing from 100 keV to 2 MeV. At the highest test electron energy, however, the amplitude of $D_{\mu\mu}$ is significantly lower than in all other cases. Both Figs. 4.30 e) and 4.31 e) also show that $D_{\mu\mu}$ forms a single peak close to $\mu = 0$ in the case of the highest electron energy, whereas all other simulations produce a double peak structure. The reason for these differences is not clear. However, it is assumed that the different behavior of the 10 MeV-electrons is related to their scattering characteristics: These high energy particles resonate with all of the initially excited waves in the simulations, which is

---

[42] However, as mentioned earlier, this cannot be proved by the plots of the energy distribution in wave number space, since the information about the direction of propagation of the waves is lost.

not the case in the simulations of less energetic electrons. Since the initial waves contain the most energy, they are also assumed to significantly influence particle transport, especially if wave-particle resonances may occur.

In fact, the $D_{\mu\mu}$ in Figs. 4.30 e) and 4.31 e) exhibit distinct peaks at early times (purple and green curves). Similar behavior is also found in simulations T6f and T7f, which are not included in Figs. 4.30 and 4.31. For the example of one time step in simulation T6f, the peak structures in $D_{\mu\mu}$ are related to wave-particle resonances calculated according to Eq. (2.131). The result is shown in Fig. 4.33, where the colored vertical lines mark the expected positions of resonances. It can be seen that the resonances coincide with the positions of the peaks in $D_{\mu\mu}$. The region around $\mu = 0$ is most densely populated by resonances, which might explain the single peak in $D_{\mu\mu}$ at later times as seen in Figs. 4.30 e) and 4.31 e).

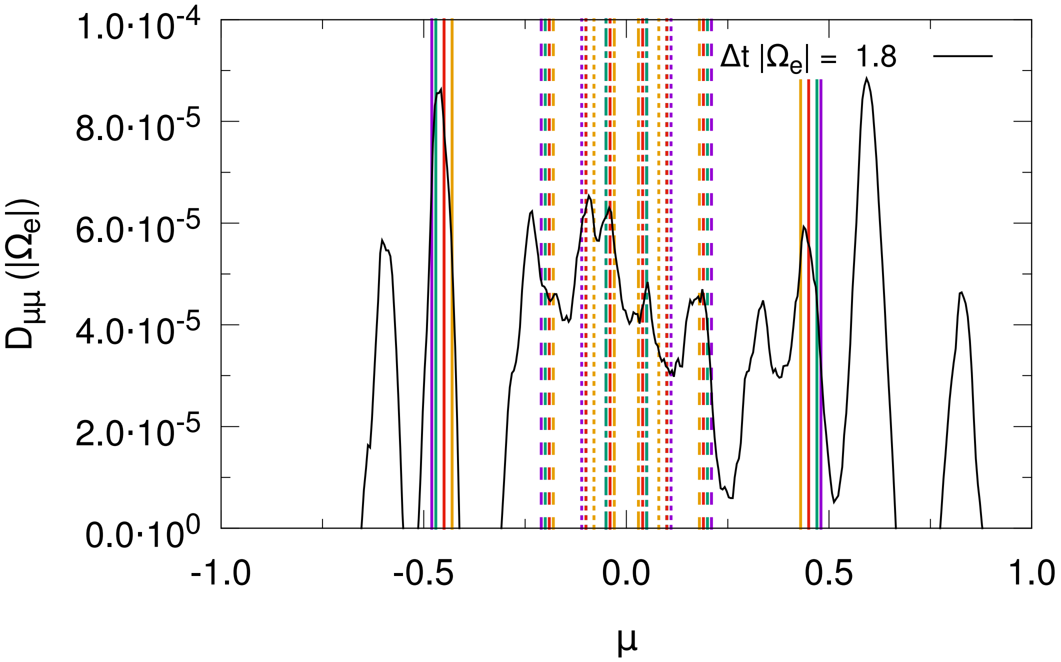

Fig. 4.33: Pitch angle diffusion coefficient $D_{\mu\mu}$ at one point in time as derived from the data of simulation T6f (black line). A noticeable number of peaks in $D_{\mu\mu}$ coincide with the positions of wave-particle resonances predicted by the resonance condition (2.131), which are marked by the colored, vertical lines. The colors denote the parallel wave numbers $k_{\|}$ (in numerical units) from one to four: purple, green, red, orange. The line style refers to perpendicular wave numbers $k_{\perp}$ (also in numerical units) from zero to three: solid, dashed, dotted, dot-dashed. For example, the red dashed lines represent the resonance with a wave at ($k_{\|} = \pm 3$, $k_{\perp} = 1$). Only resonances of the first order, i.e. $n = \pm 1$ in Eq. (2.131) are shown. Note that $k_{\perp}$ does not enter the resonance condition explicitly, but is required to calculate the frequency $\omega(k_{\|}, k_{\perp})$ according to the cold plasma dispersion relation.

Finally, Figs. 4.30 and 4.31 also include the model predictions from Eq. (4.14)[43]. Shalchi and Schlickeiser (2006) derive their equations for positive μ, but assume that the pitch angle

---

[43] The results of Eq. (4.13) are also shown in the plots, but they are only valid in a narrow region around $\mu = 0$, which is not visible to the naked eye.

diffusion coefficient is symmetric about $\mu = 0$. Thus, the black lines in Figs. 4.30 and 4.31 are exactly symmetric. As explained above, the setup of the simulations entails that the $D_{\mu\mu}$ calculated from the numerical particle data is more accurate for negative μ. Therefore, the model parameters have been chosen such that Eq. (4.14) matches the left-hand side of each panel in Figs. 4.30 and 4.31. It has been decided that the model should fit the maximum amplitude of $D_{\mu\mu}$, since the model itself does not include any time evolution of the system and no steady state has been found in the numerical results.

Some of the parameters required for Eq. (4.14) can be directly obtained from the setup of the simulations: The ratio $\delta B^2/B_0^2$ is listed in Table 4.8, the test electron speed v_e is found in Table 4.10, and the Larmor radius ρ_e can be derived from the electron cyclotron frequency Ω_e (see Table 4.10) and the test electron speed. However, the minimum wave number k_min, the spectral index s, and the anisotropy parameter Λ are not as trivial to find.

For the minimum wave number the magnetic energy spectra in Figs. 4.27 and 4.28 have been considered. The second smallest resolved wave number $k_\mathrm{min} = 2\,\Delta k$ has been chosen, where Δk is the grid spacing in wave number space. In a square simulation box, where the numbers of grid cells $N_\parallel$ and $N_\perp$ in the parallel and perpendicular directions are equal, the grid spacing is given by $\Delta k = 2\,\pi/(N_\parallel\,\Delta x) = 2\,\pi/(N_\perp\,\Delta x)$. The minimum wave number k_min marks the beginning of the downward slope of the energy spectrum. Waves at small wave numbers are assumed to dominate the interaction with the particles due to their high energy content and the steep spectral slope. Therefore, the spectral index $s = |\sigma_\perp| = 3.1$ has been chosen, in accordance with the index of the perpendicular spectrum in Fig. 4.27 a). This spectral index corresponds to simulation T6, but since the index in T7 is similar, $s = 3.1$ was used in both cases. Finally, the anisotropy parameter Λ has to be defined. From the spectral properties found in simulations T6 and T7, it is clear that Λ must be smaller than one, corresponding to an anisotropy which prefers the perpendicular transport of energy. However, this is the only assumption that could be made ab initio.

From this starting point the three parameters k_min, s, and Λ were fitted according to the numerical data from each simulation. The resulting parameters which are used in the plots in Figs. 4.30 and 4.31 are listed in Table 4.11. It can be seen that most simulations can be described with the initial choices for k_min and s explained above. Only for T6a and T7a the spectral index had to be changed slightly. For simulations T6e, T6f, T7e, and T7f, i.e. the simulations with the highest test electron energies, the minimum wave number had to be adapted. However, by looking at panels e) of Figs. 4.30 and 4.31 it becomes obvious that the model by Shalchi and Schlickeiser (2006) fails to describe the numerical data anyway, since it produces two peaks, whereas the particle data suggests only one peak.

simulation	T6a	T6b	T6c	T6d	T6e	T6f	T7a	T7b	T7c	T7d	T7e	T7f
s	3.0	3.1	3.1	3.1	3.1	3.1	3.0	3.1	3.1	3.1	2.5	2.5
Λ	0.80	0.64	0.57	0.48	0.25	0.25	3.0	3.1	3.1	3.1	2.5	2.5
$k_\mathrm{min}\,(\Delta k)$	2	2	2	2	1	1	2	2	2	2	1	1

Table 4.11: Parameters assumed for the model of Shalchi and Schlickeiser (2006): spectral index s, anisotropy parameter Λ, and minimum wave number k_min. The latter is given in units of the grid spacing $\Delta k = \{4.4,\, 8.7\} \cdot 10^{-2}\,\omega_\mathrm{p}/c$ in wave number space in simulations T6 and T7, respectively.

In general, the model describes the data surprisingly well, keeping in mind that Shalchi and Schlickeiser (2006) derived their equations for Alfvénic turbulence. The pitch angle diffusion coefficients derived from the particle data mainly exhibit a double peak structure, which is symmetric about $\mu = 0$. Although the model is not able to recover the shape of these two peaks exactly, their amplitude can be retrieved reasonably well by fitting only the anisotropy parameter while the spectral index remains (almost) constant for all simulations.

The agreement of the model and the simulation results also supports the claim that the waves at small wave numbers dominate the interactions with the particles. Otherwise, the spectral index s would have to be changed according to the particle energy. The low energy particles, e.g. 100 keV, resonate with plasma waves in the high wave number regime, where the spectrum is steeper. Thus, according to Figs. 4.27 and 4.28, the effective spectral index s should increase for these particles, if the resonant interactions with high-k waves were important. However, this seems not to be the case. One could also argue that the model for fast mode turbulence, which is also described by Shalchi and Schlickeiser (2006), should be applied in the case of resonant interaction with waves at high perpendicular wave numbers. But as the results in Figs. 4.30 and 4.31 show, a change of the model equations for $D_{\mu\mu}$ is not necessary.

The model only fails for the simulations of 10 MeV-electrons (T6e, T6f, T7e, T7f). This might already be expected from the considerations discussed above: The high energy electrons are able to resonate with the initially excited waves. These waves contain the most energy and thus dominate the interaction of the particles with the turbulent spectrum. However, the initial waves cannot be considered to be part of the power law spectrum itself. As Figs. 4.27 and 4.28 show, the energy distribution forms a plateau at smallest wave numbers, where the initial waves are located. The initial waves are also only few in number, thus not forming a continuous spectrum[44], but a population of distinct, individual waves. Thus, the whole assumption of the model by Shalchi and Schlickeiser (2006), i.e. a continuous power law spectrum, is invalid. As Fig. 4.33 shows, the pitch angle diffusion coefficient derived from the simulation data can be described reasonably well by individual resonances with a number of waves.

Finally, it is worth taking a look at simulations T6f and T7f, which have not been discussed so far. These simulations, which employ the same test electron energies as T6e and T7e, were carried out to test whether the initial particle distribution $f(\mu)$ has an influence on the resulting $D_{\mu\mu}$. It was already discussed above that the statistical fluctuations tend to become more noticeable at those μ, where fewer particles are located. Thus, reversing the slope of the initial parabola should shift the dominant influence of statistical fluctuations from positive μ to negative.

Figure 4.34 depicts the pitch angle diffusion coefficients derived from simulations T7e and T7f in panels a) and b), respectively[45]. This example is chosen because physical results for $D_{\mu\mu}$ are only obtained at negative μ at early times in T7e. Should this also be the case in T7f, this would mean that some physical process prefers the interaction of waves and energetic particles which propagate opposite to the background magnetic field. However, as Fig. 4.34 shows, this is not the case. The pitch angle diffusion coefficient derived from T7f appears to me more symmetric about $\mu = 0$ at early times.

---

[44] Representing a continuous spectrum on a discretized grid is always doomed to failure, but at larger wave numbers the higher number of individual waves at least creates a rudimentary approximation of a continuum.

[45] A similar figure depicting the comparison of T6e and T6f can be found in Appendix D.

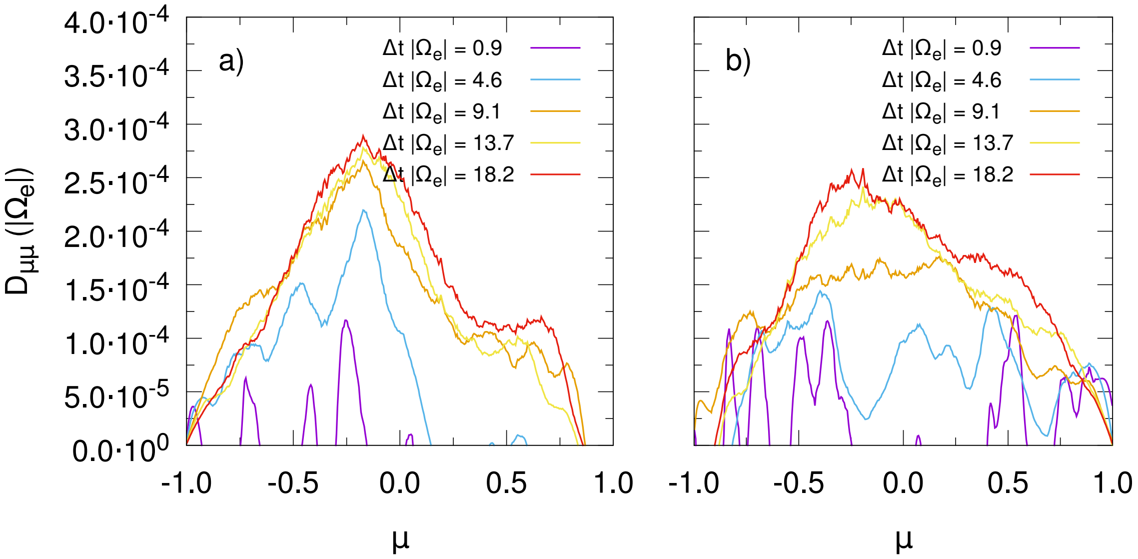

Fig. 4.34: Comparison of the pitch angle diffusion coefficients $D_{\mu\mu}$ derived from the test electron data of simulations T7e (left) and T7f (right). The two simulations differ by the slope of the parabolic particle distribution $f(\mu)$ used to initialize the test electrons. The asymmetry of $D_{\mu\mu}$ in T7e at early times is not reproduced by T7f, which suggests a numerical or statistical reason for the asymmetry. At late times the $D_{\mu\mu}$ become similar, with a single peak near $\mu = 0$ in both simulations.

At late times both simulations produce a single peak in $D_{\mu\mu}$, which is located near $\mu = 0$. The peak is slightly shifted to negative μ in both T7e and T7f. This may hint at a physical process leading to the peak not being centered exactly around $\mu = 0$. Such an asymmetry is sometimes predicted in theoretical models (e.g. Schlickeiser, 1989). However, considering the results of simulations of energetic particles and their interaction with individual waves, an asymmetry is not expected here. Simulations of two counter-propagating waves, presented in Sect. 4.2.5, clearly show that the resulting scattering amplitude is symmetric about $\mu = 0$, as would be expected from the resonance condition (2.131). Assuming that wave-particle interaction can also be described as resonant scattering in the case of turbulence, the resulting $D_{\mu\mu}$ should turn out to be symmetric if the turbulent cascade is symmetric in μ.

Thus, the results of simulations T7e and T7f depicted in Fig. 4.34 do not entirely agree with the expectations. It might be worthwhile to investigate the behavior of the pitch angle diffusion coefficient in more detail in a future project. Changing the initial particle distribution $f(\mu)$ once more (e.g. by altering the parameters A, B, and C in Eq. (3.31)) or reversing the direction of the integration over μ in the method of Ivascenko et al. (2016) might help to distinguish between a physically motivated asymmetry and numerical artifacts.

4.3.4 Résumé

In conclusion, it has to be said that no coherent picture of whistler turbulence could be established, yet. While wave-wave interaction, leading to a turbulent energy cascade, is found in all simulations, the properties of the energy spectra vary widely among the different setups.

By reproducing the results of Gary et al. (2008, 2012), it could be shown that the ACRONYM code is capable of modeling whistler turbulence (see Sect. 4.3.1). The conducted test simulations yield power law spectra of the magnetic field energy in wave number space. The measured spectral indices are in agreement with the findings of Gary et al. (2008, 2012). Numerical noise limits the energy spectra at high wave numbers, thus hindering the production of an energy cascade in the dissipation range.

In an attempt to find a suitable set of physical and numerical parameters for the simulation of a turbulent cascade over a wide range of wave numbers in both the undamped and dissipative regime, a variety of simulations have been carried out. The parameter sets have been selected according to previous numerical results and analytical considerations, which allow to estimate the length scales at which dissipation sets in and the number of resolved numerical wave vectors. However, the energy spectra resulting from most of these simulations show unexpected features, such as a plateau of constant energy after an initial power law decrease of the magnetic field energy at small k (see Fig. 4.25). With the available data the possibility of these features being numerical artifacts cannot be entirely excluded. The variety of different numerical and physical setups employed in the simulations that exhibited the unforeseen features, however, speaks for a physical process. Additional data, especially more frequent output of the electromagnetic fields, might be helpful in further investigations.

As mentioned above, the current study of turbulence simulations was aimed at finding a setup that maximizes the number of numerical wave numbers contributing to the turbulent spectrum. It was assumed that the onset of dissipation is the limiting factor and that the spectrum therefore has to begin at sufficiently low wave numbers. However, the simulations show that this is only partly true. Dissipation plays an important role as the physical process that terminates the energy cascade at large k. In the PiC simulations an additional and more constraining upper limit for the turbulent cascade is found: the energy level of the numerical background noise. Due to the steep power law slope, the magnetic field energy drops by several orders of magnitude in a very narrow range of wave numbers (typically one or two orders of magnitude in k in the simulations presented above). Thus, the magnetic field energy may ultimately reach the noise floor at wave numbers smaller than those of the dissipative regime. Therefore, setting up the initially excited waves at smaller and smaller wave numbers does not help to produce a spectrum over a wider range of wave numbers.

The noise level is directly connected to another problem of turbulence simulations. As was illustrated in Sect. 4.3.2, the computational effort for the simulations is very high, since the PiC code requires the resolution of the Debye length, whereas larger spatial scales are relevant for the physics of the turbulent cascade. This means that large parts of the simulation are “wasted” in the sense that only a very limited region of wave number space can contribute to the turbulent energy spectrum. Coming back to the problem of numerical noise, this means that the already demanding computational effort has to be increased even further in order to reduce noise effects. Since numerical tricks, such as rescaling the grid spacing, could not be put to use to reduce the computational cost of the simulations, the available computational resources constrain the simulations.

For the work at hand the simulation setups have been restricted to two spatial dimensions in order to save computing time. Nonetheless, the total amount of computing time available for this project did not allow for an extended parameter study. Thus, the individual simulations carried out to investigate the dependence of the characteristics of the turbulent spectrum on different physical quantities present only a small sample in parameter space. Despite best efforts, it was not possible to derive a clear and consistent picture of whistler turbulence.

The simulations of energetic particle transport in kinetic turbulence have shown that the steep energy spectrum leads to wave-particle interactions primarily in the low wave number regime. While low energy particles, in principle, resonate with waves in the dispersive or dissipative regime of the turbulent cascade, these interactions are subordinate to the interactions with non-resonant waves at lower wave numbers. The reason for this is that the energy content of dispersive waves decreases rapidly with increasing wave number, due to the steep power law spectrum. Thus, the waves at low wave numbers dominate the spectrum as far as particle transport is concerned.

This can be seen when comparing simulation data to a theoretical model. The test electron data from the simulations allows to derive pitch angle diffusion coefficients $D_{\mu\mu}$ using the method of Ivascenko et al. (2016). Shalchi and Schlickeiser (2006) derive a model for $D_{\mu\mu}$ in plasma turbulence with a steep spectrum, which enables them to predict the pitch angle diffusion coefficient for Alfvénic and fast mode turbulence. The Alfvénic model describes the simulation data reasonably well. This mainly has two reasons: First, the simulated whistler turbulence behaves “Alfvénic” in the sense that the energy-rich waves are located at small oblique wave numbers, where their electromagnetic fields are mainly transverse and circularly polarized. Thus, the field structure is similar to that of Alfvén waves, while it becomes compressional only at high perpendicular wave numbers. Second, the magnetic energy spectrum is relatively flat at small wave numbers and becomes steeper at large k. However, the steepening, which is not included in the model by Shalchi and Schlickeiser (2006), needs not to be considered, since the energy content of the waves in this regime is negligible compared to those at small wave numbers, where the spectrum is still flat.

Thus, while in principle interesting, the effect of dispersion and dissipation on particle transport becomes effectively unimportant in the turbulent medium. The transport of energetic particles therefore depends mostly on the composition of the turbulent spectrum at small wave numbers.

5 Summary and Conclusions

In this last chapter of the work at hand a brief summary and an assessment of the results will be given, especially with regard to the title of the thesis. The attentive reader might ask what the presented results have to do with particle acceleration, which is, indeed, a justified question. Although particle acceleration itself was not observed, the investigated processes of wave-particle interactions are still relevant in a broader sense.

5.1 Modeling of Cyclotron Damping in PiC Simulations

Cyclotron damping in itself is a rather well-understood physical process. Thus, the simulation of cyclotron damped waves does not grant fundamentally new insights into the physics of plasma waves or their dissipation. However, studies, such as those presented in Sect. 4.1, are still important in many ways.

The value of these investigations with regard to the numerical aspects is not to be underestimated. Although it is generally assumed that the particle-in-cell method reproduces most (if not all) phenomena in a collisionless plasma, none of them are actually explicitly included in the numerical model. The model equations only treat the propagation of individual particles and the time evolution of local electromagnetic fields. Large scale phenomena then emerge from the collective behavior of particles and fields. In principle, it has to be tested for each of these collective phenomena, if they are in agreement with the expected physical process, or if they are distorted by (or even result from) numerical effects.

Regarding this aspect, the extensive study of cyclotron damping proves that the simulated dissipation of plasma waves propagating parallel to a background magnetic field is in accordance with physical theory. As already mentioned earlier in this work, the correct treatment of wave damping is crucial for the modeling of plasma turbulence in the dissipation range. Since simulations of turbulence rely on the interplay of different physical processes, from the correct representation of individual waves, over wave-wave interactions, to wave-particle resonances, they are too complex to be analyzed with respect to numerical errors in a meaningful way. The consideration of individual aspects, such as the work of Kilian et al. (2017) or the studies of cyclotron damping in the work at hand, is therefore a necessary prerequisite.

It is also worth noting that cyclotron damping works correctly in low-dimensional setups. The results of the one- or two-dimensional simulations shown in Sect. 4.1.2 are not to be misunderstood: They are definitively less accurate than those of the three-dimensional simulations, but they still show that the damping process itself is recovered as expected. Usually a reduction of the simulation's dimensionality would be accompanied by an increase of the number of particles per cell to compensate for the reduced total number of particles in the simulation. This was not done here, in order to keep as many numerical parameters constant between the different setups as possible.

Last, but not least, the studies of cyclotron damping were also used to demonstrate the analysis method developed in Sect. 3.4.2. One interesting trait of this method is that information about wave modes, which are not resolved in frequency space, can still be extracted from the simulation data (as long as their wave number is resolved). Since an adequate resolution of the low frequency regime (i.e. waves far below the electron cyclotron frequency) can hardly be achieved in PiC simulations with reasonable effort, this can be especially useful for the analysis of phenomena in this regime.

From a physical point of view cyclotron damping is, of course, one of the processes which transfers energy from the electromagnetic fields of plasma waves to the particles. This primarily leads to heating of the plasma and, as shown in Sect. 4.1.1, to a temperature anisotropy. In a collisionless plasma the temperature anisotropy is not reduced by particle-particle collisions, obviously, and can trigger new plasma instabilities if the anisotropy becomes too strong. Instabilities then can lead to the generation of new plasma waves, i.e. transfer kinetic energy back to the electromagnetic fields. This process might also be relevant for turbulence in the dissipation range, as briefly discussed in Sect. 2.5. It was, however, not observed in the simulations.

With respect to particle acceleration, cyclotron damping may play the role of a pre-accelerator. As mentioned in Sect. 1.3.3 the acceleration of heavy ions in solar flares is assumed to be related to the cyclotron resonance. Furthermore, the heating of a particle species also increases the number of particles in the high energy tail of the distribution, which are then available for Fermi acceleration.

5.2 Fundamental Understanding of Resonant Wave-Particle Scattering

The resonant interaction of waves and energetic particles is, in principle, based on the same mechanism as cyclotron damping. However, when studying the resonant scattering of energetic particles off of the magnetic fields of plasma waves, the particles are in the focus of the analysis. Thus, the analysis methods are different and the theoretical modeling is concerned with the evolution of the particle distribution rather than that of the electromagnetic fields.

While it was expected that the physical process is modeled correctly in the PiC simulations (especially after conducting the study on cyclotron damping), a theoretical model was not available for direct comparison. Based on the work of Lange et al. (2013) the analytical model presented in Sect.2.6.2 was derived. Furthermore, to double-check the results of the simulations and the new model, an adaption of the ACRONYM code was introduced (see Sect. 3.3.3), which allowed to carry out magnetostatic simulations that can be directly compared to the model of Lange et al. (2013). With these new tools a detailed study of the resonant interaction of electrons and whistler waves was prepared.

At the beginning of Sect. 4.2 the validation of the numerical and the analytical model is presented. Satisfactory agreement of the numerical results and the analytical predictions is obtained in the physical regime where the model assumptions are valid. It is worth noting that the analytical model is able to accurately describe the PiC results, although it does not consider the electric field of propagating plasma waves. This shows that the influence of the electric field on particle scattering is negligible and that the interaction is indeed dominated by the magnetic field. The analytical model also neglects changes of the particle energy, which implies the assumption that these changes are small or rather that momentum diffusion is slower than pitch angle diffusion (in terms of the Fokker-Planck diffusion model). This assumption is explicitly tested in Sect. 4.2.3. Although changes of the particles' velocities are found, these changes are small. It could also be shown that they are in agreement with expectations, if elastic scattering of the particles off of magnetic fields is assumed in the rest frame of the wave.

While these considerations are important as a validation, they do not yield any new insights into the physical effects. Similarly, the result that the analytical model fails to describe wave-particle interactions in the case of a large amplitude of the wave's magnetic field (see Sect. 4.2.4) only confirms the expected behavior. Much more interesting is the analysis of the trajectories of individual particles in phase space (see Sect. 4.2.6). The fact that the particle trajectories form closed orbits if only one plasma wave is available for scattering implies that there is no pitch angle diffusion in this case. Although the evolution of the particle distribution as a whole follows the theoretical expectations, which are originally based on the Fokker-Planck diffusion model, this does not automatically mean that diffusion actually occurs.

These results are at first counter-intuitive, but they are well-described by the model of Sudan and Ott (1971). According to this model, the electromagnetic fields of the plasma wave form a series of spatially confined potential wells. If a particle is in resonance with the wave, it is trapped inside one of these wells. The particle cannot escape, but performs oscillations inside the potential well, with the amplitude of the oscillations depending on the particle's energy. Comparisons of the model predictions for the amplitude of the oscillations and the width of the observed trajectories in phase space show good agreement, suggesting that particle trapping is responsible for the closed trajectories.

Diffusion can only occur if several plasma waves with different frequencies, wavelengths or directions of propagation are present. The spatial structure of the potential wells can then change over time, allowing particles to escape. This can be directly seen in the phase space trajectories, which then show open trajectories and particles which scatter across the resonances of the individual waves.

Although particle scattering in the electromagnetic fields of a single wave is a rather artificial case, it still leads to a better understanding of the micro-physical processes involved in the interaction of waves and particles. Especially the idea of considering a wave as a series of potential wells is an interesting approach.

Regarding particle acceleration, the resonant interaction of particles and waves plays an important role in the Fermi acceleration process in plasma turbulence. In his pioneering work on the acceleration of cosmic rays, Fermi (1949) estimates that the change of a particle's energy ΔE per collision with a moving magnetic irregularity is proportional to the square of the ratio of the particles speed and the speed of light, i.e. $\Delta E/E \propto (v/c)^2$. While this is only a rough estimate, it shows that the energy gain (or loss) depends sensitively on the energy of the particle, with faster particles gaining (or losing) more energy than slower ones. A net gain of energy is eventually achieved because head-on collisions of particles and waves (which lead to an increase of energy) are more likely than overtaking collisions (leading to a loss of kinetic energy).

Wave-particle collisions, i.e. resonant scattering, occur on cyclotron time scales and the gain of kinetic energy of the particle is a statistical process. With these facts in mind it can be assumed that the acceleration of heavy particles (protons can already be assumed to be heavy in this context) can hardly be observed in PiC simulations, simply because a massive amount of time steps and therefore computing time would be required to simulate a sufficient number of wave-particle collisions. However, the situation might be different for relativistic electrons. Being able to correctly model and predict the resonant scattering of energetic electrons and dispersive plasma waves might therefore allow to set up simulations of kinetic turbulence, which exhibit signatures of particle acceleration.

5.3 Problems and Results of Turbulence Simulations

Simulations of kinetic turbulence have proven to be more complicated than initially thought. Their demand for computational resources is immense and the results of the simulations do not allow for a final conclusion regarding the dependence of the shape of the energy spectrum on the physical setup. With the limited amount of computing time available for this project, it was not possible to carry out a comprehensive parameter study. Drawing conclusions from the relatively small sample of simulations is, therefore, difficult (see Sect. 4.3.2).

With the limited amount of data at hand, the following can be said about the distribution of the magnetic field energy in wave number space: A turbulent cascade is established, with energy being transported from small initial wave numbers towards larger wave numbers. The energy transport is anisotropic and the perpendicular cascade is preferred at small wave numbers k. The energy distribution follows a power law spectrum in both the parallel and the perpendicular wave numbers $k_\parallel$ and $k_\perp$.

In most cases, a break in the perpendicular energy spectrum was found. The position of the break depends on the plasma temperature and is likely to be related to (nonlinear) Landau damping of waves at high perpendicular wave numbers (Gary et al., 2012). The parallel spectrum does not exhibit a break and follows a power law distribution even at large parallel wave numbers. This provides an interesting scenario: While the parallel spectrum is steeper than the perpendicular spectrum at small wave numbers, this relation is reversed at larger wave numbers, beyond the break in the perpendicular spectrum. Therefore, the energy transport perpendicular to the background magnetic field is dominant at small wave numbers, but parallel transport might play an important role in the dissipation range of the spectrum, especially for high $k_\perp$. Unfortunately, this could not be directly observed in the simulations, since the extent of the energy spectrum in wave number space is severely limited by the energy level of the numerical noise.

Numerical noise is also one of the major problems of the simulations. Since the energy distribution follows a steep power law spectrum (spectral indices as steep as -8 have been found), the magnetic field energy cascade comprises a few orders of magnitude in energy, while being confined to a rather small range of wave numbers. Thus, the turbulent cascade is not limited by the assumed exponential cutoff at large k, but by the energy level of the numerical noise, which presents a lower boundary for the energy range.

In principle, this problem can be solved by employing a larger number of numerical particles per grid cell or increasing the total number of cells in the simulation. The latter would preferably be realized by expanding the simulation setup to three spatial dimensions. However, both possibilities imply a massive increase of the required computational resources. Unfortunately, these resources are typically limited and therefore restrict the size of a simulation.

Using two of the simulations of whistler turbulence as a basis, the transport of electrons with different energies was studied in Sect. 4.3.3. To analyze the simulations, the pitch angle diffusion coefficient $D_{\mu\mu}$ was derived from the test electron data, using the method of Ivascenko et al. (2016). These results were compared to a model for Alfvénic turbulence by Shalchi and Schlickeiser (2006).

The model is found to describe the data surprisingly well, implying that particle transport in kinetic turbulence is not too different from transport in Alfvénic turbulence. The steep magnetic energy spectrum observed in the simulations of whistler turbulence is assumed to be responsible for this behavior. The energy content of the waves rapidly decreases with increasing wave number. Thus, the waves at small wave numbers dominate the interaction with the particles. In particular, it seems that the part of the spectrum at high wave numbers, after the spectral break, becomes negligible for the interactions. This is supported by the model of Shalchi and Schlickeiser (2006), which is able to describe the test electron data by assuming an unbroken spectrum with a spectral index similar to that in the low wave number regime of the perpendicular magnetic energy spectrum.

Although the data is well-described by the model for most particle energies, the model is not entirely accurate. Especially towards $\mu = 0$, i.e. perpendicular propagation of the particles, the theoretical predictions and the measured $D_{\mu\mu}$ diverge, which is a common problem for QLT models. This flaw can also not be solved by applying another model derived for fast mode turbulence.

5.4 Closing Remarks

Just as every observer will demand more detailed, more accurate, better resolved, or generally *more* observations to improve the understanding of a given problem, every scientist working with computer simulations will demand for more and larger simulations. However, there are never enough computational resources available to carry out all the numerical studies that come to mind. Even with the increasing computing power in virtually every device, from the smallest laptops to the largest supercomputers, this problem will probably always remain, since the simulations also become more and more demanding. However, just to give some inspiration for future work, a few suggestions for further numerical work will be mentioned below.

The topic of kinetic turbulence was treated in some detail, but the results cannot be expected to be final. Although a massive amount of computational resources had been available, the number of simulations which could be carried out was rather limited. It would be interesting to continue the initiated parameter study in order to obtain a more complete picture of the dependence of the magnetic energy spectrum on the physical parameters.

However, before further steps into the vastness of parameter space are taken, it should also be attempted to better understand the unexplained features which have been found in some of the simulations presented here. This could be done by repeating such simulations with more frequent field output, which allows a better time and especially frequency resolution. Thus, the origin of the extended structures in wave number space, which have been found at high perpendicular wave numbers, could be further investigated. Besides the computational resources required for this endeavor, it is also worth noting that frequent output of field data requires large amounts of disk space and efficient analysis tools.

Speaking of disk space and efficient analysis tools, the particle data in turbulence simulations come to mind. The behavior of the thermal background particles in the simulations of kinetic turbulence have not been studied here. The reason is simple: the data volume for a single output time step is in the range of terabytes. Thus, it was not possible to store the particle data for a longer period of time or to analyze the data in a meaningful manner (or in a feasible amount of time). However, looking into the behavior of the thermal particles might still be interesting. Effects like plasma heating, the potential development of instabilities, or maybe even the acceleration of a fraction of the particles might be observed.

For future projects it would also be interesting to perform simulations of kinetic turbulence which produce an energy cascade throughout the dissipation range, i.e. until the energy transport comes to a halt at an abrupt cutoff. This was attempted in the work at hand. However, due to the steep energy spectra, the numerical noise limit terminates the cascade before a physical dissipation process can set in. Different results might be achieved with faster computers, more computing time, or simply with a superior simulation design.

Trying to advance the understanding of physical processes by pure force, i.e. in the form of larger and more complex simulations, might however not be the most efficient way. More detailed theoretical models will be helpful to plan future simulations and to focus on specific topics, in order to confirm or exclude certain model assumptions. Of course, new and more detailed observations are also needed. Here, the upcoming THOR (Turbulence Heating ObserveR) satellite has to be mentioned in particular, since it is designed to analyze turbulence in the solar wind with unprecedented precision. Its instruments allow measurements in the kinetic and dissipative regime of the turbulent cascade and will finally present an empirical counterpart to the large number of numerical models.

Appendix

A Wave Excitation

To stress the importance of the initial particle boost during the initialization of excited waves three simulations are carried out. The first setup contains only a thermal plasma with no artificially excited waves. The second setup uses the same parameters to create a thermal plasma, but additionally includes the initialization of five Alfvén waves propagating parallel to the background magnetic field $\boldsymbol{B}_0$. Five different parallel wave numbers are chosen for the Alfvén waves, so they can be distinguished in Fourier space. The second setup is used for two simulations: one using the wave excitation mechanism described in Sect. 3.3.1, the other using the same method only without performing the particle boost.

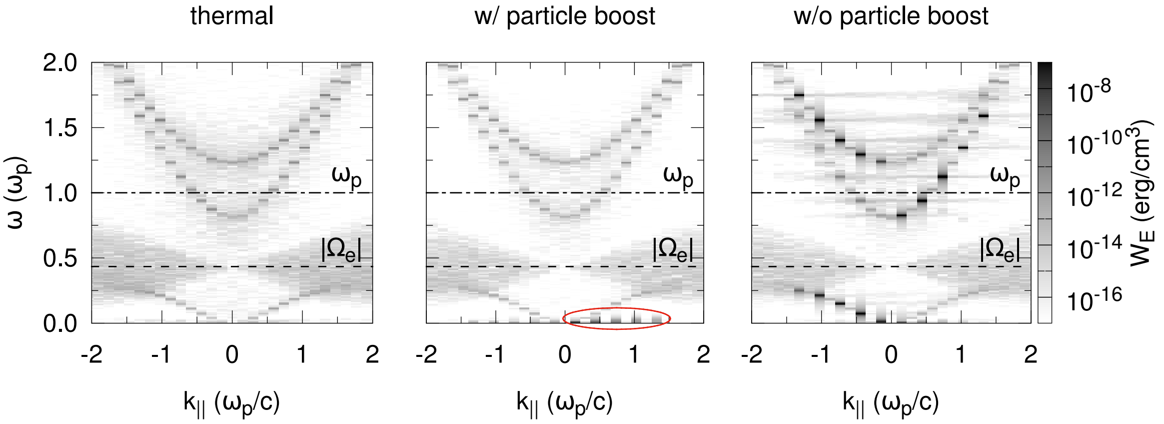

Fig. A.1: Dispersion relations obtained from a component of the electric field perpendicular to the background magnetic field $\boldsymbol{B}_0$. The data in grayscale represents the energy density W_E in the electric field as a function of the parallel wave number $k_{||}$ and the frequency ω. The three panels show data from a simulation of a thermal plasma (left) and two simulations of a plasma with excited Alfvén waves. Wave excitation is performed with (center) and without initial particle boost (right) as described in Sect. 3.3.1. The energy is confined at the positions of the five excited waves when the particle boost is enabled (marked in red). However, this is not the case without the initial boost (black spots).

Figure A.1 shows the spectral energy distribution obtained from a transverse component of the electric field in the three simulations. The thermal simulation (left panel) exhibits the dispersion relations of the parallel propagating R-, L- and whistler modes. The Alfvén mode is not well resolved due to the low frequency of the waves and can be barely made out in the two lowest frequency bins. Gyrating electrons create the darker, triangular structures which extend outward from $k_{||} = 0$. These areas mark the regime in which cyclotron damping occurs.

The center panel of Fig. A.1 refers to the simulation with excited waves and initial particle boost. Dark spots in the lowest frequency bins represent the excited Alfvén waves. The energy of these waves is strictly confined in wave number space and expands only slightly to higher frequencies than intended. This frequency broadening mainly results from the so-called leakage effect of the discrete Fourier transformation, which occurs if the length of the transformed interval is not an integer multiple of the wave's period. The choice of a windowing function reduces the effect, but cannot suppress it completely[46].

Finally, the right panel of Fig. A.1 shows the data from the simulation without initial particle boost. Here most of the energy is not located at the expected positions along the dispersion relation of the Alfvén mode. Instead dark spots can be found along the whistler, L-, and R-mode. Note that left-handed waves (Alfvén and L-mode) are excited with propagation along $\boldsymbol{B}_0$, whereas right-handed waves (whistler and R-mode) propagate anti-parallel to $\boldsymbol{B}_0$. Since the electromagnetic fields of the Alfvén waves are only initialized at the beginning of the simulation no information about the polarization, direction of propagation or frequency is included. The energy of the excited fluctuations is therefore redistributed to several waves, similar to the observations of López et al. (2014), who study the parametric decay of an Alfvénic pump wave. Also note that horizontal lines stretch out from the dark spots on the dispersion relations of the high frequency modes. This effect also occurs if the amplitude of the excited wave is too high.

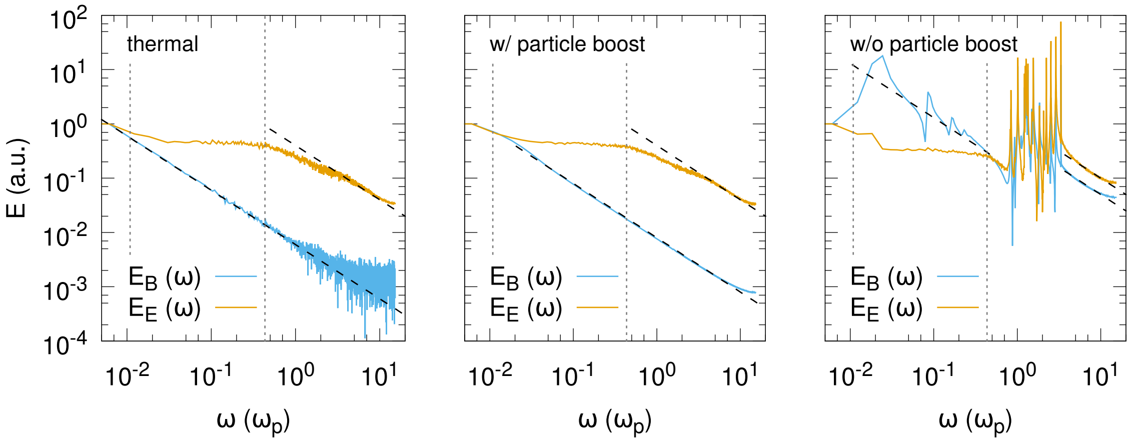

Fig. A.2: One-dimensional spectra of the magnetic and electric field energy E_B and E_E in the three simulations discussed in the text. The vertical, gray, dotted lines mark the proton and electron cyclotron frequencies (left to right). A $1/\omega$ slope is indicated by the black, dashed lines. The spectra are normalized to the field energy in the lowest frequency bin. The absolute energy of the magnetic field in the thermal simulation lies several orders of magnitude below the energy in simulations with excited waves. Therefore, small fluctuations in the magnetic field energy of the thermal simulation are clearly visible, leading to the noisy high frequency tail seen in the left panel.

---

[46] Additionally, the frequency is broadened because of wave damping, which leads to a Lorentzian shape of the spectral energy distribution of a damped wave. The width of the Lorentzian curve scales with the damping rate and, therefore, should increase with increasing wave number. However, this is not observed in the example shown in Fig. A.1 and it can be assumed that frequency broadening is mainly caused by the leakage effect.

The energy distribution in frequency space is depicted in Fig. A.2, where one-dimensional spectra of the magnetic and electric energy $E_B\left(\omega\right)$ and $E_E\left(\omega\right)$ are shown. The three panels again show data from the thermal simulation, and the simulations with and without initial particle boost (left to right). In the thermal simulation a magnetic field energy spectrum $E_B\left(\omega\right) \propto 1/\omega$ can be found, whereas the electric field energy spectrum is entirely flat between the proton and electron cyclotron frequencies and steepens at higher frequencies. A similar result is obtained in the simulation with excited Alfvén waves where the initial particle boost is applied. The frequencies of the excited waves are not resolved and therefore do not show up in the spectrum.

In the simulation in which the particle boost is disabled the spectra show completely different features. The excited whistler waves clearly leave their mark in $E_B\left(\omega\right)$, which exhibits several bumps in the frequency regime between the proton and electron cyclotron frequencies. Starting around the plasma frequency ω_{p} and continuing to higher frequencies the excited high frequency waves are visible in both $E_B\left(\omega\right)$ and $E_E\left(\omega\right)$. The $1/\omega$ slope of the spectra becomes visible at even higher frequencies, well above the frequencies of the excited waves.

B Cyclotron Damping

Velocity Spectra

The parallel and perpendicular velocity spectra of protons and electrons in one of the simulations from set A_1 (see Sect. 4.1.1) are shown in Figs. B.1 and B.2, respectively. The different panels in each figure depict the velocity distributions at the beginning and the end of the simulation (panels a and b) and the deviations of the actual distribution from a best fit Gaussian (panels c and d). Gaussian velocity distributions would be expected for thermal particles. However, the dissipation of the electromagnetic fields of a damped wave leads to particle acceleration perpendicular to the background magnetic field $\boldsymbol{B}_0$, as Fig. 4.2 in Sect. 4.1.1 suggests. This process leads to characteristic features in the velocity distributions.

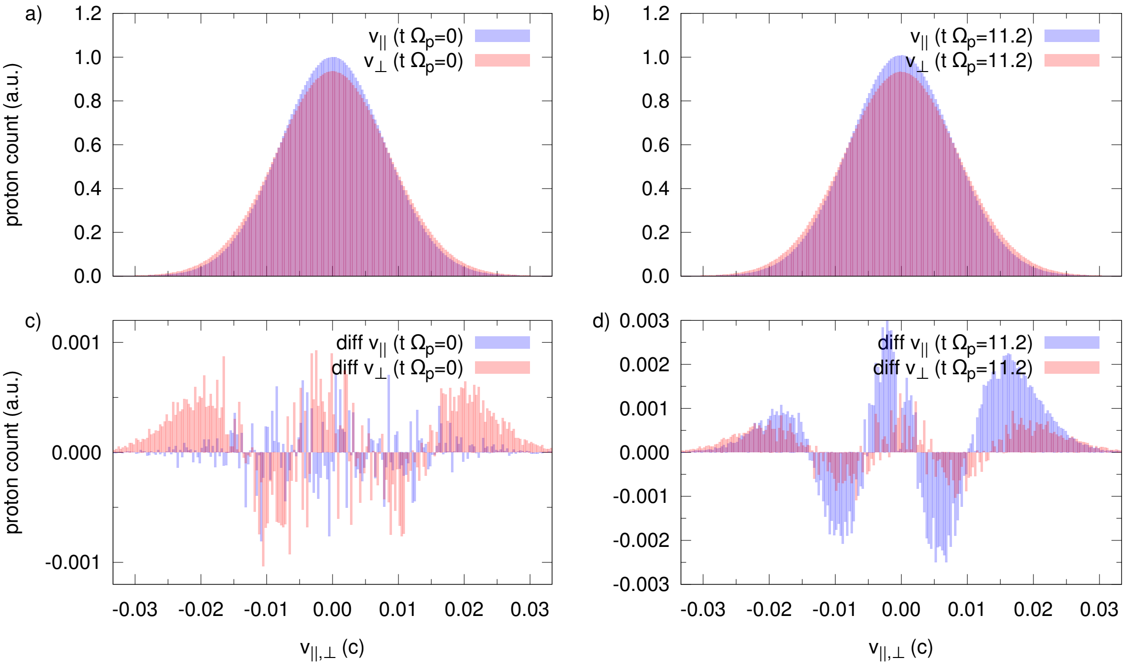

Fig. B.1: Top panels: Histograms of the protons' parallel and perpendicular velocity components at the beginning (left) and the end (right) of one of the simulations from set A_1. The histograms are normalized to the number of particles in the bin around $v_{||} = 0$ at the beginning of the simulation. Bottom panels: The deviations of the velocity distributions from a best fit Gaussian distribution at the beginning (left) and the end (right) of a simulation are shown. While the qualitative shape of the deviations in $v_\perp$ does not change over time, new features arise for $v_{||}$, which hint at an acceleration of particles parallel to the propagation of the decaying waves. Figure according to Schreiner et al. (2017a).

The perpendicular velocity distribution of the protons exhibits systematic deviations from a Gaussian curve right from the start of the simulation. As explained in Sect. 4.1.1 this results from the initialization of the excited waves according to the method described in Sect. 3.3.1. The qualitative picture of these deviations does not change over the course of the simulation, although the perpendicular proton temperature $T_{\perp,\mathrm{p}}$ increases. However, the parallel velocity distribution changes. As Fig. B.1 d) shows, an efficient acceleration of particles parallel to $\boldsymbol{B}_0$ emerges. It is suspected that a slight acceleration of the bulk plasma is incurred, carrying the momentum of the decayed waves. This assumption is, however, not supported nor excluded by the data, since no sufficient signal to noise ratio can be obtained.

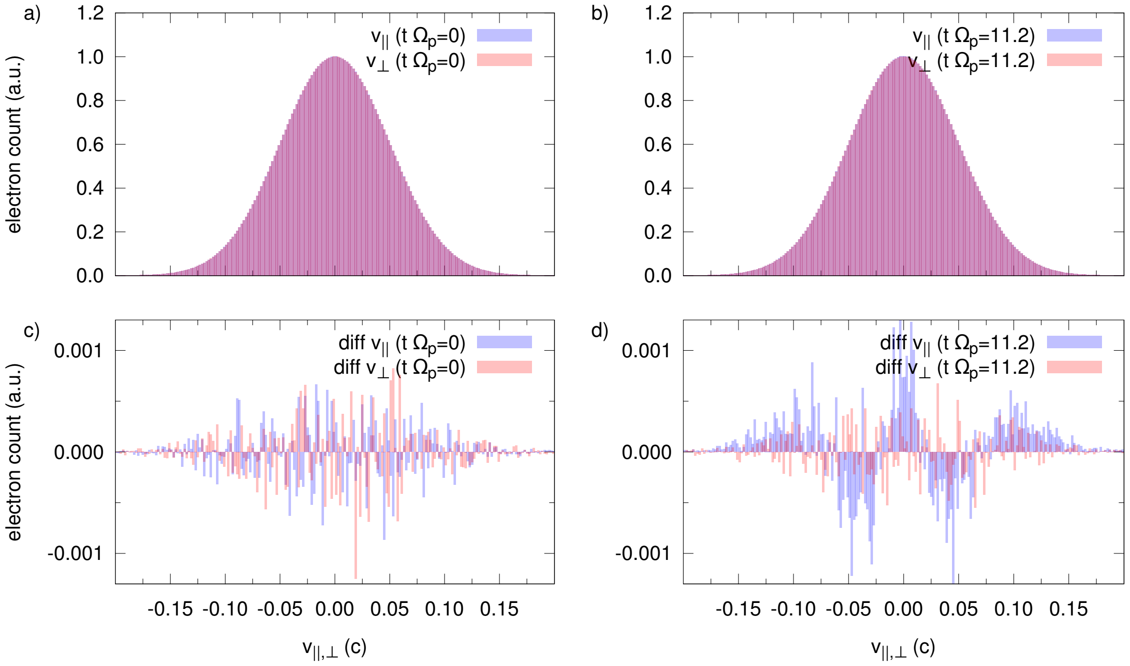

Fig. B.2: Top panels: Histograms of the electrons' parallel and perpendicular velocity components at the beginning (left) and the end (right) of one of the simulations from set A_1. The histograms are normalized to the number of particles in the bin around $v_{\|} = 0$ at the beginning of the simulation. Bottom panels: The deviations of the velocity distributions from a best fit Gaussian distribution at the beginning (left) and the end (right) of a simulation are shown. Other than for the protons the electrons show no systematic deviations in the perpendicular velocity component. However, the parallel component exhibits similar structures as observed for the protons. Figure according to Schreiner et al. (2017a).

The histograms of parallel and perpendicular velocity components of the electrons show that no noticeable anisotropy of the electron temperature is present at the beginning of the simulation or induced later. Also, the deviations of the perpendicular spectrum from a Gaussian distribution appear to be random, which is consistent with the idea that only protons are accelerated by the decaying left-handed waves. However, the spectrum of the parallel velocity component exhibits similar deviations from a Gaussian as observed for the protons. This would be consistent with the assumption that the particles carry the momentum of the decaying waves: While the protons would carry most of the momentum, the electrons would also be accelerated to counter the electric current caused by a finite proton bulk velocity.

Evolution of the Energy Density in 3D Simulations

Figure B.3 shows the time evolution of the energy densities W of the ten waves in the three-dimensional simulations described in Sect. 4.1.1. The three panels correspond to the three interval lengths $t_{\text{int}} \in \{1000, 3000, 5000\}\,\Delta t$, which determine the time resolution of the energy data. As can be seen from Fig. B.3 a longer interval t_{int} leads to a decreased noise level, as indicated by the lowest data points: For the shortest t_{int} the noise level is of the order $W_{\text{noise}} \approx 10^{-11}$ (panel a), whereas the other two panels show $W_{\text{noise}} \approx 10^{-12}$, i.e. a decrease by one order of magnitude.

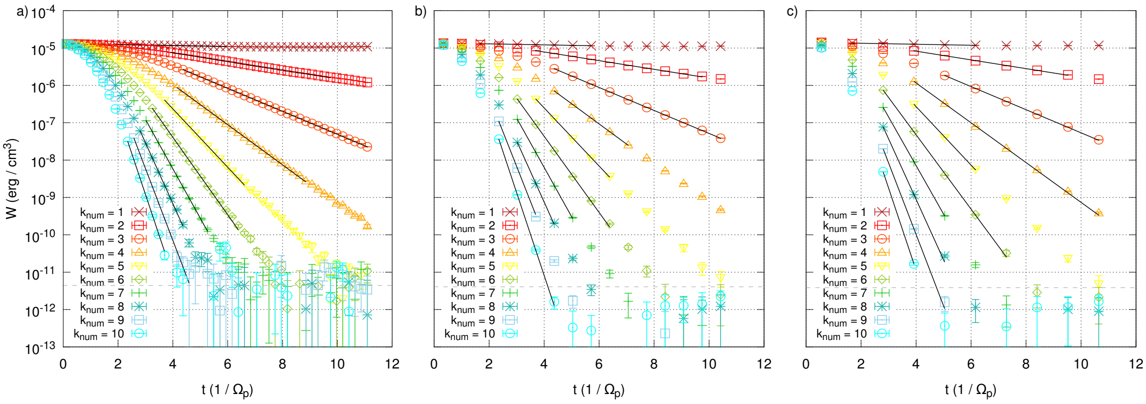

Fig. B.3: Energy densities $W(t)$ as functions of time for the ten different waves included in the three-dimensional simulations discussed in Sect. 4.1.1. The panels a), b) and c) correspond to three different interval lengths $t_{\text{int}} \in \{1000, 3000, 5000\}\,\Delta t$. Black lines indicate the exponential fits which are used to determine the damping rates, gray, dashed lines mark the expected noise level averaged over time and k_{num}. Figure according to Schreiner et al. (2017a).

The downside of a longer interval t_{int} is, however, that less data points are available for the exponential fit that determines the damping rate Γ. With a large t_{int} often only two or three data points per wave are available (panel c), whereas the exponential fit can be applied to several more points even for the fastest decaying wave if a short interval is chosen (panel a). The interested reader may find the exact values of the measured damping rates (corresponding to the slopes of the exponential fits in Fig. B.3) in Schreiner et al. (2017a, Appendix B).

Weakly Damped Wave

In Sect. 4.1.1 it was mentioned that the measured damping rate of the wave with $k_{\text{num}} = 1$ diverges from the expected value by two orders of magnitude. The reason for this deviation can be found by looking at the time evolution of the wave's energy density, which is presented in Fig. B.4. It can be seen that the energy density decays exponentially in the interval

$2 < t\,\Omega_\mathrm{p} < 6$. This is where the damping rate was measured, as indicated by the solid, black line labeled with “1”. However, the decay of the electromagnetic fields slows down at later times, although the energy density is still far above the numerical background noise.

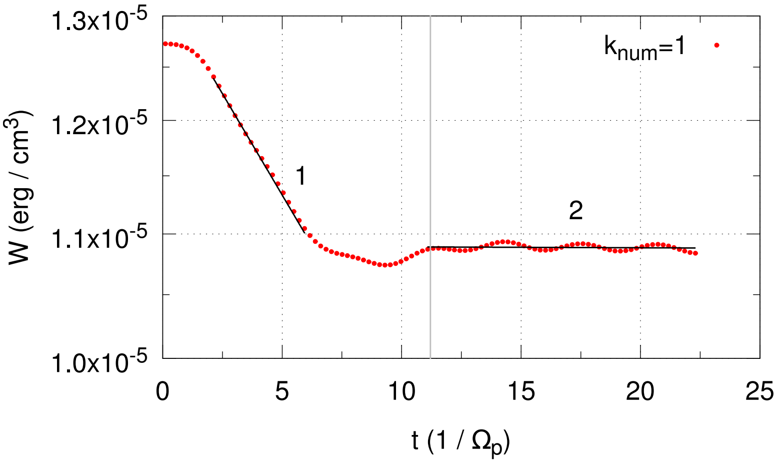

Fig. B.4: Time evolution of the energy density of a wave with $k_\mathrm{num} = 1$, as obtained from a single simulation. The standard setup for the simulations discussed in Sect. 4.1.1 covers a physical duration of $t\,\Omega_\mathrm{p} \approx 11$, indicated by the vertical, gray line. Restarting the simulation from a checkpoint and doubling its number of time steps produces field data up to $t\,\Omega_\mathrm{p} \approx 22.5$. Two exponential fits are applied to the data, marked by the solid, black lines with labels “1” and “2”. The first one does not yield a damping rate which is in agreement with theory, whereas the second one does (see discussion in the text). Figure according to Schreiner et al. (2017a).

The end of the simulation is marked by the vertical, gray line in Fig. B.4. To further investigate the behavior of the wave, the simulation was restarted using the checkpoint data written at the end of the regular simulation. The continued simulation covers the physical duration up to $t\,\Omega_\mathrm{p} \approx 22.5$, as the data in Fig. B.4 shows. The energy density of the wave stays almost constant, oscillating slightly. An exponential fit can be applied to the data right of the gray line, as denoted by the solid, black line labeled with “2”. Thus, a new damping rate can be found which matches the theoretical expectations. However, the uncertainties of the fit are immense and a statistical error of more then 100% was obtained.

It is not clear what causes the fast, initial decay of the wave and why this process stops after a few cyclotron time scales. The measured damping rate from the second half of the restarted simulation shows that the correct cyclotron damping is restored after the initial drop of the energy density. Unfortunately, the simulation must run twice as long as the standard setup used for the simulations in Sect. 4.1.1, doubling the computational cost. This, together with the fact that the exponential fit is not very meaningful due to the small damping rate and the large relative error, lead to the decision to exclude waves with $k_\mathrm{num} = 1$ from the further analysis. However, there is no principal problem with the modeling of weak damping in PiC simulations.

Evolution of the Energy Density in 2D Simulations

The time evolution of the energy densities of excited, damped waves in the two-dimensional simulations discussed in Sect. 4.1.2 are shown in Fig. B.5. Note that the wave at $k_{\rm num} = 1$ is excluded, as argued in the previous section. Compared to the three-dimensional simulations the numerical noise level is increased by two orders of magnitude (see Fig. B.3). This reduces the number of available data points for the exponential fits, which especially affects the measurement of damping rates at high parallel wave numbers, where damping is strong. The exponential fits are denoted by solid black lines in Fig. B.5. The measured rates are listed in Schreiner et al. (2017a, Appendix D).

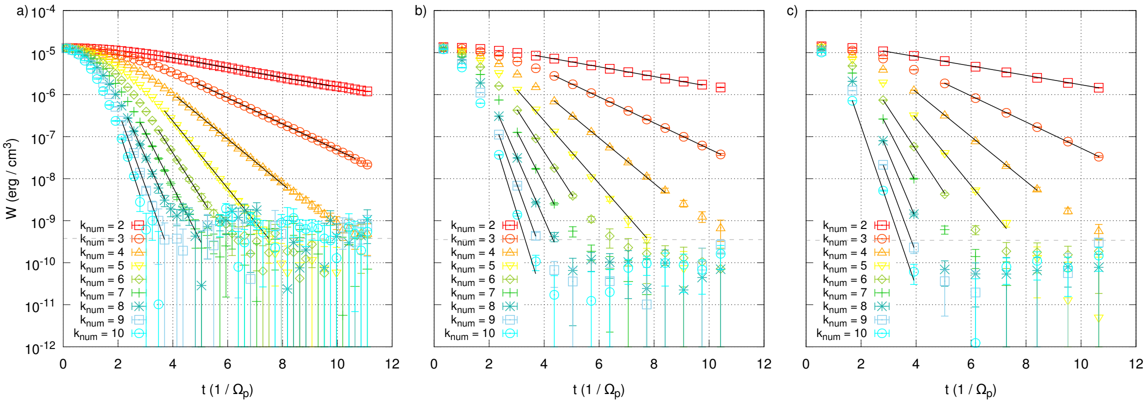

Fig. B.5: Energy densities $W(t)$ as functions of time for the nine different waves included in the two-dimensional simulations discussed in Sect. 4.1.2. The panels a), b) and c) correspond to three different interval lengths $t_{\rm int} \in \{1000, 3000, 5000\}\,\Delta t$. Black lines indicate the exponential fits which are used to determine the damping rates, gray, dashed lines mark the expected noise level averaged over time and $k_{\rm num}$. Figure according to Schreiner et al. (2017a).

Evolution of the Energy Density in 1D Simulations

The time evolution of the energy densities of excited, damped waves in the one-dimensional simulations discussed in Sect. 4.1.2 is shown in Fig. B.6. Again, the wave at $k_{\rm num} = 1$ is excluded for reasons explained above. The numerical noise level in the one-dimensional simulations exceeds that in the three-dimensional simulations by four orders of magnitude (compared to Fig. B.3). This drastically limits the number of data points that can be used for the exponential fits. With an initial energy density of around $10^{-5}\,\mathrm{erg/cm^3}$ and a noise level of $10^{-7}\,\mathrm{erg/cm^3}$ (Fig. B.6 a) or $10^{-8}\,\mathrm{erg/cm^3}$ (Fig. B.6 b and c) there is hardly any room for the exponential slope to develop. This can be seen by the black lines which represent the exponential fits and which mostly cover only three to five data points. Strong deviations from theoretical predictions and large uncertainties in the measurements can therefore be expected. The exact values of the measured damping rates and their standard errors can be found in Schreiner et al. (2017a, Appendix E).

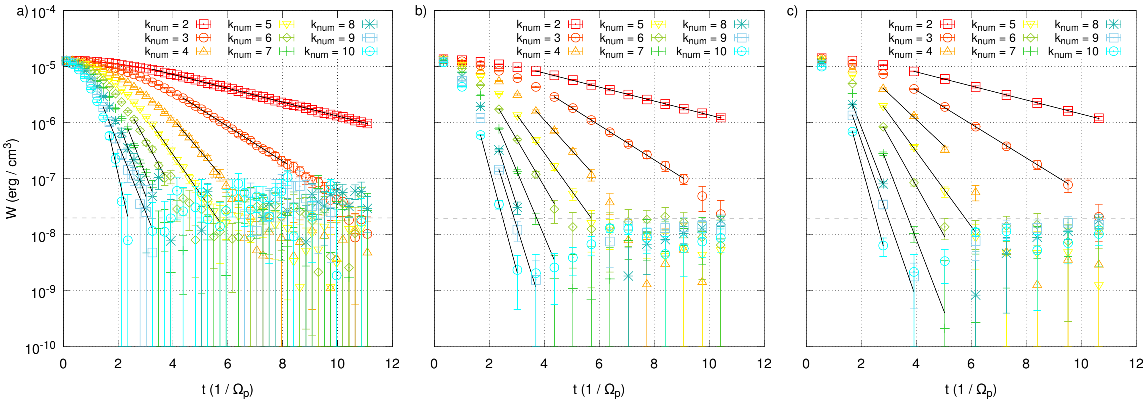

Fig. B.6: Energy densities $W(t)$ as functions of time for the nine different waves included in the one-dimensional simulations discussed in Sect. 4.1.2. The panels a), b) and c) correspond to three different interval lengths $t_{\text{int}} \in \{1000, 3000, 5000\}\,\Delta t$. Black lines indicate the exponential fits which are used to determine the damping rates, gray, dashed lines mark the expected noise level averaged over time and k_{num}. Figure according to Schreiner et al. (2017a).

Evolution of the Energy Density in Simulations with Fewer Particles per Cell

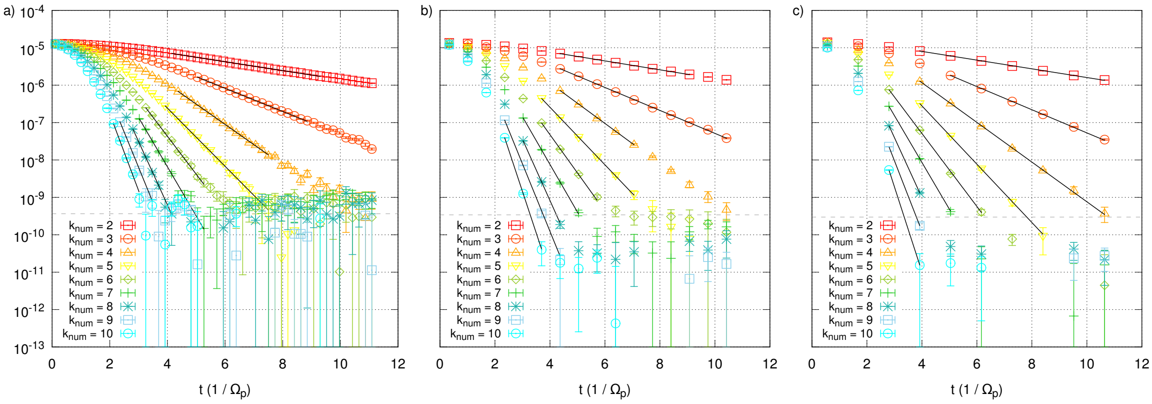

Fig. B.7: Energy densities $W(t)$ as functions of time for the nine different waves included in the simulations discussed in Sect. 4.1.3. Compared to the simulations presented in Sect. 4.1.1 the number of numerical particles per cell has been decreased. The panels a), b) and c) correspond to three different interval lengths $t_{\text{int}} \in \{1000, 3000, 5000\}\,\Delta t$. Black lines indicate the exponential fits which are used to determine the damping rates, gray, dashed lines mark the expected noise level averaged over time and k_{num}.

The energy densities of the individual waves in the simulations of set D are shown in Fig. B.7 as functions of time. The three panels a), b), and c) refer to the three interval lengths $t_{\text{int}} \in \{1000, 3000, 5000\}\,\Delta t$. Simulations of set D are initialized with only four particles per cell, compared to 128 in the previously discussed simulations (see Sect. 4.1.3).

As noted earlier, the chosen interval length influences the energy level of the (averaged) numerical background noise. For the shortest t_{int} the noise level is about one order of magnitude higher than for the other two t_{int}. Compared to the three-dimensional reference simulations with 128 particles per cell the noise level is increased by two orders of magnitude. Therefore, the noise level is comparable to that in the two-dimensional simulations (see Fig. B.5). Since the total number of numerical particles in the two-dimensional simulations is comparable to the total particle count in the simulations of set D it can be assumed that this number is primarily responsible for the level of the numerical noise.

Evolution of the Energy Density in Simulations with Fewer Grid Cells

Series E employs less grid cells in the directions perpendicular to the background magnetic field (see Sect. 4.1.3). This also reduces the total number of numerical particles in the simulation and, therefore, leads to a higher numerical noise level in the electromagnetic fields. The time evolution of the field energy densities are shown in Fig. B.8 a), b), c), where each panel includes data obtained with one of the three interval lengths t_{int}.

In fact, the total number of particles is the same as in the two-dimensional simulations presented earlier. The numerical noise level is, therefore, also comparable to that in the two-dimensional simulations.

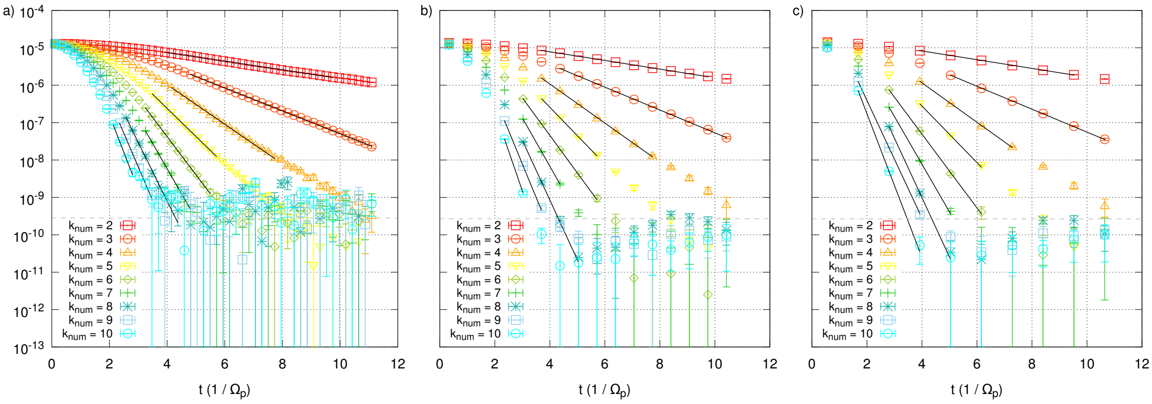

Fig. B.8: Energy densities $W(t)$ as functions of time for the nine different waves included in the simulations discussed in Sect. 4.1.3. Compared to the simulations presented in Sect. 4.1.1 the number of grid cells in the directions perpendicular to the background magnetic field has been decreased. The panels a), b) and c) correspond to three different interval lengths $t_{\text{int}} \in \{1000, 3000, 5000\}\,\Delta t$. Black lines indicate the exponential fits which are used to determine the damping rates, gray, dashed lines mark the expected noise level averaged over time and k_{num}.

C Resonant Proton Scattering

After the first attempt to model resonant scattering of energetic protons and Alfvén waves (Schreiner and Spanier, 2014), a few simulations have been carried out to study the interaction of protons and whistler waves. These are only proof of concept simulations, i.e. the main question that is addressed by the simulations is whether protons can resonate with right-handed whistler waves at all.

A series of eight simulations (PS1 through PS8, where "PS" stands for proton scattering) are set up as follows: Each simulation is initialized with a thermal background plasma, a single excited plasma wave according to the method described in Sect. 3.3.1, and a population of mono-energetic test protons, as described in Sect. 3.3.2. All simulations are based on a thermal plasma with an electron thermal velocity $v_{\mathrm{th,e}} = 0.080\,c$ (protons have the same temperature) and an electron plasma frequency $\omega_{\mathrm{p,e}} = 5.0 \cdot 10^8\,\mathrm{rad/s}$. The ratio of proton to electron mass is set to $m_\mathrm{p}/m_\mathrm{e} = 10.7$ to reduce the overall computational cost of the simulations. This mass ratio is used for both background and test protons. The Alfvén speed is $v_\mathrm{A} = 0.054\,c$ and the cyclotron frequency of the protons is $\Omega_\mathrm{p} = 1.64 \cdot 10^{-2}\ \omega_{\mathrm{p,e}}$. The numerical parameters common to all simulations are the length of each time step $\Delta t = 1.30 \cdot 10^{-2}/\omega_{\mathrm{p,e}}$, the number of time steps $N_t = 47\,000$ (resulting in $t_{\max} \cdot \Omega_\mathrm{p} \simeq 25$), the grid spacing $\Delta x = 2.26 \cdot 10^{-2}\ c/\omega_{\mathrm{p,e}}$ and the number of grid cells $N_\perp = 56$ in both directions perpendicular to the background magnetic field, which is enough to resolve the gyration of thermal protons.

Simulation	$N_\parallel$ (cells)	$k_\parallel$ ($\Omega_\mathrm{p}/v_\mathrm{A}$)	ω (Ω_p)	μ_res	v_p (c)	E_kin (MeV)
PS1	3500	0.10	0.10	0.44	0.81	3.86
PS2	1900	0.19	0.20	0.63	0.48	0.76
PS3	1300	0.28	0.30	0.67	0.35	0.37
PS4	1000	0.36	0.40	0.69	0.29	0.25
PS5	830	0.44	0.50	0.68	0.27	0.21
PS6	710	0.51	0.60	0.67	0.24	0.16
PS7	630	0.58	0.70	0.71	0.22	0.14
PS8	560	0.65	0.80	0.72	0.20	0.11

Table C.1: Numerical and physical parameters for test proton simulations: number of grid cells $N_\parallel$ parallel to B_0, parallel wave number $k_\parallel$ and frequency ω of the excited wave, resonant pitch angle cosine μ_res, as well as speed v_p and kinetic energy E_kin of the test protons.

A list of changing numerical and physical parameters can be found in Table C.1, summarizing the number of grid cells parallel to the background field $N_\parallel$, the different wave numbers $k_\parallel$ and frequencies ω of each initialized wave, as well as the anticipated resonant pitch angles μ_{res} and the speed v_{p} and kinetic energy E_{kin} of the test protons. Although the total volume of the simulation box changes with each simulation, the total number of test protons, N_{p}, is held approximately constant by adjusting the number of test particles per cell. Thus, N_{p} ranges between $1.04 \cdot 10^7$ and $1.25 \cdot 10^7$ depending on the simulation run, which allows for meaningful statistical analysis.

Figure C.1 depicts results from the simulations (except from PS3 and PS6, which are omitted for brevity) at time $t\,\Omega_{\mathrm{p}} = 12.6$. The color coded test proton data shows the particle density in $\bar{\mu}$-$\Delta\mu$-phase space, where $\bar{\mu}$ and $\Delta\mu$ are the mean pitch angle cosine and the change of the pitch angle cosine. Predictions from the analytical model introduced in Sect. 2.6.2 can be compared to the numerical results.

The analytical prediction agrees perfectly with the numerical results in Fig. C.1 a), i.e. simulation PS1. The height and position of the resonance peak, as well as the shapes of the ballistic peaks are accurately reproduced by the model. However, with increasing frequency of the excited plasma wave and decreasing particle energy the agreement of particle data and analytical model becomes worse. The shape of the particle distribution in phase space becomes less clear and the edges of the distribution become fuzzy (see e.g. panel c). This effect is more noticeable in simulations with smaller test proton speed (compare e.g. panels c) and f).

It is expected that the blurring of the particle distribution is a numerical effect. The simulations with lower test proton energy are smaller, thus there are less background particles and the numerical noise is increased. This, together with the lower test particle energy, causes additional random scattering of the test protons with fluctuations in the background plasma. Thus, the clear shape of the particle distribution is softened and especially the edges of the distribution become less sharp.

The numerical data produces a resonance peak which is slightly tilted. This is especially obvious in those simulations, where a substructure is visible inside the peak (Fig. C.1 b) through f). The reason for the tilt is not clear and it is not expected. Looking at the analytical prediction for the shape and amplitude of the resonance peak it can be seen that the peak height is not symmetric about $\Delta\mu = 0$, as was mentioned in Sect. 2.6.2.

Despite the above mentioned deviations of theory and simulation and the numerical artifacts, it can be concluded that energetic protons can interact with dispersive, right-handed waves. Although there are no direct objections against this process in theory, it is seldom considered when proton transport is discussed. It is therefore reassuring to see that proton scattering off of whistler waves can be easily modeled with PiC simulations and could be included in more complex numerical particle transport models.

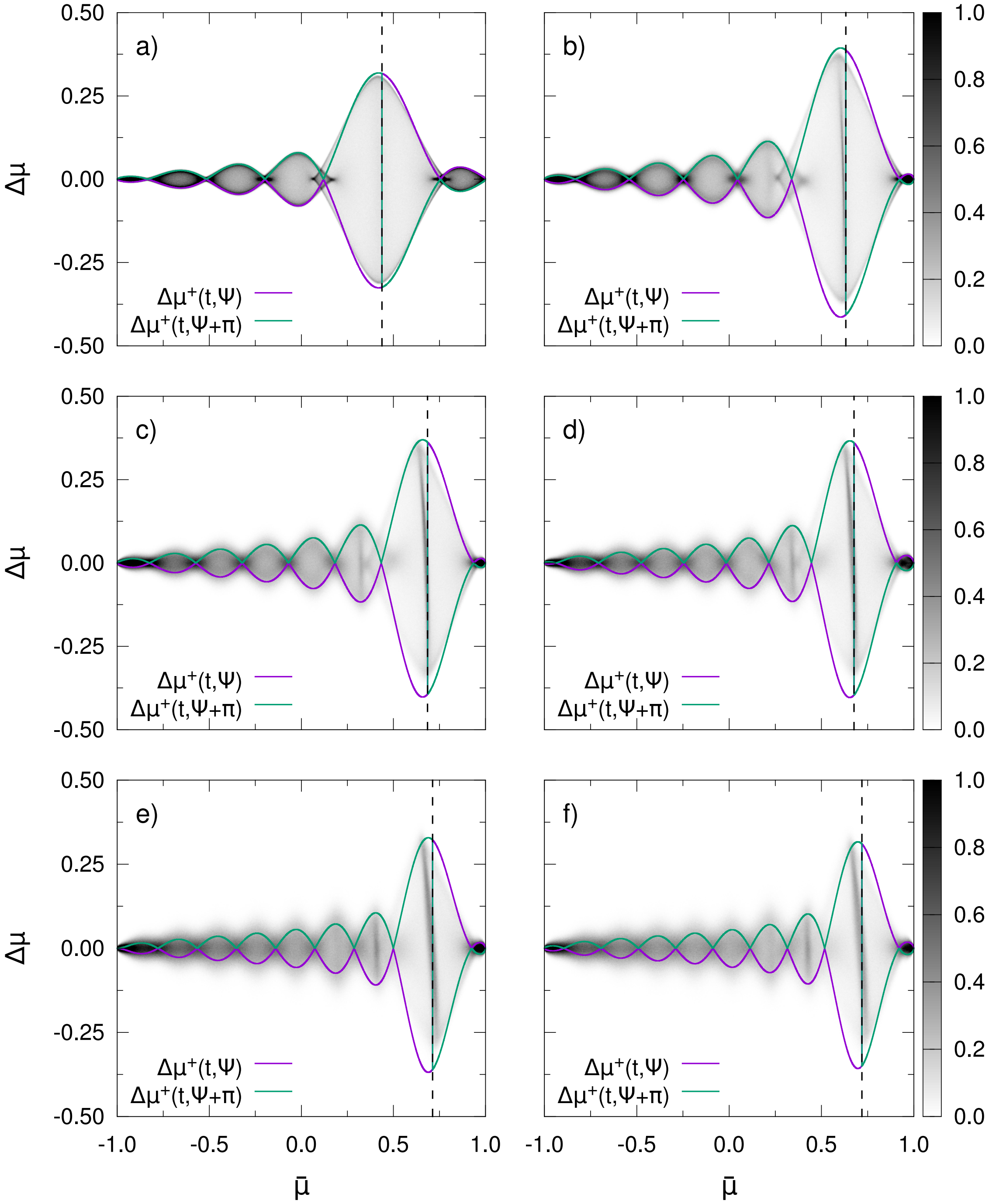

Fig. C.1: Scatter plots representing the test proton distribution in pitch angle phase space. The individual panels (a through f) show the data from simulations PS1, PS2, PS4, PS5, PS7 and PS8, where the particle density is indicated by the gray color (normalized to $10^{-4}\,N_{\mathrm{p}}$ with the number of test protons N_{p}). The dashed, vertical lines mark the positions of the resonant pitch angle cosines μ_{res}. The predictions from the analytical model presented in Sect. 2.6.2 are represented by the colored lines.

D Turbulence Analysis

Reduced Parallel and Perpendicular Spectra

While numerical noise is always a problem in PiC simulations, there are a few ways to reduce the noise level. It is, of course, possible to increase the number of particles per cell or the number of cells per simulation. However, this is costly and therefore might not be feasible in larger simulations. Especially for the one-dimensional spectra of the magnetic field energy E_B as function of $k_\parallel$ or $k_\perp$ there is another possibility.

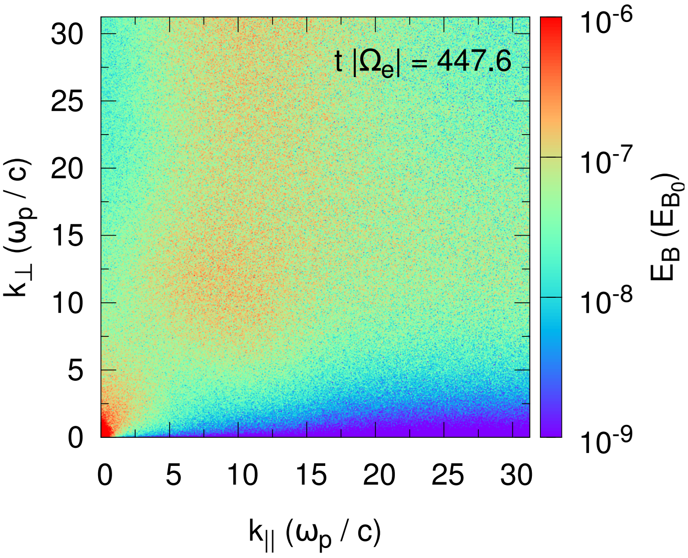

Fig. D.1: Magnetic energy distribution in two-dimensional wave number space for one point in time in simulation T2 (see Sect. 4.3.1). The full range of available parallel and perpendicular wave numbers is shown. The color-coded energy range is set according to the typical numerical noise levels in the simulation. It can be seen that the noise level increases towards larger wave numbers.

Looking at Fig. D.1, which shows the full range of the two-dimensional spectra in wave number space (Figs. 4.21 and 4.23 in Sect. 4.3.1 show only an excerpt at small wave numbers), it can be seen that the noise level increases towards high wave numbers. This can also partly be seen in the plots of $E_B(k)$ in panels a) of both Figs. 4.22 and 4.24 in Sect. 4.3.1. In the two- and one-dimensional spectra $E_B(k_\parallel, k_\perp)$ and $E_B(k)$ the low wave number regime, which contains the power law energy distribution, is not affected by this noise at high wave numbers.

For the one-dimensional parallel and perpendicular spectra $E_B(k_\parallel)$ and $E_B(k_\perp)$, however, the situation is different. Consider the parallel spectrum $E_B(k_\parallel)$, which is obtained by integrating $E_B(k_\parallel, k_\perp)$ over the perpendicular wave number $k_\perp$. This implies that the numerical noise at high $k_\perp$ also contributes to the magnetic energy at small $k_{||}$. In the same way, noise at high $k_{||}$ affects the perpendicular energy spectrum at small $k_\perp$.

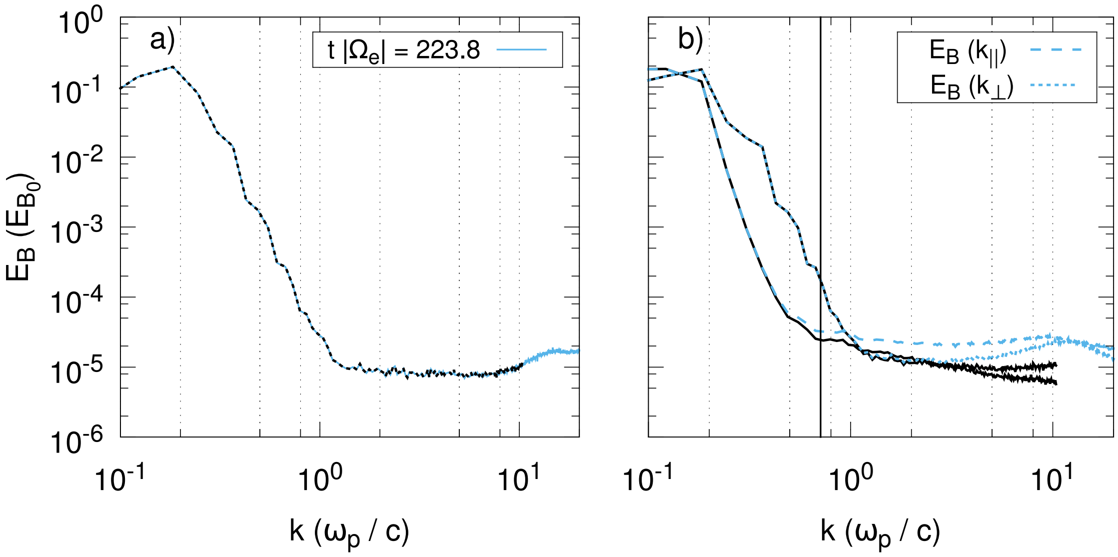

Fig. D.2: One dimensional magnetic energy spectra obtained from the data of simulation T2 (see Sect. 4.3.1). Panels a) and b) show the same data (blue lines) as the respective panels of Fig. 4.24. The black lines represent the energy spectra obtained from a reduced data set, including only one third of the available parallel and perpendicular wave numbers.

Limiting the integration to a smaller range of wave numbers can help to reduce the effective noise level in the parallel and perpendicular spectra, as can be seen in Fig. D.2 b). Here, the integration is performed over only one third of the available parallel or perpendicular wave numbers (black lines). While this limits the extent of the energy spectrum, it also reduces the noise level. It seems that in particular the parallel spectrum benefits from this method. The magnetic energy $E_B(k)$ as a function of the absolute of the wave vector is not affected, as is expected (see Fig. D.2 a).

Effects of Spatial Resolution

The simulations of Gary et al. (2008, 2012) are set up with a grid spacing $\Delta x = \lambda_\mathrm{D}$ equal to the Debye length. This is the limit for numerical accuracy of the simulation, and it might be suspected that the simulations can be improved by increasing the grid resolution. A higher spatial resolution, which automatically conditions a higher time resolution, might especially reduce the increase of numerical noise over time.

To test this assumption a simulation T2b is prepared, which is based on the setup of the two-dimensional simulation T2 (see Sect. 4.3.1). The numerical parameters of T2b are changed such that the physical extent of the simulation box is the same as in T2. Thus, with decreased grid spacing Δx, the energy spectrum in wave number space starts at the same minimum wave number, but extends to a higher maximum. The relevant regime at small wave numbers is therefore comparable in T2 and T2b. The complete set of numerical parameters of both simulations is given in Table D.1.

simulation	$N_\parallel\,(\Delta x)$	$N_\perp\,(\Delta x)$	$N_t\,(\Delta t)$	$\Delta x\,(c\,\omega_{\mathrm{p,e}}^{-1})$	$\Delta t\,(\omega_{\mathrm{p,e}}^{-1})$	ppc
T2	1024	1024	$1.0 \cdot 10^5$	0.10	0.05	128
T2b	1464	1464	$7.5 \cdot 10^4$	0.07	0.04	128

Table D.1: Numerical parameters for simulations T2 and T2b: number of cells $N_\parallel$ and $N_\perp$ in the directions parallel and perpendicular to the background magnetic field, number of time steps N_t, grid spacing Δx, time step length Δt, and ppc, i.e. the number of particles (electrons and protons combined) per cell. Fewer time steps have been chosen for T2b, since it is not necessary to reproduce the entire time evolution of the energy spectrum in T2.

Figure D.3 depicts the perpendicular spectra $E_B(k_\perp)$ obtained from the data of T2 (panel a) and T2b (panel b). It can be seen that there is hardly any difference in the low wave number regime, where the energy distribution follows a power law. In both simulations the time evolution of the spectrum leads to a flatter slope at later times. There are even individual features which are the same in both panels, such as the spike exhibited by the orange lines at $k_\perp\,c/\omega_\mathrm{p} = 5 \cdot 10^{-1}$.

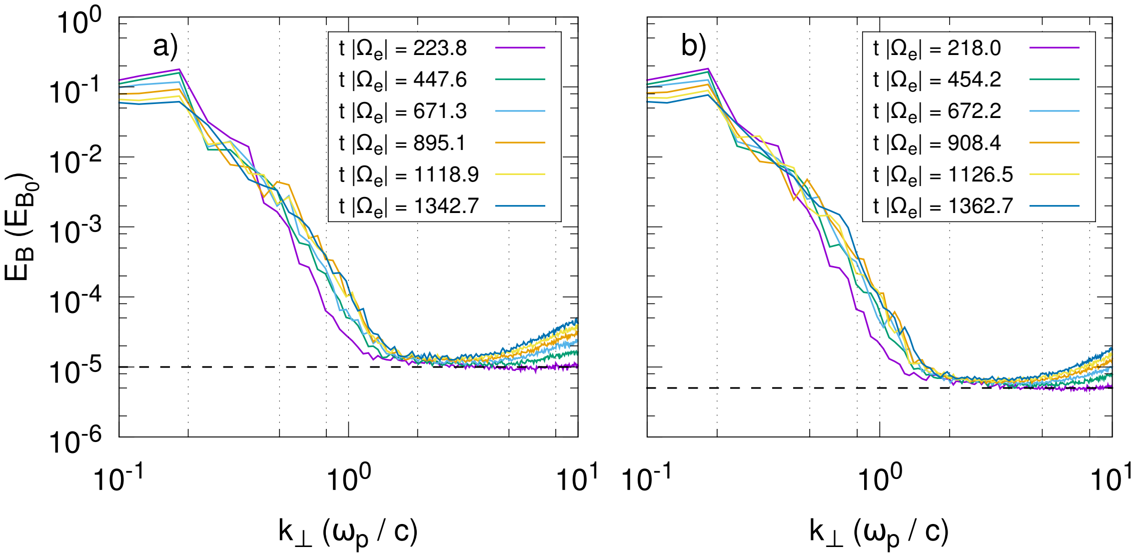

Fig. D.3: Perpendicular spectra $E_B(k_\perp)$ obtained from simulations T2 (panel a) and T2b (panel b) at different points in time. The dashed, black line indicates the numerical noise level at an early stage in both simulations. The noise levels in both simulations differ by a factor of two, corresponding to the ratio of the number of grid cells in T2 and T2b.

Towards larger perpendicular wave numbers the spectra reach the noise level. Here a difference between T2 and T2b is clearly visible. The numerical noise level indicated by the dashed line in Fig. D.3 b) is lower than the corresponding level in panel a). The analysis shows that the energy levels vary by a factor of two, which corresponds to the ratio of the number of grid cells in both simulations.

The lower noise level in T2b also allows the power law spectrum to extend to larger wave numbers. However, a spectral break or a steepening beyond $k_\perp\,c/\omega_\mathrm{p} = 1$, as found in the three-dimensional simulation T1 (see Sect. 4.3.1), can still not be seen.

In both panels a) and b) of Fig. D.3 the magnetic energy reaches a minimum, indicated by the dashed lines, and then rises again towards even higher wave numbers. However, the positive slope sets in at higher $k_\perp$ in panel b), suggesting that the increase is a numerical effect which occurs at high numerical wave numbers, independent of any characteristic physical scale.

In conclusion, the higher resolution of simulation T2b does not change the representation of physics at small wave numbers. Since phenomena at small wave numbers correspond to large scale structures in real space, they are well resolved both in T2 and T2b. Thus, the slightly higher spatial resolution is not expected to have an effect on the physics at these scales. However, if setting the grid spacing to $\Delta x = \lambda_\mathrm{D}$ should cause numerical instability or trigger any other numerical effects, all spatial scales might be affected. This does not seem to be the case here, as the example simulations have shown.

Turbulence Spectra of Simulations T3, T4 and T5

The parallel and perpendicular spectra $E_B(k_\parallel)$ and $E_B(k_\perp)$ of the magnetic field energy from simulations T3 through T5 are shown in Figs. D.4 and D.5. The setups for these simulations can be found in Tables 4.8 and 4.9 in Sect. 4.3.2.

As stated in Sect. 4.3.2, the energy transport in these simulations is anisotropic. This can be seen when the parallel and perpendicular spectra are compared: At small wave numbers both follow a power law in all three simulations. The parallel spectrum $E_B(k_\parallel)$, however, is noticeably steeper than $E_B(k_\perp)$.

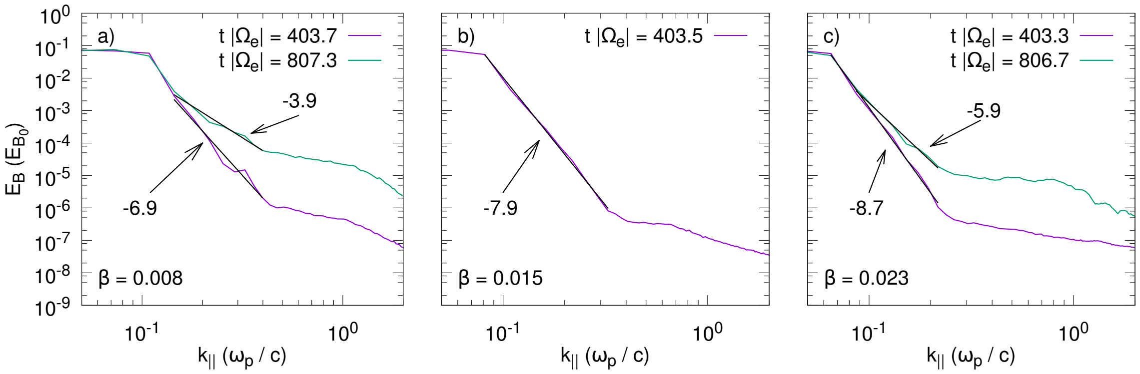

Fig. D.4: Parallel spectra of the magnetic field energy $E_B(k_\parallel)$ for simulations T3 (panel a), T4 (panel b), and T5 (panel c). Black lines indicate power law behavior, with the spectral indices denoted by the numbers in the plots.

It is interesting to note that the parallel spectrum flattens over time, as can be seen in Fig. D.4 a) and b). This might be partly related to the overall increase of the numerical noise, but the triangular structures at larger $k_\perp$, which can be seen in Fig. 4.26, also contribute. The presence of the plateau around $k\,c/\omega_\mathrm{p} \approx 1$, which can be seen in Fig. 4.25, is less obvious in the parallel spectrum. This is in accordance with the almost isotropic halo of constant energy for $k\,c/\omega_\mathrm{p} \leq 1.5$ seen in the two-dimensional energy distribution in Fig. 4.26, which is less pronounced for quasi-parallel wave vectors.

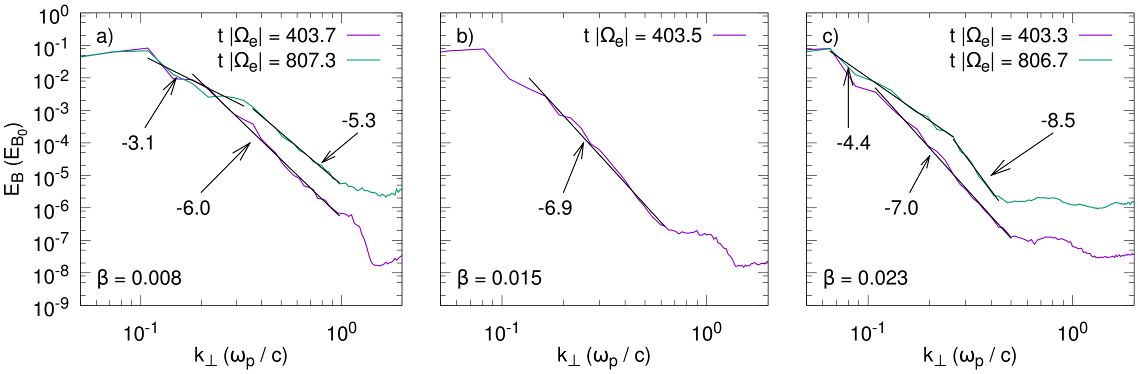

Fig. D.5: Perpendicular spectra of the magnetic field energy $E_B(k_\|)$ for simulations T3 (panel a), T4 (panel b), and T5 (panel c). Black lines indicate power law behavior, with the spectral indices denoted by the numbers in the plots.

The perpendicular spectra $E_B(k_\perp)$ in Fig. D.5 are very similar to the plots of the energy density $E_B(k)$ as a function of the absolute k of the wave vector, which are presented in Fig. 4.25. The magnetic energy distribution can be described by an unbroken power law for small perpendicular wave numbers at early and intermediate times (purple lines). However, at late times the spectrum breaks and splits into a flatter part before and a steeper regime beyond the break. The spectral indices found for the perpendicular spectra $E_B(k_\perp)$ are in good agreement with those in Fig. D.5 (with the exception of the late time spectrum from simulation T5 in panel c). The agreement of the spectral indices found for $E_B(k_\perp)$ and $E_B(k)$ indicates that the turbulent cascade is indeed dominated by perpendicular energy transport.

Pitch Angle Diffusion

Figure D.6 presents a comparison of the pitch angle diffusion coefficients $D_{\mu\mu}$ derived from the test electron data from simulations T6e and T6f. The details of these simulations can be found in Sect. 4.3.3. The test electrons in both simulations are initialized with a kinetic energy of $E_{\text{kin,e}} = 10\,\text{MeV}$. However, the initial particle distribution $f(\mu)$ in pitch angle space differs: In T6e it is defined as a parabola with a negative slope, $f(\mu) = 3/2\left((\mu-1)/2\right)^2$, whereas a positive slope is employed in T6f, $f(\mu) = 3/2\left((\mu+1)/2\right)^2$.

The simulations are compared in order to investigate if the choice of the slope affects the derived pitch angle diffusion coefficients. In particular, it is assumed that the divergence of $D_{\mu\mu}$ at $\mu = 1$ is an artifact of the method of Ivascenko et al. (2016), which occurs if the derivative $df(\mu)/d\mu$ becomes zero. This idea is supported by the fact that no such divergence is found in T6f. Instead, the pitch angle diffusion coefficient becomes negative near $\mu = -1$ in this simulation. This can again be traced back to the particle distribution $f(\mu)$: In T6f only few particles populate the phase space near $\mu = -1$, making the method of Ivascenko et al. (2016) prone to error due to statistical fluctuations in this regime.

At late times in the simulations the derived $D_{\mu\mu}$ become similar and both form a single peak around $\mu = 0$. This implies that the pitch angle diffusion coefficients found at those times are physically motivated and not dominated by statistical fluctuations or numerical

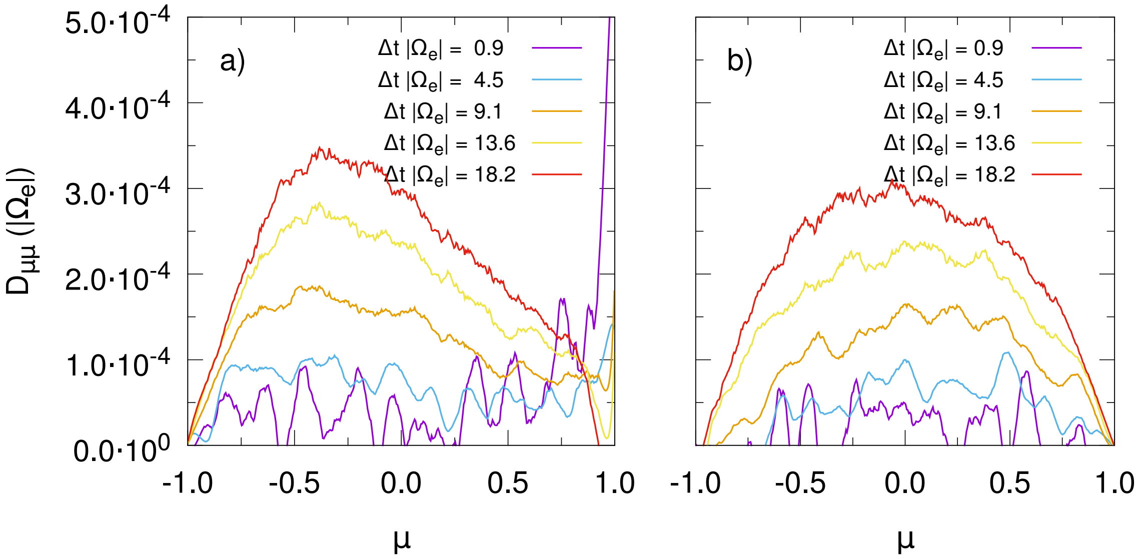

Fig. D.6: Comparison of the pitch angle diffusion coefficients $D_{\mu\mu}$ derived from the test electron data of simulations T6e (left) and T6f (right). The two simulations differ by the slope of the parabolic particle distribution $f(\mu)$ used to initialize the test electrons. The divergence of $D_{\mu\mu}$ at $\mu = 1$, which is found in T6e at early times, is not reproduced in T6f. This supports the idea that the divergence is a numerical artifact from the method of Ivascenko et al. (2016), which fails if the derivative of $f(\mu)$ becomes zero. At late times the two simulations yield similar results. However, it appears that T6f produces a more symmetric $D_{\mu\mu}$.

artifacts. The peak in Fig. D.6 b) appears to be more symmetric about $\mu = 0$, in contrast to the results of simulations T6e, T7e and T7f, which show slightly asymmetric $D_{\mu\mu}$ (see Figs. D.6 and 4.34 in Sect. 4.3.3).

Bibliography

Abramowitz, M. and Stegun, I. A., editors. *Handbook of Mathematical Functions with Formulas, Graphs, and Mathematical Tables.* Number 55 in Applied Mathematics Series. United States Department of Commerce, National Bureau of Standards; Dover Publications, Washington D.C.; New York, ninth reprint with additional corrections of tenth original printing with corrections (december 1972); first ed. edition, 1983. ISBN 978-0-486-61272-0.

Achatz, U., Dröge, W., Schlickeiser, R., and Wibberenz, G. Interplanetary transport of solar electrons and protons: Effect of dissipative processes in the magnetic field power spectrum. *Journal of Geophysical Research*, 98:13261–13280, 1993. DOI: `10.1029/93JA00450`.

Aguilar-Rodriguez, E., Blanco-Cano, X., Russel, C. T., Luhmann, J. G., Jian, L. K., and Ramírez Vélez, J. C. Dual observations of the interplanetary shocks associated with stream interaction regions. *Journal of Geophysical Research*, 116:A12109, 2011. DOI: `10.1029/2011JA016559`.

Alexandrova, O., Saur, J., Lacombe, C., Mangeney, A., Mitchell, J., Schwartz, S. J., and Robert, P. Universality of solar-wind turbulent spectrum from mhd to electron scales. *Physical Review Letters*, 103:165003, 2009. DOI: `10.1103/PhysRevLett.103.165003`.

Alfvén, H. On the existence of electromagnetic-hydrodynamic waves. *Arkiv för Matematik Astronomi och Fysik*, 29B(2), 1942a.

Alfvén, H. Existence of electromagnetic-hydrodynamic waves. *Nature*, 150(3805):405–406, 1942b.

Allis, W. P. Waves in a plasma. *MIT Research Lab Electronics Quarterly Report*, 54:5, 1955.

André, M. Dispersion surfaces. *Journal of Plasma Physics*, 33:1–19, 1985. DOI: `10.1017/S0022377800002270`.

Åström, E. On waves in an ionized gas. *Arkiv för Fysik*, 2(42), 1950a.

Åström, E. Magneto-hydrodynamic waves in a plasma. *Nature*, 165(4208):1019–1020, 1950b. DOI: `10.1038/1651019b0`.

Balogh, A. and Treumann, R. A. *Physics of Collisionless Shocks.* Number 12 in ISSI Scientific Report Series. Springer, New York Heidelberg Dordrecht London, 2013. ISBN 978-1-4614-6098-5. DOI: `10.1007/978-1-4614-6099-2`.

Bellan, P. M. *Fundamentals of plasma physics.* Cambridge University Press, first edition, 2008. ISBN 9780521528009.

Bellan, P. M. Circular polarization of obliquely propagating whistler wave magnetic field. *Physics of Plasmas*, 20:082113, 2013. DOI: `10.1063/1.4817964`.

Beresnyak, A. Spectra of strong magnetohydrodynamic turbulence from high-resolution simulations. *Astrophysical Journal Letters*, 784(2):L20, 2014. DOI: `10.1088/2041-8205/784/2/L20`.

Bergman, J. and Eliasson, B. Linear wave dispersion laws in unmagnetized relativistic plasma: Analytical and numerical results. *Physics of Plasmas*, 8(5):1482–1492, 2001. DOI: `10.1063/1.1358313`.

Bernstein, I. B. Waves in a plasma in a magnetic field. *Physical Review*, 109:10–21, 1958. DOI: `10.1103/PhysRev.109.10`.

Bethe, H. A. and Critchfield, C. L. The formation of deuterons by proton combination. *Physical Review*, 54:248–254, 1938. DOI: `10.1103/PhysRev.54.248`.

Biermann, L. Kometenschweife und solare Korpuskularstrahlung. *Zeitschrift für Astrophysik*, 29:274, 1951.

Biermann, L. Solar corpuscular radiation and the interplanetary gas. *The Observatory*, 77: 109–110, 1957.

Birdsall, C. K. and Fuss, D. Clouds-in-clouds, clouds-in-cells physics for many-body plasma simulation. *Journal of Computational Physics*, 135(2):141 – 148, 1997. ISSN 0021-9991. DOI: `10.1006/jcph.1997.5723`.

Birdsall, C. K. and Langdon, A. B. *Plasma physics via computer simulation*. Taylor and Francis, New York, 2005. ISBN 0750310251 9780750310253.

Biskamp, D. and Welter, H. Dynamics of decaying two-dimensional magnetohydrodynamic turbulence. *Physics of Fluids B*, 1:1964–1979, 1989. DOI: `10.1063/1.859060`.

Bittencourt, J. A. *Fundamentals of Plasma Physics*. Published by Springer-Verlag New York, Inc., third edition, 2004. ISBN 0-387-20975-1.

Boldyrev, S. Spectrum of magnetohydrodynamic turbulence. *Physical Review Letters*, 96 (11):115002, 2006. DOI: `10.1103/PhysRevLett.96.115002`.

Boris, J. P. Relativistic plasma simulation – Optimization of a hybrid code. In *Proceedings of the Fourth Conference on Numerical Simulation Plasmas*, pages 3–67. Naval Research Laboratory, Washington, D. C., 1970.

Borovsky, J. E. and Funsten, H. O. Role of solar wind turbulence in the coupling of the solar wind to the Earth's magnetosphere. *Journal of Geophysical Research: Space Physics*, 108, 2003. DOI: `10.1029/2002JA009601`.

Boyd, T. J. M. and Sanderson, J. J. *The Physics of Plasmas*. Cambridge University Press, 2003. ISBN 0-521-45912-5.

Bruno, R. and Carbone, V. The solar wind as a turbulence laboratory. *Living Reviews in Solar Physics*, 10(2), 2013. DOI: `10.12942/lrsp-2013-2`.

Büchner, J. Vlasov-code simulation. In Usui, H. and Omura, Y., editors, *Advanced Methods for Space Simulations*, pages 23–46. TERRAPUB, Tokyo, 2007. ISBN 978-4-88704-138-7.

Burkart, T., Elbracht, O., Ganse, U., and Spanier, F. The Influence of the Mass Ratio on the Acceleration of Particles by Filamentation Instabilities. *Astrophysical Journal*, 720: 1318–1324, 2010. DOI: `10.1088/0004-637X/720/2/1318`.

Cai, D., Li, Y., Nishikawa, K.-I., Xiao, C., Yan, X., and Pu, Z. Parallel 3-D electromagnetic particle code using high performance FORTRAN: Parallel TRISTAN. In Büchner, J., Scholer, M., and Dum, C. T., editors, *Space Plasma Simulation*, pages 25–53. Springer Berlin Heidelberg, Berlin, Heidelberg, 2003. ISBN 978-3-540-36530-3. DOI: `10.1007/3-540-36530-3_2`.

Camporeale, E. Resonant and nonresonant whistlers-particle interaction in the radiation belts. *Geophysical Research Letters*, 42:3114–3121, 2015. DOI: `10.1002/2015GL063874`.

Canuto, V., Chou, C. K., and Fassio-Canuto, L. Plasma astrophysics. *Fundamentals of Cosmic Physics*, 3:221–339, 1978. ISSN 0094-5846.

Chandran, B. D. G., Pongkitiwanichakul, P., Isenberg, P. A., Lee, M. A., Markovskii, S. A., Hollweg, J. V., and Vasquez, B. J. Resonant interactions between protons and oblique Alfvén/ion-cyclotron waves in the solar corona and solar flares. *The Astrophysical Journal*, 722(1):710, 2010. DOI: `10.1088/0004-637X/722/1/710`.

Chang, O., Gary, S. P., and Wang, J. Whistler turbulence at variable electron beta: Three-dimensional particle-in-cell simulations. *Journal of Geophysical Research: Space Physics*, 118:2824–2833, 2013. ISSN 2169-9402. DOI: `10.1002/jgra.50365`.

Chang, O., Gary, S. P., and Wang, J. Whistler turbulence forward cascade versus inverse cascade: Three-dimensional particle-in-cell simulations. *The Astrophysical Journal*, 800 (2):87, 2015. DOI: `10.1088/0004-637X/800/2/87`.

Che, H., Goldstein, M. L., and Viñas, A. F. Bidirectional energy cascades and the origin of kinetic Alfvénic and whistler turbulence in the solar wind. *Physical Review Letters*, 112:061101, 2014. DOI: `10.1103/PhysRevLett.112.061101`.

Chen, C. H. K., Horbury, T. S., Schekochihin, A. A., Wicks, R. T., Alexandrova, O., and Mitchell, J. Anisotropy of solar wind turbulence between ion and electron scales. *Physical Review Letters*, 104(25):255022, 2010. DOI: `10.1103/PhysRevLett.104.255002`.

Chen, L., Thorne, R. M., Shprits, Y., and Ni, B. An improved dispersion relationfor parallel propagating electromagnetic waves in warm plasmas: Application to electron scattering. *Journal of Geophysical Research: Space Physics*, 118:2185–2195, 2013. DOI: `10.1002/jgra.50260`.

Clemmow, P. C. and Mullaly, R. F. Dependence of the refractive index in magneto-ionic theory on the direction of the wave normal. In *Physics of the ionosphere: Report of the Physical Society conference on the physics of the ionosphere held at Cavendish Laboratory, Cambridge, September 1954*, page 340. Physical Society, London, 1955.

Cole, J. High-accuracy Yee algorithm based on nonstandard finite differences: New developments and verifications. *IEEE Transactions on Antennas and Propagation*, 50(9): 1185–1191, 2002. ISSN 0018-926X. DOI: `10.1109/TAP.2002.801268`.

Compton, A. H. An apparent effect of galactic rotation on the intensity of cosmic rays. *Physical Review*, 47:817–821, 1935. DOI: `10.1103/PhysRev.47.817`.

Coroniti, F. V., Kennel, C. F., and Scarf, F. L. Whistler mode turbulence in the disturbed solar wind. *Journal of Geophysical Research*, 87:6029–6044, 1982. DOI: `10.1029/JA087iA08p06029`.

Courant, R., Friedrichs, K., and Lewy, H. Über die partiellen Differenzengleichungen der mathematischen Physik. *Mathematische Annalen*, 100(1):32–74, 1928.

Cranmer, S. R. and van Ballegooijen, A. A. Alfvénic turbulence in the extended solar corona: Kinetic effects and proton heating. *The Astrophysical Journal*, 594(1):573, 2003. DOI: `10.1086/376777`.

Datlowe, D. Relativistic electrons in solar particle events. *Solar Physics*, 17:436–458, 1971. DOI: `10.1007/BF00150046`.

Debye, P. and Hückel, E. Zur Theorie der Elektrolyte. *Physikalische Zeitschrift*, 24(9): 185–206, 1923.

Dröge, W. Particle scattering by magnetic fields. In Bieber, J. W., Eroshenko, E., Evenson, P., Flückiger, E. O., and Kallenbach, R., editors, *Cosmic Rays and Earth: Proceedings of an ISSI Workshop, 21–26 March 1999, Bern, Switzerland*, pages 121–151. Springer Netherlands, Dordrecht, 2000. ISBN 978-94-017-1187-6. DOI: `10.1007/978-94-017-1187-6_7`.

Dupree, T. H. A perturbation theory for strong plasma turbulence. *Physics of Fluids*, 9: 1773–1782, 1966. DOI: `10.1063/1.1761932`.

Elsasser, W. M. The hydromagnetic equations. *Physical Review*, 79:183, 1950. DOI: `10.1103/PhysRev.79.183`.

Esirkepov, T. Z. Exact charge conservation scheme for Particle-in-Cell simulation with an arbitrary form-factor. *Computer Physics Communications*, 135(2):144–153, 2001. ISSN 0010-4655. DOI: `10.1016/S0010-4655(00)00228-9`.

Fairfield, D. H. Whistler waves observed upstream from collisionless shocks. *Journal of Geophysical Research*, 79:1368–1378, 1974. DOI: `10.1029/JA079i010p01368`.

Fang, N., Liao, C., and Ying, L.-A. Darwin approximation to Maxwell's equations. In Allen, G., Nabrzyski, J., Seidel, E., van Albada, G. D., Dongarre, J., and Sloot, P. M. A., editors, *Computational Science – ICCS 2009, 9th International Conference Baton Rouge, LA, USA, May 25-27, 2009 Proceedings, Part I*, pages 775–784. Springer Berlin Heidelberg, 2009. ISBN 978-3-642-01969-2. DOI: `10.1007/978-3-642-01970-8_77`.

Fermi, E. On the origin of the cosmic radiation. *Physical Review*, 75:1169–1174, 1949. DOI: `10.1103/PhysRev.75.1169`.

Fisk, L. A. He-3-rich flares – A possible explanation. *The Astrophysical Journal*, 224: 1048–1055, 1978. DOI: `10.1086/156456`.

Fitzpatrick, R. *Plasma Physics: An Introduction.* CRC Press, Taylor & Francis Group, 2014. ISBN 9781466594265.

Fonseca, R. A., Silva, L. O., Tsung, F. S., Decyk, V. K., Lu, W., Ren, C., Mori, W. B., Deng, S., Lee, S., Katsouleas, T., and Adam, J. C. OSIRIS: A three-dimensional, fully relativistic particle in cell code for modeling plasma based accelerators. In *Proceedings of the International Conference on Computational Science-Part III*, ICCS '02, pages 342–351, London, UK, UK, 2002. Springer-Verlag. ISBN 3-540-43594-8.

Forbush, S. E. Three unusual cosmic-ray increases possibly due to charged particles from the Sun. *Physical Review*, 70:771–772, 1946. DOI: `10.1103/PhysRev.70.771`.

Franci, L., Landi, S., Matteini, L., Verdini, A., and Hellinger, P. High-resolution hybrid simulations of kinetic plasma turbulence at proton scales. *The Astrophysical Journal*, 812:21, 2015. DOI: `10.1088/0004-637X/812/1/21`.

Franci, L., Verdini, A., Matteini, L., Landi, S., and Hellinger, P. Solar wind turbulence from MHD to sub-ion scales: High-resolution hybrid simulations. *The Astrophysical Journal Letters*, 804(2):L39, 2015. DOI: `10.1088/2041-8205/804/2/L39`.

Fried, B. D. and Conte, S. D. *The plasma dispersion function.* Academic Press, 1961.

Ganse, U. *Typ II Radiobursts bei koronalen Masseauswürfen - Simulation mit PiC-Codes.* diploma thesis, Julius-Maximilians-Universität Würzburg, 2009.

Ganse, U. *Kinetische Simulationen solarer Typ II Radiobursts.* phd thesis, Julius-Maximilians-Universität Würzburg, 2012.

Gary, S. P. *Theory of space plasma microinstabilities.* Cambridge atmospheric and space science series. Cambridge University Press, 1993. ISBN 0-521-43167-0.

Gary, S. P. Short-wavelength plasma turbulence and temperature anisotropy instabilities: Recent computational progress. *Philosophical Transactions of the Royal Society of London A: Mathematical, Physical and Engineering Sciences*, 373(2041), 2015. ISSN 1364-503X. DOI: `10.1098/rsta.2014.0149`.

Gary, S. P. and Nishimura, K. Kinetic Alfvén waves: Linear theory and a particle-in-cell simulation. *Journal of Geophysical Research*, 109, 2004. DOI: `10.1029/2003JA010239`.

Gary, S. P. and Saito, S. Particle-in-cell simulations of Alfvén-cyclotron wave scattering: Proton velocity distributions. *Journal of Geophysical Research*, 108:1194, 2003. DOI: `10.1029/2002JA009824`.

Gary, S. P. and Smith, C. Short-wavelength turbulence in the solar wind: Linear theory of whistler and kinetic Alfvén fluctuations. *Journal of Geophysical Research*, 114, 2009. DOI: `10.1029/2009JA014525`.

Gary, S. P., Saito, S., and Li, H. Cascade of whistler turbulence: Particle-in-cell simulations. *Geophysical Research Letters*, 35, 2008. DOI: `10.1029/2007GL032327`.

Gary, S. P., Chang, O., and Wang, J. Forward cascade of whistler turbulence: Three-dimensional particle-in-cell simulations. *The Astrophysical Journal*, 755(2):142, 2012. DOI: `10.1088/0004-637X/755/2/142`.

Gary, S. P., Hughes, R. S., Wang, J., and Chang, O. Whistler anisotropy instability: Spectral transfer in a three-dimensional particle-in-cell simulation. *Journal of Geophysical Research: Space Physics*, 119:1429–1434, 2014. DOI: `10.1002/2013JA019618`.

Goedbloed, J. P., Keppens, R., and Poedts, S. *Advanced Magnetohydrodynamics*. Cambridge University Press, 2010. ISBN 9780521705240.

Goldreich, P. and Sridhar, S. Toward a theory of interstellar turbulence. II: Strong Alfvénic turbulence. *Astroparticle Physics*, 438:763–775, 1995. DOI: `10.1086/175121`.

Goldreich, P. and Sridhar, S. Magnetohydrodynamic turbulence revisited. *Astroparticle Physics*, 485:680–688, 1997. DOI: `10.1086/304442`.

Görler, T., Lapillonne, X., Brunner, S., Dannert, T., Jenko, F., Merz, F., and Told, D. The global version of the gyrokinetic turbulence code GENE. *Journal of Computational Physics*, 230:7053–7071, 2011. DOI: `10.1016/j.jcp.2011.05.034`.

Gosling, J. T., Asbridge, J. R., Bame, S. J., Feldman, W. C., Zwickl, R. D., Paschmann, G., Sckopke, N., and Hynds, R. J. Interplanetary ions during an energetic storm particle event: The distribution function from solar wind thermal energies to 1.6 MeV. *Journal of Geophysical Research: Space Physics*, 86:547–554, 1981. DOI: `10.1029/JA086iA02p00547`.

Hale, G. E. On the probable existence of a magnetic field in Sun-spots. *The Astrophysical Journal*, 28:315, 1908. DOI: `10.1086/141602`.

Hale, G. E., Ellerman, F., Nicholson, S. B., and Joy, A. H. The Magnetic Polarity of Sun-Spots. *The Astrophysical Journal*, 49:153, 1919. DOI: `10.1086/142452`.

Hasselmann, K. and Wibberenz, G. A note on the parallel diffusion coefficient. *The Astrophysical Journal*, 162:1049, 1970. DOI: `10.1086/150736`.

Hess, V. F. Über Beobachtungen der durchdringenden Strahlung bei sieben Freiballonfahrten. *Physikalische Zeitschrift*, 13:1084, 1912.

Hockney, R. W. and Eastwood, J. W. *Computer simulation using particles*. Bristol: Hilger, 1988. ISBN 0-85274-392-0.

Hollweg, J. V. Kinetic Alfvén wave revisited. *Journal of Geophysical Research*, 104:14811–14819, 1999. DOI: `10.1029/1998JA900132`.

Howes, G. G. A dynamical model of plasma turbulence in the solar wind. *Philosophical Transactions of the Royal Society of London Series A*, 373:20140145–20140145, 2015a. DOI: `10.1098/rsta.2014.0145`.

Howes, G. G. Kinetic turbulence. In Lazarian, A., de Gouveia Dal Pino, E. M., and Melioli, C., editors, *Magnetic Fields in Diffuse Media*, volume 407 of *Astrophysics and Space Science Library*, 2015b. DOI: `10.1007/978-3-662-44625-6_6`.

Howes, G. G. The dynamical generation of current sheets in astrophysical plasma turbulence. *The Astrophysical Journal Letters*, 827(2):L28, 2016. DOI: `10.3847/2041-8205/827/2/L28`.

Howes, G. G. and Nielson, K. D. Alfvén wave collisions, the fundamental building block of plasma turbulence. I. Asymptotic solution. *Physics of Plasmas*, 20(7):072302, 2013. DOI: `10.1063/1.4812805`.

Howes, G. G., Dorland, W., Cowley, S. C., Hammett, G. W., Quataert, E., Schekochihin, A. A., and Tatsuno, T. Kinetic simulations of magnetized turbulence in astrophysical plasmas. *Physical Review Letters*, 100:065004, 2008. DOI: `10.1103/PhysRevLett.100.065004`.

Huba, J. D., Book, D., Burn, T., and Scott, R. *NRL (Naval Research Lab) plasma formulary*. Naval Research Laboratory, Washington, D. C., revised 2007 edition, 2007.

Iroshnikov, P. S. Turbulence of a conducting fluid in a strong magnetic field. *Astronomicheskii Zhurnal*, 40:742, 1963.

Iroshnikov, P. S. Turbulence of a conducting fluid in a strong magnetic field. *Soviet Astronomy*, 7:566, 1964.

Ivascenko, A., Lange, S., Spanier, F., and Vainio, R. Determining pitch-angle diffusion coefficients from test particle simulation. *The Astrophysical Journal Supplement Series*, 833(2):223–231, 2016. DOI: `10.3847/1538-4357/833/2/223`.

Jokipii, J. R. Cosmic-Ray Propagation. I. Charged Particles in a Random Magnetic Field. *The Astrophysical Journal*, 146:480–487, 1966. DOI: `10.1086/148912`.

Jokipii, J. R. Rate of energy gain and maximum energy in diffusive shock acceleration. *The Astrophysical Journal*, 313:842–846, 1987. DOI: `10.1086/165022`.

Jones, F. C. and Ellison, D. C. The plasma physics of shock acceleration. *Astronomy and Astrophysics*, 58(3-4):259–346, 1991. DOI: `10.1007/BF01206003`.

Kempf, A., Ganse, U., Kilian, P., and Spanier, F. Note on the use of Yee-lattices in (semi-) implicit particle-in-cell codes. *Journal of Computational Physics*, 237(0):56 – 60, 2013. ISSN 0021-9991. DOI: `http://dx.doi.org/10.1016/j.jcp.2012.11.045`.

Kempf, A. A. *Plasma instabilities of particle beams in the intergalactic medium*. phd thesis, Ruhr-Universität Bochum, 2016.

Kennel, C. and Petschek, H. Limit on stably trapped particle fluxes. *Journal of Geophysical Research*, 71:1–28, 1966. DOI: `10.1029/JZ071i001p00001`.

Kilian, P. *Teilchenbeschleunigung an kollisionsfreien Schockfronten*. phd thesis, Julius-Maximilians-Universität Würzburg, 2015.

Kilian, P., Burkart, T., and Spanier, F. The influence of the mass ratio on particle acceleration by the filamentation instability. In Nagel, W. E., Kröner, D. B., and Resch, M. M., editors, *High Performance Computing in Science and Engineering '11*, pages 5–13. Springer, Berlin Heidelberg, 2012.

Kilian, P., Muñoz, P., Schreiner, C., and Spanier, F. Plasma waves as a benchmark problem. *Journal of Plasma Physics*, 83:707830101, 2017. DOI: `10.1017/S0022377817000149`.

Klein, K. G. and Howes, G. G. Predicted impacts of proton temperature anisotropy on solar wind turbulence. *Physics of Plasmas*, 22(3):032903, 2015. DOI: `10.1063/1.4914933`.

Koen, E. J., Collier, A. B., and Maharaj, S. K. Extracting growth rates from a particle-in-cell simulation. In van Rensburg, J. J., editor, *Proceedings of SAIP2012*. Department of Physics, University of Pretoria, 2012. ISBN 978-1-77592-070-0.

Kolmogorov, A. N. The local structure of turbulence in incompressible viscous fluid for very large Reynolds' numbers. *Doklady Akademiia Nauk SSSR*, 30:301–305, 1941a.

Kolmogorov, A. N. On degeneration (decay) of isotropic turbulence in an incompressible viscous liquid. *Doklady Akademiia Nauk SSSR*, 31:538–540, 1941b.

Kolmogorov, A. N. Dissipation of energy in locally isotropic turbulence. *Doklady Akademiia Nauk SSSR*, 32:16–20, 1941c.

Kolmogorov, A. N. The local structure of turbulence in incompressible viscous fluid for very large Reynolds numbers. *Proceedings of the Royal Society of London Series A*, 434:9–13, 1991a. DOI: `10.1098/rspa.1991.0075`.

Kolmogorov, A. N. Dissipation of energy in locally isotropic turbulence. *Proceedings: Mathematical and Physical Sciences*, 434(1890):15–17, 1991b. DOI: `10.2307/51981`.

Koskinen, H. E. J. *Physics of Space Storms*. Springer Heidelberg Dordrecht London New York, 2011. ISBN 978-3-642-00310-3. DOI: `10.1007/978-3-642-00319-6`.

Kosovichev, A. G., Schou, J., Scherrer, P. H., Bogart, R. S., Bush, R. I., Hoeksema, J. T., Aloise, J., Bacon, L., Burnette, A., DeForest, C., Giles, P. M., Leibrand, K., Nigam, R., Rubin, M., Scott, K., Williams, S. D., Basu, S., Christensen-Dalsgaard, J., Dappen, W., Rhodes, E. J., Duvall, T. L., Howe, R., Thompson, M. J., Gough, D. O., Sekii, T., Toomre, J., Tarbell, T. D., Title, A., Mathur, D., Morrison, M., Saba, J. L. R., Wolfson, C. J., Zayer, I., and Milford, P. N. Structure and rotation of the solar interior: Initial results from the MDI medium-l program. *Solar Physics*, 170:43–61, 1997.

Kraichnan, R. H. Inertial range spectrum of hydromagnetic turbulence. *Physics of Fluids*, 8:1385–1387, 1965. DOI: `10.1063/1.1761412`.

Krymskii, G. F. A regular mechanism for the acceleration of charged particles on the front of a shock wave. *Soviet Physics Doklady*, 22:327, 1977.

Kärkkäinen, M., Gjonaj, E., Lau, T., and Weiland, T. Low-dispersion wake field calculation tools. In *Proceedings of ICAP 2006*, volume 1, Chamonix, France, 2006. Joint Accelerator Conferences Website.

Landau, L. On the vibrations of the electronic plasma. *Journal of Physics (USSR)*, 10(1): 25–34, 1946.

Lang, K. R. *Astrophysical Formulae*. Springer-Verlag, Berlin Heidelberg New York, second corrected and enlarged edition, 1980. ISBN 3-540-09933-6.

Lang, K. R. *The Sun from Space.* Springer-Verlag Berlin Heidelberg, second edition, 2009. ISBN 978-3-540-76953-8.

Lange, S. and Spanier, F. Evolution of plasma turbulence excited with particle beams. *Astronomy and Astrophysics*, 546:A51, 2012. DOI: `10.1051/0004-6361/201219579`.

Lange, S., Spanier, F., Battarbee, M., Vainio, R., and Laitinen, T. Particle scattering in turbulent plasmas with amplified wave modes. *Astronomy and Astrophysics*, 553:A129, 2013. DOI: `10.1051/0004-6361/201220804`.

Langmuir, I. Oscillations in ionized gases. *Proceedings of the National Academy of Science*, 14:627–637, 1928. DOI: `10.1073/pnas.14.8.627`.

Lapenta, G. Particle in cell methods. PDF on research website, 2011. URL `https://perswww.kuleuven.be/~u0052182/pic/book.pdf`.

Lazar, M. and Schlickeiser, R. Covariant kinetic dispersion theory of linear transverse waves parallel propagating in magnetized plasmas with thermal anisotropy. *Physics of Plasmas*, 13(1):012110, 2006. DOI: `10.1063/1.2167308`.

Lee, M. A. Coupled hydromagnetic wave excitation and ion acceleration at interplanetary traveling shocks. *Journal of Geophysical Research*, 88:6109–6119, 1983. DOI: `10.1029/JA088iA08p06109`.

Lee, M. A. and Lerche, I. Waves and irregularities in the solar wind. *Reviews of Geophysics and Space Physics*, 12(4):671–687, 1974. DOI: `10.1029/RG012i004p00671`.

Lerche, I. and Schlickeiser, R. Cosmic ray transport in anisotropic magnetohydrodynamic turbulence. I. Fast magnetosonic waves. *Astronomy and Astrophysics*, 378:279–294, 2001. DOI: `10.1051/0004-6361:20011080`.

Li, H., Gary, S. P., and Stawicki, O. On the dissipation of magnetic fluctuations in the solar wind. *Geophysical Research Letters*, 28(7):1347–1350, 2001. DOI: `10.1029/2000GL012501`.

López, R. A., Muñoz, V., Viñas, A. F., and Valdivia, J. A. Particle-in-cell simulation for parametric decys of a circularly polarized Alfvén wave in relativistic thermal electron-positron plasma. *Physics of Plasmas*, 21:032102, 2014. DOI: `10.1063/1.4867255`.

Maron, J. and Goldreich, P. Simulations of incompressible magnetohydrodynamic turbulence. *The Astrophysical Journal*, 554:1175–1196, 2001.

Marsch, E. and Tu, C.-Y. Heating and acceleration of coronal ions interacting with plasma waves through cyclotron and Landau resonance. *Journal of Geophysical Research*, 106 (A1):227–238, 2001. DOI: `10.1029/2000JA000042`.

Matthaeus, W. H., Qin, G., Bieber, J. W., and Zank, G. P. Nonlinear collisionless perpendicular diffusion of charged particles. *The Astrophysical Journal Letters*, 590(1):L53, 2003. DOI: `10.1086/376613`.

Maxwell, J. C. A dynamical theory of the electromagnetic field. *Philosophical Transactions of the Royal Society of London*, 155:459–512, 1865. DOI: `10.1098/rstl.1865.0008`.

Melzani, M., Winisdoerffer, C., Walder, R., Folini, D., Favre, J. M., Krastanov, S., and Messmer, P. Apar-T: Code, validation, and physical interpretation of particle-in-cell results. *Astronomy and Astrophysics*, 558:A133, 2013. DOI: `10.1051/0004-6361/201321557`.

Michałek, G. and Ostrowsky, M. Cosmic ray momentum diffusion in the presence of nonlinear Alfvén waves. *Nonlinear Processes in Geophysics*, 3:66–76, 1996. DOI: `10.5194/npg-3-66-1996`.

Miller, J. A., Cargill, P. J., Emslie, A. G., Holman, G. D., Dennis, B. R., LaRosa, T. N., Winglee, R. M., Benka, S. G., and Tsuneta, S. Critical issues for understanding particle acceleration in impulsive solar flares. *Journal of Geophysical Research*, 102:14631–14660, 1997. DOI: `10.1029/97JA00976`.

Minoshima, T., Matsumoto, Y., and Amano, T. Multi-moment advection scheme for Vlasov simulations. *Journal of Computational Physics*, 230(17):6800–6823, 2011. DOI: `10.1016/j.jcp.2011.05.010`.

Möbius, E., Scholer, M., Hovestadt, D., Klecker, B., and Gloeckler, G. Comparison of helium and heavy ion spectra in He-3-rich solar flares with model calculations based on stochastic Fermi acceleration in Alfvén turbulence. *The Astrophysical Journal*, 259: 397–410, 1982. DOI: `10.1086/160177`.

Moya, P. S., Viñas, A. F., Muñoz, V., and Valdivia, J. A. Computational and theoretical study of the wave-particle interaction of protons and waves. *Annales Geophysicae*, 30 (9):1361–1369, 2012. DOI: `10.5194/angeo-30-1361-2012`.

Ng, C. K. and Reames, D. V. Focused interplanetary transport of approximately 1 MeV solar energetic protons through self-generated Alfvén waves. *The Astrophysical Journal*, 424(2):1032–1048, 1994.

Ng, C. K. and Reames, D. V. Shock acceleration of solar energetic protons: The first 10 minutes. *The Astrophysical Journal Letters*, 686:L123, 2008. DOI: `10.1086/592996`.

Nielson, K. D., Howes, G. G., and Dorland, W. Alfvén wave collisions, the fundamental building block of plasma turbulence. II. Numerical solution. *Physics of Plasmas*, 20(7): 072303, 2013. DOI: `10.1063/1.4812807`.

Palmroth, M., Archer, M., Vainio, R., Hietala, H., Pfau-Kempf, Y., Hoilijoki, S., Hannuksela, O., Ganse, U., Sandroos, A., von Alfthan, S., and Eastwood, J. P. ULF foreshock under radial IMF: THEMIS observations and global kinetic simulation Vlasiator results compared. *Journal of Geophysical Research: Space Physics*, 120:8782–8798, 2015. DOI: `10.1002/2015JA021526`.

Parker, E. N. Dynamics of the interplanetary gas and magnetic fields. *The Astrophysical Journal*, 128:664, 1958. DOI: `10.1086/146579`.

Penn, G., Stoltz, P. H., Cary, J. R., and Wurtele, J. Boris push with spatial stepping. *Journal of Physics G: Nuclear and Particle Physics*, 29(8):1719–1722, 2003. DOI: `10.1088/0954-3899/29/8/337`.

Petrov, G. M. and Davis, J. A generalized implicit algorithm for multi-dimensional particle-in-cell simulations in Cartesian geometry. *Physics of Plasmas*, 18(7):073102, 2011. DOI: `10.1063/1.3603837`.

Piel, A. *Plasma Physics.* Springer-Verlag Berlin Heidelberg, 2010. ISBN 978-3-642-10490-9. DOI: `10.1007/978-3-642-10491-6`.

Pulkkinen, P. and Tuominen, I. Velocity structures from sunspot statistics in cycles 10 to 22. I. Rotational velocity. *Astronomy and Astrophysics*, 332:748–754, 1998.

Qin, G., Matthaeus, W. H., and Bieber, J. W. Perpendicular transport of charged particles in composite model turbulence: Recovery of diffusion. *Astrophysical Journal*, 578:L117–L120, 2002. DOI: `10.1086/344687`.

Reames, D. V. Particle acceleration at the Sun and in the heliosphere. *Space Science Review*, 90:413–491, 1999. DOI: `10.1023/A:1005105831781`.

Reames, D. V. Solar energetic particle variations. *Advances in Space Research*, 34:381–390, 2004. DOI: `10.1016/j.asr.2003.02.046`.

Reames, D. V., Barbier, L. M., and Ng, C. K. The spatial distribution of particles accelerated by coronal mass ejection-driven shocks. *The Astrophysical Journal*, 466:473, 1996. DOI: `10.1086/177525`.

Reames, D. V., Kahler, S. W., and Ng, C. K. Spatial and temporal invariance in the spectra of energetic particles in gradual solar events. *The Astrophysical Journal*, 491:414–420, 1997. DOI: `10.1086/304939`.

Roth, I. and Temerin, M. Enrichment of ^{3}He and heavy ions in impulsive solar flares. *The Astrophysical Journal*, 477:940–957, 1997.

Saha, M. N. Ionization in the solar chromosphere. *Philosophical Magazine Series 6*, 40(238): 472–488, 1920. DOI: `10.1080/14786441008636148`.

Saha, M. N. On a physical theory of stellar spectra. *Proceedings of the Royal Society of London A*, 99:135–153, 1921. DOI: `10.1098/rspa.1921.0029`.

Sahraoui, F., Goldstein, M. L., Robert, P., and Khotyaintsev, Y. V. Evidence of a cascade and dissipation of solar-wind turbulence at the electron gyroscale. *Physical Review Letters*, 102:231102, 2009. DOI: `10.1103/PhysRevLett.102.231102`.

Sahraoui, F., Goldstein, M. L., Belmont, G., Canu, P., and Rezeau, L. Three dimensional anisotropic k spectra of turbulence at subproton scales in the solar wind. *Physical Review Letters*, 105:131101, 2010. DOI: `10.1103/PhysRevLett.105.131101`.

Saito, S., Gary, S. P., Li, H., and Narita, Y. Whistler turbulence: Particle-in-cell simulations. *Physics of Plasmas*, 15(10):102305, 2008. DOI: `10.1063/1.2997339`.

Savitzky, A. and Golay, M. J. E. Smoothing and differentiation of data by simplified least squares procedures. *Analytical Chemistry*, 36:1627–1639, 1964. DOI: `10.1021/ac60214a047`.

Schekochihin, A. A., Cowley, S. C., Dorland, W., Hammett, G. W., Howes, G. G., Quataert, E., and Tatsuno, T. Astrophysical gyrokinetics: Kinetic and fluid turbulent cascades in magnetized weakly collisional plasmas. *The Astrophysical Journal Supplement Series*, 182(1):310, 2009. DOI: `10.1088/0067-0049/182/1/310`.

Schlichenmaier, R. and Stix, M. The phase of the radial mean field in the solar dynamo. *Astronomy and Astrophyics*, 302:264, 1995.

Schlickeiser, R. Cosmic-ray transport and acceleration. I - Derivation of the kinetic equation and application to cosmic rays in static cold media. II - Cosmic rays in moving cold media with application to diffusive shock wave acceleration. *The Astrophysical Journal*, 336:243–293, 1989. DOI: `10.1086/167009`.

Schlickeiser, R. Cosmic-ray transport and acceleration. *The Astrophysical Journal Supplemet Series*, 90:929–936, 1994. DOI: `10.1086/191927`.

Schlickeiser, R. On the propagation of light in relativistic Maxwellian plasmas. *Astronomy and Astrophysics*, 294(2):615–625, 1995.

Schlickeiser, R. *Cosmic Ray Astrophysics*. Springer-Verlag Berlin Heidelberg New York, corrected second printing edition, 2003. ISBN 3-540-66465-3.

Schlickeiser, R. Linear theory of temperature anisotropy instabilities in magnetized thermal pair plasmas. *The Open Plasma Physics Journal*, 3(1):1–19, 2010. DOI: `10.2174/1876534301003010001`.

Schlickeiser, R., Fichtner, H., and Kneller, M. Revised Landau damping rates of magnetohydrodynamic waves in hot magnetized equilibrium plasmas and its consequences for cosmic ray transport in the interplanetary medium. *Journal of Geophysical Research*, 102(A3):4725–4739, 1997. DOI: `10.1029/96JA03432`.

Schreiner, C. *Resonante Welle-Teilchen-Wechselwirkung in kinetischen Plasmen*. master thesis, Julius-Maximilians-Universität Würzburg, 2013.

Schreiner, C. and Spanier, F. Wave-particle-interaction in kinetic plasmas. *Computer Physics Communications*, 185:1981–1986, 2014. DOI: `10.1016/j.cpc.2014.03.028`.

Schreiner, C. and Spanier, F. Effects of dispersive wave modes on charged particles transport. In *Proceedings of the ICRC 2015*, Proceedings of Science, 2015. URL `http://pos.sissa.it/archive/conferences/236/177/ICRC2015_177.pdf`. PoS(ICRC2015)177.

Schreiner, C., Kilian, P., and Spanier, F. Recovering the damping rates of cyclotron damped plasma waves from simulation data. *Communications in Computational Physics*, 21(4): 947–980, 2017a. DOI: `10.4208/cicp.OA-2016-0091`.

Schreiner, C., Kilian, P., and Spanier, F. Particle scattering off of right-handed dispersive waves. *The Astrophysical Journal*, 834(2):161–179, 2017b. DOI: `10.3847/1538-4357/834/2/161`.

Schrijver, C. J. The coronae of the Sun and solar-type stars. In Garcia Lopez, R. J., Rebolo, R., and Zapaterio Osorio, M. R., editors, *11th Cambridge Workshop on Cool*

Stars, Stellar Systems and the Sun, volume 223 of *Astronomical Society of the Pacific Conference Series*, page 131, 2001.

Schwabe, H. Sonnen-Beobachtungen im Jahre 1843. *Astronomische Nachrichten*, 21:234–235, 1844. DOI: `10.1002/asna.18440211505`.

Schwenn, R. and Marsch, E., editors. *Physics of the Inner Heliosphere*, volume 20 of *Physics and Chemistry in Space, Space and Solar Physics*. Springer Berlin Heidelberg, 1990. ISBN 978-3-642-75363-3. DOI: `10.1007/978-3-642-75361-9`.

Seough, J. J. and Yoon, P. H. Analytic models of warm plasma dispersion relations. *Physics of Plasmas*, 16:092103, 2009. DOI: `10.1063/1.3216459`.

Shalchi, A. and Schlickeiser, R. Cosmic ray transport in anisotropic magnetohydrodynamic turbulence. IV. Steep wave spectra. *Astronomy and Astrophysics*, 454:1–9, 2006. DOI: `10.1051/0004-6361:20054572`.

Shalchi, A., Bieber, J. W., Matthaeus, W. H., and Qin, G. Nonlinear parallel and perpendicular diffusion of charged cosmic rays in weak turbulence. *The Astrophysical Journal*, 616(1):617, 2004. DOI: `10.1086/424839`.

Shibata, K., Masuda, S., Shimojo, M., Hara, H., Yokoyama, T., Tsuneta, S., Kosugi, T., and Ogawara, Y. Hot-plasma ejections associated with compact-loop solar flares. *The Astrophysical Journal Letters*, 451:L83, 1995. DOI: `10.1086/309688`.

Shiota, D., Isobe, H., Chen, P. F., Yamamoto, T. T., Sakajiri, T., and Shibata, K. Self-consistent magnetohydrodynamic modeling of a coronal mass ejection, coronal dimming, and a giant cusp-shaped arcade formation. *The Astrophysical Journal*, 634:663–678, 2005. DOI: `10.1086/496943`.

Skender, M. and Tsiklauri, D. Whistler wave generation by non-gyrotropic, relativistic, electron beams. *Physics of Plasmas*, 21(4):042904, 2014. DOI: `10.1063/1.4871723`.

Sonnerup, B. U. Ö. and Su, S.-Y. Large amplitude whistler waves in a hot collision-free plasma. *Physics of Fluids*, 10:462–464, 1966. DOI: `10.1063/1.1762132`.

Sridhar, S. and Goldreich, P. Toward a theory of interstellar turbulence. I: Weak Alfvénic turbulence. *Astroparticle Physics*, 432:612–621, 1994. DOI: `10.1086/174600`.

Stawicki, O., Gary, S. P., and Li, H. Solar wind magnetic fluctuation spectra: Dispersion versus damping. *Journal of Geophysical Research*, 106(A5):8273–8281, 2001. DOI: `10.1029/2000JA000446`.

Steinacker, J. and Miller, J. A. Stochastic gyroresonant electron acceleration in a low-beta plasma. I - Interaction with parallel transverse cold plasma waves. *The Astrophysical Journal*, 393:764–781, 1992. DOI: `10.1086/171544`.

Stix, M. *The Sun*. Astronomy and Astrophysics Library. Springer Berlin Heidelberg, second edition, 2002. ISBN 978-3-642-56042-2. DOI: `10.1007/978-3-642-56042-2`.

Stix, T. H. Generation and thermalization of plasma waves. *Physics of Fluids*, 1(308): 125–133, 1958. DOI: `10.1063/1.1705889`.

Stix, T. H. *The Theory of Plasma Waves.* McGawn-Hill, Inc., 1962.

Stix, T. H. *Waves in Plasma.* Springer-Verlag, New York, Inc., 1992. ISBN 0-88318-859-7.

Strauss, H. R. Nonlinear, three-dimensional magnetohydrodynamics of noncircular tokamaks. *Physics of Fluids*, 19:134–140, 1976. DOI: `10.1063/1.861310`.

Sudan, R. N. and Ott, E. Theory of triggered VLF emissions. *Journal of Geophysical Research*, 76:4463–4476, 1971. DOI: `0.1029/JA076i019p04463`.

Temerin, M. and Roth, I. The production of He-3 and heavy ion enrichment in He-3-rich flares by electromagnetic hydrogen cyclotron waves. *The Astrophysical Journal Letters*, 391:L105–L108, 1992. DOI: `10.1086/186408`.

Told, D., Cookmeyer, J., Muller, F., Astfalk, P., and Jenko, F. Comparative study of gyrokinetic, hybrid-kinetic and fully kinetic wave physics for space plasmas. *New Journal of Physics*, 18(6):065011, 2016. DOI: `10.1088/1367-2630/18/6/065011`.

Tonks, L. and Langmuir, I. Oscillations in ionized gases. *Physical Review*, 33(2):195–210, 1929. DOI: `10.1103/PhysRev.33.195`.

Trotta, E. M. and Zimbardo, G. Quasi-ballistic and superdiffusive transport for impulsive solar particle events. *Astronomy and Astrophysics*, 530:A130, 2011. DOI: `10.1051/0004-6361/201016278`.

Vainio, R. Charged-particle resonance conditions and transport coefficients in slab-mode waves. *The Astrophysical Journal Supplement Series*, 131(2):519, 2000. DOI: `10.1086/317372`.

Vainio, R. and Kocharov, L. Proton transport through self-generated waves in impulsive flares. *Astronomy and Astrophysics*, 375:251–259, 2001. DOI: `10.1051/0004-6361:20010846`.

Vainio, R. and Laitinen, T. Monte Carlo simulations of coronal diffusive shock acceleration in self-generated turbulence. *The Astrophysical Journal*, 658:622–630, 2007. DOI: `10.1086/510284`.

Vainio, R., Laitinen, T., and Fichtner, H. A simple analytical expression for the power spectrum of cascading Alfvén waves in the solar wind. *Astronomy and Astrophysics*, 407:713–723, 2003. DOI: `10.1051/0004-6361:20030914`.

Vay, J. Simulation of beams or plasmas crossing at relativistic velocity. *Physics of Plasmas*, 15(5):056701–1–056701–6, 2008. DOI: `10.1063/1.2837054`.

Vay, J.-L., Geddes, C., Cormier-Michel, E., and Grote, D. Numerical methods for instability mitigation in the modeling of laser wakefield accelerators in a Lorentz-boosted frame. *Journal of Computational Physics*, 230(15):5908 – 5929, 2011. ISSN 0021-9991. DOI: `10.1016/j.jcp.2011.04.003`.

Verkhoglyadova, O. P., Tsurutani, B. T., and Lakhina, G. S. Properties of obliquely propagating chorus. *Journal of Geophysical Research*, 115:A00F19, 2010. DOI: `10.1029/2009JA014809`.

Vlasov, A. A. On vibration properties of electron gas. *Journal of Experimental and Theoretical Physics*, 8(3):291–318, 1938.

Völk, H. J. Nonlinear perturbation theory for cosmic ray propagation in random magnetic fields. *Astrophysics and Space Science*, 25:471–490, 1973. DOI: `10.1007/BF00649186`.

Weibel, E. S. Dimensionally correct transformations between different systems of units. *American Journal of Physics*, 36(12), 1968. DOI: `10.1119/1.1974378`.

Wisniewski, M., Spanier, F., and Kissmann, R. Diffusion of energetic particles in turbulent MHD plasmas. *The Astrophysical Journal*, 750(150), 2012. DOI: `10.1088/0004-637X/750/2/150`.

Yee, K. Numerical solution of inital boundary value problems involving Maxwell's equations in isotropic media. *IEEE Transactions on Antennas and Propagation*, 14(3):302–307, 1966. ISSN 0018-926X.

Zank, G. P., Rice, W. K. M., and Wu, C. C. Particle acceleration and coronal mass ejection driven shocks: A theoretical model. *Journal of Geophysical Research*, 105:25079–25096, 2000. DOI: `10.1029/1999JA000455`.

List of Publications

Peer-reviewed Publications

- **Schreiner, C.** and Spanier, F.: Wave-particle-interaction in kinetic plasmas. *Computer Physics Communications*, 185 (2014), 1981–1986, DOI: 10.1016/j.cpc.2014.03.028.
- Kempf, A., Kilian, P., Ganse, U., **Schreiner, C.**, and Spanier, F.: PICPANTHER: A simple, concise implementation of the relativistic moment implicit Particle-in-Cell method. *Computer Physics Communications*, 188 (2015), 198–207, DOI: 10.1016/j.cpc.2014.11.010.
- **Schreiner, C.**, Kilian, P., and Spanier, F.: Particle scattering off of right-handed dispersive waves. *The Astrophysical Journal*, 834 (2017), 161, DOI: 10.3847/1538-4357/834/2/161.
- **Schreiner, C.**, Kilian, P., and Spanier, F.: Recovering the damping rates of cyclotron damped plasma waves from simulation data. *Communications in Computational Physics*, 21 (2017), 947–980, DOI: 10.4208/cicp.OA-2016-0091.
- Kilian, P., Muñoz, P., **Schreiner, C.**, and Spanier, F.: Plasma waves as a benchmark problem. *Journal of Plasma Physics*, 83 (2017), 707830101, DOI: 10.1017/S0022377817000149.

Other Publications

- **Schreiner, C.** and Spanier, F.: Transport of energetic particles in the heliosphere. In Wagner, S., Bode, A., Satzger, H., and Brehm, M. (editors): *High Performance Computing in Science and Engineering – Garching/Munich 2014*, 38–39, ISBN 978-3-9816675-0-9.
- **Schreiner, C.** and Spanier, F.: Effects of dispersive wave modes on charged particles transport. In *Proceedings of the ICRC 2015* (2015), PoS(ICRC2015)177.
- **Schreiner, C.**, Kilian, P., Ganse, U., Kempf, A., Spanier, F., and Mannheim, K.: Modeling dispersive plasma waves with particle in cell simulations. In Wagner, S., Bode, A., Brüchle, H., and Brehm, M. (editors): *High Performance Computing in Science and Engineering – Garching/Munich 2016*, 36–37, ISBN 978-3-9816675-1-6.

Conferences and Workshops

- Spring Meeting of the German Physical Society, Berlin, 2014 (two talks).
- Extreme Scaling Workshop, Leibniz Supercomputing Centre (LRZ), Garching/Munich, 2014.
- Annual Meeting of the German Astronomical Society (AG), Bamberg, 2014 (talk).
- CHPC National Meeting, Skukuza, 2014 (talk).
- Spring Meeting of the German Physical Society, Bochum, 2015 (talk).
- AstroLab (High-level Support and Code Optimization Workshop), Leibniz Supercomputing Centre (LRZ), Garching/Munich, 2015.
- International Cosmic Ray Conference (ICRC), Den Haag, 2015 (talk).
- SuperMUC Status and Results Workshop, Leibniz Supercomputing Centre (LRZ), Garching/Munich, 2016 (invited talk).

Acknowledgments

The success or failure of projects, such as the PhD thesis at hand, does not depend on a single person[47]. Many people contribute, assist and collaborate during the process of such a project, and it is these people who should be remembered and thanked here.

First of all I would like to express my gratitude to Prof. Felix Spanier, who proposed the topic of this thesis and who was my supervisor. I am sure that it was not easy to convince me to accept the offer of this PhD project, but I am glad that he succeeded. The cooperation and flexibility which he displayed are rarely found among people in general and supervisors or employers in particular. Working in his group felt more like working *with* him than working *for* him. Meaning no offense, I would not say that he always knew the answers to my questions, but he never hesitated to sit down and discuss the problem until an acceptable solution was found. The freedom to address whichever problem I felt was most important at a given time was also something I appreciate. There were hardly any deadlines for specific projects and still it almost always worked out in the end. As one of Prof. Felix Spanier's most important traits, his boundless optimism has to be named. Without his words of motivation many projects would have likely been left unfinished.

Furthermore I would like to thank Petro Sieberhagen, who is probably the second most important person among those who have made this PhD project possible. Without her support I would have never made my way through the bureaucratic jungle which accompanies the registration, maintenance and completion of such a PhD project. I would like to honestly express my respect for her staying on top of all the different forms, applications, reports and whatsoever.

In no particular order I would like to thank my colleagues, both those who still remain true to science and those who have left to find something new. All of them have made countless contributions (big or small) to my work and it is impossible to adequately name and valuate all of them in a short section of text. In the following I will therefore just pick a few individual topics. One important group of persons is the so-called *ACRONYM collaboration*, which is partly organized in the "Verein zur Förderung kinetischer Plasmasimulationen e.V.", and consists of a bunch of truly amazing people who seem to like writing new code more than doing physics. Without the work of Dr. Urs Ganse, Dr. Patrick Kilian, Dr. Andreas Kempf and Dr. Patricio Muñoz the ACRONYM code would not be as fast, multi-functional, stable, and user-friendly as it is today. Furthermore, these four gentleman provide their service and advice whenever needed, nearly 24 hours a day and seven days a week. Apart from their knowledge and skills in numerical questions, they are, of course, also capable physicists.

Dr. Patrick Kilian is probably the person, with whom I had the most discussions on plasma physical topics, and I am thankful for all of them. However, I would like to emphasize the few, but dedicated discussions with Dr. Sebastian Lange, to whom I am especially grateful. Even years after he had turned his back on science he was still available for and open to discussions of his work and provided helpful comments on my problems.

---

[47] Well, failure sometimes might...

Of course I have to mention my “companion in misfortune” and fellow PhD student, Alex Ivascenko, whom I would like to thank for interesting discussions, on both work related and completely unrelated topics, and for teaching me the use of his analysis method for the calculation of diffusion coefficients. He was also a valuable companion on various conferences and road trips.

I would also like to express my gratitude to Prof. Rami Vainio for sharing his extensive knowledge on particle transport and acceleration in the solar wind. The discussion of resonant wave-particle interactions and the requirements for pitch angle diffusion were especially fruitful and helped to significantly improve the work presented in this thesis.

Special thanks go to Prof. Karl Mannheim, who agreed to become the manager of my *SuperMUC* project and who provided me with an office at the University of Würzburg. The project *pr84ti*, “Numerical Modeling of the Microphysical Foundation of Astrophysical Particle Acceleration”, was crucial for the success of this PhD thesis, since it allowed me to access the computational resources at the Leibniz Supercomputing Centre (LRZ) in Garching/Munich, namely their supercomputer *SuperMUC*. Professor Karl Mannheim also supported me in various other ways, from office supplies over the access to hard- and software to even financial support, during my time in Würzburg, for which I am truly grateful.

While I'm at it, I would also like to thank my “neighbors” in Würzburg for the fun times we had (sorry, it cannot really be called “work”). Jonas Trüstedt and Katha Leiter were always fun to talk to (also, Jonas' tea was excellent), Markus Zenk's mathematical view on physical problems often lead to interesting discussions, and Dr. Alejandro Bolaños was simply the best indoor gardener of the institute. Also many thanks for the countless times you had to co-sign any of my South African documents.

Next comes the official, but nevertheless heartfelt acknowledgment for my use of *SuperMUC*: The authors gratefully acknowledge the Gauss Centre for Supercomputing e.V. (www.gauss-centre.eu) for funding this project by providing computing time on the GCS Supercomputer SuperMUC at Leibniz Supercomputing Centre (LRZ, www.lrz.de). Said computing time amounted to 10 million CPU-hours in project *pr84ti* and a little rest from the previous project *pr85li*. Most of the provided resources have actually been used.

During project *pr84ti* I have also met a few members of the team which keeps the users happy and *SuperMUC* running. In the context of the AstroLab support workshop I would like to name and thank Dr. Nicolay Hammer, Dr. Anupam Karmakar and Dr. Sandra Méndez, who helped to analyze and improve the output routines of the ACRONYM code.

Last, but not least, I want to thank Dr. Patrick Kilian and Dr. Stephan Richter for proofreading this work. Their effort and their detailed comments helped to improve this thesis regarding both its content and language. I am sorry for writing so much text and I will get you some new red pencils some time or another.

There are still more people, whom I wish to thank and who are missing here, either because I wish to speak to them in person, or because of my poor memory. If you feel like you belong to the latter group, then please accept my apologies and feel free to complain at any time.